Development, Modeling and Testing of a Slow-Burning Solid Rocket Propulsion System

by

Matthew T. Vernacchia

B.S. in Aerospace Engineering with Information Technology
Massachusetts Institute of Technology, 2015

Submitted to the Department of Aeronautics and Astronautics
in partial Fulfillment of the requirements for the degree of

Master of Science in Aeronautics and Astronautics

at the

Massachusetts Institute of Technology

June 2017

Signature of Author: Signature redacted

Matthew T. Vernacchia
Department of Aeronautics and Astronautics
May 30, 2017

Certified by: Signature redacted

R. John Hansman, Jr.
T. Wilson Professor of Aeronautics and Astronautics
Thesis Supervisor

Accepted by: Signature redacted

Youssef M. Marzouk
Associate Professor of Aeronautics and Astronautics
Chair, Graduate Program Committee

Development, Modeling and Testing of a Slow-Burning Solid Rocket Propulsion System

by

Matthew T. Vernacchia

Submitted to the Department of Aeronautics and Astronautics
on May 30, 2017 in partial Fulfillment of the requirements
for the degree of Master of Science in Aeronautics and Astronautics

Abstract

Small, unmanned aerial vehicles (UAVs) are expanding the capabilities of aircraft systems. However, a gap exists in the size and capability of aircraft: no aircraft smaller than 10 kilograms are capable of flight faster than 100 meters per second. A small, fast aircraft requires a propulsion system which is both miniature and high-power, requirements which current UAV propulsion technologies do not meet. To meet this need, a slow-burning solid rocket motor has been developed. Such motors require slow-burning solid propellants with tailorable burn rate.

This thesis reports experimental results and combustion theory for a slow-burning solid propellant. It also describes a rocket motor designed to use this propellant, and the manufacturing process used to produce it. This propellant burns slowly enough for the low-thrust, long-endurance needs of UAV propulsion. Its burn rate can be predictably tailored by addition of the burn rate suppressant oxamide.

Further, this thesis presents a concept for a small, fast aircraft designed around this novel propulsion technology. The motor integrates elegantly into the aircraft's structure, and compact thermal protection system insulates other vehicle systems from the heat of combustion.

These results demonstrate the feasibility slow-burning rocket propulsion systems, and their application to small aircraft. It should be possible for small, rocket-propelled UAVs to sustain powered, transonic flight for several minutes. With this technology, kilogram-scale UAVs could be able to quickly deploy over tens of kilometers, and fly joint missions alongside manned fighter jets.

Thesis Supervisor: R. John Hansman, Jr.
Title: T. Wilson Professor of Aeronautics and Astronautics

Acknowledgements

I thank my friend and colleague Tony Tao for his mentorship and comradery in this project. I have learned much from exploring your kingdom of UAVs. It has been an honor to design the Firefly UAV with you.

I thank MIT Lincoln Laboratories and the United States Department of Defense for sponsoring this research. Dr. Marc Viera, Dr. Bryan Tipton, and their colleagues at Lincoln Labs have been excellent advocates of our work.

I thank my co-workers in this project: graduate researcher Jonathan R. Spirnak and undergraduates Kelly J. Mathesius, Carlos R. Garcia, Madeleine C. Jansson, Zhishen Wang, Zachary J. Bierstedt, Michael Trinh, Andrew Adams, Jonathan Zdasiuk, Brad Jokubaitis, and Timothy Nguyen. I am particularly grateful to Mr. Garcia for a literature review which uncovered the burn rate suppressant oxamide, which became a critical thrust of this research.

I greatly appreciate the help of Todd Billings and David Robertson, the Aero Astro shop instructors, in building the hardware for this project. They taught me how to turn ideas into metal.

I am indebted to Jake Hecla of the MIT Nuclear Science and Engineering Department for performing x-ray imaging of our propellant samples. In a remarkable feat of improvisation, he built a functional x-ray imager from spare parts in a single afternoon.

I thank Mark Kirby and Carl Hamann of Renishaw plc. for their excellent additive manufacturing services.

I am grateful to my parents, Katherine and John Vernacchia, for always indulging my curiosity. I am also grateful to the community of MIT for being my "second family" for the past six years. This campus is a beautiful place, where I have felt inspired, loved and respected.

Finally, I thank my thesis supervisor Prof. R. John Hansman for his support and guidance during my graduate studies.

Software tools

I would like to thank the creators of the following software tools, which were instrumental to this research and the preparation of this document:

- **The *SciPy* python scientific computing stack, produced by Travis Oliphant, Pearu Peterson, Eric Jones, John D. Hunter, Wes McKinney, and a large community of developers [1]. The stack includes:**
  - ***NumPy*, the fundamental package for scientific computing with Python. Free, open-source, available at http://www.numpy.org/**
  - ***Matplotlib*, a plotting library. Free, open-source, available at http://matplotlib.org/**
  - ***Pandas*, a library for data structures and data analysis tools. Free, open-source, available at http://pandas.pydata.org/**
- ***rpy2*, an interface between python and the *R* statistical computing language produced by Laurent Gautier et. al. Free, open-source, available at https://rpy2.readthedocs.io**
- ***Cantera*, a software toolkit for chemical kinetics, thermodynamics, and transport processes by David G. Goodwin, Harry K. Moffat, and Raymond L. Speth. Free, open-source, available at https://www.cantera.org**
- ***Rocket Propulsion Analysis*, an analysis tool for conceptual and preliminary design of chemical rocket engines produced by Alexander Ponomarenko. Paid, closed-source, executables may be purchased from http://propulsion-analysis.com**
- ***SolidWorks*, a computer-aided design (CAD) and simulation program, produced by Dassault Systèmes. Paid, closed-source, executables may be purchased from http://www.solidworks.com/**

Contents

Nomenclature

Acronyms

AP – Ammonium perchlorate, NH_4ClO_4, an oxidizer used in solid propellants

APCP – Ammonium perchlorate composite propellant

AN – Ammonium nitrate, NH_4NO_3, an oxidizer used in solid propellants

CAO-5 – an antioxidant used in solid propellant

DSC – differential scanning calorimetry

GAP – glycidyl azide polymer, an energetic binder used in solid propellants

HTPB - Hydroxyl-terminated polybutadiene, a rubberlike binder used in solid propellants

HMX – a nitroamine high explosive

HX-752 – A bonding agent used in solid propellants

LPL – lower pressure limit of combustion, the lowest pressure at which a solid propellant will sustain combustion

MDI - methylene diphenyl diisocyanate, a curative used in solid propellants

MIT – Massachusetts Institute of Technology

RDX - a nitroamine high explosive

TGA – thermal gravimetric analysis

Ti-6-4 or Ti-6Al-4V – an alloy of titanium. Specifically, Ti-6Al-4V Extra Low Interstitial (ASTM B348, Grade 23) was used in this work

UAV – Unmanned aerial vehicle

Units of measure

The standard abbreviations are used for the *Système international d'unités* (SI units) [2].

In some places, English Engineering Units are also provided to make the work more accessible to a US audience. They are abbreviated as:

lbm – pound mass
lbf – pound force
in – inch
ft – feet
psi – pound force per square inch
ksi – 1000 pound force per square inch
knot – nautical mile per hour
F – degrees Fahrenheit

phr – parts per hundred rubber by mass, is a unit typical in polymer science which is used to measure additive concentrations in some propellant formulas.

Mathematical symbols

$*$ - denotes properties of a propellant in its fully dense burn rate modifier free condition. Note that c^* is an exception to this notation.

$\gamma = c_p/c_v$ - ratio of specific heats, unitless

λ – the oxamide parameter (in the context of propellant burn rate), or wavelength (in the context of lasers)

ρ – density

ρ_s – density of solid propellant

σ – standard deviation

σ_p – temperature sensitivity of burn rate for a solid propellant, units of inverse temperature

$\phi = r/r^*$ - burn rate multiplier

ϕ_{om} – burn rate multiplier due to oxamide

ϕ_v – burn rate multiplier due to voids

A - area

A_t – throat area of a rocket nozzle

A_b – area of the burning solid propellant surface in a solid rocket motor

a – burn rate coefficient in Vieille's Law, units of $[velocity \times pressure^{-n}]$

b_v – void parameter, a parameter of a model for the effect of relative density on propellant burn rate

C_F – Thrust coefficient of a rocket nozzle expansion process

c^* - characteristic velocity of propellant combustion

c_p – specific heat capacity and constant pressure

D – drag force

$D_r = \rho_s/\rho_s^*$ - relative density of a solid propellant

d_t – throat diameter of a rocket nozzle

F – thrust force

$g_0 = 9.81\ \mathrm{m\ s^{-2}}$ – acceleration due to gravity at Earth's surface

h - specific enthalpy or convection coefficient, depending on context

I - impulse

I_{sp} – specific impulse

j – mass flux

J – radiation power flux

$K = A_b/A_t$ – area ratio of a solid rocket motor, unitless

M – Mach number, unitless

$\mathcal{M}$ - molar mass

m – mass

$\dot{m}$ – mass flow

Nu - Nusselt number, unitless

n – burn rate exponent in Vieille's Law, unitless

Pr - Prandtl number, unitless

p – pressure

p_c – chamber pressure, combustion pressure

q – heat flux

$\mathcal{R} \approx 8.314\ \mathrm{J\ K^{-1}\ mol^{-1}}$ – universal gas constant

R – specific gas constant

Re - Reynolds number, unitless

r – solid propellant burn rate, units of velocity

T - temperature

T_c – chamber temperature, combustion temperature

t - time

t_f – flight time or endurance

V – volume

V_c – chamber volume in a solid rocket motor

v – velocity

w – mass fraction

w_{AP} – mass fraction of ammonium perchlorate in a solid propellant

w_{Al} – mass fraction of aluminum in a solid propellant

w_{HTPB} – mass fraction of hydroxyl-terminated polybutadiene in a solid propellant

w_{om} – mass fraction of oxamide in a solid propellant

z – altitude above mean sea level

Propellant designations

Propellant formations are designated according to the following convention:

OX.WW.XX-Bind-Add.YY-Add.ZZ

- Oxidizer specification
  - OX: 2 letter chemical identifier
    - AN for ammonium nitrate
    - AP for ammonium perchlorate
  - WW: Mass fraction
  - XX: Max particle size, or min/max particle size. Units are micrometers.
- Binder
  - Bind: Short chemical identifier
    - HTPB for hydroxyl terminated polybutadiene
  - The mass fraction of the binder is not listed – it is assumed to make up the balance left by the oxidizer and additives.
  - Binder modifiers (opacifier, plasticizer, curative) are not specified in the propellant name - they are assumed to be consistent for a particular binder. Special modifiers may be listed after the binder identifier with a slash, i.e. HTPB/HX752.
- Additives
  - Add: Chemical formula or other short identifier
  - YY: Mass fraction

Example: AP.63.125/250-HTPB/HX752-Mg.06-Om.08 propellant contains:

- Ammonium perchlorate oxidizer, making up 63% of the propellant's mass, with a particle size range of 125 to 250 μm,
- hydroxyl terminated polybutadiene binder with HX-752 bonding agent,
- magnesium powder additive, making up 6% of the propellant's mass, and
- oxamide burn rate suppressant additive, making up 8% of the propellant's mass.

1 Motivation: propulsion for small, fast aircraft

A gap exists in the size and capability of flight vehicles: no vehicles smaller than 10 kg (22 lbm) are currently capable of flight faster than 100 m s^{-1} (170 knots). The small and fast gap is illustrated by Figure 1, which plots the speed, size, and range of current US military aircraft. Speed and mass are plotted on logarithmic axes, so that a variety of aircraft, from tiny UAVs to supercruise fighter jets, can be included in a single plot. Each aircraft is represented by a dot plotted in speed versus mass space, and the area of the dot is proportional to the aircraft's flight range (very short-range aircraft show a "+" instead). The aircraft's propulsion technology is coded by the color of the dot.

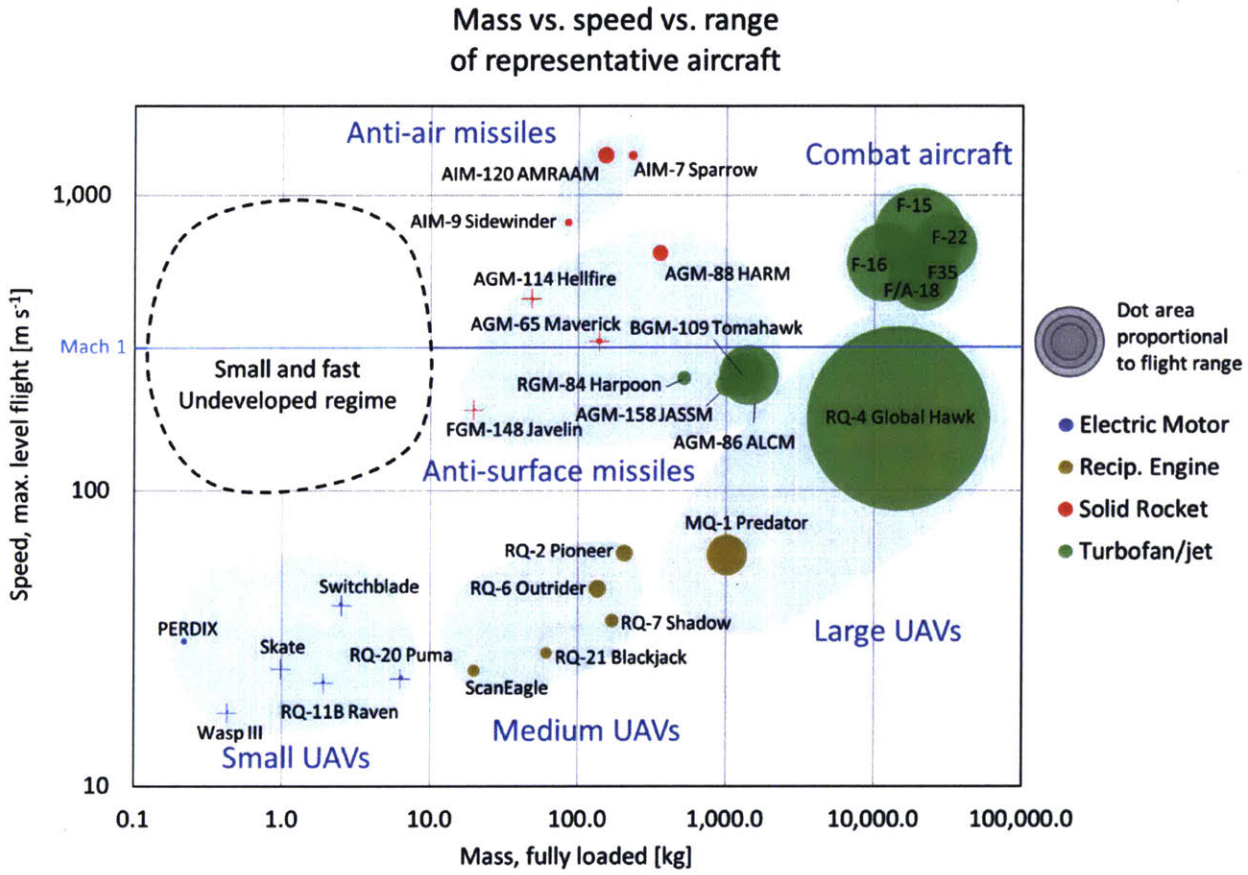

Figure 1: The speed vs size design space currently lacks small, fast aircraft. The mass axis uses maximum takeoff mass for aircraft, and launch mass (incl. payload and propellant) for missiles. Data from [3] [4] [5] [6] [7] [8].

The aircraft can be grouped into six classes:

1. *Small unmanned aerial vehicles (UAVs),* which are propelled by electrical motors and propellers, have flight speeds below 45 m s^{-1}, mass of a few kilograms or less, and short range (3 - 30 km).
2. *Medium UAVs*, which are propelled by reciprocating engines and propellers, have flight speeds below 70 m s^{-1}, mass of 10 – 200 kg, and moderate range (100 – 200 km).
3. *Large UAVs*, which are propelled by reciprocating or turbine engines, have flight speeds between 60 and 180 m s^{-1}, mass of several tons, and long range (> 1000 km).
4. *Combat aircraft*, which are propelled by turbine engines, have maximum flight speeds between 530 and 730 m s^{-1} (Mach 1.8 to 2.4), mass of 20 – 30 tons, and long range (> 1000 km).

5. *Anti-surface missiles*, which are propelled by turbine engines or solid rockets, have flight speeds between 190 and 640 m s^{-1} (Mach 0.6 to 2.1), mass of 20 – 360 kg, and short to moderate range (5 – 200 km).
6. *Anti-air missiles*, which are propelled by solid rockets, have flight speeds near 1000 m s^{-1} (Mach 2.7 to 4.5), mass near 100 kg, and short to moderate range (5 – 200 km).

There is a gap which the existing aircraft classes do not cover: small, fast aircraft with speed above 100 m s^{-1} and mass below 10 kg. This undeveloped regime is outlined in black on Figure 1. Small, fast aircraft in this regime would be advantageous for many missions [Appendix 1]. New aircraft should be developed which fill this gap.

1.1 Desired capabilities and preliminary vehicle concept

To explore the aircraft design space, this work selects a point in the regime of small, fast aircraft, and examines what would be required to develop an aircraft for that point. The selected design point is a representative choice from the middle of the unexplored region shown in Figure 1. The objectives of the vehicle concept are to:

1. have a mass less than 2 kilograms,
2. cruise at approximately Mach 0.8, and
3. maximize endurance, ideally providing several minutes of powered flight.

Conceptual sketches of a vehicle for this design point are shown in Figure 2. The vehicle concept has a length slightly over 400 mm (16 in), a fuselage volume of 1 L and a mass of 1.2 kg. It is designed for cruise at Mach 0.8 and 9 km altitude. The vehicle is expected to have a drag of 5 to 10 N in cruise [Section 1.3.1]. The drag and dimensions of this concept motivate the propulsion trade study presented in the following section. Potential missions for such a vehicle are proposed in Appendix 1.

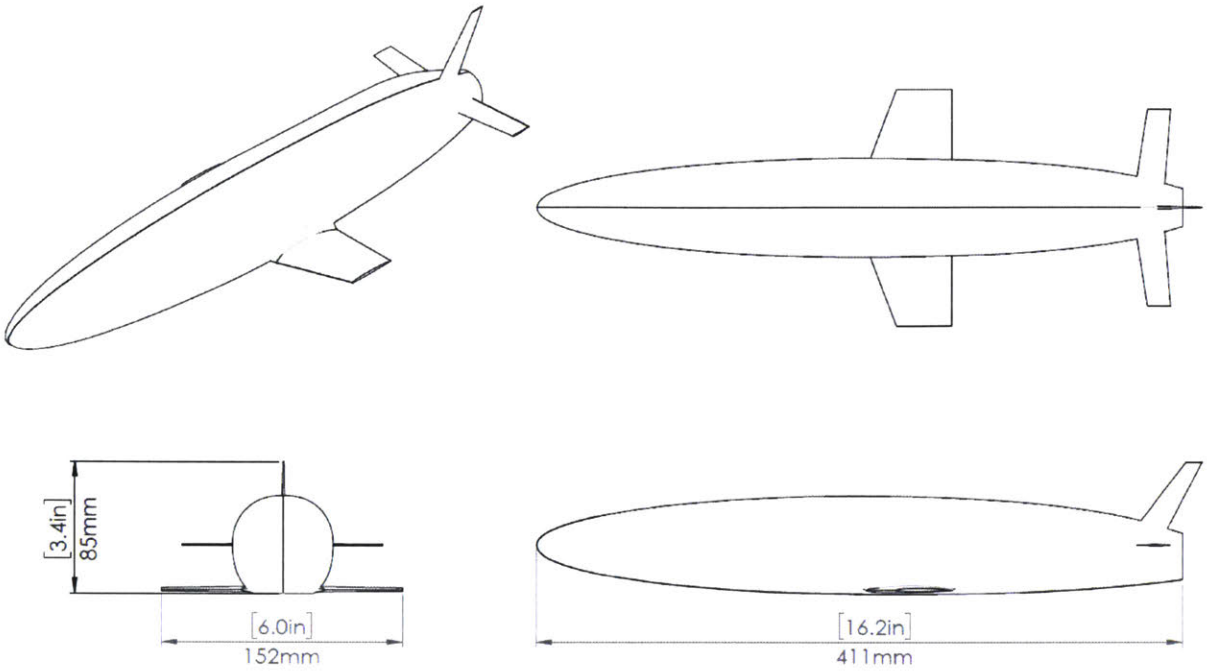

Figure 2: These concept sketches show the configuration and rough sizing of the vehicle concept.

1.2 Propulsion technology to fill the small and fast gap

Many technical challenges face the development of a small, fast aircraft. One significant challenge is that current propulsion systems do not fit the power needed for high-speed flight into a small package. Research must be undertaken to adapt propulsion technologies to the needs of this class of vehicle. The problem is thus: Of the propulsion technologies shown in Figure 1, which can be moved into the small, fast regime by miniaturization or an increase in flight speed capability?

The size and speed regimes in which various propulsion technologies are currently used is illustrated in Figure 3. Four categories of propulsion technology are in use:

1. *Electric motors / propellers*, which are used exclusively on small UAVs with low flight speeds,
2. *Reciprocating engines / propellers*, which are used on medium to large UAVs with flight speeds up to 70 m s^{-1},
3. *Solid rockets*, which are used on fast, medium-sized missiles, and
4. *Turbine engines*, which are used on large, fast combat aircraft, cruise missiles, and UAVs.

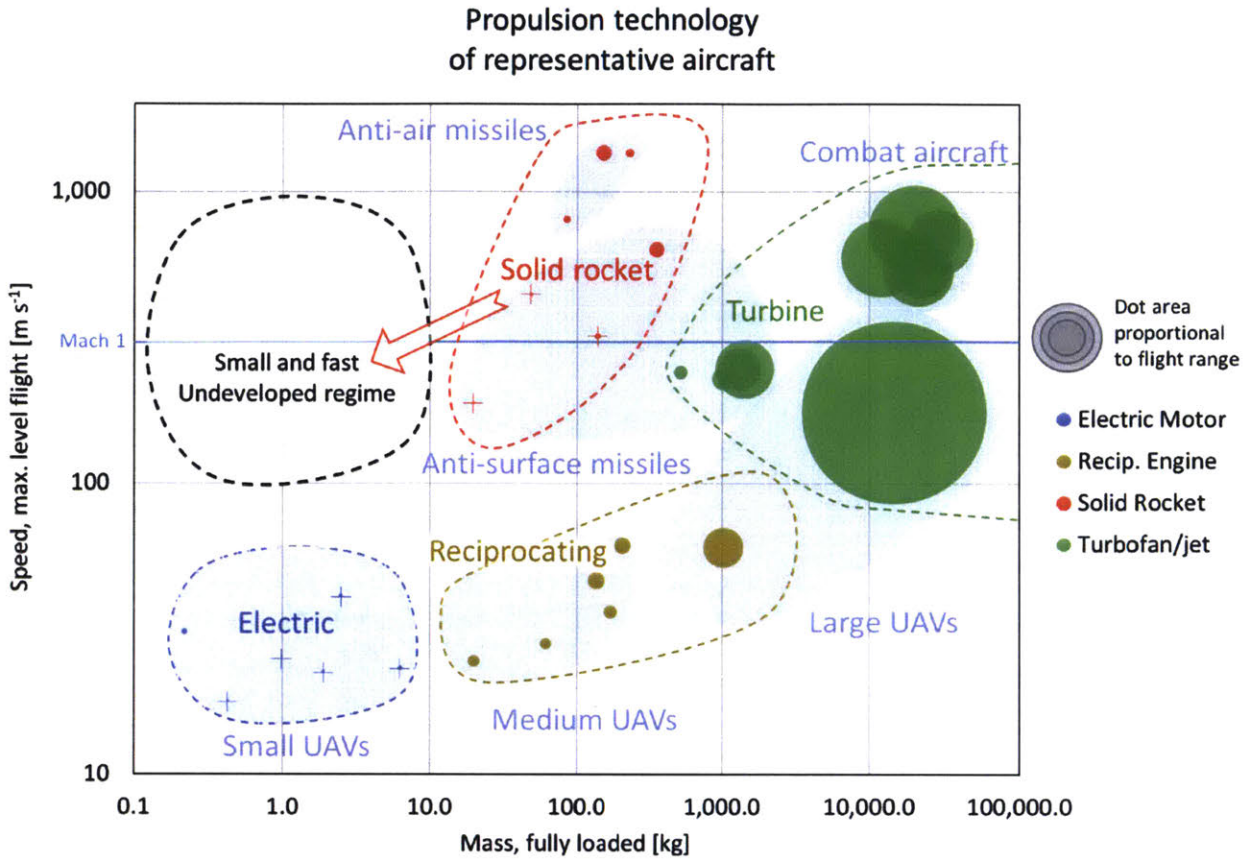

Figure 3: The size and speed regimes in which propulsion technologies are currently used. Solid rockets are the propulsion technology best suited for adaptation to small, fast aircraft.

The following subsections define the propulsion requirements of small, fast aircraft and evaluate the four propulsion technology categories against these requirements. Of these technologies, solid rockets appear best suited to the propulsion needs of small, fast aircraft.

1.2.1 Propulsion requirements for small, fast aircraft

Small, fast aircraft impose two key requirements on their propulsion systems:

1. *Thrust*: The propulsion system must provide sufficient thrust at high speed to counter the vehicle's drag. For this work's vehicle concept, the thrust level is 5 to 10 N at Mach 0.8. An analysis of vehicle's drag, presented in Subsection 1.3.1, justifies this thrust level.
2. *Compactness*: The propulsion system must fit within the vehicle, and package well with other vehicle systems. In the vehicle concept proposed above, the propulsion system can be afforded about half of the available mass and volume: 0.5 L and 0.5 kg.

Subject to these constraints, maximizing the vehicle's powered-flight endurance is a design objective.

Specific missions may impose additional requirements for storage, deployment, reliability or other concerns. Additionally, vehicle manufacturers will desire a propulsion system that can be produced at low cost, although this concern is typically secondary to other requirements in defense applications [9].

1.2.2 Propulsion system technical parameters

Several technical parameters can be used to evaluate whether a propulsion technology can meet the above objectives:

Specific power is the operating power of a power conversion device divided by the mass of its inert components. The propulsion system's power conversion device must have sufficiently high specific power to produce sufficient thrust, while being compact enough to fit within the vehicle. The vehicle concept has a drag power of 1-3 kW, but the power level of the propulsion system will be higher due to inefficiencies. The available propulsion system mass is 0.5 kg, but some of this must be reserved for energy storage. Thus, the minimum feasible specific power is roughly 10 kW kg^{-1}.

Miniaturization: minimum demonstrated size – It must be possible to miniaturize the propulsion system to meet the compactness requirement. Miniaturization potential is captured by the minimum size scale at which this propulsion technology has be demonstrated to produce useful thrust

Energetic density: specific energy[1] *and specific impulse*[2] – The propulsion technology and energy storage medium should provide long endurance within the vehicle's limited volume and mass constraints. To do so, the energy density of the storage medium and the specific impulse of the propulsion system should be as high as possible.

Cost and manufacturability – To achieve low cost the propulsion system should have few, mechanically simple components, which are easy to manufacture. Two metrics are used as proxies for cost: mechanical complexity and the cost of analogous hobby-grade components.

1.2.3 Propulsion technology comparison

Solid rocket motors appear to be the propulsion technology best suited for adaptation to small, fast aircraft. Electric motors, reciprocating engines, and turbojets all face difficult technical limitations, which restrict their applicability to this domain. The relative merits of these technologies are presented in Table 1.

---

[1] Specific energy is the useful energy capacity of a storage medium divided by its mass.

[2] Specific impulse is the thrust of a propulsion system divided by the propellant "weight flow":

$$I_{sp} \stackrel{\text{def}}{=} \frac{F}{\dot{m}\, g_0}$$

Table 1: A comparison of three propulsion technologies against the requirements of transonic UAV propulsion.

** The effective specific impulse for electric motors is defined as the ratio of impulse delivered to weight of batteries drained.*

Requirement or design objective	Metric	Required Value	Propulsion Technology			
			Solid Rocket motor	**Turbojet engine**	**Electric motor + propeller**	**Reciprocating engine + propeller**
Thrust	Specific power	> 10 kW kg^{-1}	~ 100 kW kg^{-1}	~ 100 kW kg^{-1} [10]	5 ~ 10 kW kg^{-1} [11]	~ 1 kW kg^{-1} [12]
Compactness	Minimum demonstrated size	Small	~ 1 mm [13]	~ 50 mm [10]	~ 1 mm	~ 10 mm [14]
Endurance	Specific energy of storage medium	High	10 MJ kg^{-1}	43 MJ kg^{-1}	0.5 MJ kg^{-1}	43 MJ kg^{-1}
	Specific impulse of propulsion system in Mach 0.8 flight	High	170 – 260 s	2000 – 3500 s	100 – 200 s *	2000 – 4000 s
Cost and manufacturability	Mechanical complexity	Low	Low	High	Medium	High
	Typical cost of hobby-grade systems	Low	$100	$3000	$100	$ 300

Electric motors + propellers are small, but motors and batteries have poor power and energy density; they cannot meet the energetic demands of fast flight. Reciprocating engines + propellers are difficult, but possible, to miniaturize. However, they suffer from a very low specific power (~1 kW kg^{-1} at small scales), and therefore cannot meet the thrust and compactness requirements. Both technologies are unsuited to high-speed flight because the effectiveness of propellers declines at high speeds.

Turbine engines are the most efficient propulsion solution for high-speed flight and have high specific power, but are difficult to miniaturize. Turbojets are sensitive to tight-tolerance dimensions (e.g. rotor tip clearance) which do not scale well at small sizes. Turbojets have specific impulse an order of magnitude better than rockets, but this is not fully realized as an endurance benefit for small UAVs. Compared to sold rockets, turbojets have bulkier inert components and a less-dense propellant. Thus, if a given mass and volume is allocated to the propulsion system (inert + propellant), the turbojet system will be able to carry less propellant than the rocket system. For a kilogram-scale vehicle, a turbojet propulsion system has about 2x the endurance of a rocket, not 10x as indicated by the specific impulse alone.

Solid rockets can provide the power required for high speed flight, and can be miniaturized to the size of kilogram-scale aircraft. Unlike propellers (or, to a lesser extent, turbojets), the thrust of a rocket does not diminish as flight speed increases. Solid rockets are mechanically simple, allowing them to be small and cheap: 100-gram scale rockets are commercially available for under 100 USD [15], and 10-milligram

scale rockets have been demonstrated in research settings [13]. Solid rockets have a number of other advantages, such as good storability, temperature tolerance, and reliable startup.

However, because small aircraft have low thrust requirements, the thrust level of solid rocket motors for UAV propulsion will usually be on the order of 10 N. This thrust level is orders of magnitude lower than is typical for kilogram-scale solid rockets. To operate at a lower thrust level, the rocket requires a slower-burning solid propellant.

Adapting solid rockets to the low-thrust needs of small aircraft motivates the development of slow-burning solid propellants and a compact, long-endurance rocket motor. These development efforts are the focus of this thesis.

1.3 Challenges of small, slow-burning solid rocket propulsion systems

The long endurance, small size, and intimate propulsion/airframe integration of a transonic UAV pose unique challenges for the propulsion system. Slow-burning solid rocket propulsion systems significantly depart from conventional solid rocket propulsion technology. Typical solid rockets are optimized to deliver their impulse quickly, either to catch up with a target (i.e. tactical missiles) or reduce gravity losses (i.e. sounding rockets and launch vehicles). The motors considered here, by contrast, deliver a low thrust level for a long time in order to counter the drag of a streamlined aircraft.

1.3.1 Low thrust

The nominal thrust is set to balance the drag of the vehicle in steady, level flight. To estimate the typical drag of small, fast aircraft, computational fluid dynamics analysis was performed on the vehicle concept's aerodynamic configuration. It predicts a drag of 4.5 to 6 N under expected flight conditions [Figure 4]. To account for uncertainties in this estimation, a nominal thrust range of 5 - 10 N is considered for small, fast UAV propulsion systems near our design point.

By contrast, typical solid rocket motors of this impulse class (class J, 640 to 1280 N s) have thrust levels of 100 to 600 N. The lower thrust poses several challenges:

1. The motor will operate at a low chamber pressure, which reduces specific impulse. Low chamber pressure will also cause the combustion of some propellants to be unstable, so a suitable propellant must be used.
2. The motor will have a small nozzle throat. This requires more precise manufacturing, and makes the effects of nozzle dimension changes during firing (due to erosion or deposition) more significant.

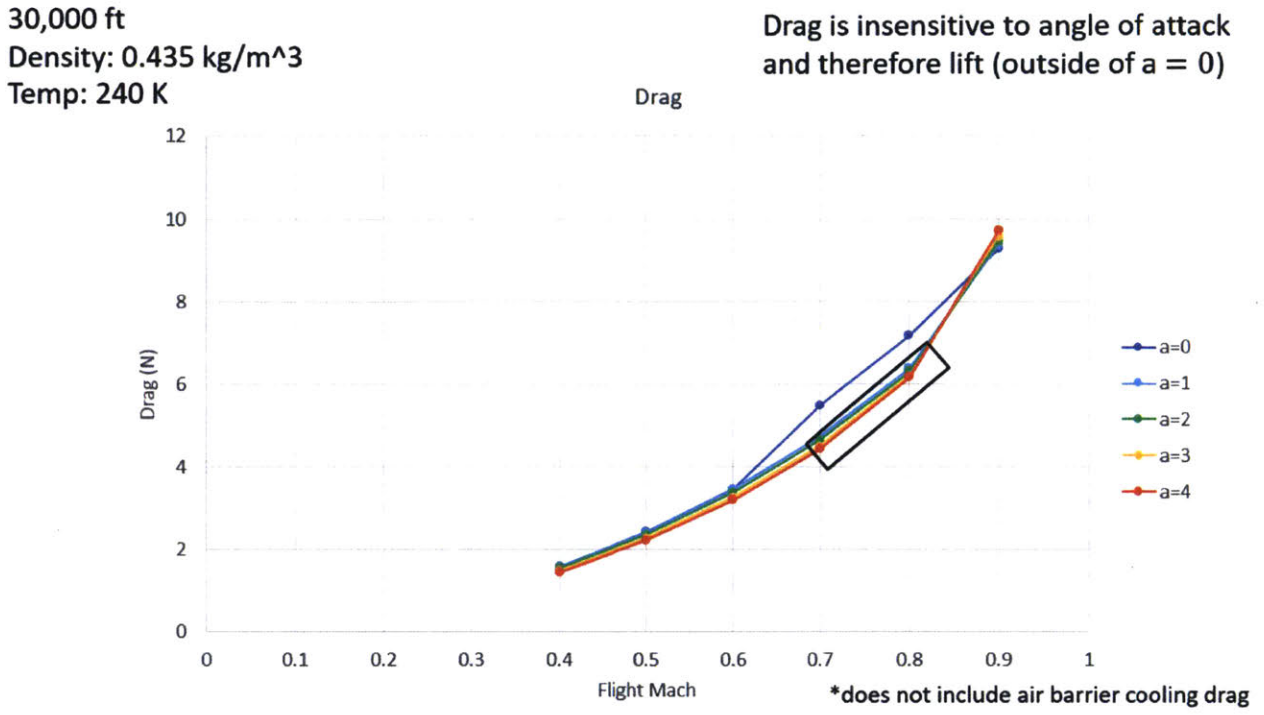

Figure 4: Computational Fluid Dynamics analysis of the vehicle concept [Figure 2] predicts a drag of 4.5 to 6 N. In the legend, "a" denotes angle of attack in degrees. The black box surrounds the intended operating regime, Mach 0.7 to 0.8 and angle of attack 1 to 4 degrees. The analysis was performed using ANSYS Fluent.

1.3.2 Long endurance

A UAV-propulsion rocket motor will need to burn for as long as possible, which is likely to be several hundred seconds. This is one to two orders of magnitude longer than typical rocket motors of the same size. The burn time of a solid rocket motor can be extended via the use of a slow-burning propellant and the design of the propellant grain. This research developed new slow-burning propellants [Chapter 2] and grain designs [Section 5.2] for these motors.

The endurance of a rocket-propelled UAV depends on its cruise speed and altitude [Figure 5]. The model assumes vehicle aerodynamics as presented in Figure 4, and a propulsion system with a fixed impulse of I = 1000 N s. The endurance t_f is computed as:

$$t_f = \frac{I}{D(z,\ M)}$$

where $D(z, M)$ is the predicted drag as a function of cruise altitude z and cruise Mach number M, at the angle of attack required for level flight. Endurance is maximized at higher altitudes and lower Mach numbers, where drag is less. However, lift requirements constrain how high and slow the aircraft can fly.

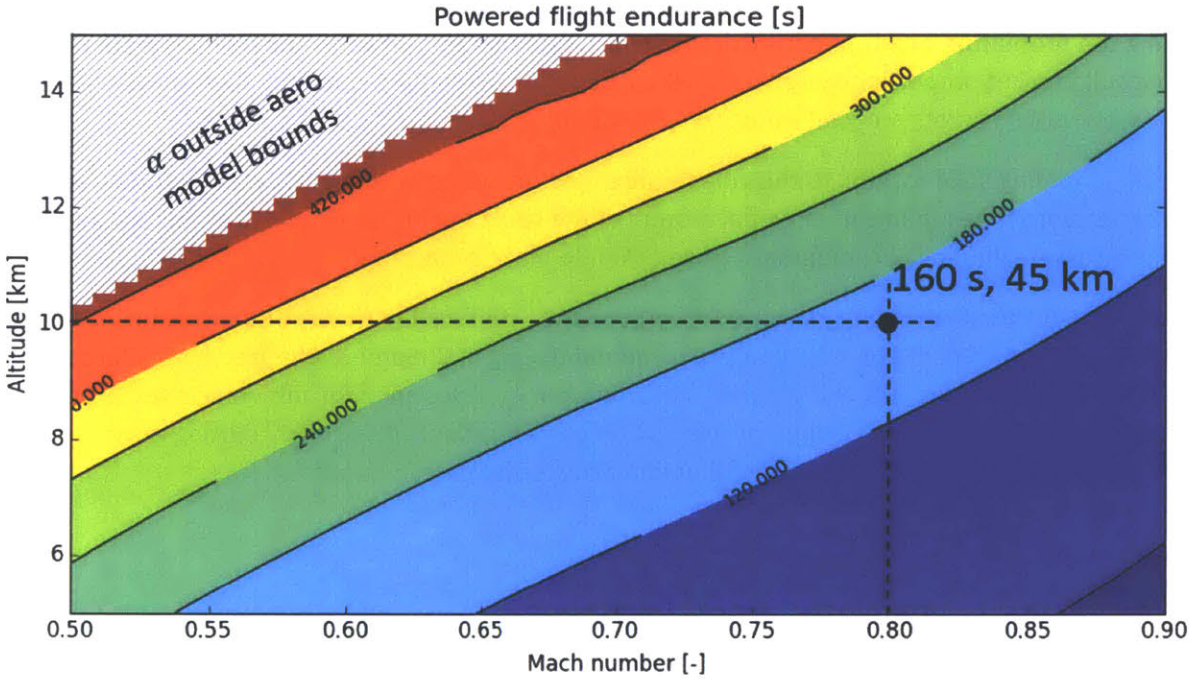

Figure 5: Contours of endurance for a small, fast UAV loaded with 1000 Ns of impulse. Longer missions are possible at higher altitudes and slower flight speeds. The concept design point (10 km, Mach 0.8, black dot) allows for about 160 s of powered flight. In the hatched region, an angle of attach α outside of the aerodynamic model's boundaries is required to produce enough lift for level flight.

The variation of endurance with cruise altitude and Mach number presents a tradeoff for vehicle and mission designers. The design point selected for this work yields an endurance of about 160 s. Future designs may seek to improve endurance by flying slower or higher.

1.3.3 Thermal management

The long burn time poses a thermal management problem. Solid rocket motors have intense internal heat fluxes. However, in a typical small motor, the heat flux is only applied for a short duration (a few seconds), so minimal thermal management is required. A slow-burning solid rocket motor must protect itself from heat for a much longer time. This is effectively accomplished with a thin ablative liner on the inside of the motor. An example ablative liner design, which uses known materials in a novel configuration, is presented in Section 5.3.

1.3.4 Unusual motor shape

The motor's shape poses a production challenge and alters the vehicle's dynamics. Small, fast UAVs can be made more structurally efficient by using the motor case to form part of the fuselage outer mold line. This requires the motor to be contoured to the aerodynamically desired shape of the fuselage. Thus, the motor's cross section varies along its length. This poses a production challenge, which can be adequately addressed with modern additive manufacturing techniques (see section 6.1).

The varying cross section also causes the motor's thrust to vary over the course of the burn. This leads to fluctuations in the vehicle's flight speed. However, this can be mitigated by varying the propellant chemistry and burn rate along the length of the propellant grain.

1.4 Document layout

Fulfilling the propulsion needs of a new class of small, fast aircraft motivates the development of slow-burning solid rocket propulsion systems. Small, fast aircraft will require compact, high-power propulsion systems, and solid rockets are well suited to fill this role.

However, adapting solid rockets to this role requires motors which produce 100x lower thrust and have 100x longer burn times than conventional motors of the same size. The remainder of this thesis documents the technology development undertaken to make such a motor.

This motor requires slow-burning solid rocket propellants: combustion theory and modeling of these propellants is treated in Chapter 2; their experimental testing in Chapter 3. Chapter 4 introduces a conceptual small, fast aircraft, and Chapter 5 presents a motor designed for this vehicle using slow-burning propellants. Chapter 6 examines production considerations, particularly cutting-edge techniques for additive manufacturing of titanium alloy motor cases.

2 Slow burning solid rocket propellant

Enabling a new capability for small, fast aircraft motivates the development of new solid rocket propulsion systems, which have orders of magnitude lower thrust and longer burn time than typical designs. Fast, kilogram-scale UAVs require compact, high specific power propulsion systems which sustain 5 – 10 N of thrust for several minutes.

Solid rocket motors can be adapted to this task, but the low thrust level imposes unique challenges. These motor will tend to operate a low chamber pressure and low propellant burn rate, and will have small nozzle throats. They require slow-burning propellants, which will sustain stable combustion at low pressure.

Ammonium perchlorate composite propellants doped with a burn rate suppressant were studied to address this need. This chapter reviews fundamentals of solid propellants, their combustion, and role in the motor design process. It then presents a novel model for the effect of burn rate suppressants, which enables predictable tailoring of propellant burn rate. With this new design tool, ammonium perchlorate composite propellants are compatible with the needs of UAV propulsion.

2.1 Solid propellants

This section identifies the performance parameters of solid propellants, and describes the chemical composition of the propellant used in this research. Efficient solid rocket motors require dense, hot-burning propellant. Composite propellants, made from ammonium perchlorate salt and a rubber-like polymer, effectively meet the performance needs of UAV propulsion. The propellant chemistry introduced here informs a discussion of the combustion process in Section 2.2.

2.1.1 Performance parameters of solid propellants

The key performance parameters of a solid propellant are specific impulse and density. *Specific impulse* is a measure of propulsive efficiency, and is the ratio of thrust to weight of propellant burned per unit time:

$$I_{sp} \stackrel{\text{def}}{=} \frac{F}{\dot{m}\, g_0}$$

Higher values of specific impulse are desirable. The specific impulse can be divided into two further parameters, the *thrust coefficient* C_F and the *characteristic velocity* c^*:

$$I_{sp} = \frac{C_F\, c^*}{g_0}$$

The characteristic velocity c^* depends on propellant combustion, while C_F depends on nozzle expansion. Solid propellants should have a high c^* to maximize the efficiency of their motor. High c^* is achieved by a hot-burning (high T_c) propellant, whose exhaust species have a low average molar mass $\mathcal{M}$. For isentropic nozzle flow, c^* is given by [16]:

$$c^* = \sqrt{\frac{T_c}{\mathcal{M}}} \left(\frac{\sqrt{\gamma\, \mathcal{R}}}{\gamma \sqrt{\left(\frac{2}{\gamma+1}\right)^{\frac{\gamma+1}{\gamma-1}}}} \right)$$

where T_c is the temperature of the exhaust gas in the combustion chamber, $\mathcal{M}$ is its average molar mass, $\gamma = c_p/c_v$ is its ratio of specific heats, and $\mathcal{R}$ is the universal gas constant. The first group of terms, $\sqrt{T_c/\mathcal{M}}$, is responsible for most of the variation in c^* between different propellants.

Solid propellants should have a high density. This reduces the volume of the motor case to contain a given mass of propellant. A lower-volume case contributes less inert mass to the vehicle. Volume-constrained motors, such as those for UAV propulsion, can carry more propellant if the propellant is denser.

The propellant should also have:

- a *burn rate* which is compatible with the motor design [see Section 2.3],
- *mechanical properties* which allow the propellant to survive the mechanical loads of production, handling and storage,
- *aging behavior* compatible with the desired shelf life, and
- low *sensitivity*, to avoid accidental ignition.

Certain applications have additional requirements. Some military applications demand low *exhaust visibility*, a reduction of the smoke an infrared signature of the exhaust plume. Others require the exhaust to be less corrosive or toxic (e.g. launch near personnel or important machinery).

The propellant development effort documented in this thesis focused mainly on propellant burn rate. The propellants developed in our research compromise on specific impulse and density to make the propellant burn more slowly and at a temperature compatible with the vehicle's thermal protection systems. Studies of the propellant's aging behavior, sensitivity, and exhaust visibility are left to future work.

2.1.2 Chemical composition of solid propellants

Solid propellants can be made from a range of chemical compositions. This work focuses on a particular composition class, composite propellants.

Composite propellants contain oxidizers and fuels in distinct solid phases. The typical oxidizers are crystalline solids with high oxygen balance, divided into small particles (10 to 500 μm) and dispersed though the propellant. A polymer matrix, the binder, binds the oxidizer particles together, giving the propellant mechanical strength. The binder serves as a fuel, giving off hydrocarbon vapors during combustion. Additional fuel may be added as hot-burning metal powder dispersed in the binder.

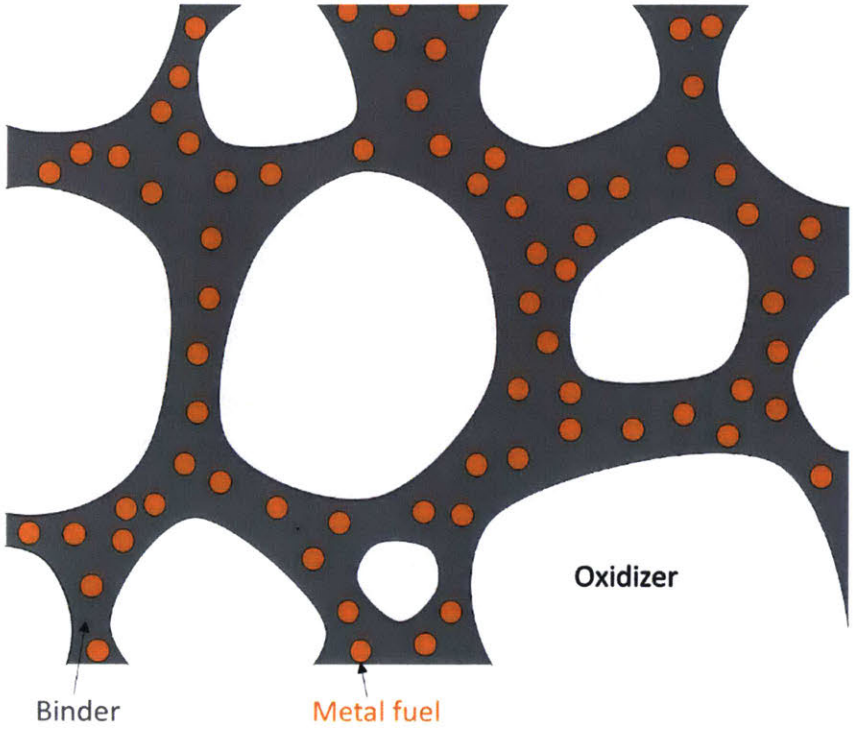

Figure 6: A composite propellant consists of crystalline oxidizer particles, and possibly a metal fuel powder, dispersed in a polymer binder.

Oxidizer – The propellants considered in this work use Ammonium perchlorate (AP, NH_4ClO_4) oxidizer. It is the most commonly used oxidizer, and is preferred for the high flame temperature and specific impulse of propellants based on it [17]. Its exothermic decomposition produces oxidizing species, such as O_2, Cl_2 and N_2O, along with H_2O, HCl, N_2 and other minor products [18].

As an alternative to AP, our group briefly considered ammonium nitrate (AN) because of the low burning rate of AN propellants. However, with a suitable burn rate suppressant, AP propellants can burn slowly enough for our application, have better density and specific impulse, and are easier to produce than AN propellant.

Binder –Hydroxyl-terminated polybutadiene (HTPB) is used as the binder in our propellants. HTPB enables higher solids loading, which leads to a closer to stoichiometric oxidizer to fuel ratio, and has good mechanical and storage properties [16]. Uncured HTPB is an oligomer of butadiene [Figure 7], and is a viscous liquid at room temperature. It is cross-linked into a solid polymer during propellant production, after solid ingredients have been mixed into the binder. Diisocyanates are used as curatives. An isocyanate ($-\mathrm{N}=\mathrm{C}=\mathrm{O}$) group reacts with a hydroxyl group to create a urethane bond [19]. Diisocyanates have two isocyanate groups and can bond to two hydroxyl groups, creating a cross link between HTPB chains [Figure 8]. During propellant combustion, HTPB decomposes into a fuel-rich vapor, mostly CH_n and $\mathrm{C}_2\mathrm{H}_n$, which burns with AP decomposition products.

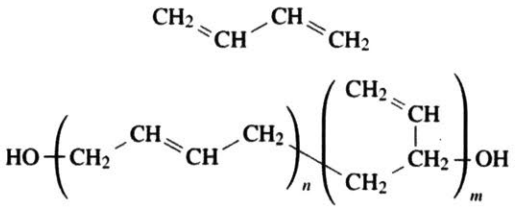

Figure 7: The 1,3-butadiene monomer and the HTPB oligomer. The oligomer has n cis and trans units and m 1,2 vinyl units. Note that the cis/trans and vinyl units may be interspersed. In typical propellant-grade HTPB, $m + n \approx 45$ and $m/n \approx 0.3$ [19].

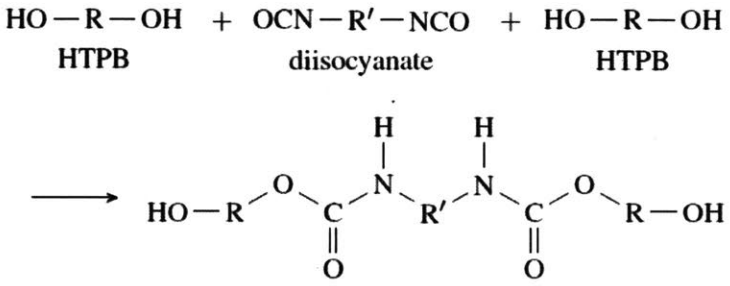

Figure 8: Diisocyanate cross-links HTPB.

The binder and oxidizer are typically mixed in a fuel-rich ratio. This ratio is chosen for reasons of performance and production. T_c is maximized by a propellant which has the stoichiometric ratio of oxidizer to fuel. Specific impulse, however, is maximized slightly fuel-rich propellants, because fuel-rich combustion has lighter exhaust species (i.e. H_2 and CO). However, propellants typically include more than the I_{sp}-optimal amount of binder for production reasons. At least 10-15% binder is required for a propellant which can be mixed and cast in slurry form, and which has acceptable mechanical properties once cured [16].

Metal fuel – Metal powder, usually aluminum, is added to solid propellants to increase their flame temperature and specific impulse. In this research, magnesium is used as the propellant's metal fuel, instead of the typical aluminum. Mg is reported to achieve more complete combustion in small motors and to burn better at low pressures [20][3]. However, using Mg in place of Al does decrease the density of the propellant.

Energetic materials – To increase specific impulse, some composite propellants include an energetic material. This material can be a solid explosive, such as HMX or RDX; or an energetic binder, such as glycidyl azide polymer (GAP). Energetic materials were not considered in the present research: they are incompatible with the requirement for low burn rate, and complicate handling and processing procedures.

[3] Metal combustion takes place mainly in the vapor phase, with a flame front surrounding a boiling droplet of liquid metal, and the reaction rate is limited by the vapor pressure of the metal [8] [19]. Magnesium's lower boiling point (1363 K vs 2743 K for Al at 0.1 MPa [23]) may allow Mg droplets to burn more quickly (i.e. before exiting a small motor) and at lower temperatures (i.e. in a lower-pressure gas, which provides less heat flux to the droplet).

Other minor ingredients can be included in the propellant. *Opacifiers* (e.g. graphite powder or nigrosin dye [21]) make the propellant opaque and emissive, which improves radiation heat transfer to the propellant surface and is necessary for good combustion. *Bonding agents* (e.g. HX-752) promote better adhesion between the oxidizer particles and the binder [22], improving mechanical properties and stabilizing combustion. *Antioxidants* (e.g. CAO-5) improve the shelf life of the propellant. *Surfactants* and *processing agents* (e.g. silicone oil, castor oil, Triton X-100) make mixing and casting easier by improving the rheological properties of the propellant slurry. *Burn rate suppressants* (e.g. oxamide) or *catalysts* (e.g. Fe_2O_3) can be added to modify the propellant's burn rate.

2.2 Internal ballistics of solid rocket motors

The design of slow-burning solid propellant rocket motors requires an understanding of the internal ballistics of solid rocket motors: the combustion process of the propellant, and how this gives rise to the motor's chamber pressure and thrust.

This section reviews established theories of internal ballistics. It describes the combustion process of AP composite propellants. It then establishes why the rate of that process, the burn rate r, is important to motor performance. This motivates the following sections, which illuminate the role of burn rate in the motor design process (2.3), and present a novel tool for its control (2.4 - 2.6).

2.2.1 Combustion process and flame structure

The combustion process of a composite propellant has many steps, and the flame structure is complex. Although the propellant is a solid, important reactions, including combustion of the fuel with the oxidizer, occur in the gas phase. A set of flames hover over the surface of the burning propellant. These flames transfer heat to the propellant surface, causing its solid components to decompose into gases. The gaseous decomposition products contain fuel vapor and oxidizing species, which supply the flames with reactants.

Importantly, the combustion process contains a feedback loop. Heat from the flames vaporizes the surface, and vapor from the surface provides fuel and oxidizer to the flames. The rate at which this process proceeds depends on chemical kinetics, mass transfer, and heat transfer within the combustion zone.

The combustion process can be divided into 6 different reactions. The locations of several of these reactions are illustrated in Figure 9.

1. *Binder decomposition* – At the binder surface, heat flux from the flames warms the binder a decomposes it into a hydrocarbon gas. If a metal fuel is present, solid metal particles are ejected from the decomposing binder. This reaction is endothermic [19].
2. *AP condensed phase reactions* – At the surface of an AP particle, AP decomposes to give off gaseous, oxidizing products. A liquid melt pool forms on the surface of the AP as an intermediate step. This reaction is exothermic [18].
3. *AP monopropellant flame* – Some of the AP products (NH_3 and $HClO_4$) burn with each other in the gas phase close to the AP particle surface. This reaction is exothermic, and has a flame temperature of 1200 – 1400 K. The standoff distance between the AP flame and the propellant surface depends on the velocity of the product gases and the kinetics of the reaction [18].
4. *"Primary", or "leading edge" flame* – The primary flame burns close over the boundary between an AP particle and the surrounding binder. At the boundary, oxidizing vapors from the AP and

hydrocarbon vapors from the binder are effectively premixed. This allows for a hot (~3000 K [23]), intense flame close to the surface. The primary flame standoff distance is mostly set by kinetics.

5. *Diffusion flame* – The diffusion flame is cooler and exists further from the surface. Oxidizer and fuel vapors which were not consumed by the primary flame diffuse toward each other, meeting at the stoichiometric surface of the diffusion flame. In fuel-rich propellants, it closes over the AP particle. As the name implies, the location and combustion rate of the diffusion flame are set by molecular diffusion.
6. *Metal droplet combustion* – Particles of solid metal fuel are ejected from the decomposing binder surface, and are warmed by passage through the flames. During this time, the particles agglomerate, melt into droplets, begin to boil, and ignite. Combustion occurs on a comet-shaped halo around the droplet. The metal droplets burn far from the propellant surface, roughly 2~200 mm [24] (compared to the ~500 μm height of the flame structure [23]). By the time the metal burns, most of the usual oxidizing species have been consumed by the primary and diffusion flames. Instead, the metal is oxidized by reducing H_2O and CO_2 in the exhaust to H_2 and CO [24].

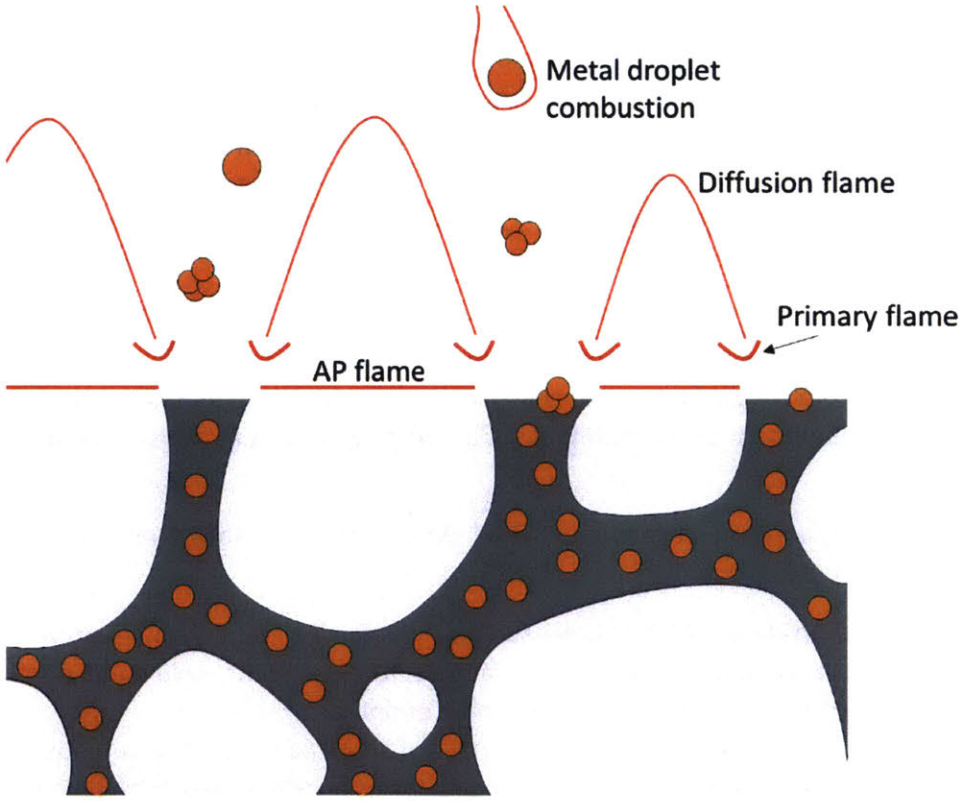

Figure 9: Flame structure over a composite propellant. Based on figures in [25] and [24].

The flame structure is important to understanding the behavior of propellants in a rocket motor. Specifically, it elucidates the effect of pressure on burning rate. At higher pressures, the gas phase is denser, causing reactions and diffusion to proceed more quickly. This moves the flame structure closer to the surface. The closer flames and denser conducing medium enhance heat transfer to the surface, which drives more decomposition, increasing the burn rate.

Although this dependence is complicated, it can be empirically modeled by Vieille's Law, which relates the burn rate r to the chamber pressure p_c via two parameters:

$$r = a\,(p_c)^n$$

r is the rate at which the surface regresses, and has units of velocity. a is the *burn rate coefficient*, which has units of $[velocity \times (pressure)^{-n}]$. n is the unitless *burn rate exponent*. The model parameters a, n must be determined by combustion experiments on the propellant.

Vieille's Law is an empirical approximation; it does not apply to certain propellants in certain propellant regimes. One deviation from Vieille's Law, plateau burning, is illustrated in Figure 10.

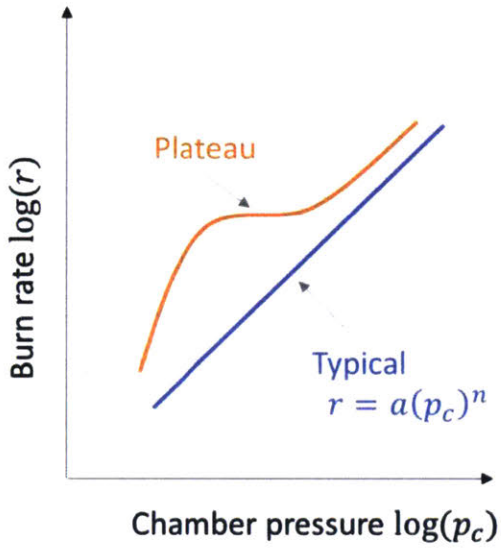

Figure 10: Typical propellants have a burn rate vs pressure dependence which forms a straight line on a log-log plot, and can be modeled by Vieille's Law. However, some propellants exhibit plateau burning, and cannot be modeled with Vieille's Law.

2.2.2 Equilibrium chamber pressure

The relation of burn rate and chamber pressure can be used to model the evolution of chamber pressure within solid rocket motor. Begin by applying the Ideal Gas Law to relate the chamber pressure p_c to the mass of gas present in the combustion chamber, m.

$$p_c = m\,R\,T_c\frac{1}{V_C}$$

where R is the specific gas constant of the combustion gases in the chamber, T_c is their temperature, and V_c is the chamber volume[4]. Assume that the gas in the chamber is sufficiently homogenized that it may be described by a single pressure, temperature and gas constant. Gas mass is added to the chamber by burning propellant, and mass flows out of the chamber through the nozzle. The rate of change of the chamber gas mass is

[4] The available chamber volume changes as solid propellant is consumed. Assume that this change is negligibly slow compared to the rates considered here.

$$\frac{dm}{dt} = \dot{m}_{in} - \dot{m}_{out}$$

Now, find expressions for the mass flow terms. Isentropic nozzle theory [16] gives the mass flow through the nozzle as:

$$\dot{m}_{out} = \frac{p_c A_t}{c^*}$$

where A_t is the nozzle throat area, and c^* is the *characteristic velocity* of combustion gas, equal to:

$$c^* = \frac{\sqrt{\gamma R T_c}}{\gamma \sqrt{\left(\frac{2}{\gamma+1}\right)^{\frac{\gamma+1}{\gamma-1}}}}$$

The gas supplied by the propellant is

$$\dot{m}_{in} = A_b \rho_s r(p_c)$$

where A_b is the burn area of the propellant, and ρ_s is the solid propellant density.

Note that the nozzle flow is linear in chamber pressure. If the burn rate r is sublinear in chamber pressure, then there exists a stable chamber pressure where

$$\frac{dm}{dt} = \dot{m}_{in} - \dot{m}_{out} = 0$$

The equilibrium pressure is given by:

$$p_c = K \rho_s r(p_c) c^*$$

$$K \stackrel{\text{def}}{=} \frac{A_b}{A_t}$$

Below this pressure, combustion flow exceeds nozzle outflow, and the pressure rises. Above this pressure nozzle outflow is exceeds combustion, and the pressure falls.

If the propellant obeys Vieille's Law, the equilibrium chamber pressure can be written in closed form:

$$p_c = (K \rho_s a c^*)^{\frac{1}{1-n}}$$

Low thrust solid rocket motors have a low equilibrium mass flow $\dot{m}$. This implies:

1. the throat area A_t will be small,
2. the chamber pressure p_c will be low, and
3. the propellant burn rate a will be slow.

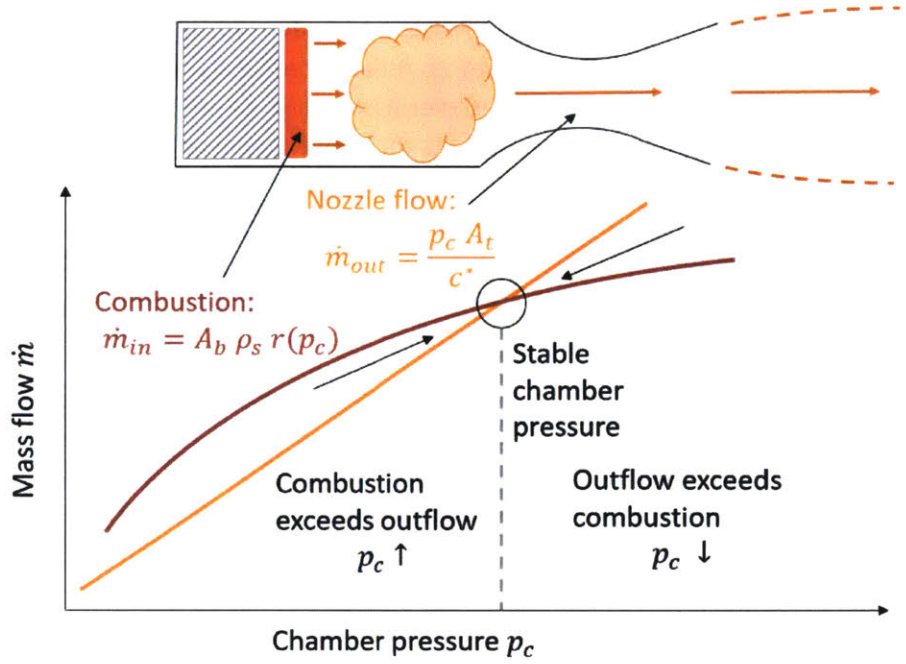

Figure 11: The chamber pressure of a solid rocket motor arises from an equilibrium between gas generation by combustion and gas expulsion through the nozzle.

The next section gives more details on how these values are selected. It applies the concepts of this chapter to the design of a solid rocket motor which operates at a particular chamber pressure and thrust level.

2.3 Design for chamber pressure and thrust

New rocket designs must achieve a target thrust and chamber pressure to comply with mission requirements and structural limitations. However, the solid rocket motor does not have controls (e.g. pumps and valves) which can adjust the pressure and thrust. Rather, the chamber pressure and thrust are determined by the propellant combustion process and the motor geometry. The motor must be designed so that the internal ballistics will equilibrate at the correct pressure and thrust level.

The preliminary motor design process uses 5 variables. Two depended variables must be matched to their required values:

1. p_c, the chamber pressure, and
2. F, the thrust force.

Three independent variables may be adjusted by the designer to set the pressure and thrust:

3. A_b, the burn area of the propellant grain,
4. A_t, the area of the nozzle throat, and
5. a, the burn rate coefficient of the propellant.

There are two caveats on this statement of the design space:

1. Capturing the entire combustion process in a single parameter a is an aggressive simplification. Other properties the propellant (n, ρ_s, c^*, γ) also affect the pressure and thrust. Further, the

relation between propellant burn rate and pressure may have plateaus which are not captured by the Vieille model ($r = ap^n$) [17]. However, to reduce complexity, this section neglects these effects. It is assumed that the propellant designer has a family of propellants which offers a range of a values at similar (n, ρ_s, c^*, γ), and fits the Vieille model near the design pressure. Oxamide-doped AP composite propellants, described in Sections 2.5 and 2.6, provide such a propellant family.

2. These variables may not take on a single value, but instead evolve over time as the motor burns. For now, consider designing for a single point in the burn profile: perhaps just after ignition, or at the peak of the pressure trace.

Imagine the motor design space as 3-space parameterized by the independent variables A_b, A_t, a. Contours of p_c and F are surfaces in this space. The task of motor design is to find a point (A_b, A_t, a) which lies on both the desired pressure surface and the desired thrust surface. The two surfaces intersect along a curve; many valid design points are possible. The intersection curve lies in a plane of A_t, particularly the plane where

$$A_t = \frac{F}{p_c C_F(p_c, p_e, \gamma)} = \frac{F}{p_c \sqrt{\frac{2\gamma^2}{\gamma-1}\left(\frac{2}{\gamma+1}\right)^{\frac{\gamma+1}{\gamma-1}}\left(1-\left(\frac{p_e}{p_c}\right)^{\frac{\gamma-1}{\gamma}}\right)}}$$

In this equation, $C_F(p_c, p_e, \gamma) \stackrel{\text{def}}{=} \frac{F}{A_t p_c}$ is the thrust coefficient of the nozzle. A pressure contour and its intersection curve with a thrust contour are illustrated in Figure 12.

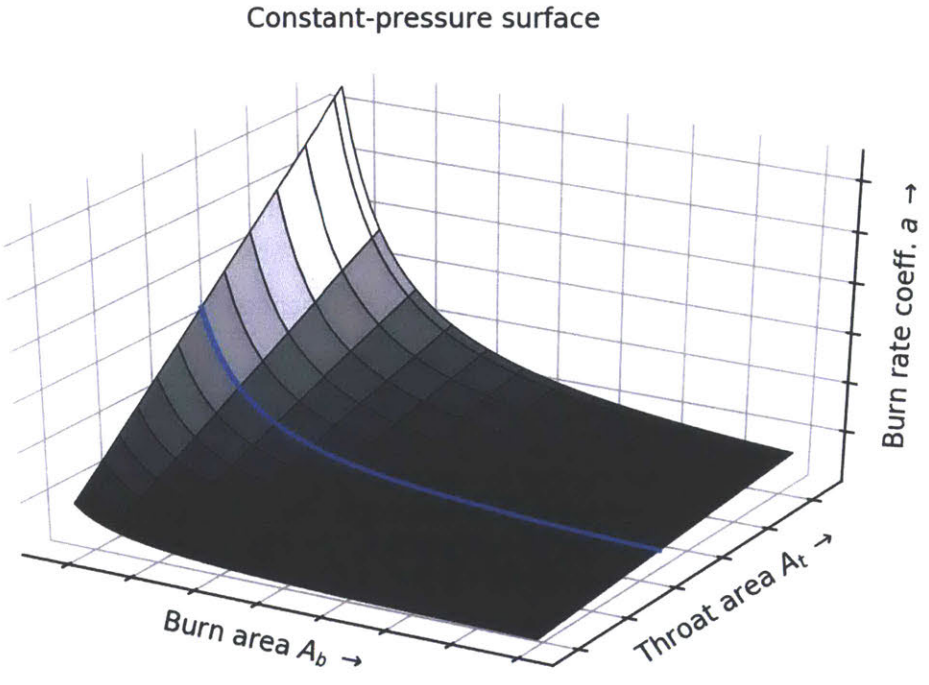

Figure 12: A surface of constant pressure in (A_b, A_t, a) space (grey), and its intersection with a particular thrust level (blue).

It is possible to simplify this relation. Recall from the previous section that the chamber pressure depends not on the distinct values of A_b and A_t, but on their ratio:

$$K \triangleq \frac{A_b}{A_t}$$

$$p_c = (K\, \rho_s\, a\, c^*)^{\frac{1}{1-n}}$$

This relation is illustrated in Figure 13. p_c increases with increasing a and increasing K. Motors with faster burning propellant, or more burn area compared to their throat area, will have higher chamber pressure.

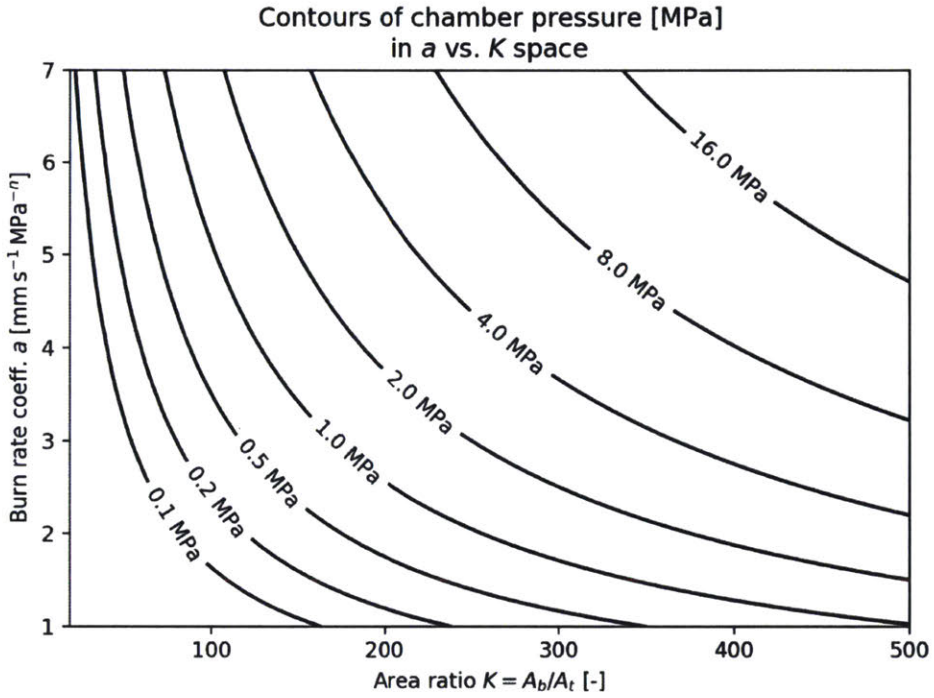

Figure 13: The chamber pressure of a solid rocket motor is set by the burn rate and the burn area / throat area ratio. This plot assumes a propellant family with $n = 0.45$, $\rho_s = 1500\ kg\ m^{-3}$, $c^* = 1300\ m\ s^{-1}$.

As currently formulated, the motor design problem is under-constrained. As shown above, the thrust and pressure constraints intersect along a curve, so many valid design points will fulfill both of them. A third constrain must be introduced.

In this typical motor design process, this constraint is introduced by selecting a particular propellant, with a known a value. Then, the motor designer must choose A_b, A_t to give the required pressure and thrust. This reduced design space is illustrated in Figure 14. The figure assumes a value for a, and plots contours of pressure and thrust on axes of burn area A_b versus throat diameter d_t. A motor designer would find the intersection of the desired pressure and thrust contours, read off the corresponding A_b and d_t, and design a motor with that geometry. If the geometry was not feasible within structural and packaging constrains, the process could be repeated with a different propellant. Most motor producers

maintain a library of propellant compositions (order of 10 compositions) [15] [26]. These propellants provide a sufficient selection of burn rates (and other properties) to cover typical missions.

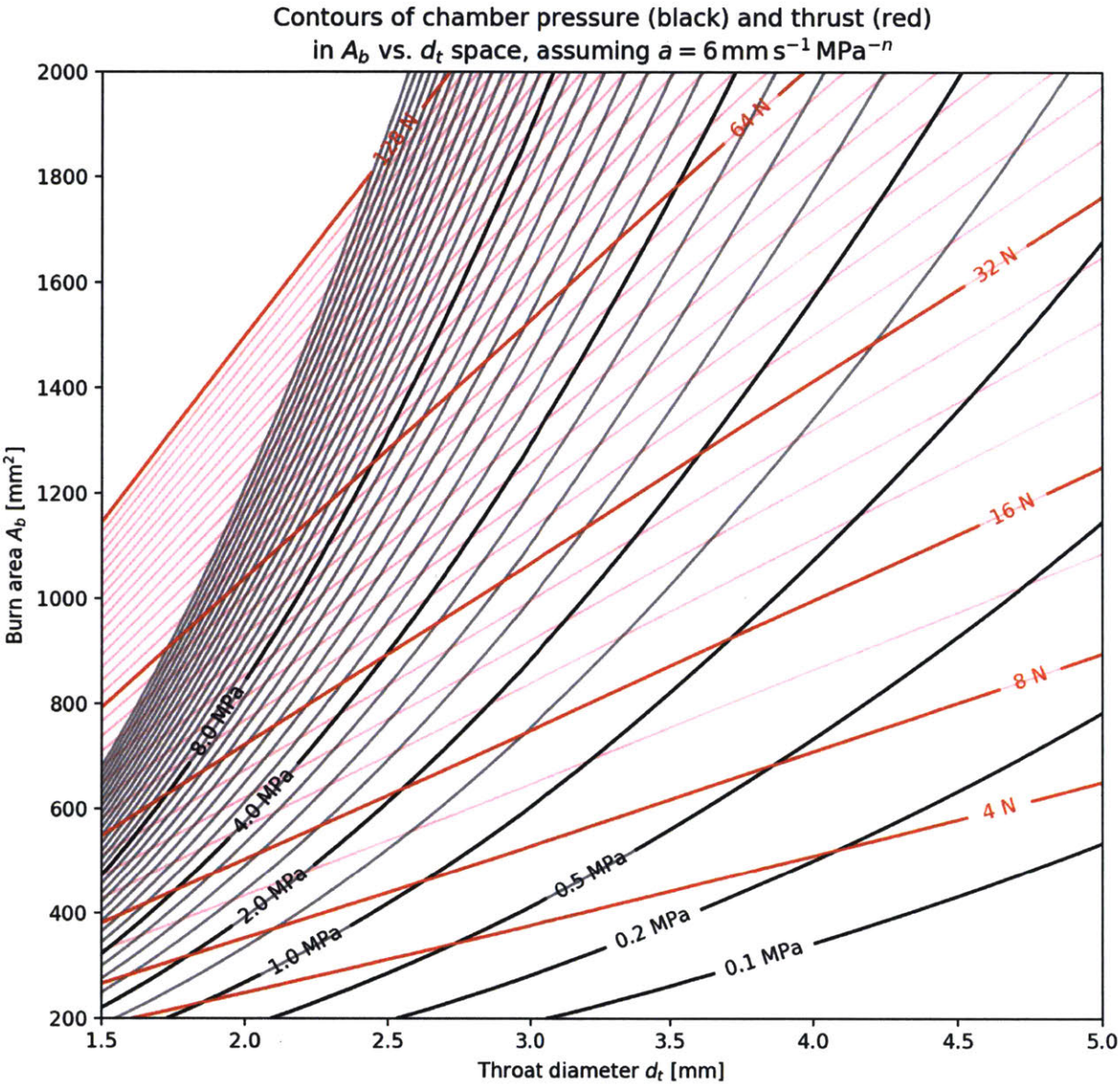

Figure 14: For a motor with fixed propellant burn rate coefficient a, the chamber pressure and thrust are set by burn area and the throat diameter. This plot assumes a propellant with $n = 0.45$, $\rho_s = 1500\ kg\ m^{-3}$, $c^* = 1300\ m\ s^{-1}$, $\gamma = 1.26$, *and expansion to* $p_e = p_a = 30\ kPa$. Minor lines show increments of 0.5 MPa and 4 N.

The design of slow-burn motors for UAV propulsion is differently constrained. Slow-burning motors use an end-burning grain to reduce thrust and maximize endurance. The difference between and end-burning grain and a more conventional internal burning grain is shown in Figure 15. End burning grains burn for longer. The burn time of an end burner is rough the motor length divided by the propellant burn rate, while the burn time of an internal burning grain is somewhat less than the motor radius divided by the burn rate. The burning area of internal-burn grains is larger, making them more suited to

high-thrust motors. Further, the burn area of an internally burning grain can be varied by changing the size or profile of the core. For and end-burner, the burn area is fixed by the motor geometry.

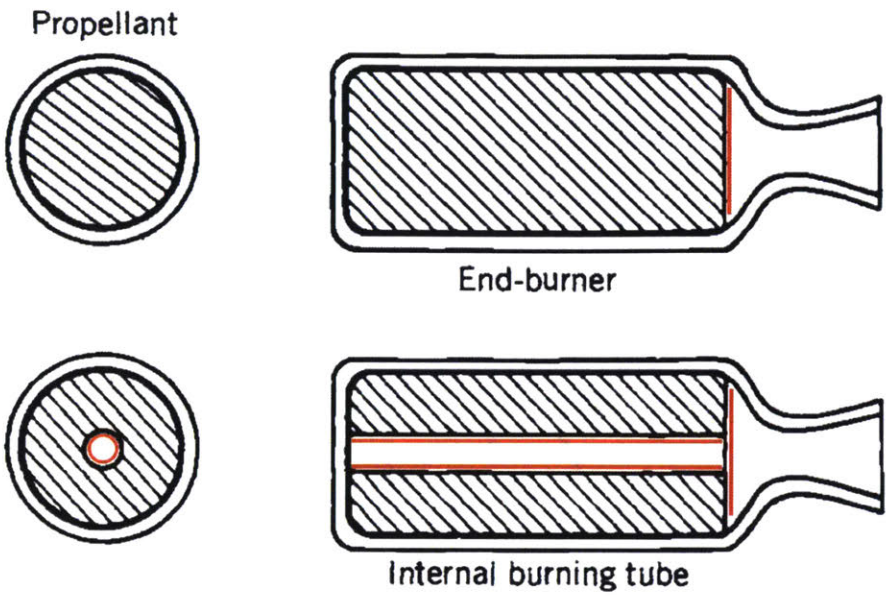

Figure 15: Comparison of end-burning and internal burning propellant grains. Reprinted from Sutton and Biblarz [16].

Therefore, at a particular point in the burn, A_b is set by the cross section of the motor, whose geometry is in turn set by the UAV configuration. In this case, the motor designer must choose a , A_t to give the required pressure and thrust. The slow, end-burn motor design space is illustrated in Figure 16. The figure assumes a value for A_b, an and plots contours of pressure and thrust on axes of burn rate coefficient a versus throat diameter d_t. Again, a motor designer would find the intersection of the desired pressure and thrust contours, but in this case read off the corresponding a and d_t. Mathematically, the desired burn rate coefficient is[5]

$$a = \frac{F\, p_c^{-n}}{C_F(p_c, p_e, \gamma)\, A_b\, \rho_s\, c^*}$$

and the desired throat diameter is

$$d_t = 2\sqrt{\frac{F}{\pi\, C_F(p_c, p_e, \gamma)\, p_c}}$$

[5] It should be noted that these equations and the contours in Figure 16 are approximate. They assume that propellant properties n, c^*, ρ_s, γ are constant. In reality, doping the propellant to modify the burn rate will change these values. Stated mathematically, n, c^*, ρ_s, and γ have a correlation with a which the above equations ignore. For example, it is estimated that c^* varies by ~20% over the range of oxamide concentrations considered in Section 2.6.

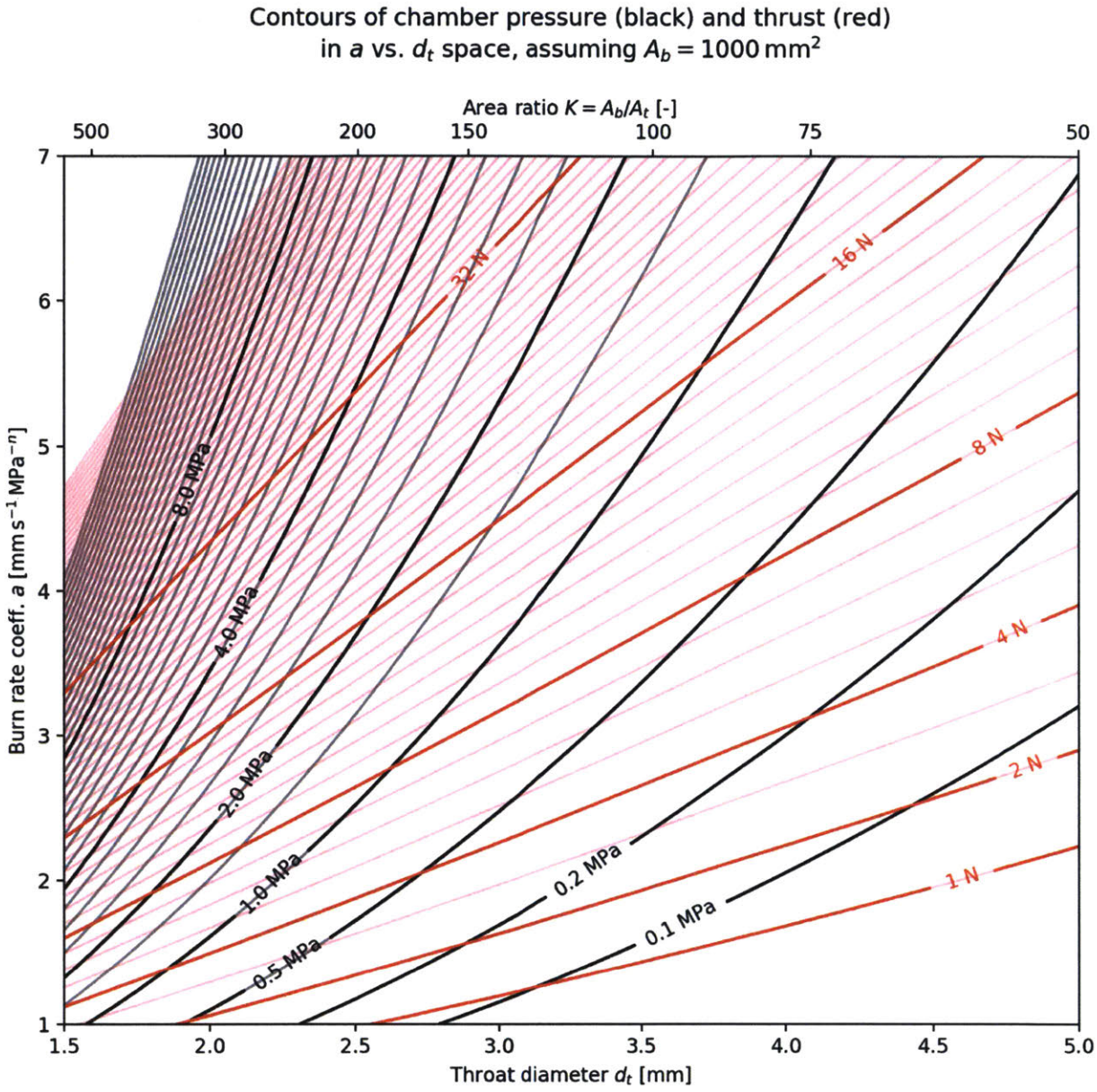

Figure 16: For a motor with a fixed burn area A_b, the chamber pressure and thrust are set by the propellant burn rate and the throat diameter. This plot assumes a propellant family with $n = 0.45$, $\rho_s = 1500\ kg\ m^{-3}$, $c^* = 1300\ m\ s^{-1}$, $\gamma = 1.26$, and expansion to $p_e = p_a = 30\ kPa$. Minor lines show increments of 0.5 MPa and 1 N.

Unlike the previous case, the problem is not solved with geometry alone. The motor design must now find or develop a propellant with the indicated burn rate coefficient a. Using a as a design knob requires a propellant with an adjustable burn rate. Preferably, the burn rate would be predictably adjustable, so a propellant composition can be easily created with a desired value of a. Predicting the burn rate of solid propellants is notoriously difficult [16] [17], which should lead the reader to question whether the proposed design method is possible. The following sections of this work show that, in the restricted domain of oxamide-doped AP composite propellants, sufficiently accurate burn rate prediction is

possible. By tailored suppression of the propellant burn rate, low-thrust long-endurance motors can be made for a particular thrust and chamber pressure.

The next section examines origins of propellant burn rate and techniques for its suppression. Sections 2.5 and 2.6 present method for predictably tailoring the burn rate of AP composite propellants using the burn rate suppressant oxamide.

2.4 Burn rate of solid propellants

The burn rate of a solid propellant arises from thermochemistry and thermodynamics of the combustion process described in Section 2.2.1. The combustion process contains feedbacks: the gas phase flame supplies heat to the surface, which decomposes to provide reactants to the flame. If these feedbacks are stronger, the burn rate is faster. Several factors can influence the burn rate: initial temperature, oxidizer substance and particle size, binder content, and the addition of catalysis or coolants. The following subsections detail each of these effects.

A large AP particle size, a high binder content, and the coolant oxamide were used to reduce the propellant burn rate to a level compatible with a low-thrust, long-endurance motor. Coolants are of particular interest because they allow for burn rate tailoring. A small addition of coolant easily and predictably reduces the burn rate.

2.4.1 Initial temperature

Propellants burn more slowly when ignited at a lower initial temperature. If the initial temperature is lower, more energy and time is required to heat the surface to its decomposition temperature. This effect is parameterized by the temperature sensitivity, σ_p

$$\sigma_p \overset{\text{def}}{=} \frac{1}{r}\left(\frac{\delta r}{\delta T_0}\right)_{p_c}$$

Typical values for σ_p are $1 - 9 \times 10^{-3}\mathrm{K}^{-1}$ [16].

2.4.2 Oxidizer substance

Substituting ammonium nitrate (AN, NH_4NO_3) for ammonium perchlorate as the oxidizer reduces the propellant burn rate. AN burns cooler and has slower decomposition kinetics than AP [17].

However, AN based propellants have issues with performance, processing and storage. AN is a less effective oxidizer than AP (lower oxygen balance), so it requires a higher solids loading (difficult to mix) and achieves a lower specific impulse. Further, AN is very hydroscopic, and has poor temperature stability in storage [17]. AN propellants also have a higher burn rate exponent n, making the motor less stable to pressure fluctuations [16].

2.4.3 Oxidizer particle size

Increasing the oxidizer particle size decreases the burn rate of AP composite propellants. A larger AP particle size increases the distance which the AP and binder decomposition products must diffuse to mix. This moves the diffusion flame farther to the propellant surface, decreasing heat feedback to the surface, and thus decreasing the burn rate [23]. This effect saturates at very small or large sizes, where the burning rate approaches the premixed limit and the AP monopropellant burn rate, respectively [Figure 17].

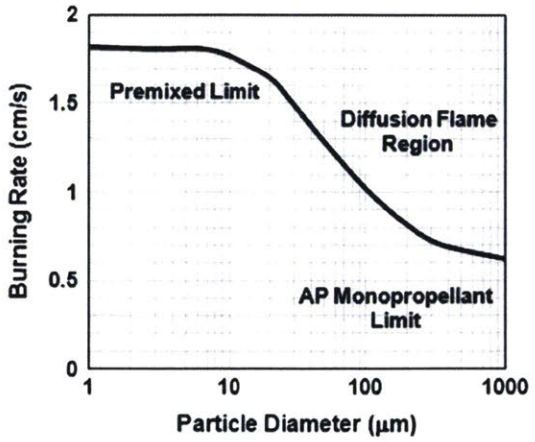

Figure 17: Increased AP particles size decreases the burning rate of AP composite propellant. The data in this figure is from detailed numerical simulations of the combustion process. Reprinted from [23].

2.4.4 Binder content

Increasing the binder content reduces the burning rate. A higher binder content results in a cooler flame[6], which decreases heat feedback to the surface. Also, increasing the binder content increases the energy required to decompose a unit volume of propellant, which further reduces the burn rate. Figure 18 illustrates these effects.

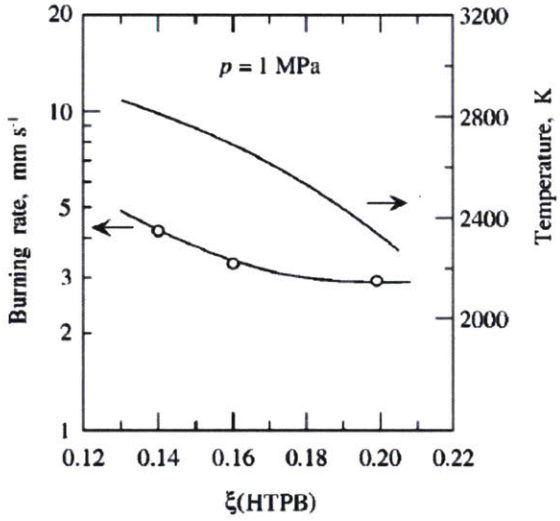

Figure 18: Increased binder content decreases the burn rate of AP composite propellants. Reprinted from [17].

2.4.5 Catalysts

Catalysts can be added to increase or decrease the burn rate. Iron (II) oxide (Fe_2O_3) is a common positive catalyst. It increases burn rate by reducing the activation energy of the AP decomposition and gas phase reactions, causing them to proceed at a faster rate [27] [17]. The effect of Fe_2O_3 addition on the burn rate is shown in Figure 19. Fe_2O_3 addition increases burn rate up to about 5% by mass, at which point

[6] Assuming the propellant is fuel-rich, which almost all composite propellants are.

the effect saturates. Fe_2O_3 acts as a surface catalyst, so the magnitude of its effect depends on the particle size (total surface area), not just the mass fraction.

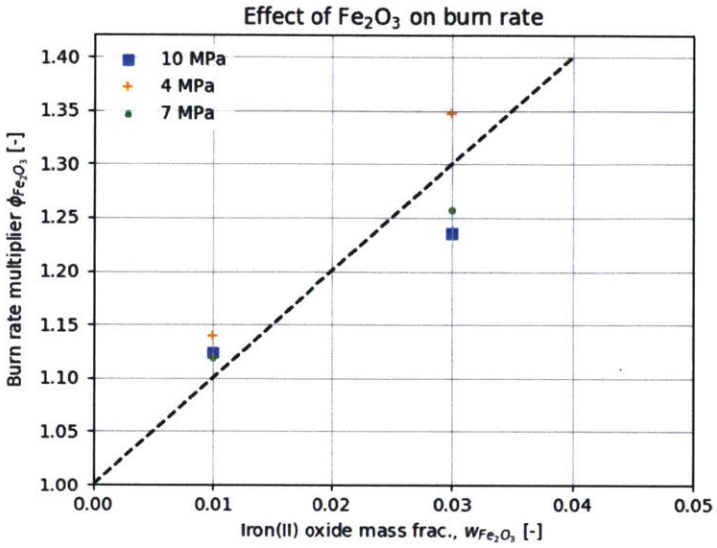

Figure 19: Addition of the catalyst Fe_2O_3 increases the burn rate of AP composite propellants. Data from [27].

Lithium Fluoride (LiF) is a negative burn rate catalyst. Its presence increases the temperature which the oxidizer must reach to fully decompose [17]. This increases the energy required to decompose a unit volume of propellant and slows the burn rate.

We chose to use a coolant, not LiF, as a burn rate suppressant in our propellant because the effect of coolants on the combustion process is easier to model.

2.4.6 Coolants

The addition of coolants reduces the burning rate of AP composite propellant. Coolants remove heat from the surface of the burning propellant, which reduces the surface temperature. The rates of the surface decomposition reactions are temperature dependent, so cooling the surface decreases its decomposition rate. Decreasing the decomposition rate reduces the mass flux available to the gas-phase flame structure, and decreases the burn rate.

At the surface of the burning propellant, suppressants decompose endothermically, and do so at a lower temperature than the other propellant ingredients [28] [29]. There are two possible routes by which this may provide a cooling effect. First, the endothermicity of suppressant decomposition increases the heat required to decompose a unit volume of solid propellant. Second, the injection of relatively cool suppressant product gases into the boundary layer above the propellant surface may reduce heat transfer.

2.5 Oxamide as a burn rate suppressant

Burn rate suppressants are a class of chemicals which can be added to composite propellants to decrease their burn rate. Oxamide is the most notable of the burn rate suppressants, but others, including melamine, urea, and azodicarbonamide, are used [28] [29]. A suppressant can reduce the burning rate of a propellant by up to 50% [29] [17].

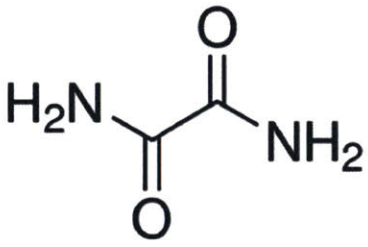

Figure 20: The chemical structure of oxamide. Image credit Sigma-Aldrich.

These burn rate suppressants act as coolants [30]. The coolant effect of oxamide is illustrated in Figure 21: compared to HTPB, the decomposition peak of its differential scanning calorimetry (DSC) trace occurs at a lower temperature, and is much more endothermic. The DSC data is scaled so the area under the DSC curves is proportional to the heat of the decomposition reaction.

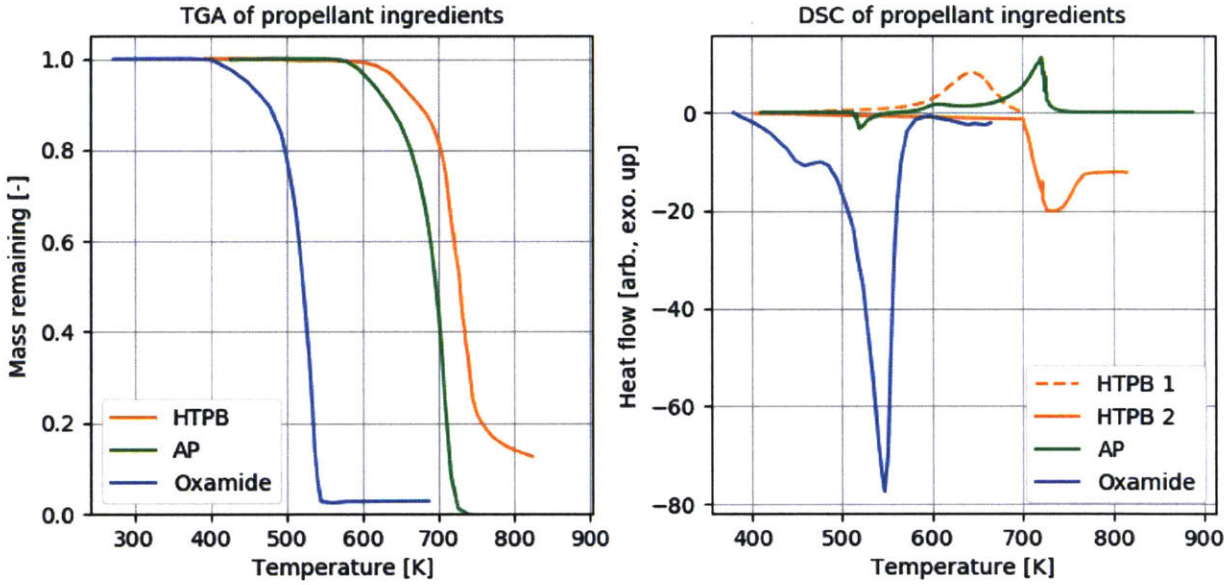

Figure 21: Oxamide decomposes at a lower temperature than, and more endothermically than, other propellant ingredients. The left plot shows thermal gravimetric analysis (TGA), and the left differential scanning calorimetry (DSC). HTPB data[7] from [31]. AP data from [17]. Oxamide data from [28]. Note that this data was taken at heating rates much lower than those of combustion.

A predictive model of oxamide's effect on burn rate has been developed, and is presented for the first time in this work. Use of this model significantly reduces the experimental effort of tailoring the burn rate of a propellant for a particular application. This predictive capacity enhances the utility of oxamide as a design tool for slow-burning solid propellants.

[7] The HTPB data contains an exothermic cyclization reaction around 650 K. This reaction occurs at the low heating rates used to collect this data, but its kinetics are so slow that it does not occur in propellant combustion [4].

2.6 Model of oxamide's effect on burn rate

This section establishes a theoretical relation between the propellant surface regression rate and the oxamide content of the propellant. The surface regression rate is expressed as a velocity r. The oxamide concentration is expressed as a mass fraction of the propellant, $w_{om} \in [0,1]$.

Predicting r from thermochemical first principles is difficult. Instead, this model predicts the fractional change in the regression rate, compared to that of the undoped propellant. Properties of the undoped ($w_{om} = 0$) propellant are denoted with the superscript $*$. The goal of this section is thus to find the function:

$$\phi_{om}(w_{om}) = \frac{r(w_{om})}{r^*} \qquad [2.1]$$

Considering the energy balance at the propellant surface leads to the following model for ϕ_{om}:

$$\phi_{om}(w_{om}) = \frac{1 - w_{om}}{1 + \lambda\, w_{om}} \qquad [2.2]$$

The model arises from physical first principles, under reasonable assumptions. It has a single dimensionless parameter, λ, which depends on the enthalpy required to gasify the propellant.

This model has the correct limiting behavior at the extremes of w_{om}, as shown in Figure 22. When no oxamide is added, the burn rate is unchanged, i.e. $\phi_{om}(0) = 1$. As more oxamide is added, the burning rate monotonically diminishes, i.e. $\lim_{w_{om} \to 1} \phi_{om}(w_{om}) = 0$.

The value of λ can be predicted from tabulated thermochemical data, as shown in Subsection 2.6.2. This model agrees well with experimental data, as shown in Chapter 3. The derivation of the model is presented below.

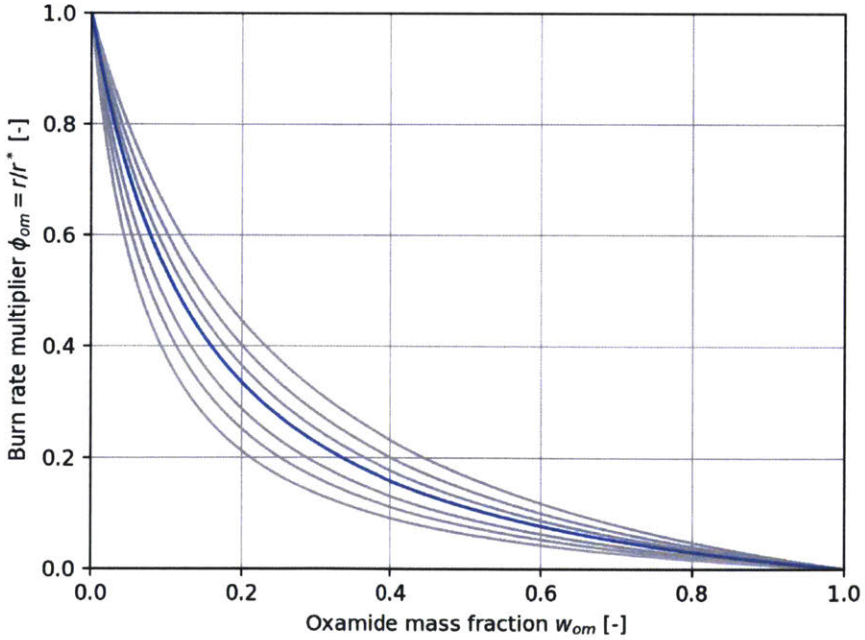

Figure 22: The family of curves represented by equation 2.2.

2.6.1 Derivation of the model

Begin by considering the application of the First Law of Thermodynamics to a control volume at the surface of the propellant. The control volume moves with the surface of the propellant as it regresses at a constant rate r. The control volume contains the surface reaction zone (and the gas-phase AP decomposition), but the main flame structure is outside of the control volume. Assume the flame is steady, so the mass and energy within the control volume do not change with time. A mass flux of solid propellant enters the side 1 of the control volume:

$$j_1 = \frac{\dot{m}_s}{A_1} = \rho_s r$$

where A_1 is the area of side 1 and ρ_s is the density of the solid propellant. A mass flux of decomposed gas leaves side 2 of the control volume to supply the leading-edge and diffusion flames:

$$j_2 = -\frac{\dot{m}_g}{A_2}$$

By conservation of mass,

$$\frac{d}{dt}\int_{CV} \rho \, dt = 0 = j_1 + j_2$$

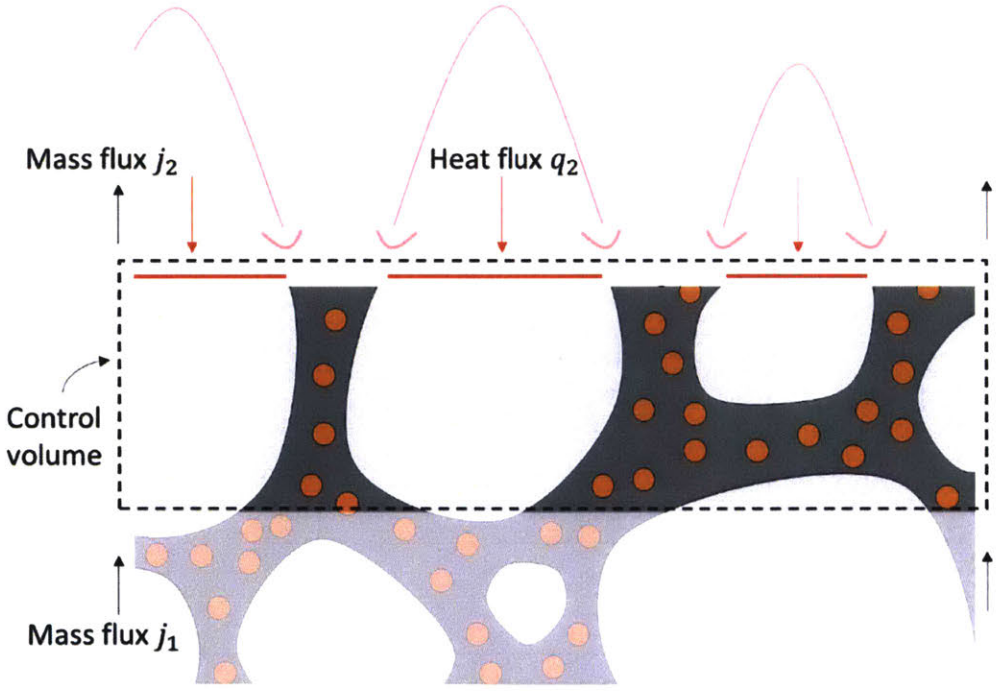

Figure 23: The control volume, which moves with the propellant surface as it regresses.

Write the First Law for the control volume, assuming no mechanical work is done:

$$\frac{d}{dt}E_{CV} = 0 = \oiint \vec{q} \cdot \overrightarrow{dA} + \oiint \left(h + \frac{|v|^2}{2}\right)\vec{j} \cdot \overrightarrow{dA} \qquad [2.3]$$

Now, make assumptions to simplify the equation:

- Kinetic energy $\frac{|v|^2}{2}$ is negligible
- The only relevant heat flux is q_2, from the flame to the surface. The conduction of heat deeper into the propellant, q_1, is negligible.

The First Law becomes:

$$0 = -q_2 A_2 + j_1 h_1 A_1 + j_2 h_2 A_2$$

where h_1 is the average specific enthalpy (thermal + chemical) of the solid enter at side 1, and h_2 is the average specific enthalpy of the gas leaving at side 2. Note that $A_1 = A_2$ (by definition) and $j_1 = -j_2$ (by conservation of mass), so the equation can be further simplified:

$$0 = -q_2 + j_1(h_1 - h_2)$$

$$0 = -q_2 + \rho_s\, r\, (h_1 - h_2)$$

Solve for the burn rate r:

$$r = \frac{q_2}{\rho_s(h_1 - h_2)}$$

Define the surface gasification enthalpy, $\Delta h_{gas} = h_1 - h_2$:

$$r = \frac{q_2}{\rho_2\, \Delta h_{gas}} \qquad [2.4]$$

This equation captures the dependence of the regression rate on the heat flux to the surface, and the energy required to gasify the surface. It is valid for:

- Endothermic surface decompositions with fast kinetics, where the rate of decomposition is limited primarily by the available energy. Exothermic surface decompositions (e.g. AP monopropellant) are not captured by this model; their regression rates depend on reaction kinetics, not on the rate of heat addition from an external flame.

Now, find the simplest possible expression for how each term in Equation 2.4 is influence by the addition of oxamide.

Heat flux, q - Modeling the surface heat flux is complex. It depends on the heat released in the gas-phase flames, the structure and size of the flames, and the heat transport properties of the gas between the flame and the propellant surface.

In the simplest plausible model, oxamide only affects the heat release, not the flame structure or transport properties. It is further assumed that oxamide and its gaseous products do not alter the gas-

phase combustion reaction, but only serve as inert diluents. Therefore, adding oxamide to the propellant reduces the heat release per unit mass by a factor of $(1 - w_{om})$. If the transport properties are not affected, then the heat flux to the surface is reduced by the same factor.

$$q = (1 - w_{om})\, q^*$$

Density ρ_s – The density of pure oxamide (1670 kg m^{-3}) and the density of the propellant (1500 to 1800 kg m^{-3}) are approximately the same. Assume that adding oxamide does not affect the propellant density.

$$\rho_s = \rho_s^*$$

Gasification enthalpy Δh_{gas} - Gasifying a unit mass of oxamide requires more energy than gasifying a unit mass of undoped propellant. The specific gasification enthalpy of a doped propellant is:

$$\Delta h_{gas} = \Delta h_{gas}^*(1 - w_{om}) + \Delta h_{gas}^{om} w_{om}$$

Where Δh_{gas}^* is the specific gasification enthalpy of undoped propellant, and Δh_{gas}^{om} is the specific gasification enthalpy of pure oxamide. This model assumes that propellant and oxamide gasify separately, i.e. the oxamide has no catalytic or inhibitory effect on the propellant's gasification reactions. To simplify the above equation, the parameter λ is introduced:

$$\Delta h_{gas} = (1 + \lambda w_{om})\Delta h_{gas}^*$$

Where:

$$\lambda \triangleq \frac{\Delta h_{gas}^{om} - \Delta h_{gas}^*}{\Delta h_{gas}^*} \qquad [2.5]$$

Substitute each of these relations into Equation 2.4:

$$r = \frac{q_2}{\Delta h_{gas}\, \rho_s} = \frac{(1 - w_{om})\, q_2^*}{(1 + \lambda w_{om})\, \Delta h_{gas}^*\, \rho_s^*} = \frac{1 - w_{om}}{1 + \lambda\, w_{om}}\, r^*$$

Therefore,

$$\phi_{om}(w_{om}) = \frac{1 - w_{om}}{1 + \lambda\, w_{om}} \quad \blacksquare$$

2.6.2 Estimation of the oxamide parameter λ with thermochemical data

The value of the oxamide parameter λ can be predicted from thermochemical data. This makes the model useful for estimating the burning rate of new doping levels in a propellant. The value of λ depends on the gasification enthalpy of the propellant; for typical ammonium perchlorate composite propellants the value is between 4 and 15.

Recall the definition of λ in Equation 2.5:

$$\lambda \triangleq \frac{\Delta h_{gas}^{om} - \Delta h_{gas}^*}{\Delta h_{gas}^*}$$

To predict the value of lambda, the gasification enthalpies of oxamide, Δh_{gas}^{om}, and the undoped propellant, Δh_{gas}^{*}, are estimated from thermochemical data. These estimates are approximate; the true values will depend on the details of the combustion process.

Gasification enthalpy of oxamide, Δh_{gas}^{om} — Roughly, the gasification enthalpy of oxamide is the heat required to raise it from its initial temperature to the temperature of the gasification reaction, plus the heat of reaction:

$$\Delta h_{gas}^{om} = c_p \left(T_{gas} - T_{init}\right) + \Delta h_{rxn}^{om}$$

The gasification reaction rate has been measured to peak near a temperature of T_{gas} = 550 K [28][8]. The decomposition of oxamide yields water and cyanogen [32]:

$$C_2H_4N_2O_2 \rightarrow 2\,H_2O + C_2N_2$$

Using heats of formation data from [33], the heat of reaction is calculated to be 3.74 MJ kg^{-1} (endothermic).

Gasification enthalpy of undoped propellant, Δh_{gas}^{*} — It can be assumed that all of the propellant ingredients decompose separately, so the total gasification enthalpy is the mass-weighted average of the individual gasification enthalpies. For a composite propellant containing AP oxidizer, Al fuel, and HTPB binder,

$$\Delta h_{gas}^{*} = w_{AP}\,\Delta h_{gas}^{AP} + w_{Al}\,\Delta h_{gas}^{Al} + w_{AP}\,\Delta h_{gas}^{HTPB}$$

For AP and HTPB,

$$\Delta h_{gas}^{AP} = c_p^{AP}\left(T_{gas}^{AP} - T_{init}\right) + \Delta h_{rxn}^{AP}$$

$$\Delta h_{gas}^{HTPB} = c_p^{HRPB}\left(T_{gas}^{HTPB} - T_{init}\right) + \Delta h_{rxn}^{HTPB}$$

The relevant values of c_p, T_{gas} and Δh_{rxn} are listed in Table 2. Note that AP decomposition is exothermic, while HTPB decomposition is endothermic.

The metal fuel does not decompose at the surface, rather solid metal particles are ejected from the decomposing surface and melt and combust far downstream [24] [34]. Therefore, the only heat absorbed by the aluminum during the surface decomposition is the sensible heat required to warm it from the initial temperature to the temperature at which the rest of the surface gasifies.

$$\Delta h_{gas}^{Al} = c_p^{Al}\left(T_{gas} - T_{init}\right)$$

[8] This measurement was taken at a heating rate of 10 K min^{-1}. In propellant combustion, the heating rate is substantially higher, and the peak rate temperature is likely somewhat higher as well.

Table 2: Thermochemical data for the decomposition of ammonium perchlorate composite propellant ingredients.

Substance	Peak decomp. Temperature	Heat of decomp.	Decomp. Products	Solid heat capacity	Enthalpy change from 300 K to decomp.
AP	720 K [17]	-0.42 MJ kg^{-1} [35] [18]	NH_3 $HClO_4$ H_2O O_2 HCl ... [17]	180 J kg^{-1} K^{-1} [33]	-0.34 MJ kg^{-1}
HTPB	720 K [19]	1.80 MJ kg^{-1} [19]	C_4H_6 CH_2O CH_n C_2H_n [19]	2386 J kg^{-1} K^{-1} [36]	2.80 MJ kg^{-1}
Aluminum	N/A	N/A	N/A	992 J kg^{-1} K^{-1} (at 500 K) [37]	0.714 MJ kg^{-1} (to 720 K)
Oxamide	550 K [28]	3.74 MJ kg^{-1}	C_2N_2 H_2O [32]	1280 J kg^{-1} K^{-1} [33]	3.85 MJ kg^{-1}

Now, the gasification enthalpy of undoped propellant, Δh^*_{gas}, and the oxamide parameter, λ, can be calculated for a range of propellant compositions, and are shown in Figure 24 and Figure 25.

Note that this theory is not applicable to all propellant formulations. As the AP content is increased, Δh^*_{gas} approaches zero, the value of λ explodes, and the theory breaks down. This is because the decomposition of AP is exothermic, and the theory is only valid for net-endothermic surface decompositions (i.e. $\Delta h^*_{gas} \gg 0$).

However, the theory is valid for most useful solid propellants. Typical solid propellants contain between 60% and 72% AP, and 4 to 17% Al [16]. Over this range, the surface decomposition is endothermic, and λ takes on values from 4 to 15.

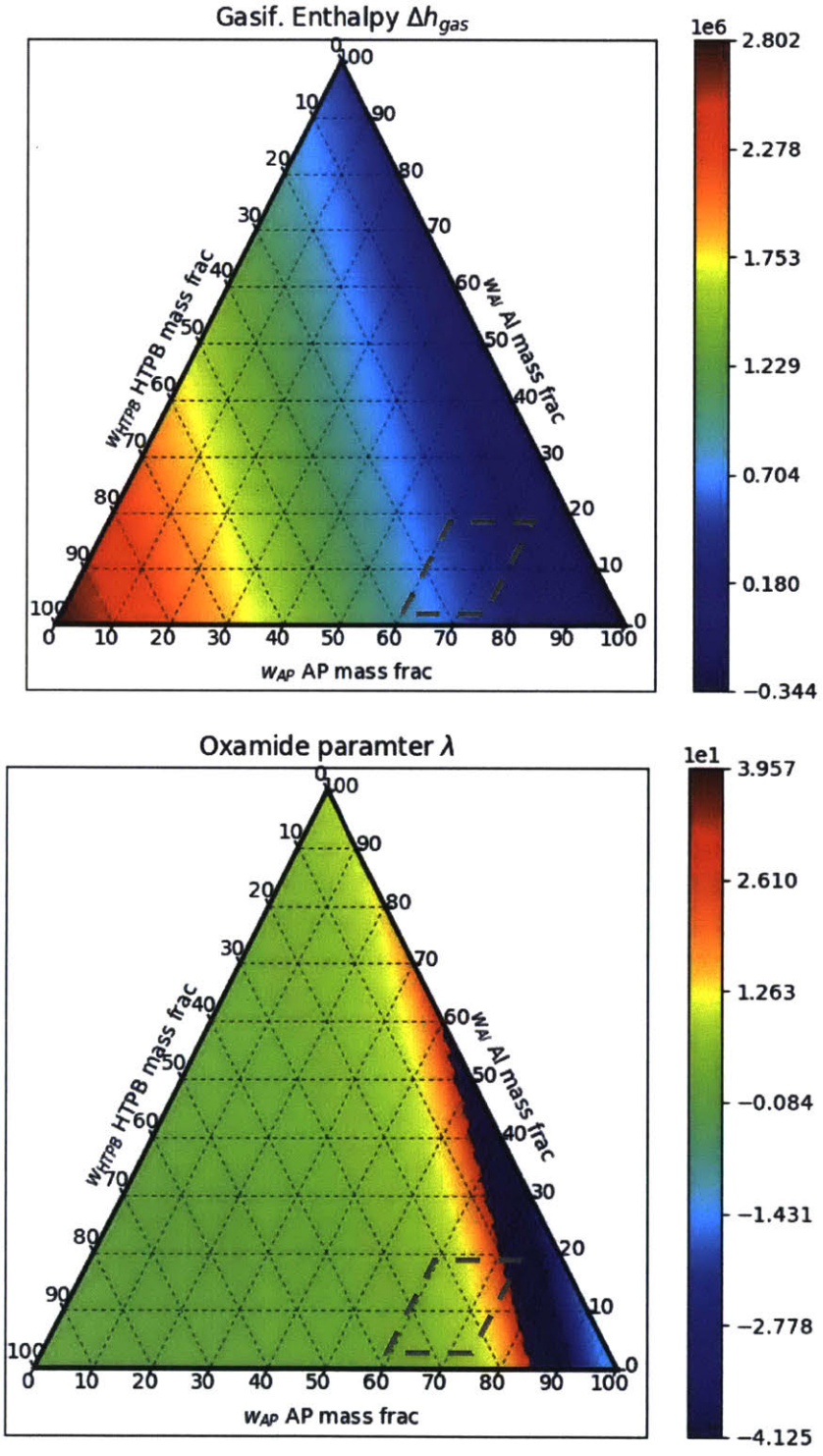

Figure 24: These ternary diagrams show the gasification enthalpy (top, units of J kg^{-1}) and λ value (bottom, unitless) for different propellant compositions. The dashed border marks the composition region occupied by most propellants.

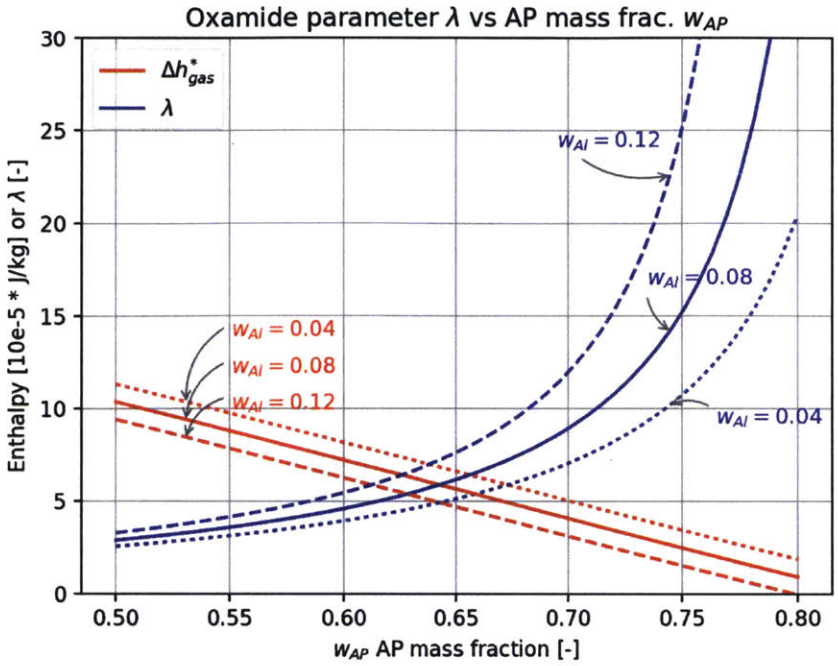

Figure 25: The value of the oxamide parameter varies with the ammonium perchlorate and aluminum content of the propellant.

2.6.3 Predictions of the oxamide burn rate theory

This theory predicts the change in the burn rate of a solid propellant when an amount of oxamide is added. These predictions are shown in Figure 26. The black curve shows the theoretical ϕ_{om} values given by Equation 2.2 with λ = 7. The theory predicts somewhat different λ values for different propellant formulations; the grey shaded region covers the expected range of λ = 4 to 15.

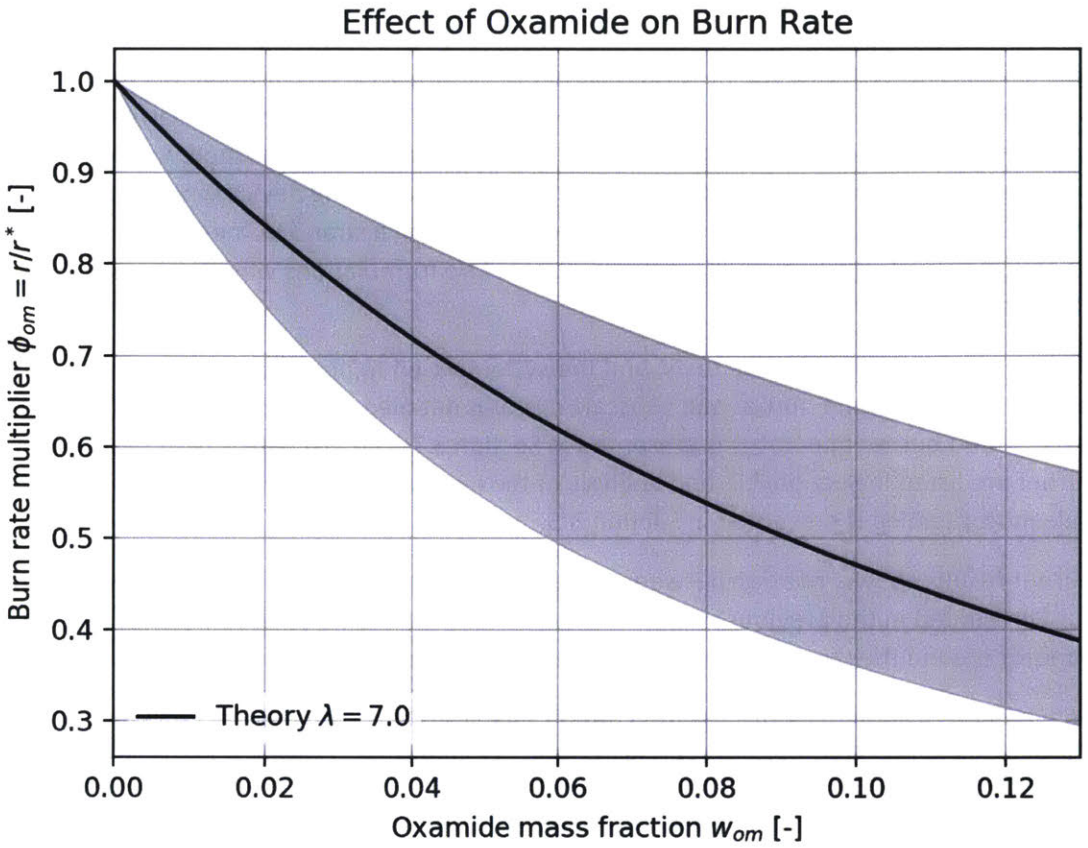

Figure 26: Theoretical prediction of oxamide's effect on propellant burn rate. The grey region indicates the range of values which the oxamide parameter λ may take on in typical ammonium perchlorate composite propellants.

These theoretical predictions show good agreement with the results of propellant combustion experiments conducted by this group and reported by others. This comparison is presented in Chapter 3.

The good agreement between subscale motor firings and model predictions indicates that the model can be used to predict the effect of oxamide doping on the burn rate of a propellant. This provides a useful tool to the designer of a slow-burning rocket motor. Suppose a designer has a propellant with a known burn rate in the undoped state, and burn rate target required by a particular motor. She can use Equation 2.2 (with $\lambda = 7$) to estimate the amount of oxamide which must be added to the propellant composition to achieve the burn rate target. This cuts the guesswork involved in the propellant design process, and reduces the experimental effort required to develop a new propellant.

3 Propellant testing

Slow burning solid rocket propellants are an important tool in the development of miniature, low thrust, long-endurance propulsion systems. The previous chapter presented a class of propellants which should fulfill this role. Those propellants were tested in order to experimentally validate their performance. To screen a large number of propellant candidates, a low-cost preliminary testing method was required. Low cost screening was performed with a strand burner, a propellant testing device which burns samples ("strands") of solid propellant at a controlled pressure. Using a strand burner, 85 propellant samples were tested to evaluate 16 propellant formulations. Two formulations were then tested in a subscale rocket motor.

This Chapter presents the results of these tests, and the systems used to perform them. First, the laser ignition system used in the strand burner and subscale motor is detailed in Section 3.1. The design and operation of the strand burner apparatus is presented in Section 3.2. The propellant tests carried out on the strand burner are listed in Section 3.3, and analysis of the resulting data is given in Section 3.4. Finally subscale motor testing is presented in Section 3.5.

The strand burner results show a relation between oxamide content and burn rate which is compatible with the theory presented in the previous chapter. As expected, propellants burn somewhat faster in the subscale motor than in the strand burner tests, regardless of oxamide content.

The propellant characterization presented in this chapter enables the design of a solid rocket motor which uses these propellants. This application is presented in Chapter 5.

3.1 Laser ignition

Context – Laser ignition is a novel development in the practice of solid propellants and pyrotechnics [38]. One objective of this research is to explore the application of laser ignition to slow-burning solid rocket propulsion systems. Laser ignition is interesting because of the potential for better safety, consistency and reliability compared to pyrotechnic ignition devices. In this work, many samples of ammonium perchlorate composite propellant were ignited with a multi-watt blue laser, and their ignition behavior was measured. This section presents a qualitative model of the laser ignition process and some experimental results. The design of laser ignition systems is presented for a strand burner in Subsection 3.2.1, for a subscale motor in Section 3.5.1, and for a flight motor in Section 5.6.

Most propellants were found to be laser-ignitable. However, very slow-burning propellants with high (>8%) oxamide content would not ignite at low pressures. Therefore, we recommend that slow-burning solid rocket propulsion systems use a laser to ignite a starter grain of faster-burning APCP, which in turn lights the slow-burning main propellant grain.

Laser ignition is appealing because of its enhanced better safety, consistency and reliability compared to pyrotechnic ignition devices. Laser ignition can be safer the pyrotechnic ignition: a laser ignition system contains no Class 1.1 energetic materials, and cannot be set off by static or stray voltages[9]. Laser ignition is also more consistent and reliable: once burned in and characterized, a properly driven laser diode will

[9] Typical laser diodes of sufficient power for propellant ignition must be supplied with several hundred milliamps of current to lase.

emit a consistent beam power for several hundred hours of service [38]. By contrast, small pyrotechnic igniters ("e-matches") are variable and can be damaged by handling.

Laser ignition was also convenient for our propellant evaluation process. It eliminated pyrotechnic igniters; unreliable, consumable components which would have to be replaced after each test. The laser system, by contrast, is reusable and requires less frequent upkeep.

3.1.1 Model of composite propellant ignition

This section provides a brief overview of a composite propellant ignition model[10]. The model is not sufficiently accurate to make quantitative predictions, but it provides useful qualitative insight on the ignition process.

The overall architecture of the model is loosely based on a classical AP combustion model by Beckstead, Derr, and Price [39]. The model architecture can be can be split into roughly three sections: the surface modeling, the heat transfer modeling, and the flame modeling itself.

The surfaces are modeled by numerically solving a differential equation on surface temperature. The surface temperature is driven by heat flux from the flames had heat release (or absorption) by reactions at the surface. The surface reaction rates, in turn, have an Arrhenius dependence on surface temperature.

The heat transfer from the flames to the surface is modeled as an exponential function of the distance from the surface, as is done in [39]. The heat transfer between the flames is not modeled.

The flame structure is not modeled in depth, but rather is assumed to take a particular structure, as done in [39]. Diffusion and reaction kinetics are used to model the standoff distances of these structures from the propellant surfaces. Diffusion, chemical kinetics, and chemical equilibrium calculations were solved with the *Cantera* software package.

Simulation results from this model qualitatively illustrate the propellant ignition process [Figure 27]. The figure's plots show the following quantities as traces against time (left to right, top to bottom):

a. the heat flux to the fuel and oxidizer surfaces, and the heat fluxes emitted from various sources (AP flame, LE (leading edge, a.k.a primary) flame and igniter),
b. the temperature of the propellant surfaces and flame fronts,
c. the heat flux consumed by various surface reactions,
d. the mass of liquid AP which has accumulated on the surface per unit area,
e. the standoff distance from the propellant surface to the flame fronts,
f. the radial position of the leading edge flame front (note the narrow range of the vertical axis; this plot is unimportant),
g. the combustion equivalence ratio (this should be near the dotted line "ϕ solid" for the model to close), and
h. the surface regression rate.

Note that the ambient pressure in the simulation is much higher (6 MPa vs ~1 MPa), and the AP particle size is much smaller (50 μm vs ~200 μm). Both differences move the flames closer to the propellant

[10] The model was developed by Samuel B. Judd and this author, and is described further in an unpublished report [82]; copies are available from the author upon request.

surface, making the burn rate and ignition more rapid. Therefore, these plots should be viewed only for their qualitative story, not for exact numerical values.

To start the reaction, an ignition heat flux pulse is supplied to the surface (top-left subplot, purple curve). The ignition pulse is centered at 2 ms simulation time. Before ignition, the surface temperature is stable at 300 K and no mass flux is emitted from the surface. After the ignition transient (t > 3.5ms), the heat fluxes, temperatures, and flame standoff distances stabilize to their stead-state values.

At the start of the ignition transient, the oxidizer and fuel surface temperatures rise due to the igniter heat flux, but no significant mass flux occurs ($t = 1.0 - 1.5$ ms, top-right plot). At $t \approx 1.6$ ms, the AP reaches its dissociation temperature (~700 K) and the HTPB is hot enough that the pyrolysis reaction can progress at a significant rate. The mass fluxes of gas from each surface increase quickly, and the AP and leading edge flames start to burn this gas. Note that there is some ringing from numerical stability problems at this point.

The heat fluxes, mass fluxes and temperatures peak at t = 2ms, when the igniter heat flux peaks. After the igniter heat flux peak, the heat fluxes, mass fluxes and temperatures begin to decrease to their steady state values. Once the igniter heat flux subsides, a self-sustaining combustion process continues.

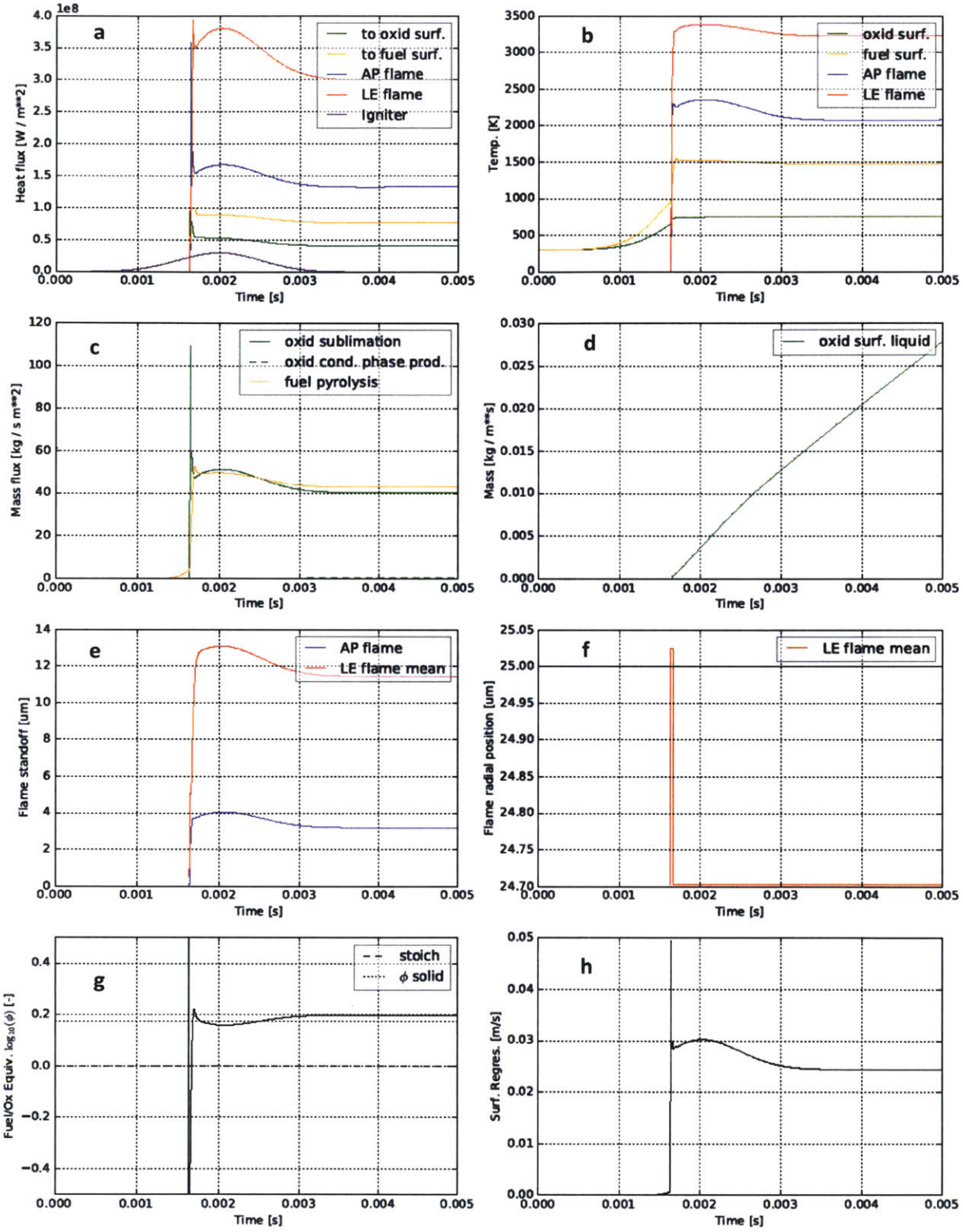

Figure 27: Simulation of the ignition of an AP composite propellant by a heat flux pulse. Note the conditions of this simulation are different from those tested in this work.

3.1.2 Testing

Tests of laser ignition were performed on many propellants as exposed samples [Figure 28], in a strand burner [Section 3.2], and in a subscale motor [Section 3.5].

These tests showed that undoped AP-based propellant can reliably be ignited with a 2 MW m^{-2} laser spot (6 W beam focused to a 2 mm diameter spot). The ignition delay can range from 100 ms to over 10 s, depending on the propellant formulation and the pressure. Propellant is easier to ignite at higher pressures, and faster-burning, hotter propellants ignite more rapidly.

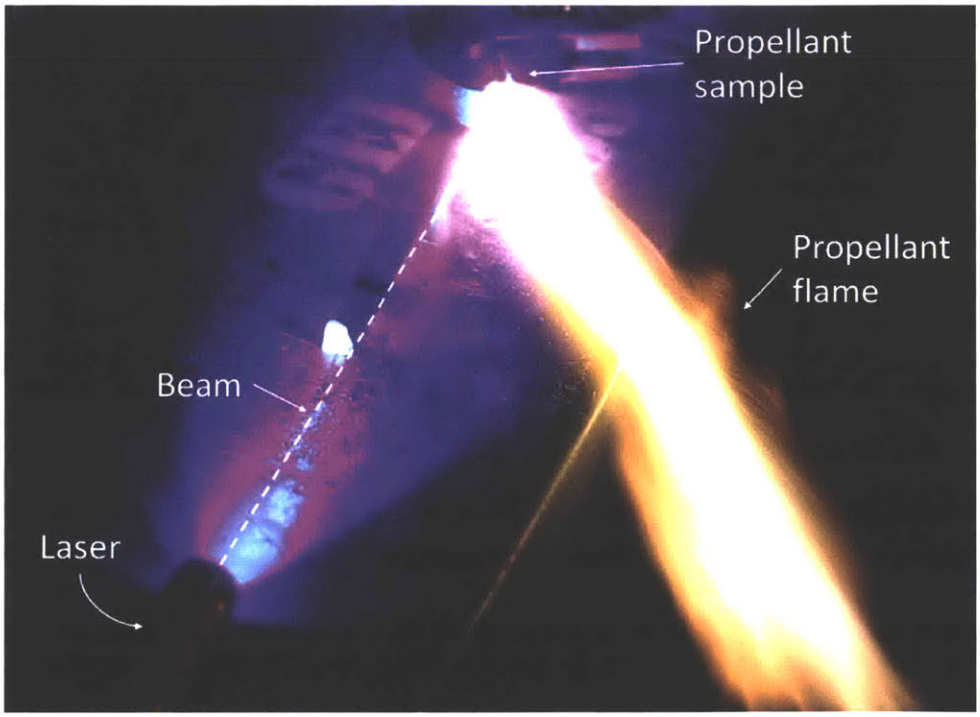

Figure 28: A sample of AP composite propellant burns (orange streak, top-middle to bottom-left) after being exposed to laser radiation (blue-purple glow, laser is at bottom-right).

Specifically, Figure 29 shows the minimum pressure at which various propellants could be ignited by a particular laser spot. The figure plots ignition pressure vs. oxamide content. The minimum ignition pressure measured for each propellant is marked with a blue dot. All propellants with oxamide content less than 8% ignited at atmospheric pressure (0.10 MPa, the lowest pressure tested). Higher-oxamide propellants had higher minimum ignition pressures. The boundary of the ignitable region in p, w_{om} space is roughly illustrated by the black dashed curve.

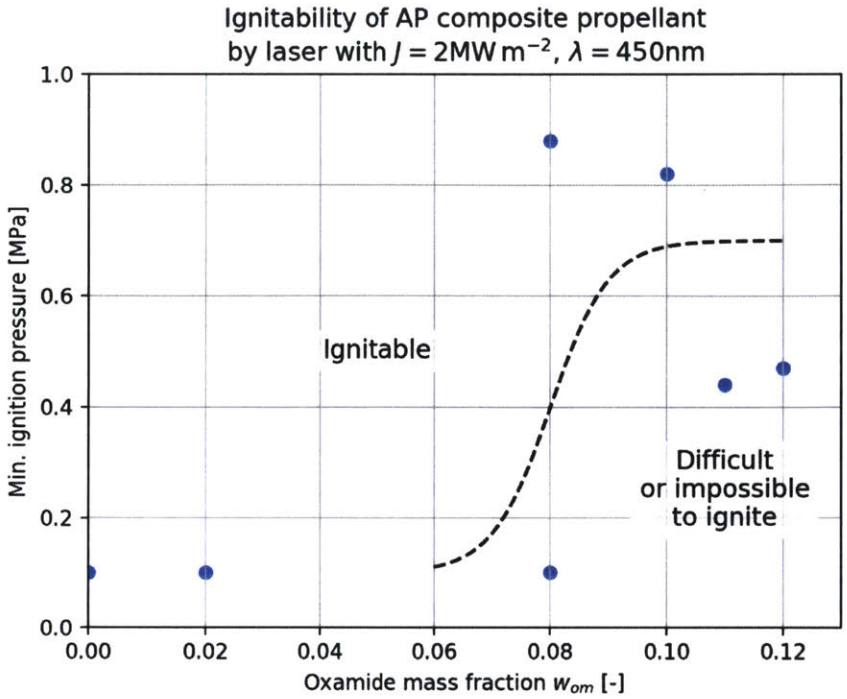

Figure 29: Oxamide content effects the minimum pressure at which an ammonium perchlorate composite propellant can be ignited by a laser spot.

3.2 Strand burner apparatus

Developing a new family of propellants requires the rapid evaluation of many candidate propellant formulations. These evaluations are performed with a strand burner, a device which burns small samples ("strands") of propellant at a controlled pressure and measures their burn rate. We designed and built a strand burner which allows for rapid exchange of propellant samples, laser ignition of the propellant, and optical observation of the flame front.

This section presents the design of the strand burner hardware [Subsection 3.2.1] and its operation [Subsection 3.2.2]. The following sections present the tests performed using the strand burner [Section 3.3] and analysis of the data collected [Section 3.4].

3.2.1 Strand burner mechanical design

The strand burner has four subsystems:

1. The *sample holder* holds the propellant sample and the laser igniter. The sample is contained in a quartz glass tube, which allows for optical observation of the flame front.
2. The *plenum* collects combustion gases from the burning propellant sample. Gas is vented from the plenum through the *backpressure regulator*. A large plenum smooths out variations in pressure, and allows solid particles to settle out before reaching the backpressure regulator.
3. The *backpressure regulator* maintains the desired pressure in the plenum by venting gas if the pressure exceeds the set-point. The backpressure regulator is sensitive to clogging, so it is place

on the far side of the plenum (to allow solid particles to settle out of the flow) and is protected by a filter.

4. A *pressure sensor* measures the pressure in the plenum.

A camera is set up to record the progress of the flame front through the sample. An analog to digital converter and computer record the plenum pressure and the laser current.

The sample holder is the most mechanically complex part of the strand burner, and is detailed in Figure 30. The purpose of the sample holder is to hold the propellant sample in alignment with the laser, and to create a sealed, pressurized path from the propellant sample to the plenum.

The sample holder has two sets of moving parts:

1. A toggle which retracts to allow the propellant sample to be removed and replaced, and
2. A door which opens to allow the laser window to be cleaned.

These motions are illustrated in the top part of Figure 30.

The internal components of the sample holder are shown in cross section in the middle of Figure 30. The laser beam path is shown in blue. At the right end of the beam path is the laser, and at the left end is the right face of the propellant sample. A quartz glass window is placed in the middle of the beam path; it protects the laser from the combustion gases. A second passage joins the beam path passage at a right angle (into the page); this connects to the plenum.

The propellant sample is contained in a quartz glass sample tube. The right end of the sample tube is inserted a few millimeters into the beam path passage, and the left end is held in place by a toggle clamp. O-ring face seals are used at both ends of the sample tube and on the laser window.

When the propellant is hit with the laser beam, its right face ignites and the flame front progresses along the sample from right to left. An example image of the flame front is shown in the bottom of Figure 30. The image's field of view is marked with black dashes in the middle of Figure 30.

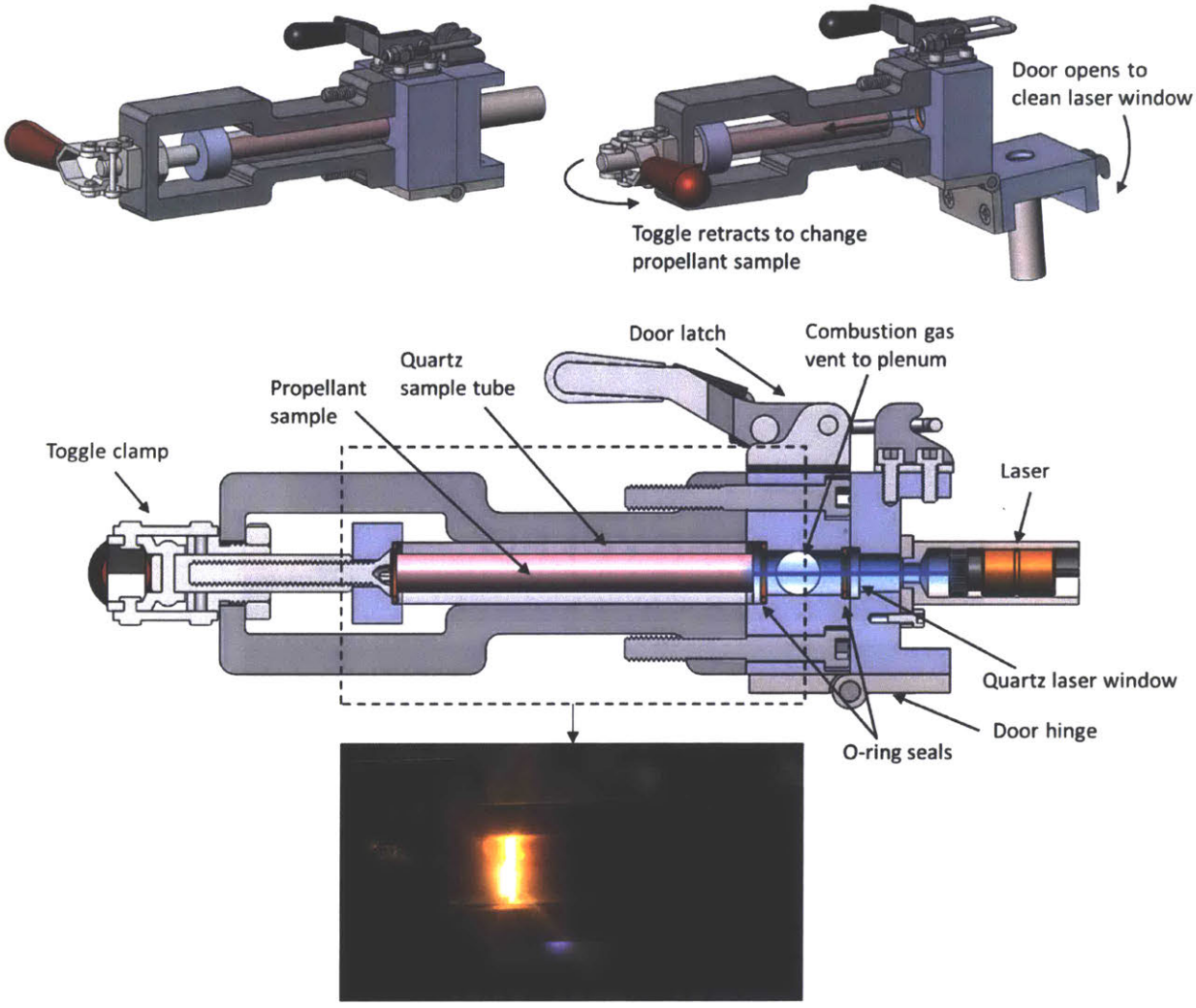

Figure 30: Details of the strand burner sample holder. Top: the sample holder opens to change samples and clean the laser window. Middle: a cross section showing the laser beam path and components of the sample holder. Bottom: view of the sample holder during a propellant test. The dashed rectangle on the middle subfigure outlines the image field of view.

3.2.2 Strand burner operation

To perform a propellant test with the strand burner, first a batch of propellant is mixed and cast into quartz glass sample tubes. Each tube holds about 10 g of propellant, and typically 5 or 10 tubes are filled in a batch. The propellant is then left to cure.

Next, the strand burner is set up in a blast chamber and connected to its data logging and control electronics. A sample tube (full of propellant) is loaded into the strand burner sample holder. The strand burner is then pressurized to the desired test pressure with argon. The test personnel leave the blast chamber and remotely trigger the laser to ignite the sample. After the sample has burned, the test personnel enter the blast chamber, exchange the spent sample tube and adjust the pressure for the next test.

Afterwards, videos of the propellant test are analyzed to measure the burn rate. Typical video frames are shown in Figure 31.

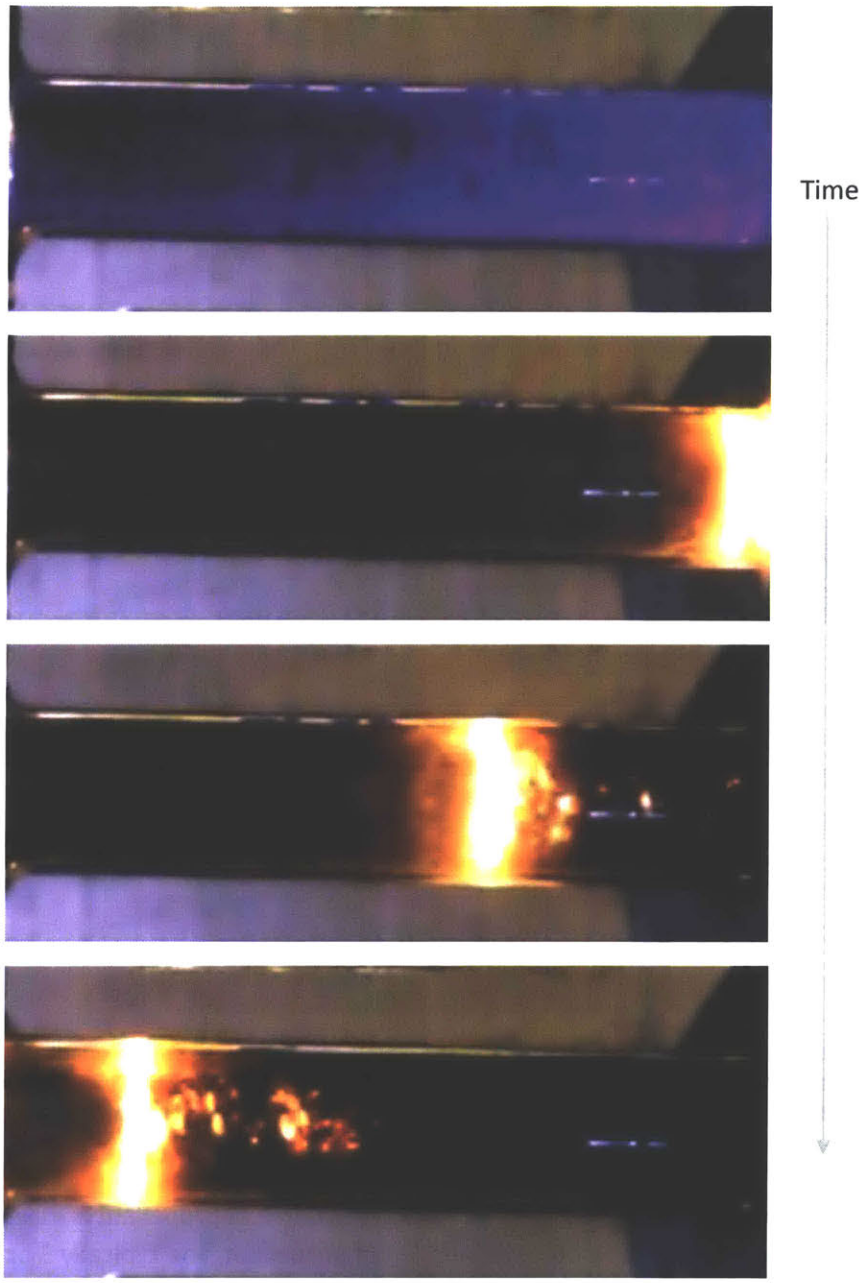

Figure 31: Burning of a strand burner sample. A blue flash is visible through the propellant when the laser ignition system is fired (top). Then, the flame front progresses across the sample (middle and bottom).

3.3 Strand burner tests

In the search for a suitable family of slow-burning propellants, many propellant formulations were tested in the strand burner. We tested a few ammonium nitrate (AN) based propellants and many ammonium perchlorate (AP) propellants doped with the burn rate suppressant oxamide. This section describes the tests carried out, and provides a qualitative overview of the results. A statistical analysis of the oxamide result is presented in the next section.

While AN based propellants burned more slowly that AP/oxamide propellants, they had less stable combustion and were more difficult to manufacture. We therefore chose the sufficiently slow and better-behaved AP/oxamide propellants as the focus of the remainder of our research.

Before delving into the details of the tests, it should be noted that strand burner tests are a preliminary screening, and do not exactly replicate the combustion conditions within a rocket motor. Propellant typically burns slower in a strand burner because the isolated strand of propellant loses heat to the surrounding environment [16]. This effect is more pronounced in our strand burner because the propellant burns inside of a clear, solid sample tube which leads to high radiation and conduction losses[11].

3.3.1 Strand burner test objectives

The objectives of strand burner tests are to:

1. Establish whether a propellant formulation exhibits stable combustion, and if so measure the pressure range over which combustion is stable. Many propellants have a lower pressure limit of combustion (LPL), below which they will not burn.
2. Determine an empirical relationship between burn rate and pressure. Ideally, this would be well-characterized by Vieille's Law

$$r = a\,p^n$$

3. Determine the laser power flux required to ignite the propellant, and the ignition delay time.

3.3.2 Strand burner tests of ammonium nitrate based propellants

AN-based propellants are a common class of slow-burning propellants, typically used in gas generators for turbomachinery [16]. We evaluated several AN-based propellants, but chose not to pursue them as propellants for slow-burning solid rockets in UAVs. AN propellants have several unfavorable qualities. Generally, they have poor specific impulse and require high solids loading, and the propellants we tested did not burn well at low pressures.

Twenty samples from 4 formulations of AN-based propellant were produced and tested. Of these, only 12 samples from 3 formulations burned successfully. The burn rates and pressures of those samples are presented in Figure 32. The propellants burn slowly (0.9 to 1.9 mm s^{-1}), but have high lower pressure limits of combustion (1.3 to 1.5 MPa). These LPL values are too high for the structural limitations of some UAV propulsion motor cases [see Section 5.5].

Two techniques were identified to vary the burn rate of the AN propellant; their effects are illustrated in Figure 32. First, the burn rate increased when smaller AN particles were used. This is expected from combustion theory [see Section 2.4]: smaller oxidizer particles create a smaller flame structure closer to the propellant surface, which increases heat transfer to the surface. Second, the burn rate was reduced by substituting some of the magnesium fuel for a halide catalyst (NaCl). The mechanism of action here is unknown to the author; halide catalysts are generally thought to increase the burn rate of AN [40].

---

[11] In a typical strand burner, a strand of propellant is burned in a large, opaque pressure vessel, with perhaps a small window. Compared to this design, our strand burner flame loses more heat to radiation (through the clear glass tube) and conduction (to the solid glass in contact with the flame).

The AN propellants exhibited somewhat unstable combustion in the strand burner; the flame front would occasionally jump forward by a large amount. This instability was worse in a subscale motor: two grains of AN.80.125/250-HTPB-Mg.05 propellant exploded shortly after ignition during subscale motor tests.

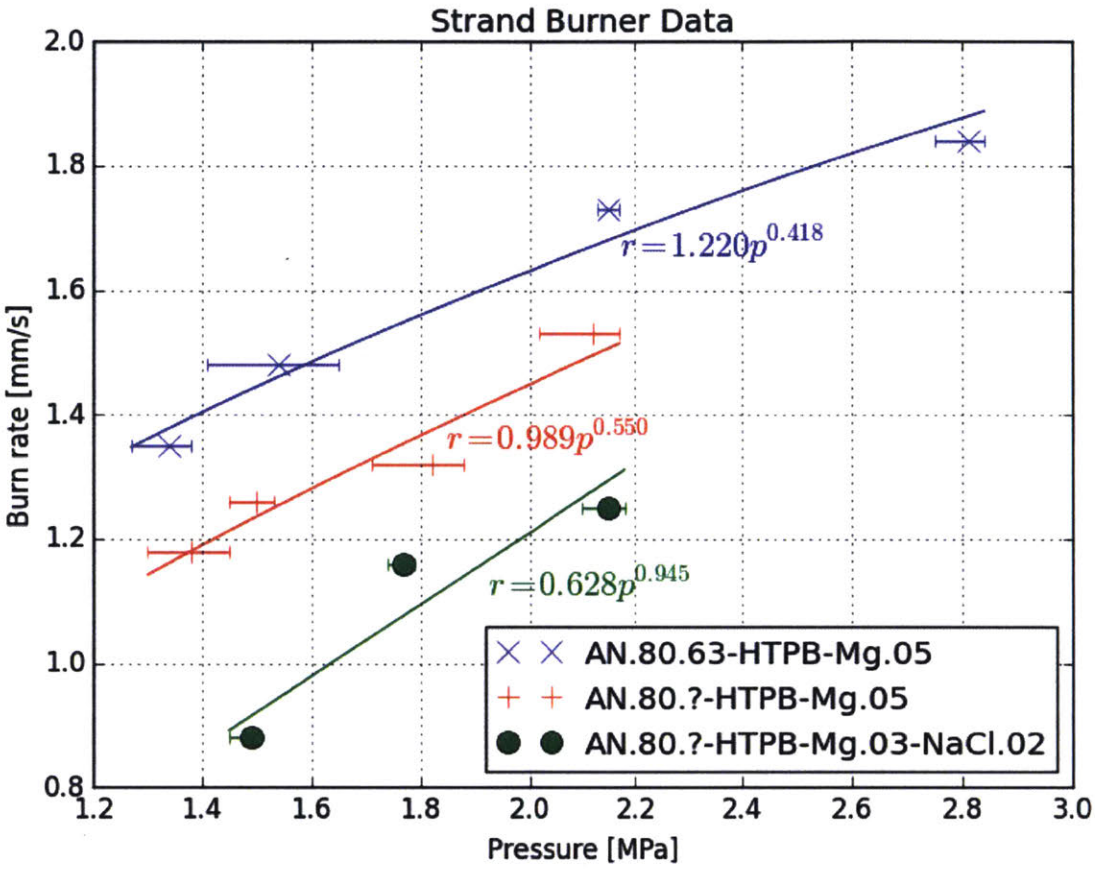

Figure 32: Burn rate vs pressure for ammonium nitrate based propellants. Using AN particle size increases burn rate (blue curve, particles < 63 μm). Reducing magnesium content and introducing a chlorine catalyst decreases burn rate (green curve, 3% Mg and 2% NaCl).

Further, the AN propellants were difficult to produce. AN is highly hydroscopic, thus AN propellants must be mixed in a low humidity (< 10% RH) space. AN has a low oxygen balance, so AN propellants have a high solids loading. This makes the propellants difficult to mix and impossible to pour, requiring that they be packed instead. Packing leaves voids in the propellant[12], which may have contributed to the combustion instability of our AN propellants. Even with high solids loading, AN propellants still burn at a low temperature and deliver poor specific impulse.

[12] Unless the propellant is subsequently compacted with a hydraulic press [75] [76]; a technique which was not available in our research.

Because of the drawbacks surrounding AN based propellants, we did not select them for our slow-burning rocket motor. Instead, we focused on a different class of slow-burning propellant: AP propellants suppressed with oxamide.

3.3.3 Strand burner tests of oxamide doped ammonium perchlorate propellants

AP-based propellants typically burn too quickly for slow-burning solid rockets. However, as previously discussed [Sections 2.4 - 2.6], their burn rate can be suppressed via the addition of coolants such as oxamide. Using the strand burner, we evaluated many formulations of AP/oxamide propellant. We selected a family of propellants from this class for further development and use in slow-burning solid rocket motors for UAV propulsion.

Thirty-five samples from 7 formulations of AP/oxamide propellant were produced and tested. Of these, 27 samples yielded useful burn rate data. We found the propellants to burn smoothly if properly produced. Most propellants had LPLs below 0.1 MPa, except for the highest-oxamide formulations. As expected, the burn rate declined with increasing oxamide content. Other factors, such as small variations in metal or AP content, had no significant effect on burn rate.

The distributions of various variables within the AP/oxamide strand burner dataset are shown in Figure 33. From left to right, the figure shows:

1. AP mass fraction, w_{AP}, which covers the range 60% to 71%. Over this narrow range, w_{AP} is only expected to have a mild effect on burn rate.
2. AP mean particle size, which has a bimodal distribution clustered at 175 µm and 300 µm.
3. Measured density, which has a mode near 1500 kg m^{-3} but a long low-density tail.
4. Hardness, which covers the range from 40 to 65 on the Shore A scale. The low end of this range (< 50 Shore A) is unusually soft for AP-based composite propellants.
5. Whether the bonding agent HX-752 was used in the propellant. Most samples used the bonding agent.
6. The metal mass fraction $w_{Mg,Al}$, which intermittently covers the range from 3% to 9%.
7. Oxamide content, w_{om}, which is has a bimodal distribution clustered at low (2%) and high (8-12%) concentrations. There is no coverage of moderate (3-7%) oxamide concentrations.
8. Test pressure, which covers the range 0.1 to 2.5 MPa.
9. Burn rate, which covers the range 0.5 to 5 mm s^{-1}.
10. Relative density D_r, defined as measured density divided by the theoretical maximum density.

$$D_r = \frac{\rho_{meas}}{\rho_{theory}}$$

The relative density distribution peaks at 93-97%, but has a long low-density tail reaching down to 77%. Low relative density samples contain voids, and may burn unsteadily or at an accelerated rate. Note that 3 samples have relative density $D_r > 1$. This is not physically possible, and indicates error in the density measurement.

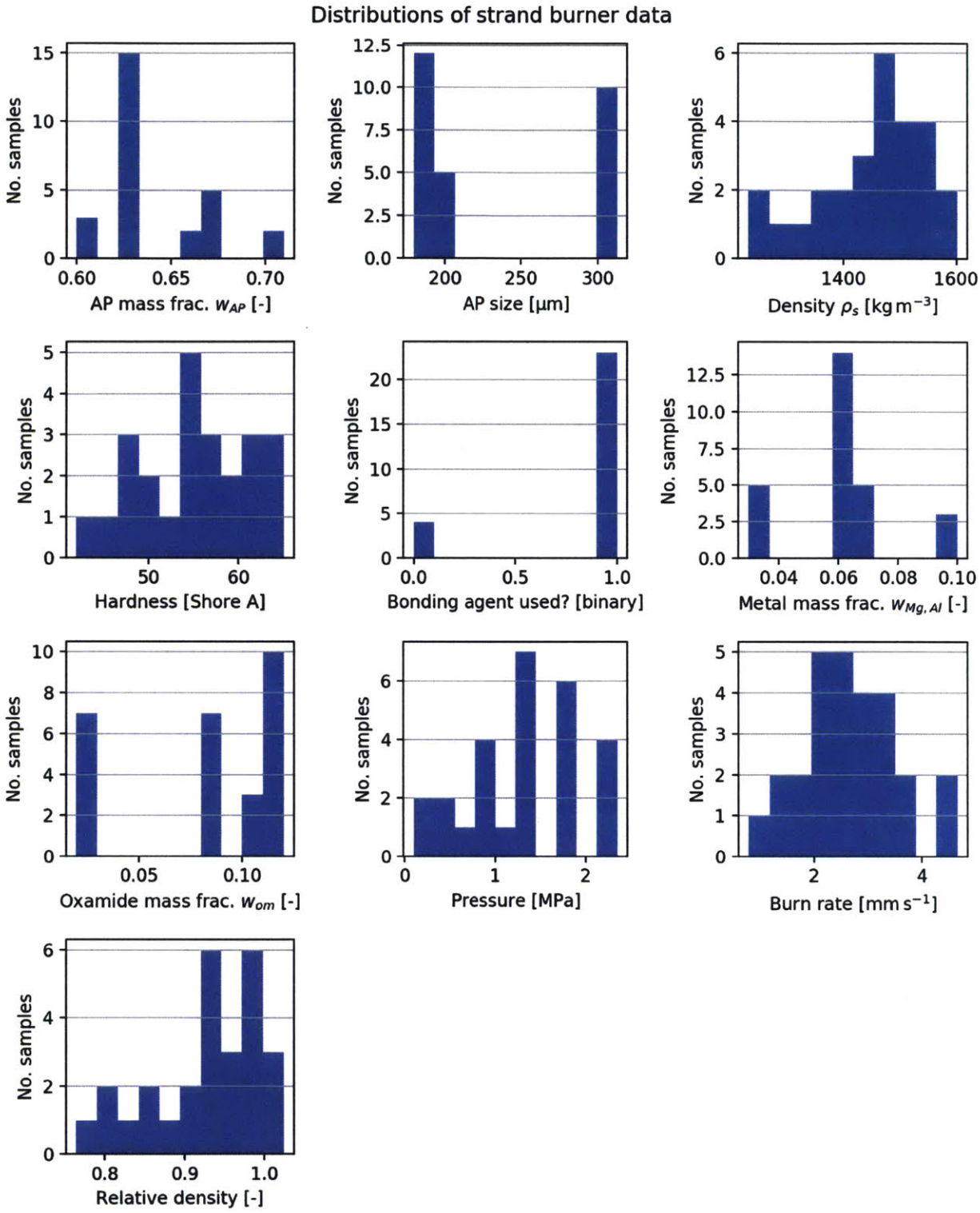

Figure 33: Distributions of the variables measured in strand burner testing of oxamide-doped propellants. 27 samples are included in the dataset.

It should be noted that this data was collected during exploratory phase of research, so the variation of independent variables was somewhat haphazard. New techniques and questions arose as the research progressed. Several variables correlate with date, changing as our processing technique improved. Particularly, relative density and hardness improved after vacuum processing and the HX-752 bonding agent were introduced.

The variables were then assessed for their effect on the primary variable of interest, burn rate r. We fit Vieille's Law to the burn rate r vs pressure p data for each propellant, to find its values of a and n:

$$r \sim a\, p^n$$

We then plotted a and n for each propellant formula against that formula's average value of the other variables. Only oxamide content w_{om} and relative density[13] D_r showed promising correlations with a; their effect on burn rate is analyzed further in Section 3.4. The only variable to show a significant correlation with the burn rate exponent n was the use of bonding agent [Figure 34]. Bonding agent was necessary to achieve the desired value of n (0.4 to 0.5); propellant formulations without bonding agent had dangerously high n.

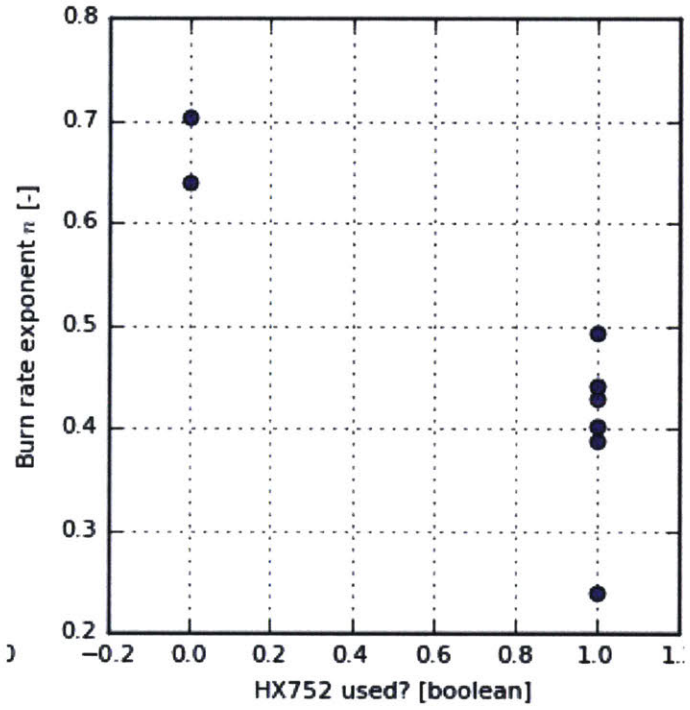

Figure 34: The bonding agent HX-752 improves the stability of propellant combustion. Propellants which used bonding agent have n between 0.4 and 0.5, typical of AP composite propellants. Propellants without bonding agent had n between 0.6 and 0.7, closer to the instability threshold 1.

[13] Hardness also showed a promising correlation, but hardness strongly correlated with relative density. Relative density has a more plausible causal link to burn rate than hardness [77].

3.4 Regression analysis of strand burner tests

Oxamide suppresses the burning rate of ammonium perchlorate composite propellants. Section 2.6 presented a model for oxamide's effect on burn rate, derived from physical first principles. This theory must be tested against experimental evidence. The theory will be shown shown to agree well with subscale motor data collected in this research and by other researchers.

This research also collected 27 strand burner measurements of the burn rate of oxamide-doped propellant. This section presents statistical analysis on the strand burner data. Specifically, nonlinear regression is used to estimate the value of the oxamide parameter λ [introduced in Section 2.6.1, Equations 2.2 and 2.5]. The range of values for λ estimated from the strand burner regression overlaps with the range predicted by the burn rate theory and thermochemical data. This supports the validity of the burn rate theory.

The oxamide burn rate theory was used to design a family of burn-rate-tailored solid propellants which were then tested in subscale motors [Section 3.5] and used in the design of a slow-burning rocket propulsion system for a small, fast UAV [Chapter 5].

The strand burner data, its regression fit, and agreement with theoretical predictions are shown in Figure 35. Each strand burner sample (light red dot) is plotted on axes of $\phi_{om} = \frac{r}{r^*}$ vs. w_{om}. r is the measured burn rate, and r^* is the expected burn rate based on the samples pressure and relative density (but not oxamide content); thus ϕ_{om} is the burn rate multiplier due to oxamide, as in Section 2.6. w_{om} is the mass fraction of oxamide in the propellant. A regression fit of $\phi_{om}(w_{om})$ on the strand burner data (dashed red curve) and its $\pm 2\sigma$ confidence interval (light red region) are also plotted. The theoretically predicted $\phi_{om}(w_{om})$ (black curve) and its expected range of variation (grey region) are shown as well. Note that the regression confidence interval is mostly within the expected range.

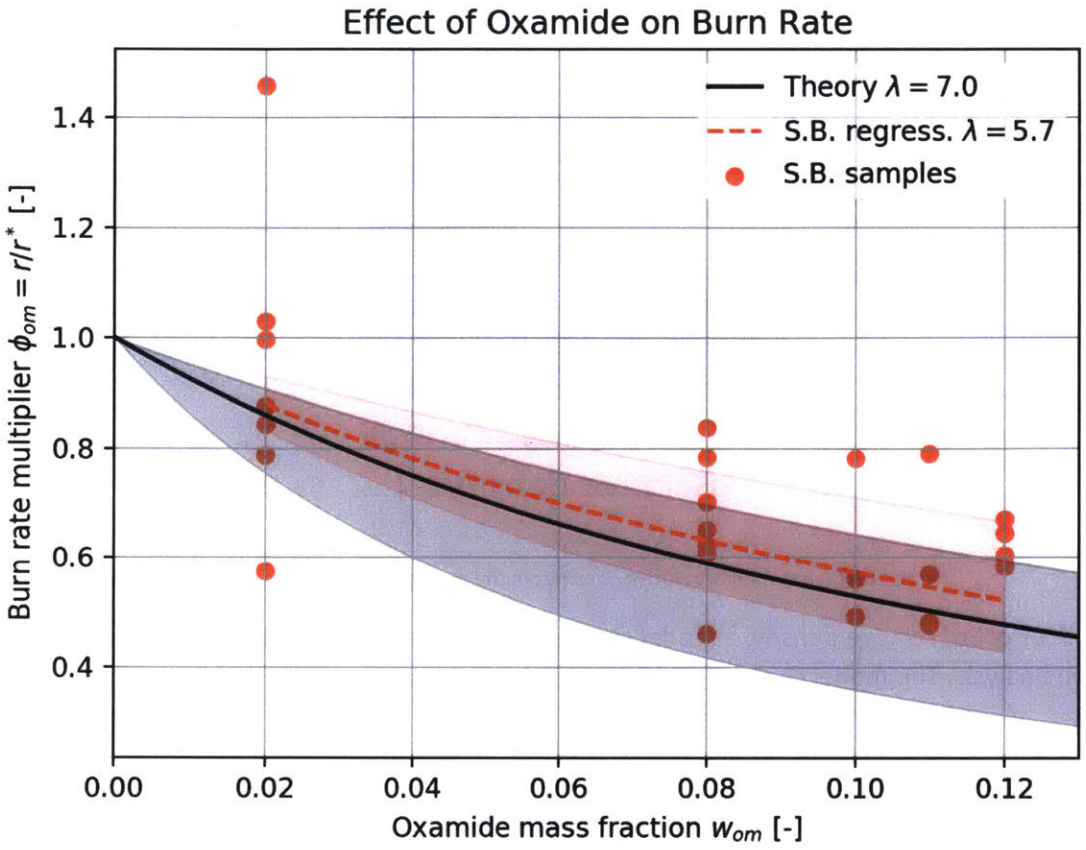

Figure 35: The strand burner data shows that burn rate decreases with increasing oxamide content. The data (red dots) is noisy, but a regression on the data (red dashed line shows mean, red region shows $\pm 2\sigma$ confidence) overlaps with the theoretical prediction (black line, grey region).

3.4.1 Relative density: a confounding variable

To analyze the effects of oxamide content on burn rate, the influence of a confounding variable, relative density, should be removed. Low relative density indicates voids in the propellant, which can accelerate the burning rate [41]. The relative densities in our propellant vary, in part randomly and in part due to improvements in the propellant product process over the course of data collection [Figure 36].

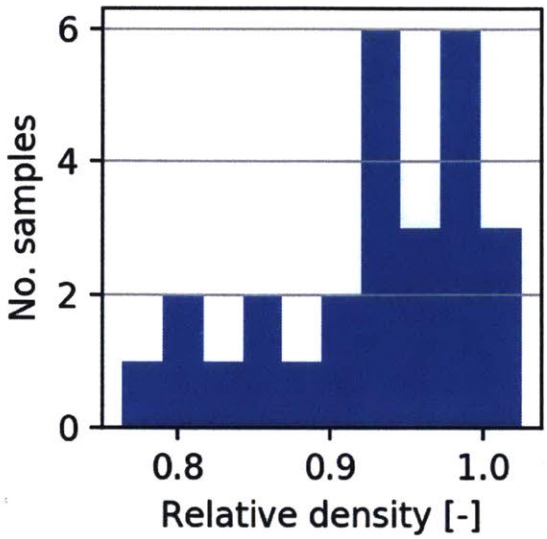

Figure 36: Distribution of relative densities in the strand burner dataset.

To remove the effect of relative density, a model of its effect on burn rate must be made and included in the regression analysis. The model chosen for this work is:

$$\phi_v(D_r) = \frac{r(D_r)}{r^*} = b_v\,(D_r - 1) + 1 \qquad [3.1]$$

Where ϕ_v is the burn rate multiplier due to voids, D_r is the relative density, and b_v is a model parameter called the *void parameter*. b_v should be negative, i.e. relative densities less than one should increase the burn rate.

The choice of the (linear) functional form and an estimate of the value of the void parameter are drawn from a numerical model. This numerical model simulates the progress of a flame front through a propellant with voids. The model draws heavily on a previous model developed by Toft [41], and is detailed in Appendix 3. The model predicts $b_v = -10$.

3.4.2 Regression problem statement

A nonlinear regression was performed on the 27-sample strand burner data set. The burn rate was regressed against models for the effect of pressure, oxamide content, and relative density:

- Pressure is modeled with Vieille's Law:

  $$r = a^* p^n$$

  Where the undoped burn rate coefficient a^* and the burn rate exponent n are model parameters to be estimated by the regression.
- The effect of oxamide is modeled with Equation 2.2:

  $$\phi_{om}(w_{om}) = \frac{1 - w_{om}}{1 + \lambda\, w_{om}}$$

  Where the oxamide parameter λ is to be estimated by the regression.
- The effect of relative density is modeled with Equation 3.1:

$$\phi_v(D_r) = b_v\,(D_r - 1) + 1$$

Where the void parameter b_v is to be estimated by the regression.

These effects combine multiplicatively, i.e.

$$r = a^*\,p^n\,\phi_{om}(w_{om})\,\phi_v(D_r)$$

In sum, the regression model is

$$r \sim \boldsymbol{a^*}\,p^{\boldsymbol{n}}\left(\frac{1 - w_{om}}{1 + \boldsymbol{\lambda}\,w_{om}}\right)\left(\boldsymbol{b_v}\,(D_r - 1) + 1\right) \qquad [3.2]$$

The variables to be estimated by the regression are $a^*, n,\ \lambda, b_v$, and are highlighted in blue in Equation 3.2.

Note that this form of the regression problem requires all propellant formulations to take on the same value of the burn rate exponent n, a somewhat restrictive assumption. However it may be acceptable in the present case because neither of the independent variables in the regression (i.e. w_{om} and D_r) has a significant interaction with n. Further, almost all propellant formulations in the dataset (except those without HX-752) have similar values of n when their samples are separately fitted to Vieille's Law.

The regression analysis was performed with R's *nls* package [42], using the *rpy2* python interface [43].

3.4.3 Regression results

The results of the regression analysis indicate that oxamide has a significant effect on burn rate, and that the value of the oxamide parameter is within the range predicted by burn rate theory and thermochemical data. As expected, pressure (via Vieille's Law a and n) has a very significant effect on burn rate. Surprisingly, relative density has a weak effect: the estimated value of the void parameter $b_v = -0.55$ is much smaller in magnitude than the value predicted by numerical simulations ($b_v = -10$). Further, the confidence interval includes $b_v = 0$, so we cannot reject the null hypothesis that relative density has no effect on burn rate.

The value of the undoped burn rate coefficient $a^* = 3.70 \pm 0.31$ mm s^{-1} MPa$^{-\mathrm{n}}$ is in the range of typical values for AP composite propellant [16]. However, the value of the burn rate exponent $n = 0.31 \pm 0.065$ is unusually low.

Table 3: Results of nonlinear least squares regression of the strand burner oxamide dataset.

Variable	Estimate	Std. Error	t value	$\Pr(>\|t\|)$	Significance Level
Oxamide parameter λ [-]	5.72	± 1.54	3.73	0.0011	High $p < 0.01$
Undoped burn rate coefficient a^* [mm s^{-1} MPa^{-n}]	3.70	± 0.31	11.7	2.79×10^{-11}	Very high $p < 10^{-3}$
Burn rate exponent n [-]	0.311	± 0.065	4.79	7.84×10^{-5}	Very high $p < 10^{-3}$
Void parameter b_v [-]	-0.550	± 0.531	-1.04	0.311	Not significant $p > 0.05$

3.4.4 Regression residuals

The residuals of the regression were examined for remaining trends not captured by the model [Figure 37]. The left plot of Figure 37 shows the burn rate residual vs. the predicted burn rate. The spread of residuals, roughly ± 0.5 mm s^{-1}, is fairly wide, indicating that much noise is present in the data. However, there is no visually obvious trend in this scatter plot, a positive indication for the completeness of the model. A probability plot (q-q plot, bottom right of Figure 37) shows the residual distribution to have only slight deviations from normality, another positive indication for the completeness of the model.

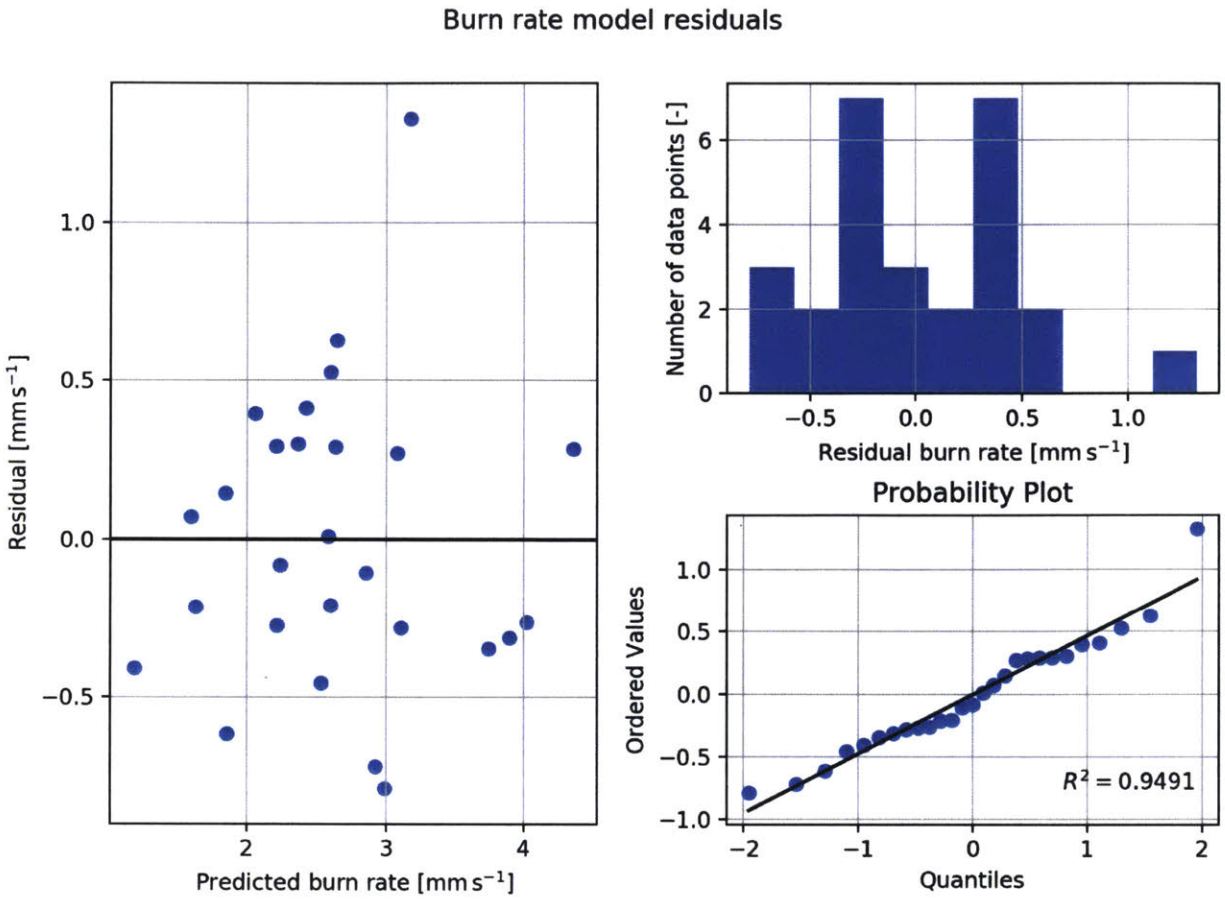

Figure 37: Residuals of the burn rate model regression on strand burner data. The top right plot shows the distribution of residuals. The bottom right plot assesses the normality of the residual distribution; points from a normal distribution should fall along the black line.

3.5 Subscale motor tests

The most promising propellant formulas from the strand burner tests were then evaluated in a subscale motor. This step is needed because propellants burn differently in strand burners than in motors. To reduce cost and hasten the development schedule, these initial tests were conducted in a cheap, robust subscale motor. This motor was designed and built by our research team, and used to evaluate two propellant formulations with different oxamide content. This section presents the design of the subscale motor and the results of its tests.

We found that both propellants tested burned well at low pressures. As expected, the burn rates were somewhat higher in the motor than in the strand burner, but were still compatible with the needs of slow-burning solid rocket motors. The results of these tests inform the design of a solid rocket motor for UAV propulsion, presented in Chapter 5.

3.5.1 Subscale motor design

This subsection presents the design of the subscale motor. The subscale motor is designed to be cheap and robust. It accommodates testing new ablative liners, the laser ignition system, and various nozzle size and K area ratios. A firing of the motor is shown in Figure 38.

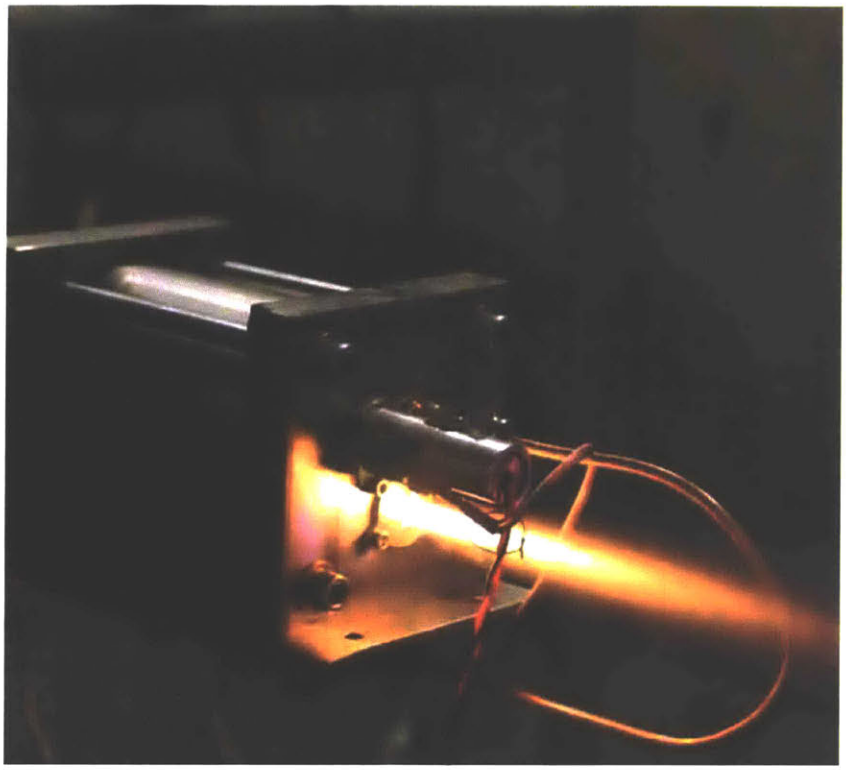

Figure 38: The subscale motor in operation.

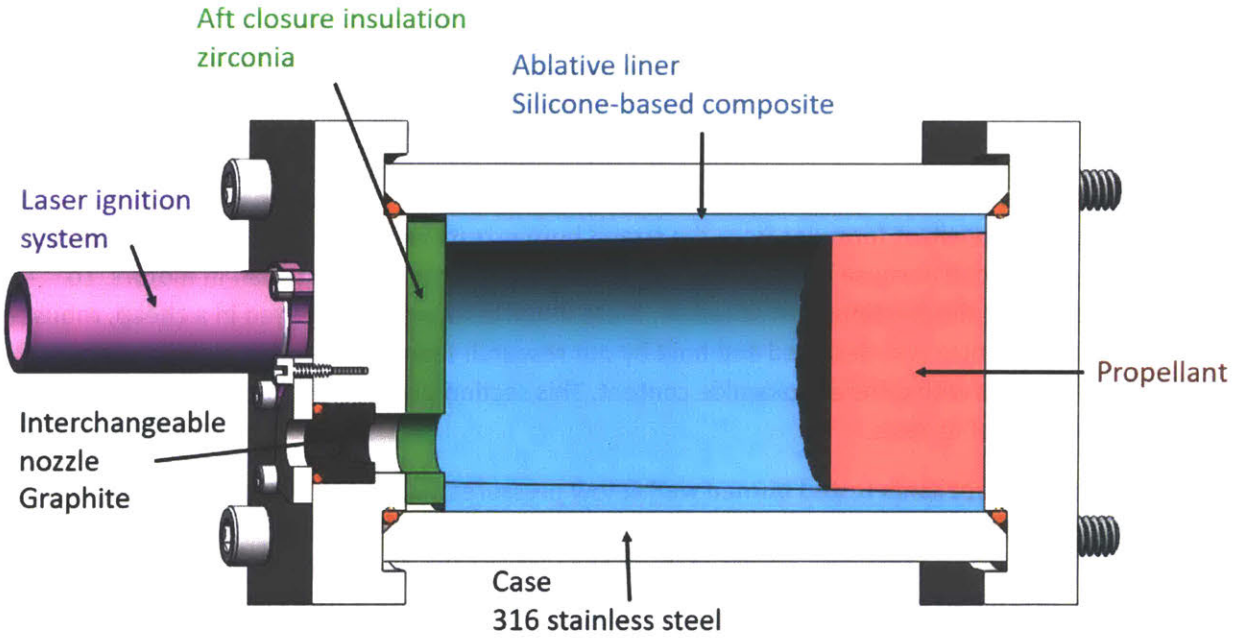

Figure 39: Components of the subscale motor.

The motor has 5 major components, shown in cross section in Figure 39:

1. The *case* (shown in grey), is made from a tube of 316 stainless steel, capped with two plates. The plates are held together by four 1/4-20 bolts. The case walls and plates are overbuilt (designed for internal pressures > 10 MPa), so they will not fail if the motor over-pressurizes. The bolts act as a structural fuse; they will fail if the case pressure exceeds 10 MPa, venting the motor. The internal face of the front plate is protected from combustion gases by a layer of zirconia ceramic (green).
2. The *nozzle* (black), is made of graphite. It is mounted onto the front plate, and the mounting system is designed for easy replacement. This allows the motor to be operated at different area ratios $K = A_b/A_t$.
3. The laser ignition system (purple) is mounted into the front plate. A quartz window (not shown in Figure 39), similar to the window in the strand burner sample holder, allows the laser to shine into the motor onto the surface of the propellant grain.
4. The end-burning *propellant grain* (pink) is placed inside the case.
5. An *ablative liner* (blue) surrounds the propellant grain.

The motor is instrumented to record test data. A pressure transducer measures the chamber pressure (via a tap on the front plate, not shown in Figure 39). The current supplied to the laser is also measured. The entire motor is mounted on a thrust balance [Figure 40], which collects thrust measurements.

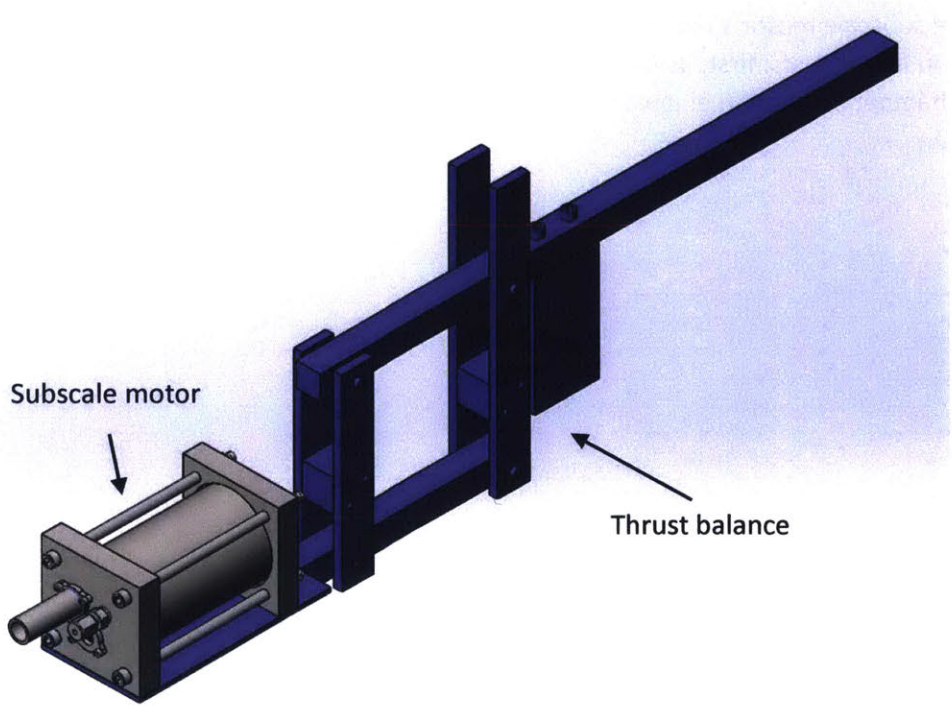

Figure 40: The motor (grey) mounted on a thrust balance (indigo).

3.5.2 Subscale motor test results

Three tests of the subscale motor are presented in this subsection: one unsuccessful test with AN-based propellant, and two successful tests with AP/oxamide propellant.

The unsuccessful AN propellant test is documented in Figure 41. In this test, the motor over-pressurized during startup, causing several structural failures in the motor. The over-pressurization occurred because the propellant grain burned on it sides. To remedy this failure mode, future propellant grains were inhibited by a layer of fiberglass and epoxy bonded to the grain sides [see subsection 6.2.1].

Figure 41 shows a pressure trace of the test, and six frames from a video of the test:

a. In the first frame, the laser is turned on and the motor ignites. Because the propellant would not ignite at ambient pressure, an energetic material was applied to the propellant surface to aid ignition. The pressure rises rapidly as the energetic material burns and ignites the propellant.
b. The pressure peaks as all the energetic material is consumed. The pressure then begins to decline. However, the pressure peak broke the laser window: gas pressure begins to push the laser out of its holder tube.
c. The laser is ejected from its holder tube.
d. The propellant grain begins to burn on its sides, causing the pressure to rise. The burnt sides of the propellant grain are shown in Figure 42.
e. The pressure spikes to over 7 MPa, saturating the pressure transducer.
f. The nozzle fails. This vents the motor and extinguishes the propellant.

Because of the subscale motor's robust design, it was quickly refurbished after the failure. We made two modifications in future tests: first, using AP-based propellants which are easier to ignite and provide more stable chamber pressure (i.e. lower n); second, more strongly inhibiting the outer surfaces of the propellant grain.

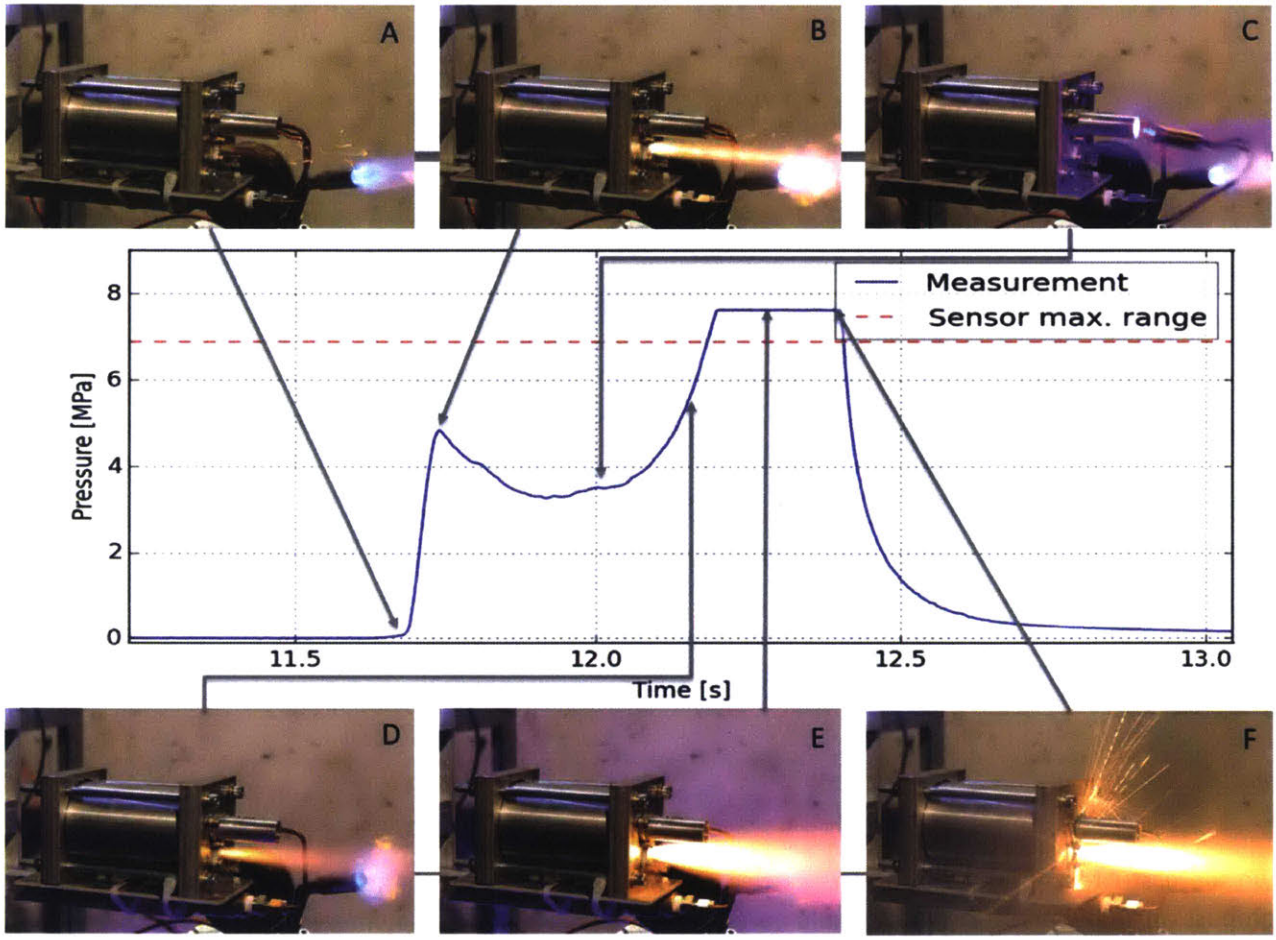

Figure 41: An unsuccessful test with AN-based propellant, in which the motor over-pressurized during startup.

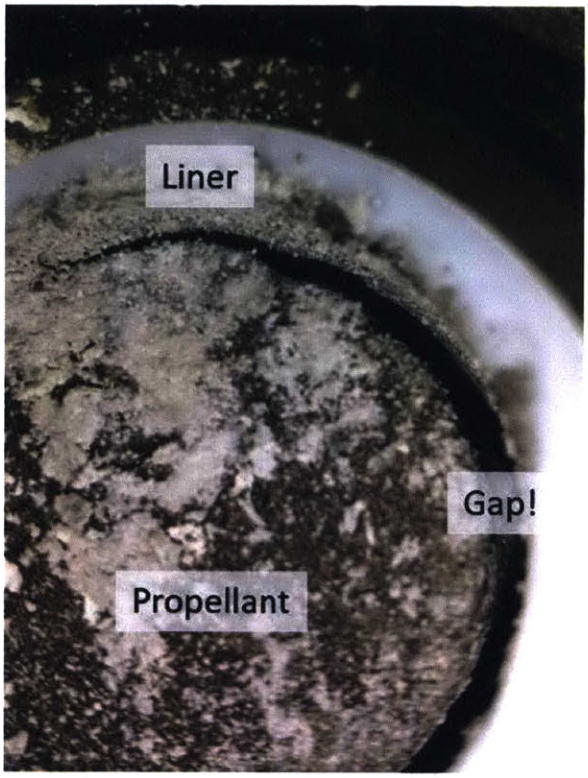

Figure 42: A gap between the propellant grain and the liner shows that the propellant burned on its sides.

Two successful tests of the motor were carried out with AP-based propellants. Both tests showed stable combustion at low pressures, acceptable burn rates, and long ignition delay times.

Data from the tests is shown in Table 4, Figure 43 and Figure 44. Both tests show a stable, level operational chamber pressure, 0.60 MPa for the first test and 0.34 MPa for the second. However, both tests also show very long ignition delays: the time from "laser on" to "action start"[14] is over 10 seconds. This is an unacceptably long delay for a useful motor.

Table 4: Subscale motor test data for AP/oxamide propellants

Propellant	Chamber pressure, steady state p_c	Burn rate r	Burn rate coefficient a, assuming $n = 0.45$	Area ratio K
AP.71.125/250-HTPB-Mg.06-Om.02	0.60 MPa	3.96 mm s^{-1}	5.27 mm s^{-1} MPa^{-n}	108
AP.63.125/500-HTPB-Mg.06-Om.08	0.34 MPa	2.05 mm s^{-1}	3.37 mm s^{-1} MPa^{-n}	105

The long delay has three causes. First, the slow-burning propellant is difficult to ignite. Second, the subscale motor has a large free volume, as seen in Figure 39. The large free volume increases the pressure rise time constant. Third, the nozzle was not capped during startup on these tests. Capping the

[14] When the chamber pressure begins to rise significantly [12].

nozzle helps build up pressure in the chamber; the cap is designed to blow out as the chamber reaches full pressure.

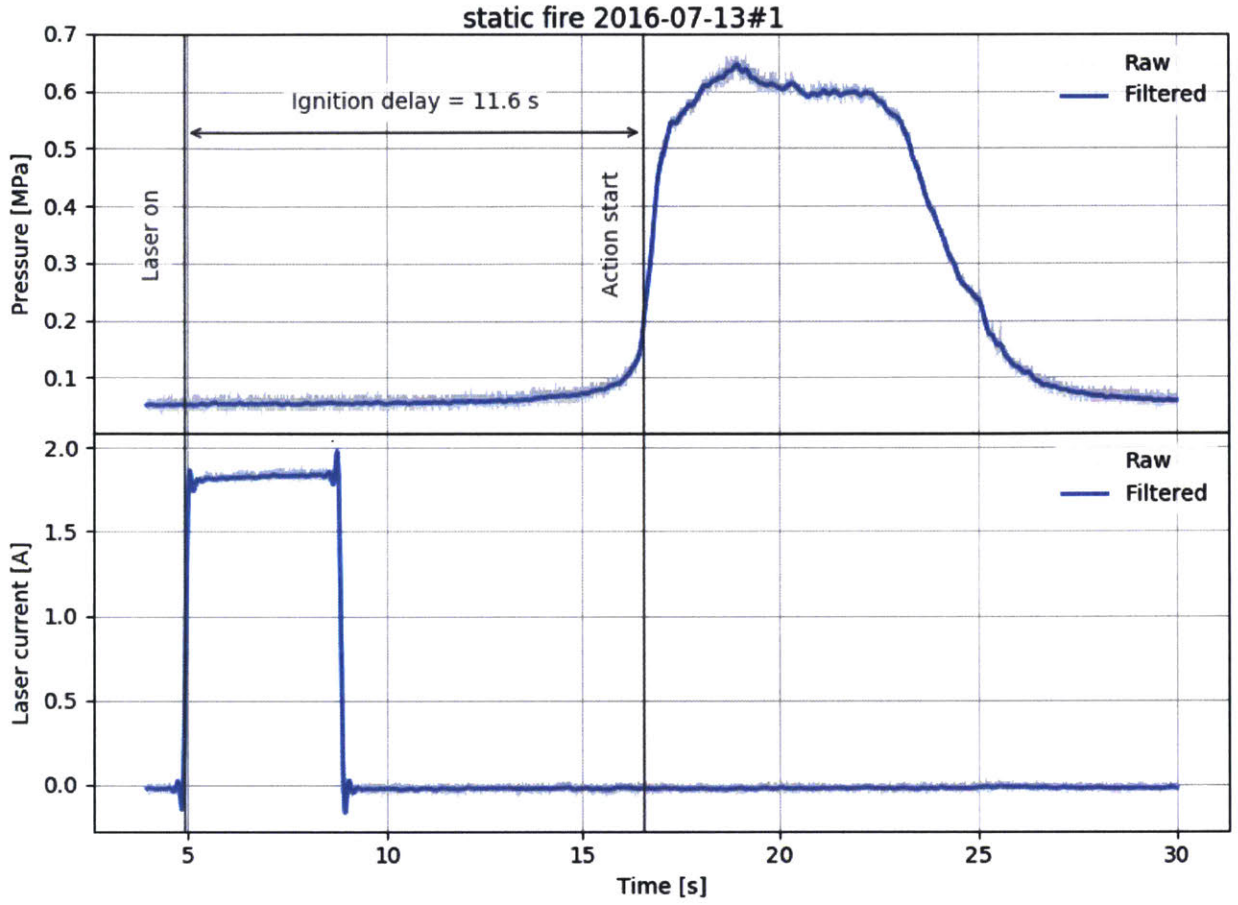

Figure 43: Data from a static fire of the motor, using propellant AP.71.125/250-HTPB-Mg.06-Om.02 at $K = 108$. Note the very long ignition delay.

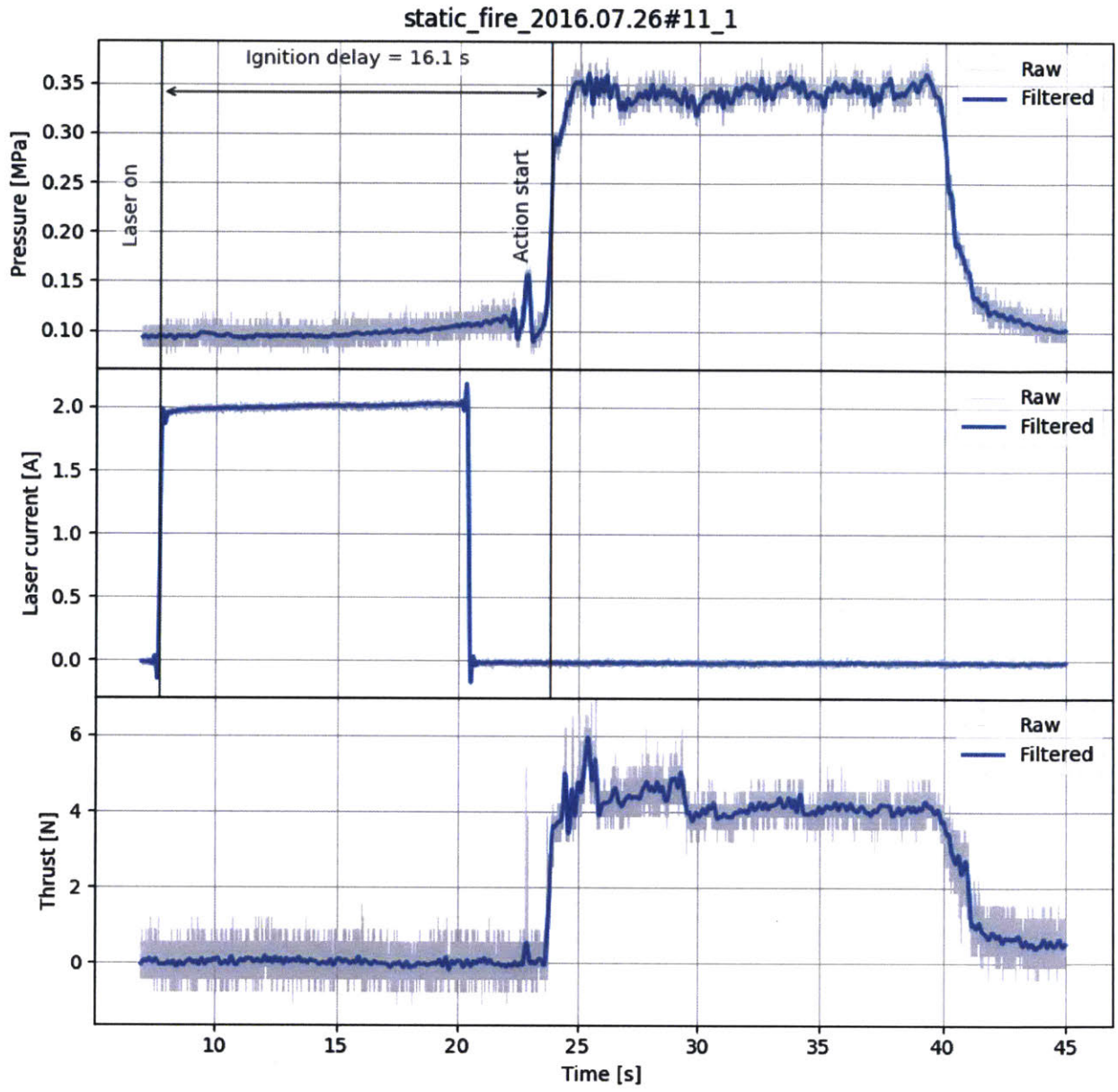

Figure 44 Data from a static fire of the motor, using propellant AP.63.125/500-HTPB-Mg.06-Om.08 at $K = 105$. Note the very long ignition delay.

The motor design presented in Chapter 5 has several features to remedy the issues discovered in these subscale tests. The laser ignites a fast-burning starter grain, rather than igniting the slow-burning main propellant grain directly. Also, that motor has a much smaller free volume than subscale motor. These factors enable more rapid ignition.

In addition to providing useful lessons for the ignition system, the subscale motor yielded data on the effect of oxamide on burn rate. This burn rate data agrees well with the burn rate theory from Section 2.6, and with experimental results from other researchers, as shown in Figure 45. This figure restates a figure shown in Section 2.6, but is recolored to emphasize the results of the subscale motor tests in this work. The vertical axis shows the burn rate multiplier (i.e. burn rate normalized for the effects of

pressure) and the horizontal axis shows oxamide content. Our subscale motor tests are marked with pink dots. Motor and strand burn tests from other researchers are shown as grey marks. The burn rate theory,

$$\phi_{om} = \frac{1 - w_{om}}{1 + \lambda\, w_{om}}$$

is shown as a black curve ($\lambda = 7$), with the grey shaded region represented the expected range of values for λ.

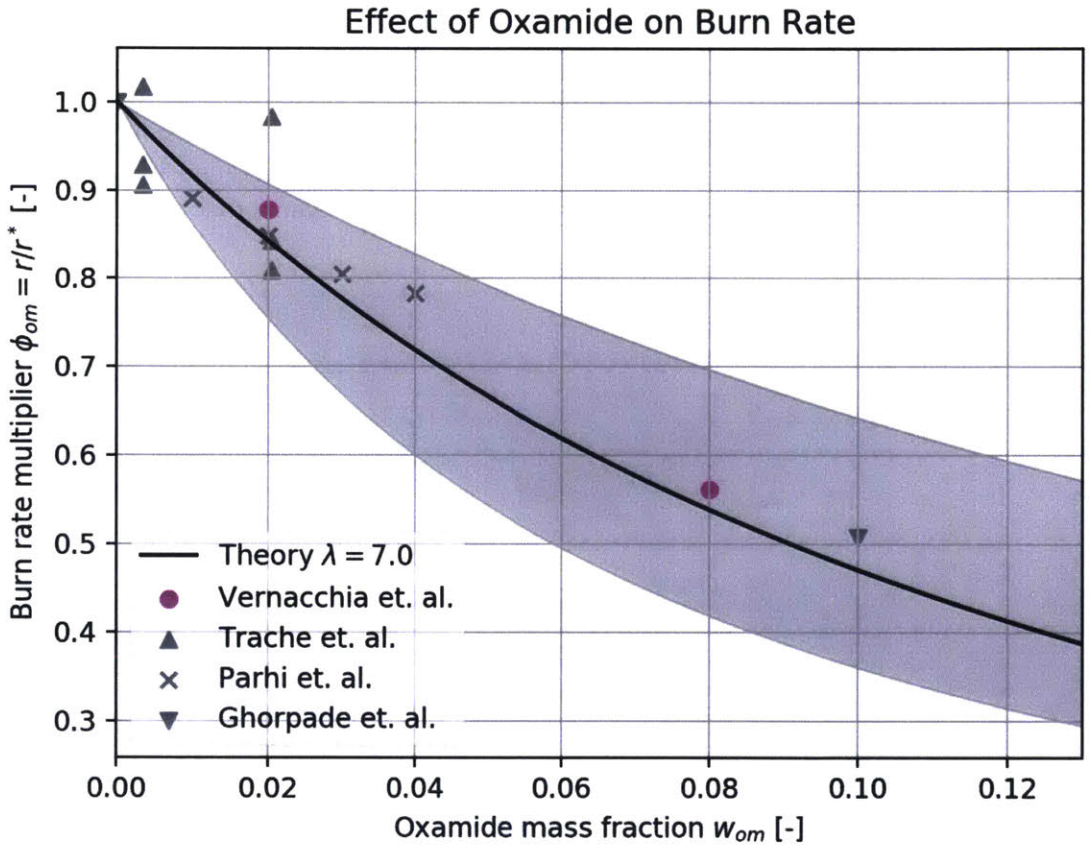

Figure 45: The effect of oxamide content on burn rate measured in our subscale motor tests (pink dots) agrees with subscale motor tests by other researchers (grey marks) [28] [44] [29] , and the combustion theory developed in Chapter 2 (black curve and grey region).

The propellant testing presented in this chapter characterized a family of slow-burning AP/oxamide propellants, and provided experimental confirmation for the burn rate theory presented in Chapter 2. The next chapter takes a detour from the details of propulsion to present a conceptual configuration for a small, fast air vehicle. Then, in Chapter 5, a motor design for this vehicle is described. The motor design uses this propellant family, and draws heavily upon lessons learned from the propellant testing described above.

4 Concept for a small, fast air vehicle

The remaining chapters of this thesis apply the preceding propellant development and design theory to a slow-burning solid rocket propulsion system. This application is presented in the context of an example aircraft, which is representative of the small, fast UAV design space. This chapter presents the design of the example aircraft, with particular focus on the role of the propulsion system in vehicle configuration and operations.

Particularly, this work uses "Firefly", a transonic UAV being developed by the MIT Department of Aeronautics and Astronautics and Lincoln Laboratories, as a representative example for the configuration, operation and propulsion requirements of a small, fast UAV. As a specific example, Firefly provides a useful foundation for discussion and will be referred to throughout this thesis. However, the ideas presented here a generally applicable to the regime of small, fast aircraft.

Firefly is a deployable UAV; it is designed to launch from a larger host aircraft in transonic flight, as illustrated in Figure 46. Deployment from a larger host bypasses the fundamental range limitations of small aircraft: Firefly can be carried to and deployed near a mission target, even if that target is far from available launch sites.

Figure 46: Concept art of the Firefly UAV launching from a larger host aircraft.

Firefly is a pioneer in the space of small, fast aircraft, and we incorporated several novel inventions in the course of its development. The vehicle's configuration is based around a unique and effective integration of a solid rocket motor case into an aircraft fuselage. The vehicle's structure is made of cutting-edge composites and additively manufactured metal components which push the precision

limits of modern printers. The wings and tail feature miniature, high-precision deployment and actuation mechanisms.

The Firefly vehicle concept was designed by Tony Tao of the MIT Department of Aeronautics and Astronautics. The concept is an evolution of Mr. Tao's previous work on Locust/Perdix [5], a smaller, low-speed deployable UAV.

4.1 Configuration

Given the tight packaging demanded by the vehicle concept, the propulsion system and vehicle configuration were designed together as an integrated idea. The configuration is driven by the propulsion system in several ways. First, a long, narrow rocket offers superior endurance[15], so the entire bottom half of the vehicle is devoted to the rocket motor. Second, the motor case (the outer structure of the rocket motor) must be a strong pressure vessel; the configuration utilizes this long, stiff member as the chassis to support other components. Finally, the heat load from the motor requires thermal protection for the payload, avionics and control mechanisms.

The propulsion system design is also driven by the aerodynamic configuration. Because the motor case forms the bottom half of the fuselage outer mold line, it is contoured to reduce drag. This has interesting implications for motor performance (Chapter 5) and production (Chapter 6).

[15] As described in Chapter 2, low thrust solid rocket motors use end-burning propellant grains. For these propellant grains, burn time is proportional to motor length.

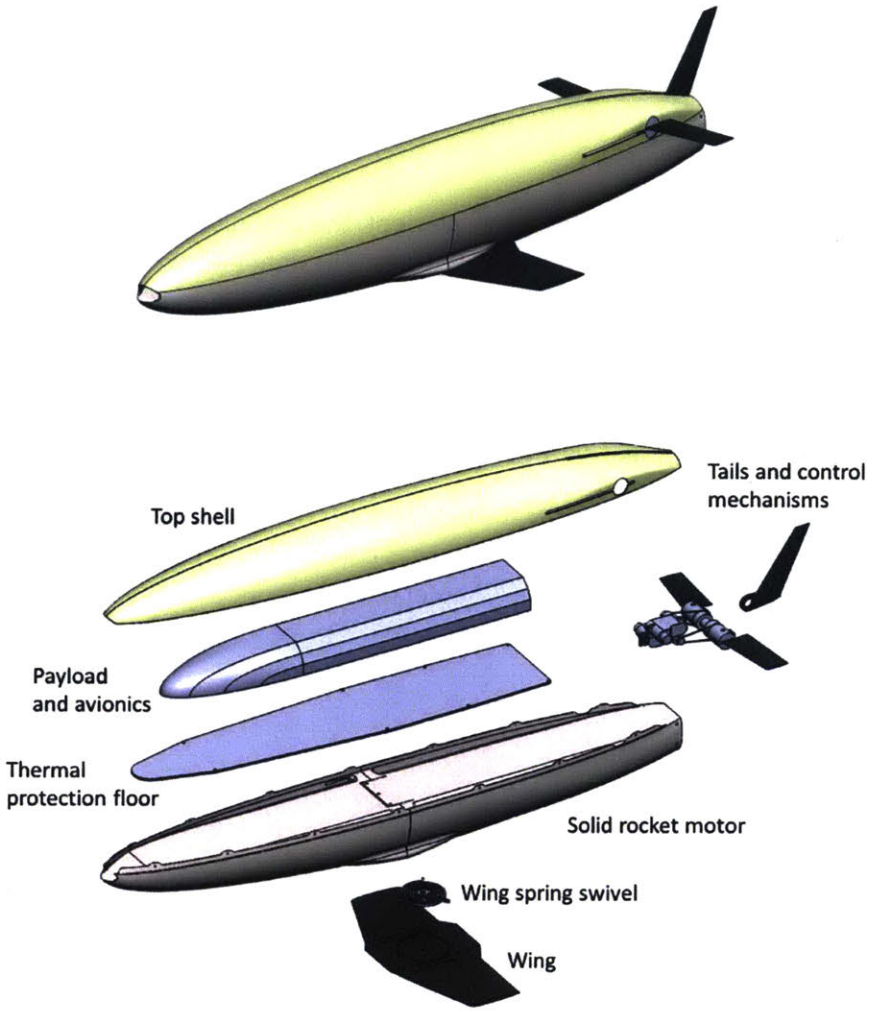

Figure 47: The configuration of Firefly is based around its long-endurance solid rocket motor.

The major components of Firefly are configured around the motor case chassis [Figure 47]. The motor case contains the propellant package; it splits into front and aft halves so the propellant package can be loaded inside.

The payload, avionics, and control mechanisms are mounted above the motor case in the top half of the vehicle. A Kevlar top shell covers the payload, avionics, and control mechanisms, and forms the top half of the fuselage outer mold line.

There is thermal protection between the payload/avionics/control mechanisms and the motor case. A floor is mounted beneath the payload and avionics to form a thermal barrier between them and the hot motor case. To provide cooling, a scoop at the nose of the aircraft rams air into a gap between the floor and the top of the motor case.

On the underside of the motor case is the aircraft's wing. The wing is mounted on a spring-loaded swivel so it can fold when Firefly is loaded in its deployment canister.

4.2 Concept of operations

This concept of operations illustrates the intended capabilities of the Firefly UAV, and is compatible with the hypothetical missions proposed in Appendix 1. Essentially, the vehicle deploys from a canister on a host aircraft and sustains several minutes of powered transonic flight. Firefly is an expendable, single-use vehicle: after its propellant is exhausted, it glides to a disposal location and crash-lands.

Preflight - Before flight, the Firefly UAV is manufactured, folded, and loaded into a deployment canister, which measures a 70 x 70 x 480 mm (2.75 x 2.75 x 19 inch). The canister is then mounted onto a host aircraft. The UAV may be stored for several years, and experience many takeoff/landing cycles of the host aircraft, before use.

Deployment - Upon command from the pilot, the canister ejects Firefly. After ejection, Firefly unfolds, orients, and lights its rocket motor. This deployment process takes one to two seconds. Nominal ejection conditions are level flight at 9.1 km (30,000 ft) above mean sea level and Mach 0.8. Firefly's aero-surfaces (wing and tails) are folded to fit into the canister, and are spring-loaded to unfold during deployment.

Powered flight - Firefly then has several minutes of powered flight in which to perform its primary mission. The vehicle's speed may vary due to maneuvering or the motor's thrust profile, but will generally be between Mach 0.75 and 0.85. During the powered flight phase, Firefly will travel about 40 km.

Glide and disposal - After the rocket motor burns out, Firefly will glide to a disposal location and intentionally crash-land. Firefly is optimized for transonic flight , and performs poorly as a glider[16]. If burnout occurs at the nominal 9 km altitude, Firefly can cover an additional 30 to 40 km during 4 to 8 minutes of gliding.

[16] A more advanced concept, referred to as Broadhead, proposes to extend the glide phase with an additional set of foldable wings. The Broadhead concept is beyond the scope of this work; it may be discussed in a forthcoming publication.

5 Motor design

Small, transonic UAVs require miniature, high power propulsion, a need which is best addressed by solid rocket motors, as discussed in Chapter 1. This need motivates the development of compact, long-endurance solid rocket motors which integrate elegantly into the configuration of small UAVs. Our research identifies technical challenges of small, slow-burning solid rocket propulsion systems, and establishes design principles for their solution. As an example application of these principles, this chapter presents the design of a solid rocket propulsion system for the Firefly transonic UAV.

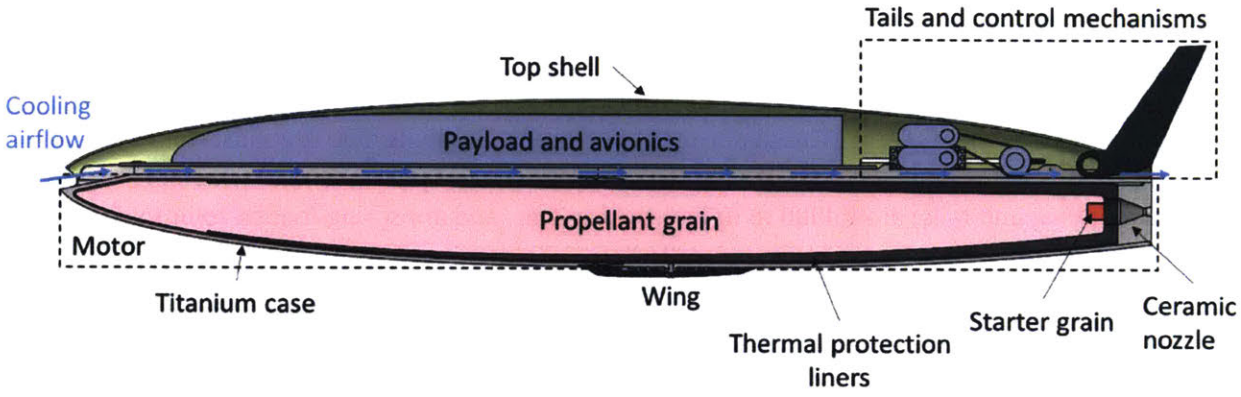

Figure 48: A cross section showing the key components of the Firefly UAV and its solid rocket motor.

The motor's position within the vehicle is shown in cross section in Figure 48. The motor occupies the bottom half of the vehicle's fuselage, while the payload, avionics and control mechanisms occupy the top. A stream of cooling air flows through the middle of the vehicle to prevent the hot motor case from overheating the components above it. The motor consists of a propellant grain, thermal protection liners, a nozzle, a motor case, and an ignition system (starter grain).

The interaction between the propulsion system and vehicle dynamics is shown in Section 5.1, which presents an example thrust curve and flight profile for the Firefly UAV.

A low burn-rate, end burning propellant grain is used to maximize the burn time of slow-burning rocket motors. The grain's burn rate coefficient varies along its length to compensate for its changing burn area, a feature which helps meet the configuration requirements of small UAVs. The design of the propellant grain is presented in Section 5.2.

A set of thermal protection liners protects the motor case and other vehicle systems from the heat of propellant combustion. The long burn time and small space constraints pose challenges to the liner design, but these can be solved with a clever arrangement of state-of-the art ablative materials and fibrous insulation. Section 5.3 presents the principles of thermal protection design.

The rocket's nozzle must withstand long exposure to hot exhaust gases. Because thrust requirements for UAV propulsion are low, the nozzle throat diameter is small. A small throat diameter makes the motor

sensitive to throat erosion, so the nozzle must be made from a high performance material which minimizes erosion. Section 5.4 presents the principles of nozzle design for slow-burning motors.

The motor case must be light weight and withstand the thermal and pressure loads of combustion. It must also integrate with the UAV's configuration. These needs are met by a thin, contoured shell additively manufactured from a high-strength titanium alloy. Section 5.5 presents the principles of motor case design.

The motor must ignite quickly and reliably when the vehicle is deployed. A starter grain of fast-burning propellant, placed in the aft end of the main grain, initiates combustion and builds up the chamber pressure. Ignition is triggered by firing a laser onto the starter grain from outside the motor. Section 5.6 presents the design of the laser ignition system.

The key design parameters of Firefly's motor are listed in Table 5, and its mechanical design is illustrated in Figure 49. The motor is designed for a nominal thrust of 7 N, although this varies from 3 to 10 N over the course of the burn. The motor case is a 1.5 mm thick shell of Ti-6Al-4V, and is designed for a maximum chamber pressure of 1.4 MPa. The propellant load, 500 g of slow-burning ammonium perchlorate composite propellant, delivers 870 Ns of impulse over ~160 s of burn time. This provides adequate powered flight endurance for Firefly's expected missions. The average specific impulse is fairly low for typical solid rockets, at 175 s. The motor has an overall length of 410 mm and mass of 1100 g (fully loaded). The motor provides the vehicle's primary structure, and comprises the majority of its mass.

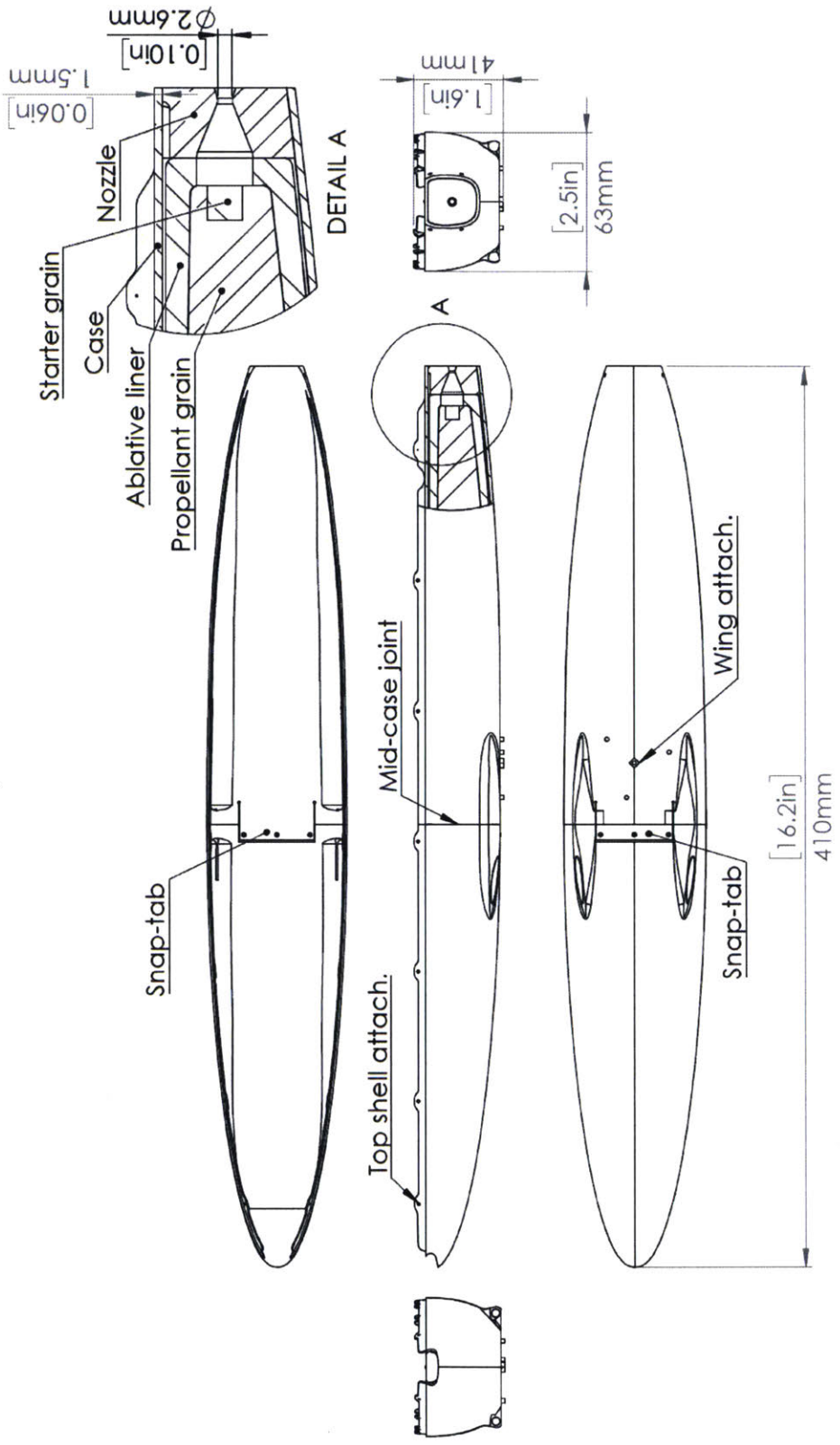

Figure 49: Components, mechanical features and major dimensions of the Firefly motor.

Table 5: The key design parameters of Firefly's motor exemplify the region of design space occupied by slow-burning solid rocket propulsion systems for UAV applications.

Parameter	Value
Thrust, nominal	7 N
Chamber pressure, max. allowable	1.4 MPa
Impulse	870 N s
Burn time	160 s
Propellant load	500 g
Propellant	Ammonium perchlorate composite propellant End burning grain Four bonded segments with varying burn rate suppressant
Specific Impulse, average	175 s
Total mass	1100 g
Throat diameter	2.6 mm
Length	410 mm
Thermal protection	Ablative liner, silicone-based composite ablative material
Case structure	Titanium Ti-6Al-4V, 1.5 mm wall thickness

5.1 Thrust curve and flight dynamics

The motor's thrust curve is complicated because the burning area and propellant burn rate change over the course of the burn [Figure 50]. The chamber pressure of solid rocket motors is set by the properties of the propellant and the burning area of the propellant[17]. Typically, a solid rocket designer who desires a constant thrust level would design a propellant grain which has a constant burning area [16]. However, the packaging constraints of a transonic require the motor case to be contoured to the outer mold line of the fuselage. The cross sectional area of the motor case, and therefore the burning area of an end-burning propellant grain, vary along the length of the motor [Figure 50, bottom-left]. With a homogeneous propellant, this would cause the chamber pressure to vary over the course of the burn.

There are also chamber pressure limits which the motor must operate within. Because of mass and packaging constraints, the cases of UAV rocket motors will be constrained to relatively low maximum operating pressures; 1.4 MPa (200 psi) in the case of Firefly. On the other side, the chamber pressure must be high enough to choke the nozzle flow and enable stable combustion of the propellant. Low chamber pressures also incur a specific impulse penalty [Figure 52].

Given the large variations in burning area (4x), no single propellant can meet the chamber pressure requirements at all points in the burn. Rather, the grain contains different propellants with different burn rates stacked along the fore-aft axis. The starting (aft) end of the propellant grain is made from a faster-burning propellant. As the flame front advances (toward the front of the vehicle), the grain area increases and the chamber pressure rises. To keep the thrust and pressure within bounds, the propellant grain switches to a slower-burning propellant. Another switch occurs to an even slower propellant, then, near the front of the motor, the grain switches back to a moderate-burn rate propellant to keep the chamber pressure up and the grain area tapers away.

[17] Readers unfamiliar with the fundamentals of solid propellant rockets should review Section 2.2 in this thesis, or Chapter 12: Solid Propellant Rocket Fundamentals of *Rocket Propulsion Elements* [1].

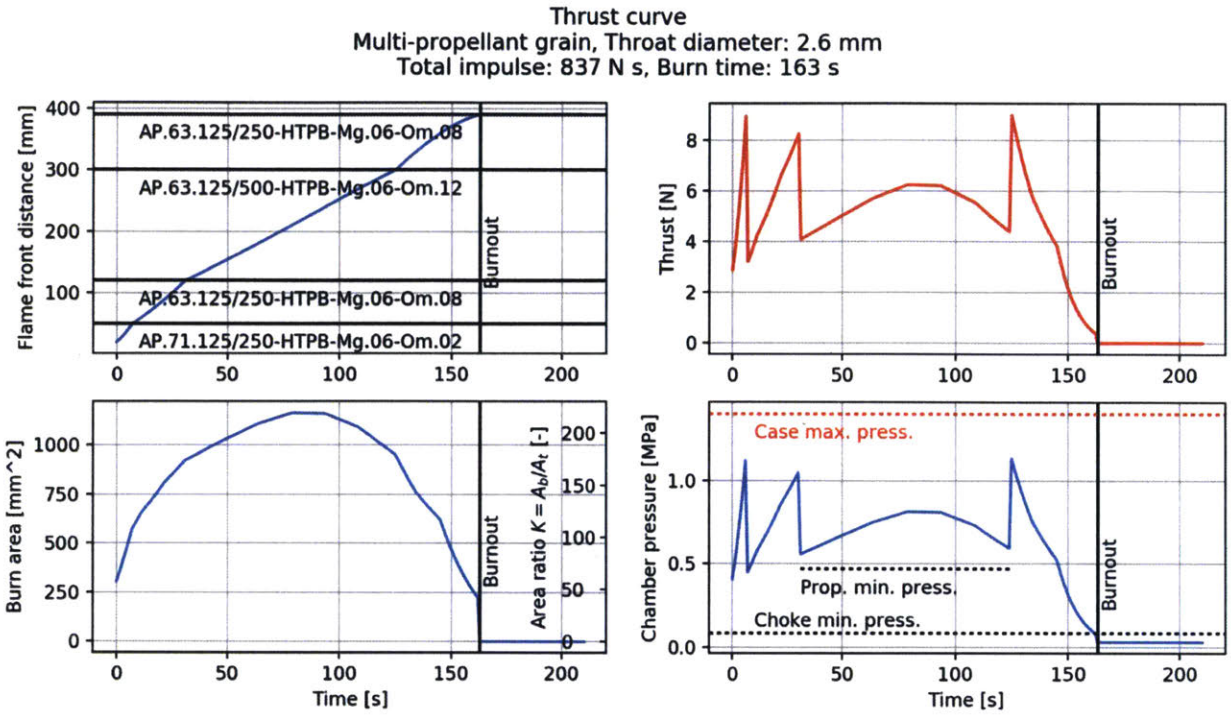

Figure 50: The motor's has a complex thrust because four segments of different propellant are used in the grain. This keeps the thrust near the nominal 7 N (top-right plot) and chamber pressure within acceptable bounds (bottom-right plot), despite variations in burning area (bottom-left plot). The top-left plot shows the progress of the flame front through the four grain segments.

Via a clever choice of the configuration and burn rate of the propellant grain segments, the vehicle's flight speed can be kept close to a constant target value throughout most of the burn [Figure 51]. This design capability requires a propellant whose burning rate can be easily tailored. Burn rate tailoring can be accomplished with the burn rate suppressant oxamide. The experimental effort of tailoring is significantly reduced by using a predictive burn rate model, which is presented in Chapter 2.

Using these design principles, a motor was designed for the Firefly UAV which achieves 160 seconds of burn time and could propel the vehicle for a range of 40 kilometers. Thus, Firefly can meet the propulsion requirements of its expected missions.

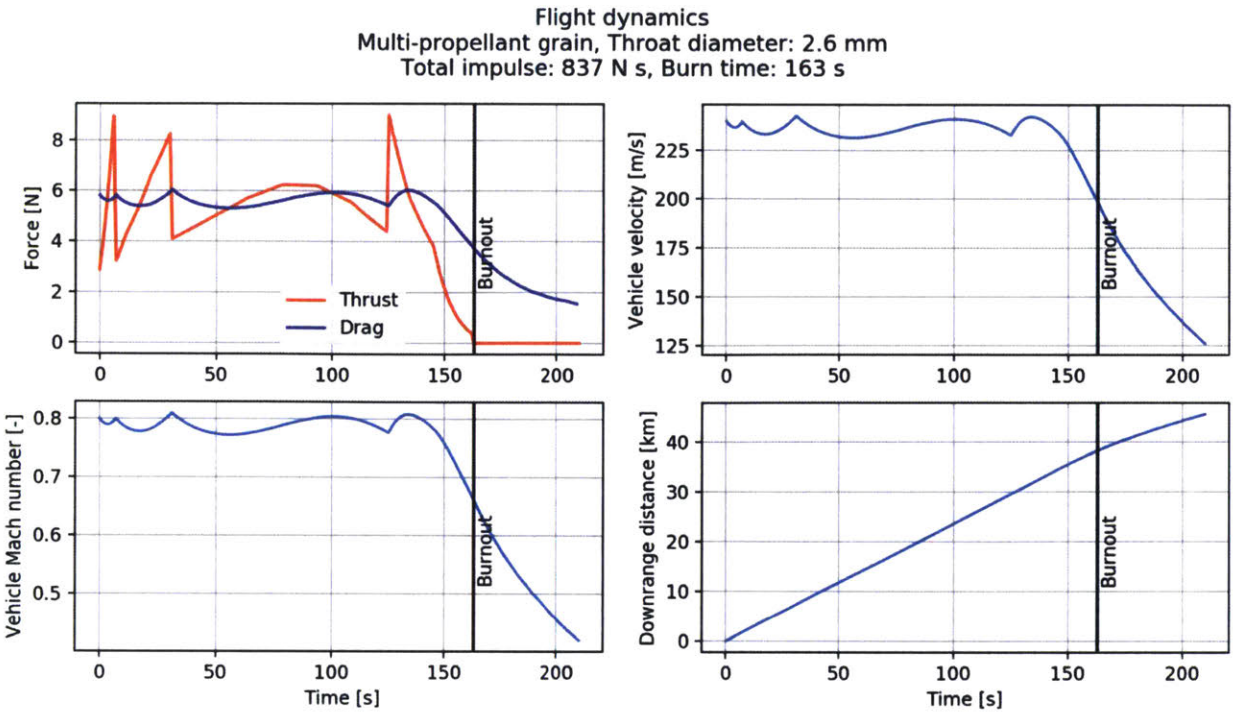

Figure 51: The vehicle's flight speed remains close to the target value of Mach 0.8, despite variations in the motor's burn area and chamber pressure. During ~160 seconds of powered flight, the vehicle can cover about 40 kilometers of downrange distance.

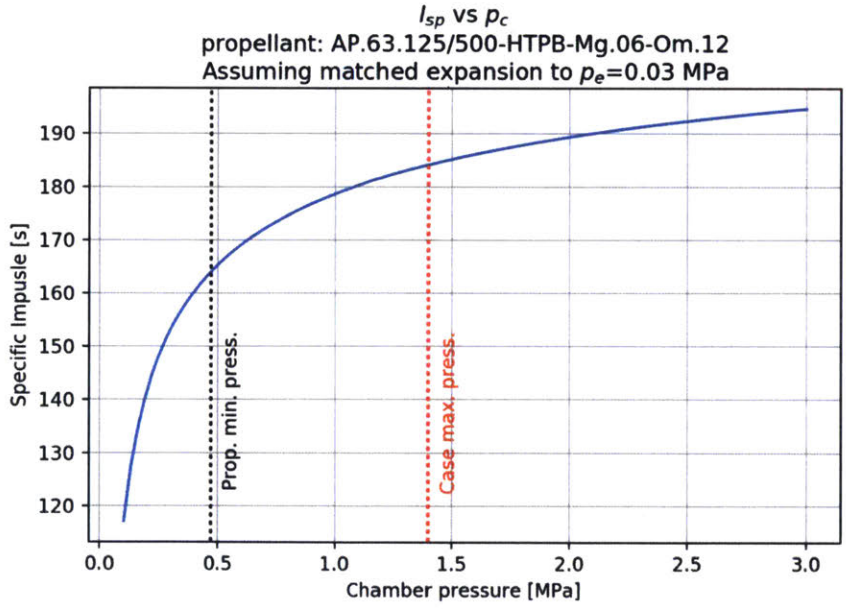

Figure 52: The specific impulse of a rocket motor declines rapidly at low chamber pressures. This plot was produced using the standard isentropic nozzle flow model, e.g. Ch. 3 of [16].

5.2 Propellant grain

This section describes the selection of a propellant and the design of a propellant grain for a slow-burning solid rocket. With burn rate suppressants, ammonium perchlorate composite propellant is suitable for slow-burning motors. An end-burning grain configuration maximizes burn time, and segments of different burning-rate propellant can be used within the grain to achieve the desired thrust profile and chamber pressure. Techniques for using suppressants to tailor the burn rate of ammonium perchlorate composite propellant were developed in Chapter 2, and are applied here.

Propellant formulation –Ammonium perchlorate composite propellant, suppressed with oxamide, is the propellant of choice for small, slow-burning rocket motors [see Chapter 2]. This research developed a family of propellants, with a range of oxamide content and burn rates. Three propellants from this family are used in Firefly's propellant grain [Figure 56].

An example of this family of propellants is presented in Table 6 and Table 7. To reduce the flame temperature and burning rate, the propellant contains a high amount of binder and a low amount of AP. Because of the high binder content and substitution of Mg for Al, the propellant has a moderate density (1500 kg m^{-3}, compared to a maximum of ~1850 kg m^{-3} for AP composites [16]). However, its density and specific impulse are enough to satisfy the propulsion requirements of Firefly and similar UAVs.

The propellant uses hydroxyl-terminated polybutadiene (HTPB) binder. A bonding agent, HX-752, is added to increases the mechanical strength of the propellant, and helps to stabilize combustion. Our experiments showed that propellant containing HX-752 burned more smoothly and had a measurably lower burning rate exponent. The mechanical strength of the propellant was measured via its proxy, hardness, and found to be acceptable at 40-50 Shore A. Processing agents are added to the binder to aid mixing and pouring. The resulting slurry viscosity, roughly 10^5 Pa s, makes the propellant vaguely pourable.

Table 6: Example properties of a slow-burning solid rocket propellant, AP.63.125/250-HTPB/HX752-Mg.06-Om.08.

**These are theoretical values computed using the Rocket Propulsion Analysis chemical equilibrium analysis tool [45].*

Category	Parameter	Value
Physical properties	Density, theoretical	1530 kg m^{-3}
	Density, typical achieved	1500 kg m^{-3}
	Slurry viscosity	~10^5 Pa s
	Cured hardness	40-50 Shore A
Combustion properties	Burn rate coefficient, a	3.3 mm s^{-1} MPa^{-n}
	Burn rate exponent, n	0.45
	Minimum pressure for stable combustion	< 0.1 MPa
	Flame temperature	1670 K *
Exhaust properties	Exhaust gas ratio of specific heats, γ	1.26 *
	Exhaust gas molar mass	22.3 g mol^{-1} *
	Characteristic velocity, c^*	1190 m s^{-1} *

Table 7: An example composition of a slow-burning solid rocket propellant, AP.63.125/250-HTPB/HX752-Mg.06-Om.08.

Component	Chemical ingredients	Mass fraction
Oxidizer	Ammonium perchlorate crystals 125 – 250 µm particle size	62.9 %
Binder	Hydroxyl-terminated polybutadiene (HTPB) resin Modified methylene diphenyl diisocyanate (MDI) curative Isodecyl pelargonate plasticizer HX-752 binding agent CAO-5 antioxidant	20.2 %
Fuel	Magnesium powder < 44 µm particle size	6.1 %
Opacifier	Graphite powder	2.5 %
Burn rate suppressant	Oxamide	8.0 %
Processing agents	Castor oil Polydimethylsiloxane fluid Triton X-100	< 1 %

Propellant grain – An end-burning grain configuration is required to maximize the burn time of small, slow-burning solid rockets. The flame front starts at the aft face of the propellant grain, and progresses forward along the length of the motor. The evolution of the propellant grain is illustrated in Figure 53.

The aft-to-front burning of the propellant grain causes a slight shift in the vehicle's center of gravity [Figure 54]. First, the c.g. moves forward as propellant is burned behind the c.g. Then, the flame front crosses in front of the c.g., and the c.g. starts to move aft. The magnitude of the c.g. shift is small because the propellant grain is tapered at the ends. This disturbance the shift causes to the flight dynamics should be easily rejected by the vehicle's control system.

Figure 53: Evolution of the end-burning propellant grain during the burn.

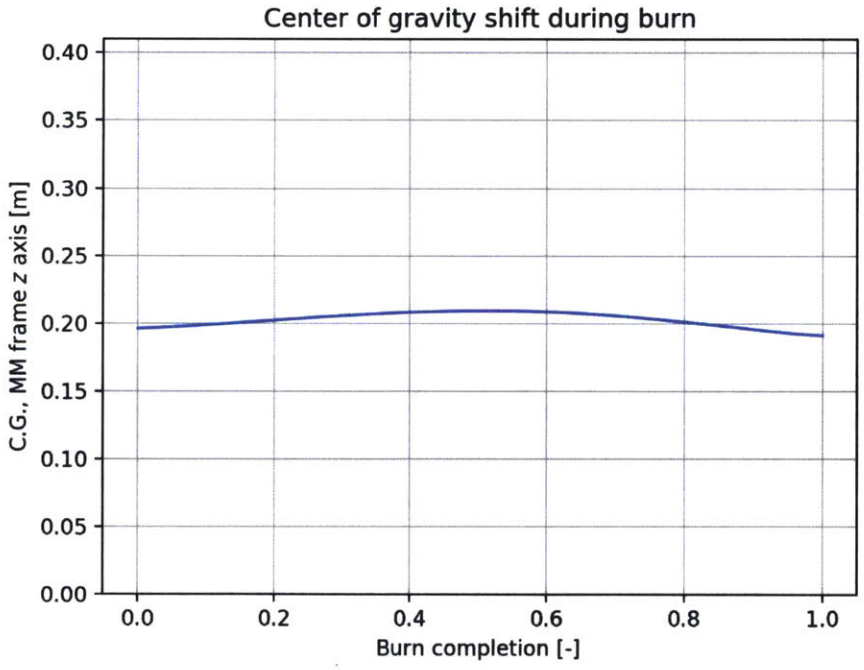

Figure 54: The vehicle's center of gravity moves slightly as propellant is burned. This plot assumes a vehicle burnout mass of 980 g and 500 g of propellant.

As described in Section 5.1, propellant grains for UAV propulsion will often require segments of different burning rate to compensate for the grain's variable burning area. The configuration of the grain

segments in Firefly's motor is shown in Figure 56. A good bond between grain segments is important to keep the grain strong and prevent sudden increases in burning area, which could explode the motor. To achieve a good bond, the segments are poured on top of each other in a single casting procedure, which ensures a strong chemical bond at their boundaries.

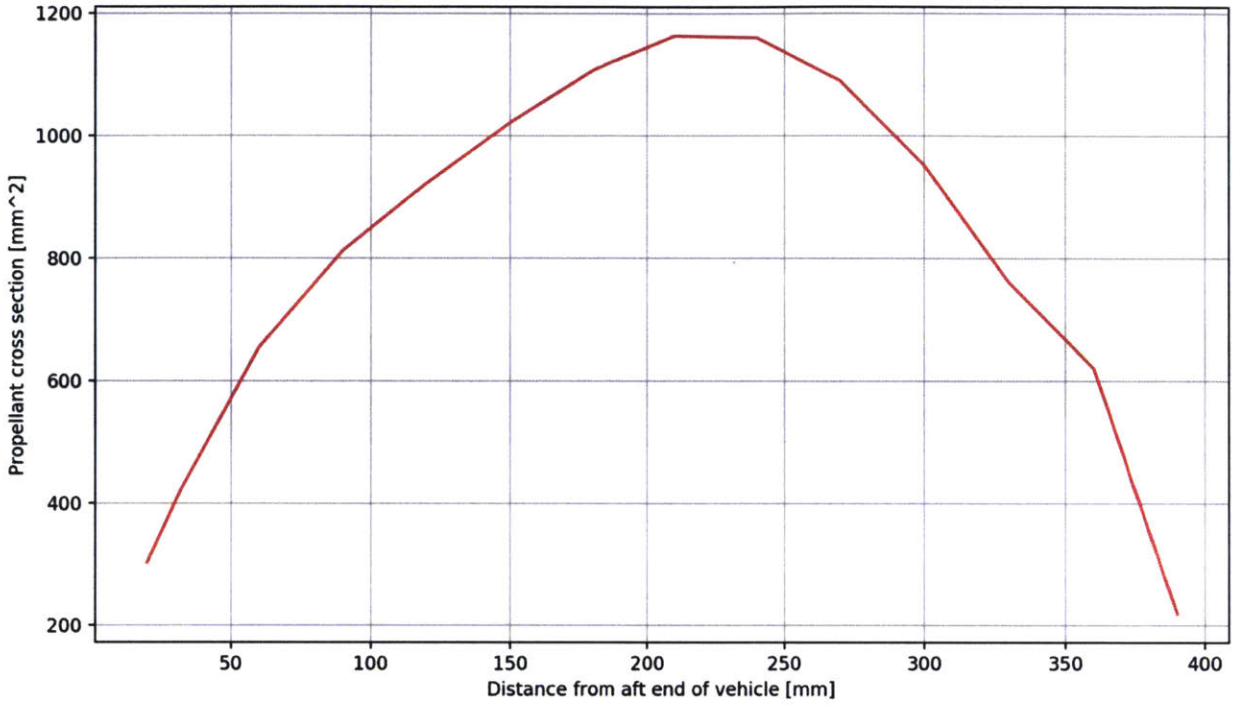

Figure 55: The cross section of the Firefly propellant grain varies by a factor of four along its length.

Figure 56: The propellant grain is cast in 4 segments, which have different burning rates due to different concentrations of the burn rate suppressant oxamide.

The simulated thrust curve shows sudden transitions in chamber pressure at the boundaries between grain segments. These could trigger combustion instabilities. However, in a real motor the pressure transition will be more gradual. Neither the flame front nor the propellant segment boundaries are perfectly planar, so the flame burns some of each propellant for a few seconds. This tends to smooth out the transition in chamber pressure.

Inhibitor - The outside edges of an end-burning grain must be inhibited to prevent their burning. Side burning would dramatically increase the burning area and chamber pressure, causing the motor to

explode. To prevent this, the propellant grain is surrounded by a fiberglass and epoxy inhibitor. The inhibitor also acts as a structural shell, which increases the grains ability to withstand mechanical loads during production and transport.

5.3 Thermal protection system

The motor case and other vehicle systems must be protected from the heat of propellant combustion. The end-burning grain configuration and long burn time make the thermal protection problem more difficult for small, slow-burning solid rockets than for typical small solid rockets. Small, slow-burning rockets require the design of specialized thermal protection systems. This section presents guiding design principles, and an example design for the Firefly motor. It will be shown that the thermal protection problem for small, slow-burning rocket motors is solvable with a clever arrangement of ablative materials and fibrous insulation.

The end-burning grain causes the interior of the case to be more exposed to combustion gases. In an internal burning grain, the remaining propellant sits between the flame front and the motor case. The propellant insulates the majority of the case, and only small regions near the throat (and possibly the front) are exposed to combustion gases. In an end-burning grain, by contrast, the propellant exposes a large interior surface as it burns away.

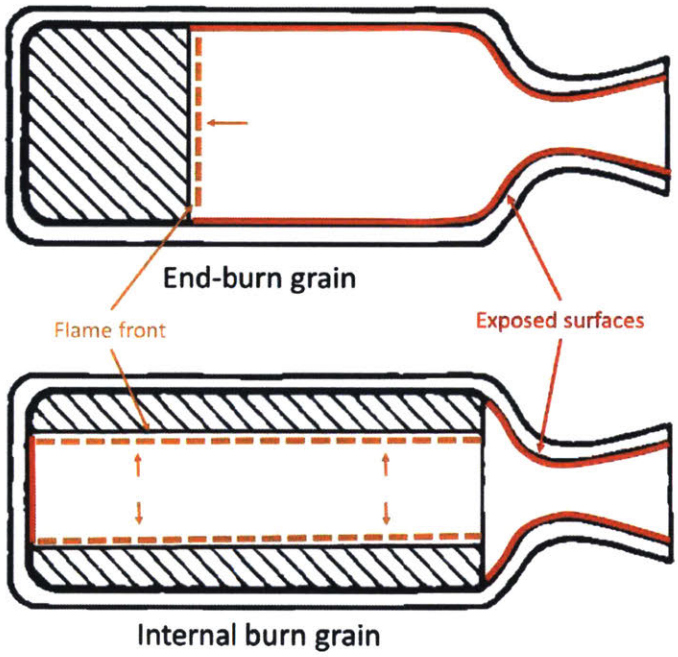

Figure 57: In an end burning motor, more of the motor interior is exposed to combustion gases. The exposed surfaces are highlighted in red; the flame front is shown by orange dashed lines.

A thermal protection system is applied to these exposed surfaces in order to block heat transfer, which would cause the case and other vehicle systems to overheat. The thermal protection should be as thin as possible: it adds inert mass to the vehicle and takes up volume which could otherwise be allocated to propellant.

The thermal protection consists of two layers between the combustion gases and the motor case: an ablative liner and fibrous insulation [Figure 58]. The inner layer, called the liner, is an ablative material which blocks the majority of the heat flux into the surface. Silicone polymer ablative composites are the material of choice because of their low thermal conductivity and low ablation rates in oxidizing environments.

The second layer, between the ablative and the case, is a thermal insulating layer made of a low-density fiberglass cloth. Because of its fibrous composition, the insulating layer has poor paths for heat conduction. If ablative material alone were used in a thin layer, an unacceptable amount of heat would leak through the ablative via conduction into the case. The fibrous insulating layer behind the ablative reduces this thermal leakage, allowing for a thinner, more performant thermal protection system.

This thermal protection system is expected to provide adequate protection in most designs. However, the exact thickness of the layers must be uniquely determined for a given application. The following subsections provide information pertinent to this design process. Subsection 5.3.1 defines the design drivers of the thermal protection system. Subsection 5.3.2 describes why an ablative material was chosen, and Subsection 5.3.3 reviews the fundamentals of the ablation process. Subsection 5.3.4 describes geometry and dimensions of the thermal protection system used on Firefly. Subsections 5.3.5 and 5.3.6 describe the selection of materials. Subsection 5.3.7 presents a simple thermodynamic model of the ablation process, which can be used to predict the required liner and insulation thicknesses. However, the models carry uncertainty, and experimental verification is required.

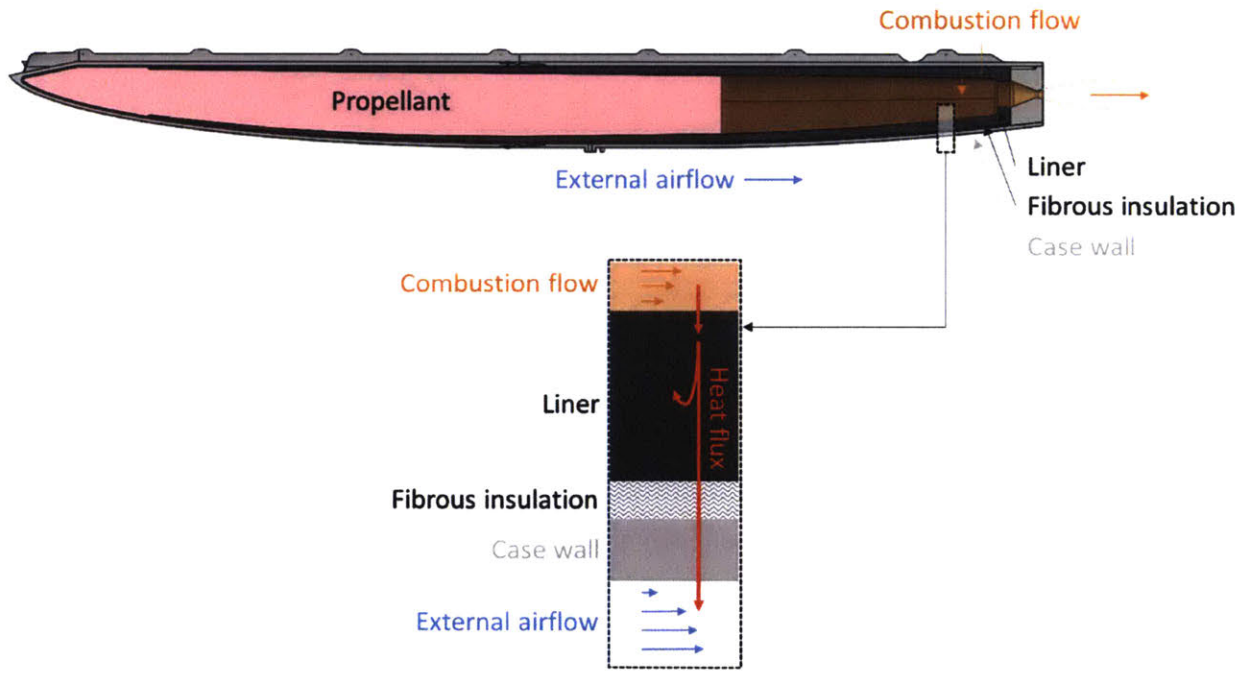

Figure 58: The thermal protection systems consist of two layers, an ablative liner and fibrous insulation, between the combustion gases and the motor case.

5.3.1 Thermal protection design drivers

In the Firefly example, the thermal protection system design is driven by the temperature limits of other vehicle systems, particularly the payload, avionics, and composite structures. To maximize motor length (and therefore endurance), the vehicle is configured with the motor in the bottom half, and the payload and avionics mounted on top of it. Therefore, temperature sensitive components are in close proximity to the motor case. The motor case temperature must therefore be limited so that these components can be kept at an acceptable temperature with the available cooling resources. This drives the design of the thermal protection system within the motor.

This constraint requires a lower case temperature than case material considerations alone. If an alternate vehicle configuration were chosen which placed temperature-sensitive components further from the case, the case could be run hotter. Certain designs using cobalt-chrome superalloys could tolerate case temperatures up to 1400 K. This would reduce the mass and volume of the thermal protection system.

5.3.2 Selection of thermal protection strategy

Ablative liners are the preferred thermal protection strategy for solid rockets [16] [46]. Regenerative liquid cooling is not an option for solid rockets. Non-ablative insulators or refractory structures typically weight and cost more than ablative solutions [46].

Ablative materials are sacrificial: they are destroyed in the process of providing thermal protection. Because they are sacrificial, ablative materials are most often applied on disposable systems; most solid rockets are disposable, as are the expected use-cases of small, transonic, deployable UAVs. Ablative materials can be employed in reusable systems, but must be periodically removed and replaced [47].

5.3.3 The ablation process

As heat is applied to an ablative material, a decomposition front advances through it. The decomposition process absorbs energy and blocks heat transfer, providing thermal protection to structures behind the ablative. The ablation rate (the speed at which the decomposition front progresses) determines the endurance of an ablative material, and depends on the fluid- and thermo-dynamics of the heat transfer process. Generally, the ablation rate is higher if the heating flow is hotter, denser, and faster [48].

Two important processes occur when an ablative material decomposes under high heat flux: gasification and charring. These processes reduce the rate of heat transfer into the ablative material, allowing it to have a usefully slow ablation rate. At some depth beneath the surface of the material, there is decomposition zone, where the virgin material has reached a high enough temperature to undergo chemical and physical reactions at a significant rate [Figure 59]. Here, the more volatile components of the material (e.g. the polymeric binder) gasify and the more refractory components (e.g. the fibers and binder residue) form a solid char. In most ablatives, the net decomposition reaction is endothermic; much of the incoming heat flux is carried away by in the chemical potential of the gaseous and char products [46]. The char layer insulates the virgin material behind it from direct exposure to the heating flow. The gaseous products diffuse out through the porous char to the surface, where they mix with the heating flow. This "injection effect" thickens the thermal boundary layer of the heating flow and reduces heat transfer to the surface [48]. Additionally, a layer of molten glass can form at the surface if the requisite species (e.g. Si and O) are present in the char.

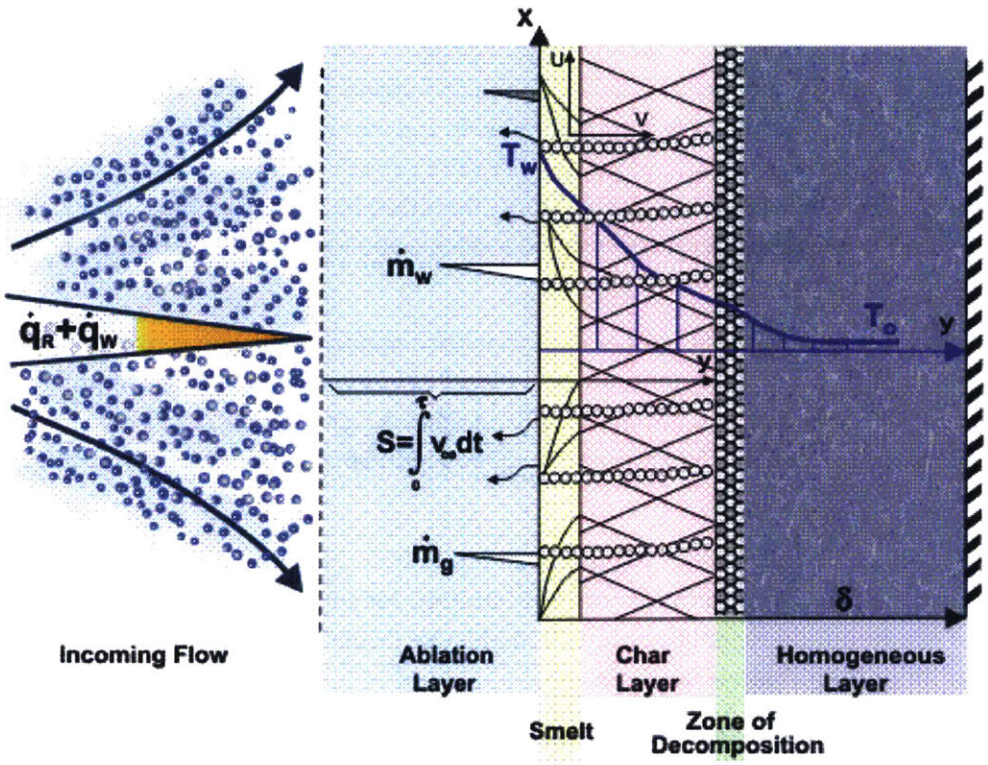

Figure 59: As an ablative composite is exposed to high heat flux, its surface gasifies and chars, processes which block heat flow deeper into the material. This protects the remaining virgin ablative and the structure behind it. Reprinted from [48].

An understanding of the ablation process informs the design of composite ablative materials. Desirable properties of the binder are a high decomposition temperature, a very endothermic decomposition enthalpy, and the deposition of a residue which contributes to the char. The fibers must have a very high melting point, and for a char which has low thermal conductivity (to resist heat transfer) and good mechanical strength (to resist erosion).

The choice of materials also depends on the chemistry of the heating flow. An oxidizing flow can react exothermically and destructively with carbonaceous or organic materials [46]. Silica (SiO_2) or silicon carbide (SiC) fibers are preferred over carbon or aramid fibers in aggressively oxidizing environments.

5.3.4 Geometry of Firefly's thermal protection system

The liner is a thin shell which surrounds the propellant grain within the motor case. The liner's thickness is tapered: because the propellant grain is end-burning, the aft end of the liner is exposed to combustion gases for a longer time, will char to a greater depth, and is therefore thicker.

The thickness of the liner is an important design parameter. If the liner is too thin, it will burn through, which could overheat the case material, causing it to fail. But extra liner thickness comes at a price it eats into the available propellant volume, which reduces the motor's total impulse and the vehicle's endurance. Therefore, by careful modeling and testing, the liner thickness should be set to the minimum value which provides adequate thermal protection. An example of this modeling is presented in Subsection 5.3.7.

The geometry of Firefly's liner is presented in Figure 60. It tapers from a thickness of 5 mm at the aft of the motor to 1 mm near the front. The very front of the propellant grain has no liner around it: this section of the motor case will only be exposed to low-pressure combustion[18] for a short period of time; it does not require thermal protection.

The liner and propellant are surrounded by 0.6 mm (0.025 in) of fibrous insulation.

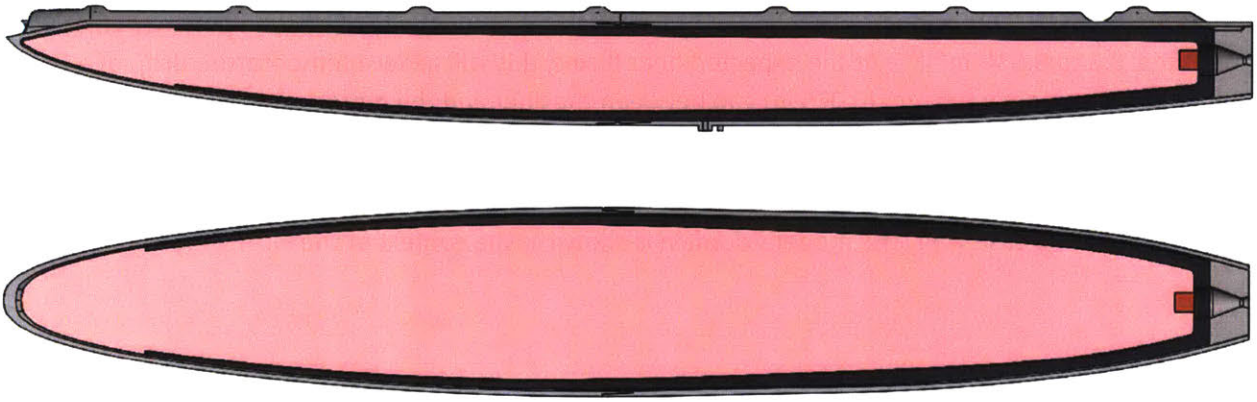

Figure 60: Cross sections of the firefly motor show the tapered ablative liner (black) surrounding the propellant grain (pink) within the motor case (grey).

5.3.5 Material selection: ablative liner

A silicone polymer ablative composite is the preferred liner material. It has superior ablative, processing, and mechanical properties to the alternatives.

In the oxidizing environment[19] of a solid rocket motor, silicone polymers leave superior char compared to carbonaceous (phenolic or epoxy) ablative materials [46]. Their siloxane backbone breaks down to form a protective silica ceramic in the char layer, which contributes the material's very low ablation rate [49].

Silicone polymer ablative composites can be cast into thin shells, a manufacturing capability required by the geometry of the liner. The material is supplied as a resin/fiber slurry; this slurry can be injected into a closed mold under vacuum to form thin, void-free parts [50]. The manufacturing process is presented in more detail in Section 6.2.

Additionally, silicone polymer ablative composites are more elastic than those based on phenolic or epoxy binders. An elastic liner around the propellant helps to mechanically isolate it from vibration or handling loads. This protects the propellant from mechanical damage, reducing the risk of motor failure and increasing the lifetime of the motor.

---

[18] At low pressures, the combustion gas density is lower and the heat transfer to the walls is proportionally less.
[19] The motor runs fuel rich, but oxidizing species are still present in the combustion zone – they can attack the liner before being consumed by the excess fuel.

5.3.6 Material selection: fibrous insulation

The fibrous insulation layer consists of several plies of dry fiberglass cloth which are placed between the liner and the motor case. This disrupts the contact path between the liner and the case, reducing heat conduction. Fiberglass cloth is selected because of its low thermal conductivity and high temperature tolerance. The cloth is also flexible enough to easily wrap around the propellant and liner.

The effective thermal conductivity of multi-ply dry fiberglass is only 0.04 to 0.06 W m^{-1} K^{-1}, according to our measurements[20]. This is much less than the typical thermal conductivity of silicone polymer ablative composites, 0.2 to 0.5 W m^{-1} K^{-1}. At the expected heat fluxes, this will allow a temperature drop of a few hundred kelvins across a 0.6 mm (0.025 in) gap between the liner and the motor case.

5.3.7 Thermal modeling

A model was made of the ablation of the liner. The model examines the transient heat flux through a 1D slice of the liner and case wall. The model's domain is shown in the context of the Firefly motor in Figure 61.

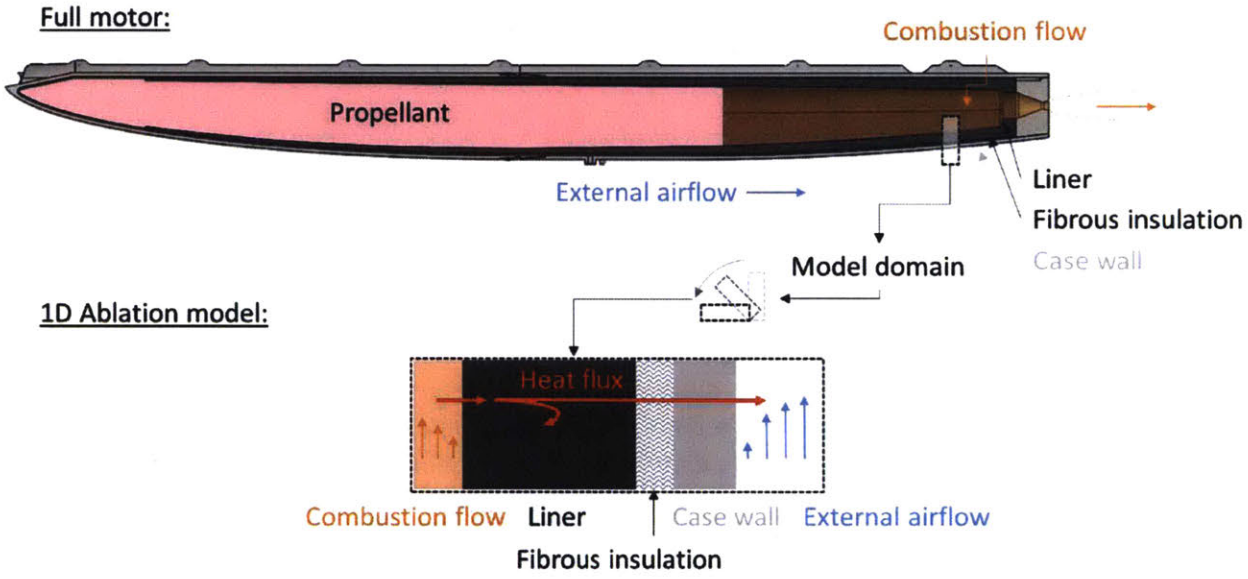

Figure 61: The ablation model captures a 1D slice through the liner and wall of the rocket motor.

Several simplifications were made to make the model tractable:

1. Heat only flows in the wall-normal direction.
2. The ablative is modeled simply as a material with a plateau in its temperature vs enthalpy $T(h)$ function [Figure 62]. When heat is added, the virgin material first warms with a constant heat capacity. Then, the material decomposes at a constant temperature, absorbing latent heat in the process. Once decomposition is complete, the char warms at a different, but also constant, heat capacity.

[20] These measurements were conducted in air at 0.1 MPa. In a firing rocket motor, the gas pressure will be higher. This will increase the density, and therefore the thermal conductivity, of the gas between the glass fibers. Therefore, the effective thermal conductivity of the wrap will be somewhat higher.

3. Gasification injection effects are ignored; the convection coefficient at the hot surface is assumed to be constant, regretless of the ablation rate.
4. Char erosion and swelling are ignored.

Next, the boundary conditions of the thermal problem must be determined. The convection coefficients for the internal (combustion gas) and external (freestream air) boundary layers were estimated via Nusselt number correlations [see Appendix 2]. The internal convection coefficient is predicted to be 80 W m^{-2} K^{-1} and the external to be 100 to 350 W m^{-2} K^{-1}.

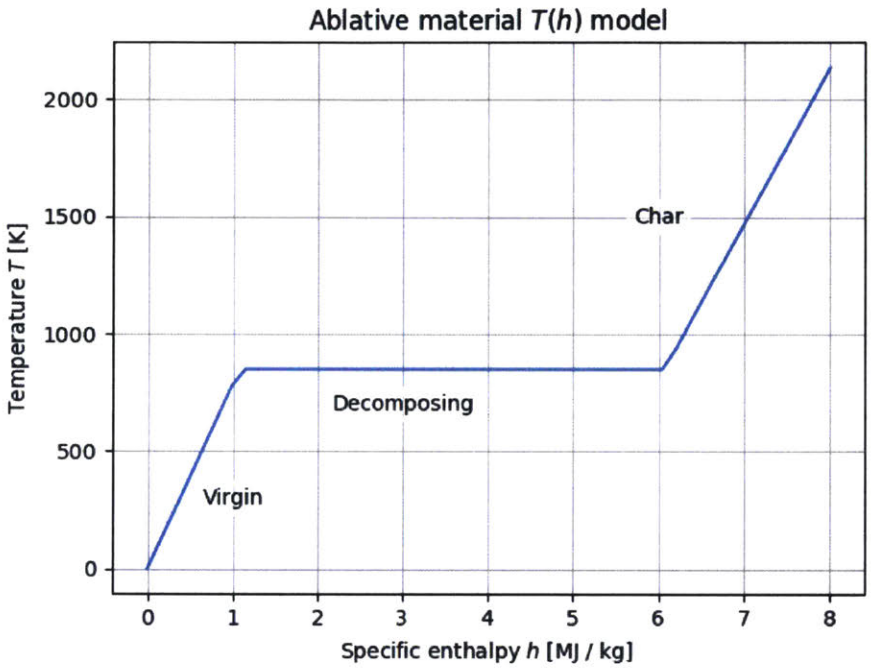

Figure 62: A simple model of the heating response of an ablative material.

The results of the model, shown in Figure 63 and Figure 64, predict that an aft-end liner thickness of 5 mm will give sufficient thermal protection with ample margin. During a 200 second burn, the decomposition front is only expected to penetrate 1 mm into the liner, and the motor case is only expected to reach 450 K. In Figure 63, the top plot shows curves of temperature through the thickness of the liner and case wall. The bottom plot shows specific enthalpy (chemical + thermal); a large (5 MJ kg^{-1}) enthalpy addition is required to decompose the ablative. Curves are plotted for different exposure times, ranging from 0 seconds (black) to 200 seconds (red) in 10 second intervals. The ripples in the temperature curves are numerical artifacts.

Simple thermal models can provide rough estimates of the required liner thickness. However, the ablation process is difficult to model [48], so these estimates should be viewed with skepticism and tested against motor firing experiments.

Because of the uncertainties of modeling, large liner thickness and case temperature margins were retained for the initial design of Firefly. Once more experimental data has been collected to refine the models, future design iterations will likely use thinner liners, which allow for more propellant.

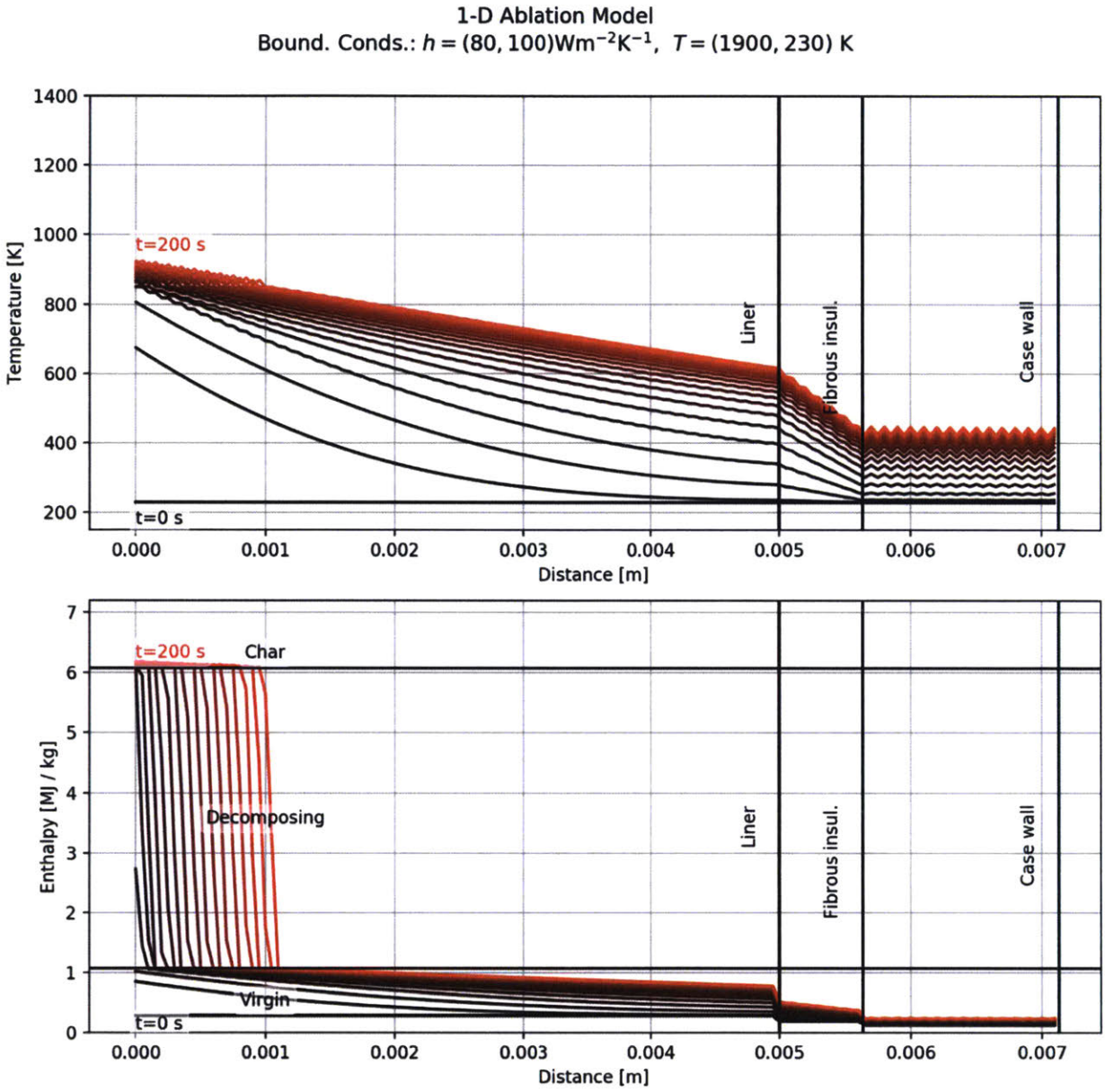

Figure 63: The ablative decomposition zone is expected to penetrate 1 mm into the liner during a 200 s burn of a typical slow-burning solid rocket motor. A 5 mm thick liner (the thickness depicted here and used at the aft end of Firefly) provides plenty of margin against liner burn-through.

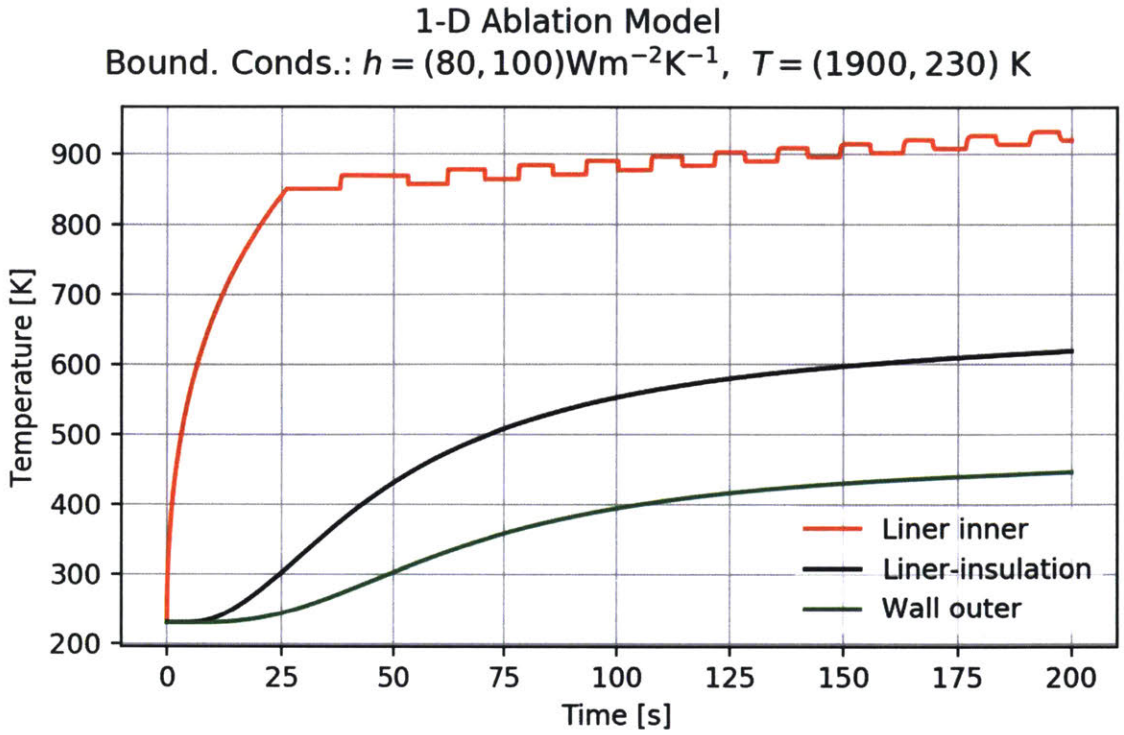

Figure 64: Simulated thermal transients show the liner provides sufficient thermal protection for the case wall. After 200 seconds of burn, the case wall temperature (green curve) is only expected to reach 450 K. The ripples in the "Liner inner" temperature curve after 25 s are numerical artifacts.

5.4 Nozzle

The nozzle accelerates the exhaust gases, converting the thermal energy of combustion into kinetic energy of the exhaust jet. Small, slow-burning rocket motors place unique challenges on the nozzle: it must have a small throat diameter (because of the low thrust) and high temperature tolerance and erosion resistance (because of the long burn time).

A monolithic nozzle block cast from zirconia ceramic effectively addresses these challenges. Zirconia has good erosion resistance and will maintain the nozzle diameter. The low conductivity of the material and the monolithic block geometry insulate components around the nozzle from the hot gas within.

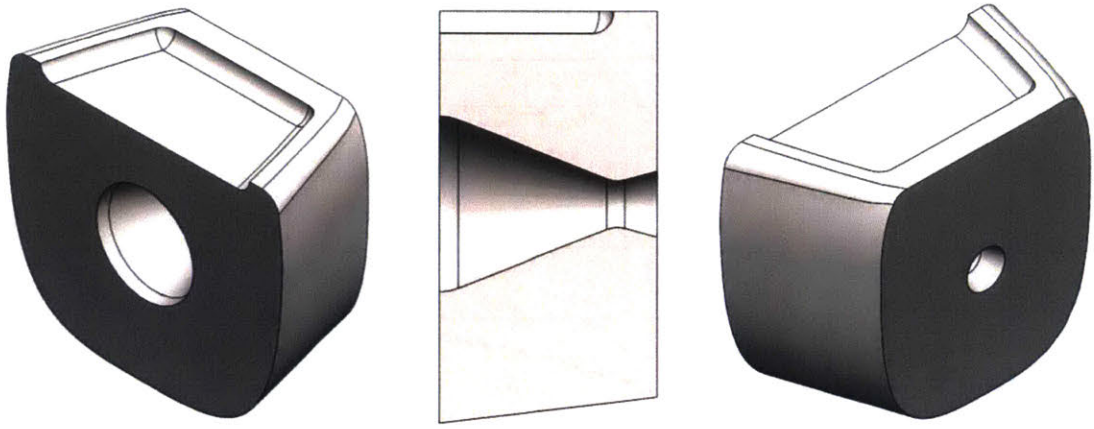

Figure 65: Three views of Firefly's ceramic nozzle.

5.4.1 Nozzle seals to the liner and case

The nozzle must form seals with the case and aft end of the liner to contain the combustion gases. Both seals are made with adhesive bonds.

The nozzle is bonded to the case with Resbond 904 zirconia adhesive. This adhesive has a high temperature tolerance, and its thermal expansion coefficient closely matches those of Ti-6Al-4V (the case material) and zirconia (the nozzle material). This will prevent thermal stresses from cracking the bond, which is a concern when stiff materials are bonded with a brittle adhesive.

The nozzle is bonded to the aft end of the liner with a silicone-based adhesive.

5.4.2 Nozzle material selection

The nozzle material must resist erosion of the nozzle throat and block heat to the motor case. These requirements demand a high temperature tolerance, low thermal conductivity, and good wear resistance.

Graphite is the default choice for solid rocket nozzles [16], but its high thermal conductivity and poor wear resistance make it ill-suited to the needs of small, slow-burning motors.

Instead, ceramics were chosen. Specifically, an engineered zirconia product (Rescor 760) was identified which meets the requirements of the Firefly nozzle. Conveniently, zirconia has almost the same thermal expansion coefficient as the motor case's Ti-6Al-4V alloy, which helps to reduce stress at their interface.

Table 8: Materials considered for the nozzle, and the case material for comparison.

Material	Conductivity [W / m K]	Heat capacity [J / kg K]	Density [kg / m^3]	Melting or sublimation point @ 1 atm	Coefficient of thermal expansion, linear [10^{-6} K^{-1}]
Graphite, polycrystalline, 720 K	70 [51]	1600 [51]	2200	~3900 K	8
Alumina, Rescor 960 [52]	4.6 [52]	880 [53]	3900 [53]	2100 K [52]	7.7 [52]
Alumina silicate, Rescor 902 [54]	1.1 [54]	1200 [55]	2300 [54]	2000 K [54]	3.2
Zirconia, Rescor 760	0.94 [56]	570 [57]	5500	2500 K [56]	10.
Titanium 6Al-4V	6.7	586	4429		9.7 [58] Average from 290 to 920 K

5.4.3 Nozzle thermal loads

Modern finite element analysis (FEA) software combined with some rough approximations of convection boundary conditions enables prediction of the thermal loads on the nozzle. The key value to be predicted is the maximum temperature reached in the motor case. This must be compared against a strength vs temperature curve for the case material and the expected stress state in this portion of the case.

A steady-state analysis is sufficient because the nozzle has very little heat capacity compared to the heat fluxes it experiences. A steady-state thermal analysis of the Firefly nozzle is presented below. The boundary condition assumptions used in this model are presented in Table 9, and were estimated using the Nusselt number technique described in Appendix 2. SolidWorks Simulation was used to perform the FEA calculations.

For the Firefly motor, maximum predicted temperature in the case near the nozzle is 730 K. These temperatures are acceptable. The predicted temperatures are close to the 50% yield tensile strength limit of Ti-6Al-4V (780 K), and there is inaccuracy in the estimation of the convection coefficients. Therefore, it is likely that the titanium wall around the nozzle will see significant softening, especially on the top side. However, some softening is acceptable. The mechanical analysis in Section 5.4.4 shows that this part of the wall is lightly loaded – only 9 MPa, or 1% of Ti6-4's room-temperature yield strength.

Because the top side of the motor case is not exposed to external air flow, it has less cooling capacity. To prevent the top of the motor case from becoming excessively hot, the top side of the nozzle is pocketed to reduce its contact area with the motor case.

Table 9: Boundary conditions used in the nozzle thermal model.

Location →	**Blast tube / nozzle inlet**	**Convergent Section**	**Nozzle throat**	**Divergent section**	**Nozzle exit**
Prandtl number	0.4998		0.5194		0.5301
length scale [m]	0.01		0.002		0.005
viscosity [Pa s]	7.30E-05		6.80E-05		4.20E-05
heat capacity [J / kg K]	2127		2027		1649
velocity [m/s]	28		952		2100
density [kg/m^3]	1.67		1.04		0.081
Reynolds number	6.41E+03		2.91E+04		2.03E+04
Nusselt number	20.7		70.4		53.0
convection [W/ m^2 K]	**644.0**	**4994.3**	**9344.6**	**5364.6**	**1384.6**
Gas static temperature [K]	**2210**	**2100.0**	**1990**	**1500.0**	**1010**

Location →	**External air: flowing [59]**	**Cooling duct air flow [59]**	**External air: recirculating at base**	**Ablation gas: pocket**
convection [W/ m^2 K]	**100**	**28**	**10**	**10**
Gas static temperature [K]	**210**	**317**	**300**	**800**

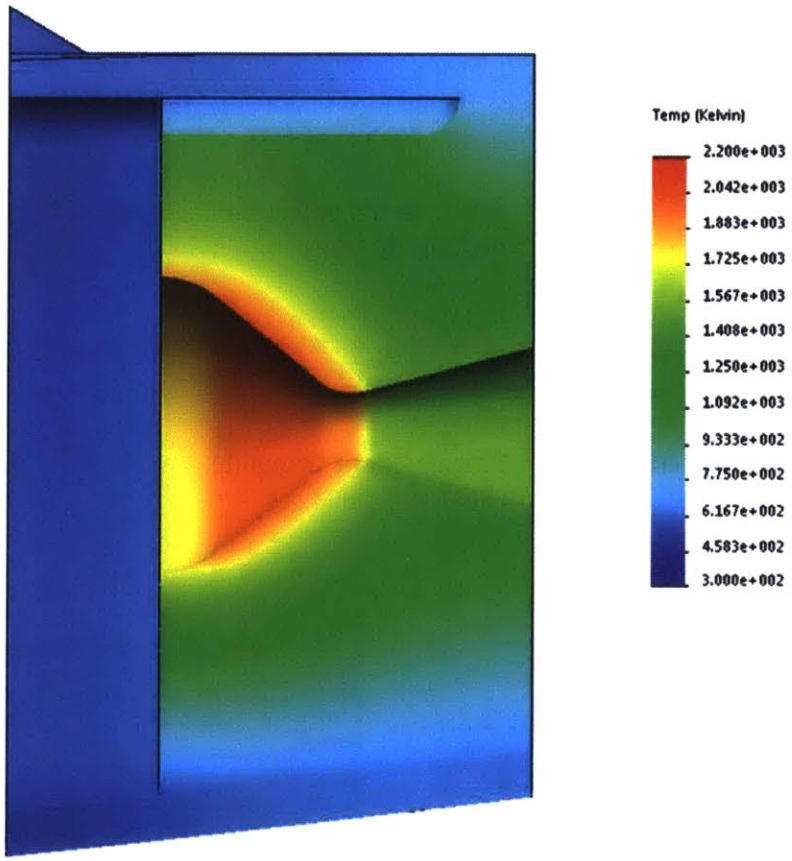

Figure 66: Simulated steady-state temperature profile in the nozzle and aft end of the motor case. The maximum predicted temperature of the case is 730 K, an acceptable temperature for lightly-loaded Ti-6Al-4V.

5.4.4 Nozzle mechanical loads

When designing the nozzle, FEA software should be used to predict the stress state in the nozzle and case as a result of thermal expansion and pressure loads. The stress state should then be compared against an appropriate failure criterion for the materials used, and a factor of safety calculated. The design should then be adjusted until the appropriate factor of safety (typically 1.5 [60]) is met.

As an example, the analysis for the Firefly nozzle is presented below. The applied load is an internal pressure of 1.4 MPa (200 psi). In the ductile Ti-6Al-4V case, the stress state is evaluated against the von Mises yield criterion. The brittle nozzle material uses the Mohr-Coulomb failure criterion [61]. Further assumptions of the FEA model are listed in Table 10.

The results of the finite-element analysis are presented in Figure 67 and Figure 68. The factor of safety is acceptable everywhere in the nozzle except at the forward corner of the bond with the case. However, I suspect that numerical artifacts and an unrealistic assumption of perfect bonding over predict the stress there.

Table 10: Assumptions of the nozzle mechanical loads model.

Category	Property	Value
Loads	Internal pressure	1.4 MPa
Fixtures	Fixed geometry on sectioned face of the case (left side of figures)	
Material properties	Strength	Zirconia: 8.3 MPa flexural, 28 MPa compressive [56]
		Ti-6Al-4V: 520 MPa tensile yield
	Elastic modulus	Zirconia: 100 GPa
		Ti-6Al-4V: 110 GPa
	Poisson's ratio	Zirconia: 0.27
		Ti-6Al-4V: 0.31
	Yield criterion	Zirconia: Mohr-Coulomb
		Ti-6Al-4V: von Mises

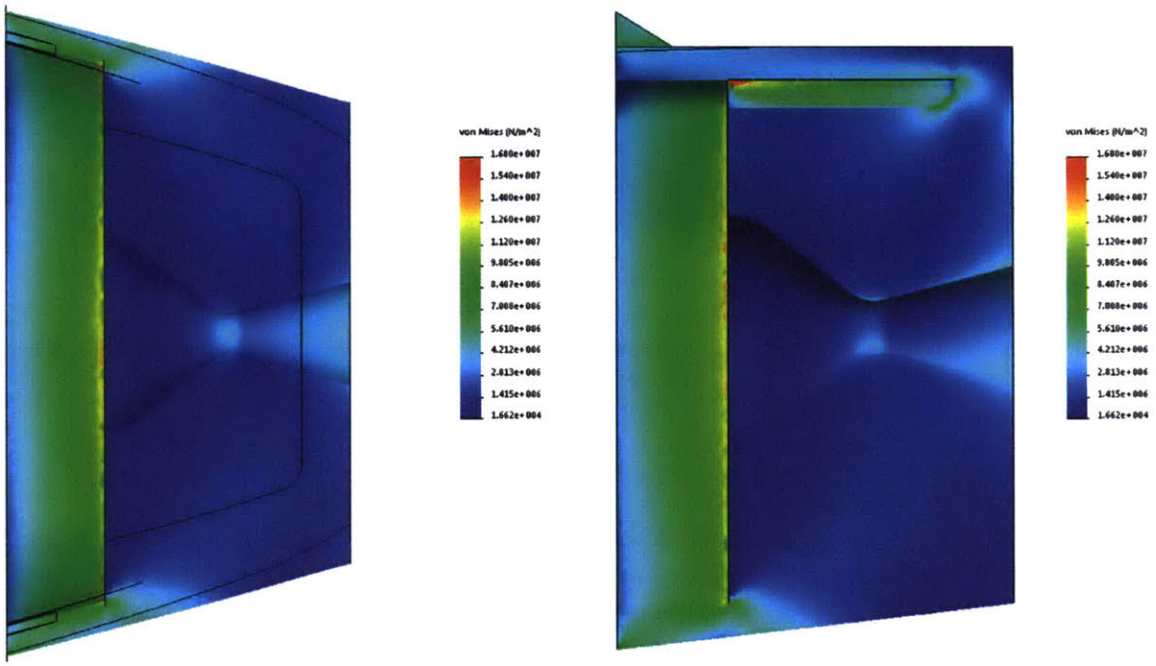

Figure 67: The predicted von Mises stress in the nozzle and case aft is within the acceptable limits for the case material.

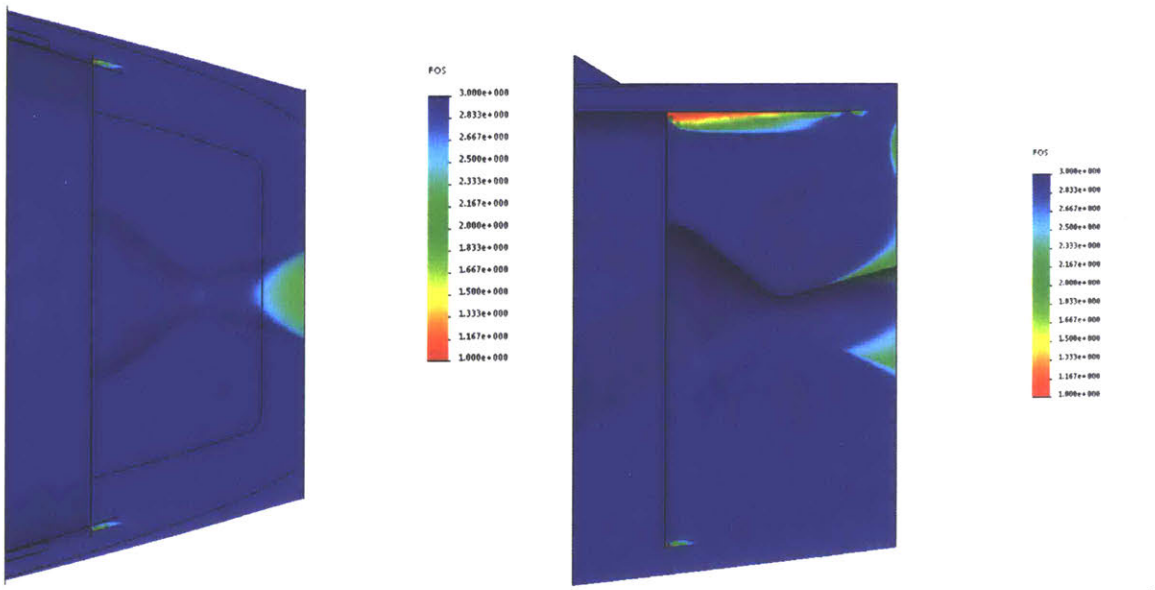

Figure 68: Predicted factor of safety in the nozzle and case aft. The nozzle (brittle zirconia) uses the Mohr criterion, wall (ductile Ti) uses the von Mises criterion. Note that the high stresses (low FoS) at the nozzle-wall contact may be numerical artifacts.

5.5 Motor case

Solid rockets require a motor case which contains the propellant and can withstand the heat and pressure loads produced by propellant combustion. In the context of small, transonic UAVs, the motor case must also meet unique structural integration requirements and serve as a chassis to which other vehicle systems are mounted.

Advances in additive manufacturing (3D printing) present an exciting, novel option for the manufacture of motor cases. The UAV propulsion application requires a motor case with light, thin walls and a complex geometry; attributes which match well to the unique advantages of 3d printing. Therefore, this research explores the application of 3D printing to small solid motor cases.

This section presents case design considerations for small, slow-burning solid rockets. Subsection 5.5.1 presents compact joints for connecting case segments. Subsection 5.5.2 examines material selection for motor cases. Subsections 5.5.3 and 5.5.4 present example thermal and mechanical analyses for a motor case. The additive manufacturing process is described in Section 6.1 of the next chapter.

5.5.1 Mid-case joint

Because the case of a typical UAV rocket motor is tapered at both ends (for aerodynamic reasons), in must split and the middle, its widest point, to allow for the insertion of the propellant grain and thermal protection liners ("propellant package") during assembly. A joint between the forward and aft halves, the mid-case joint, must be designed. It must withstand the axial tension forces applied by the motors internal pressure.

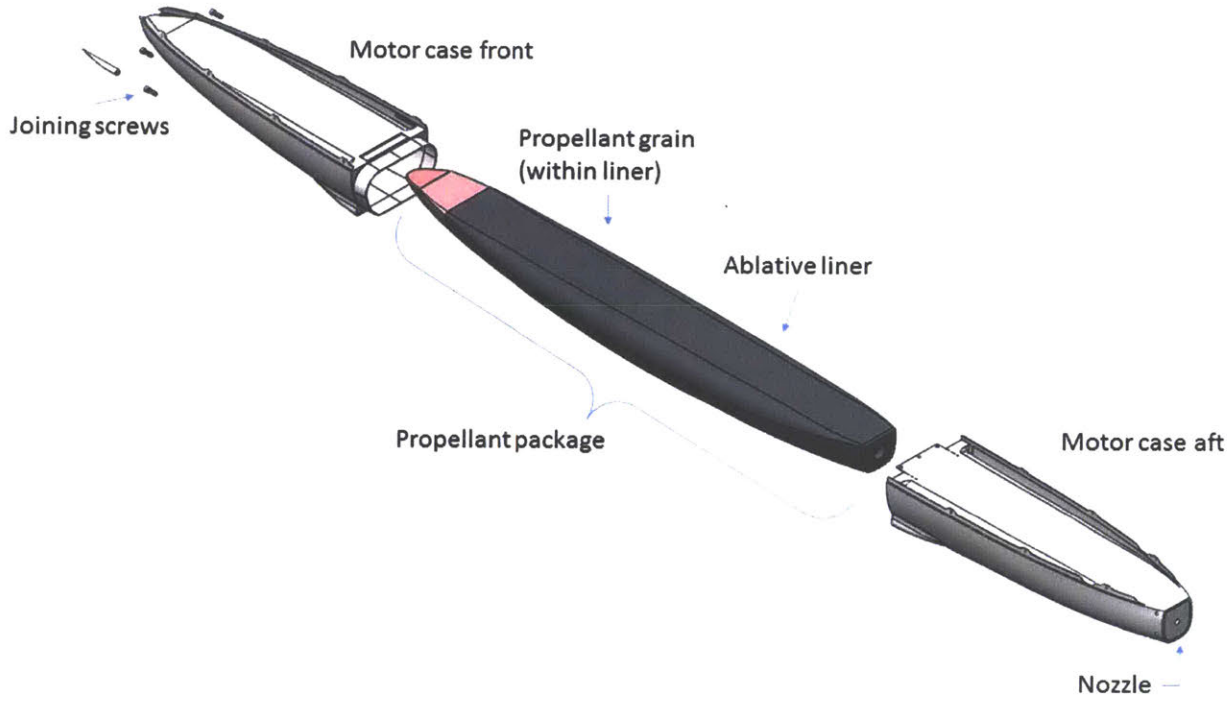

Figure 69: The mid-case joint allows the motor case to be assembled around the propellant package.

Firefly employs two redundant joint structures. One, a set of two snap-tabs, is smaller and lighter, but pushes the limits of the manufacturing process, and is of uncertain strength [Section 6.1.3 describes its manufacture and testing]. The other, a set of four axial bolts, is bulkier but stronger. If the snap tabs can be made to work reliably, the axial bolts may be eliminated from future design iterations.

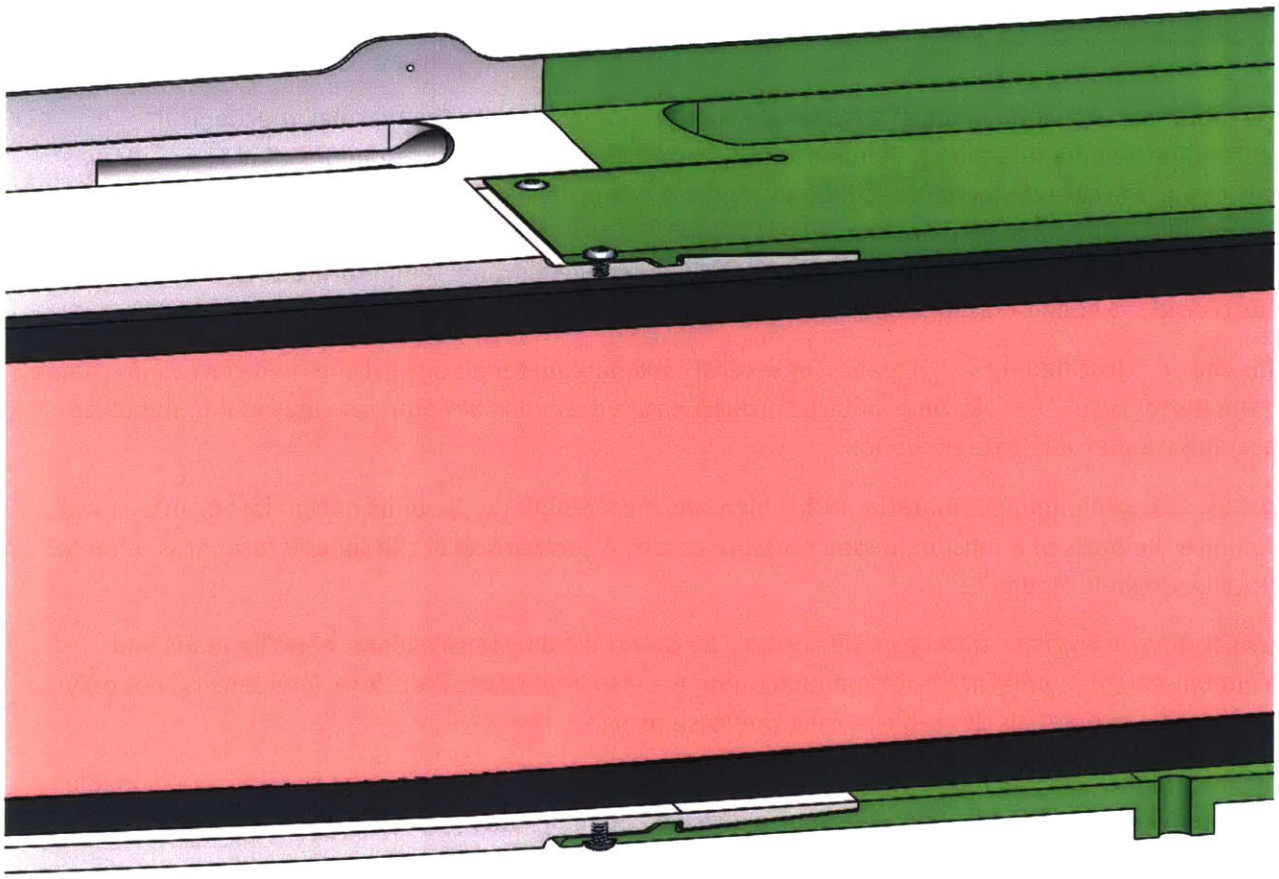

Figure 70: The snap-tab features on the mid-case joint.

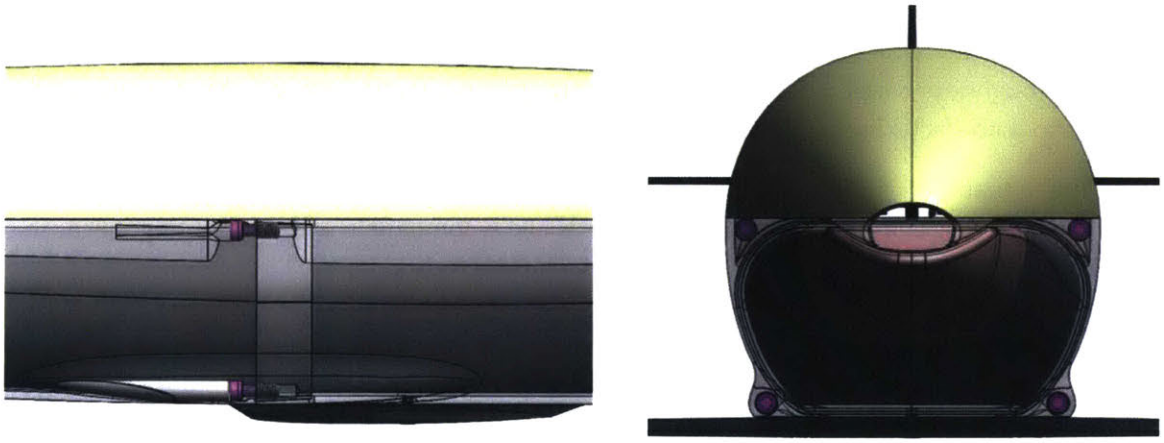

Figure 71: Four axial bolts (shown in pink) help support the axial tension load on the mid-case joint.

5.5.2 Case material selection

The motor case must be made of a material which is compatible with the thermal, mechanical, operational and manufacturing demands of the motor design. For Firefly, titanium alloy Ti-6Al-4V was selected as the case material for its high strength, low density, high temperature tolerance, and compatibility with additive manufacturing. Ti-6Al-4V is likely the correct choice for most small, slow-burning solid rocket motors. However, designs which require extreme temperature tolerance in the case may consider a cobalt-chrome superalloy (e.g. EOS MP1 or Renishaw CoCr-0404).

This choice is justified by an evaluation of several candidate materials against the material requirements of the motor case. The following material properties are desired in a motor case material to minimize case mass and ensure safe operation:

Specific strength (high) – A material with a high specific strength (σ_y/ρ, units of N m kg^{-1} or m^2 s^{-2}) will minimize the mass of a tension-loaded pressure vessel. A comparison of the specific strengths of metal alloys is shown in Figure 72.

Density (low) – The case thickness will not only be determined by tensile loads: bending loads and minimum-gauge requirements for manufacturing are also important. Therefore, low density, not only high specific strength, is desirable to minimize case mass.

Ductility (high) - Ductile materials yield (stretch) before breaking. Elongation at break is a reasonable quantitative metric for ductility. 5% can be a division between "ductile" and "brittle".

A ductile case is desired so that a case failure is safer. Ductile pressure vessels tend to peel open like a banana; while brittle pressure vessels eject shrapnel. Shrapnel generation poses a risk to the host aircraft if the rocket motor fails upon ignition.

Temperature tolerance (high) - Temperature tolerance is quantified by the temperature at which the material's tensile yield strength is reduced to 50% of its room temperature value. This value should be as high as possible to make the thermal protection problem easier.

Fracture toughness (high) - The mode I fracture toughness K_{Ic} is the stress intensity factor at which a thin crack in the material will begin to grow. It has units of Pa m$^{1/2}$.

A high fracture toughness is desired so that defects in the case will grow more slowly. This will make it more resilient to manufacturing or handling errors.

Several candidate materials are evaluated on these properties to explore the material design space [Table 11]. The materials considered are primarily metal alloys compatible with 3D printing, because of this technology's appeal as a research area.

This evaluation shows the favorability of titanium alloy Ti-6Al-4V. It has one of the highest specific strengths in Table 11, exceeded only by maraging steels and composites. However, Ti-6Al-4V has distinct advantages over both: the high density of maraging steels will increase case mass[21], and composites

[21] When minimum gauge and bending load considerations are taken into account.

cannot withstand the high temperatures reached in long-endurance rocket motors. Ti-6Al-4V also has sufficient fracture toughness and ductility to be robust against defects and fail safely.

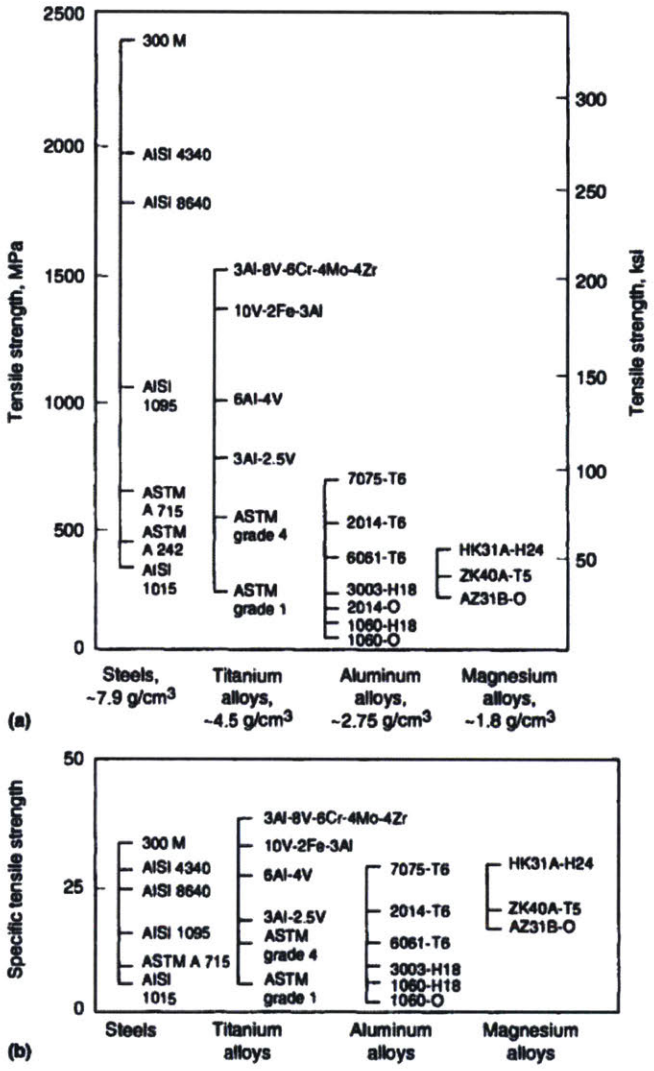

Figure 72: Comparison of the strength and specific strength of metal alloys. Reprinted from [62].

*Table 11: Comparison of properties of potential case materials. (ann) denotes annealed condition, (HT) denotes heat treated, and (HIP) denotes treatment by hot isostatic pressing. * The Heat Deflection Temperature of West Systems 105/205 epoxy.*

Type	Alloy	Yield tensile strength [MPa]	Specific strength [kN m kg^{-1}]	Elongation at break [%]	Temp for 50% YTS reduction [K]	Fracture toughness [MPa $m^{1/2}$]	Thermal conductivity [W m^{-1} K^{-1}]	3D printing?
Aluminum	2024-T3	290	105	14%	530	25	120	No
	6061-T6	276	102	12-17%	520	29	170	No
	7075-T6 [63]	480	173	7%	480	20-29	130	No
	AlSi10Mg [64]	230	86	4-11%	570	40-60	103	Yes
Titanium	Ti-6Al-4V ELI [65]	1000 (HT) 890 (HIP)	226 (HT) 200 (HIP)	3-12% (HT) 18-20% (HIP)	780	75	7	Yes
Steel	4340M (300M) [66]	1240	158	6%		60		No
	C300 maraging [64]	830 (ann) 1970 (HT)	104 (ann) 246 (HT)	16% (ann) 8% (HT)	810	175	15-20	Yes
	316 [64]	290	36	50%	922	112-278	16	Yes
	17-7PH TH1050 [64]	1030	135	6%	780	76	17-21	Yes
Superalloy	Inconel EOS In718 [64]	1034 (HT)	127	26%	>900	Not avail.	11	Yes
	Cobalt-Chrome EOS MP1 [64]	1200 (as printed)	144	8-28%	~1400	Not avail.	13-33	Yes
Composite	E-glass / BPA epoxy [16]	1000	510	1.4%	320 *	Not avail.	Highly anisotropic	No

5.5.3 Case thermal loads

As detailed in the above sections, Firefly's motor case is expected to reach a temperature of 450 K in the regions protected by the liner, and 730 K at the aft of the case around the nozzle. The effects of elevated temperature on the strength of Ti-6AL-4V are shown in Figure 73. At 450 K (most of the case), the yield strength of Ti-6Al-4V is 80% of its room temperature value, or 800 MPa. At 730 K (the aft section of the case around the nozzle), the yield strength will be 620 MPa.

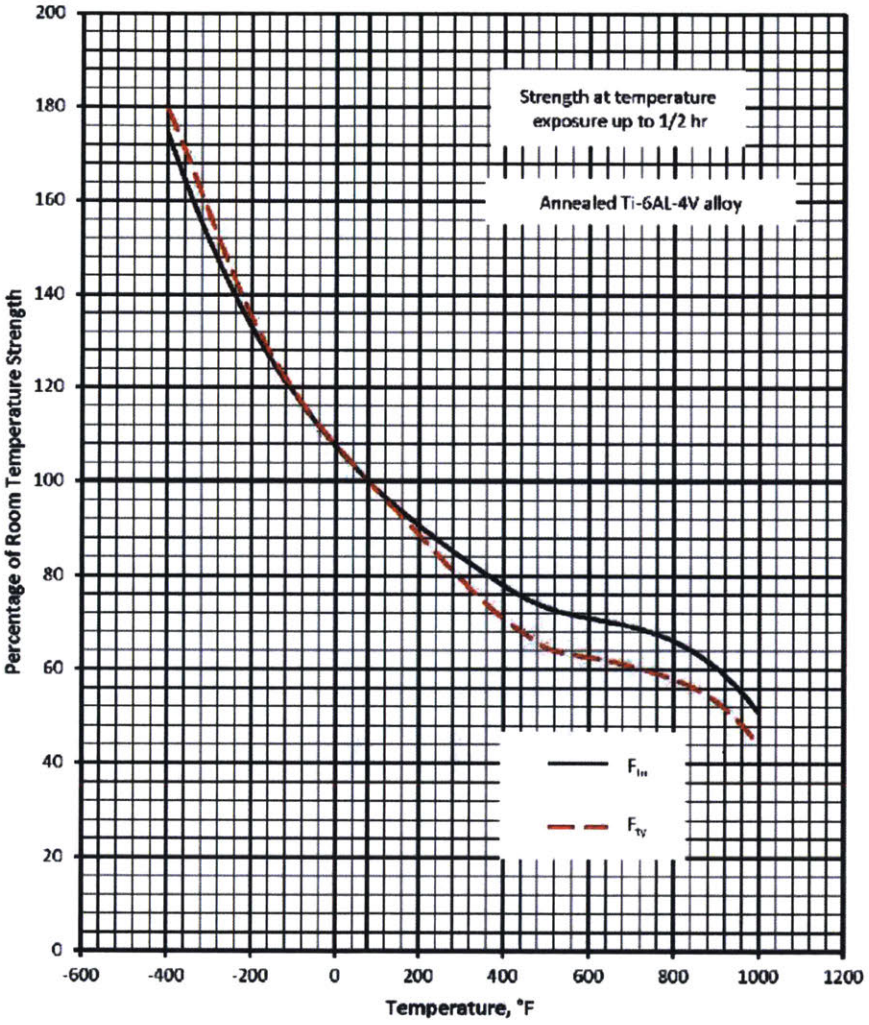

Figure 5.4.1.1.1. Effect of temperature on the tensile ultimate strength (F_{tu}) and the tensile yield strength (F_{ty}) of annealed Ti-6Al-4V alloy (all wrought products).

Figure 73: Reprinted from [63].

5.5.4 Case mechanical loads

The design of a motor case requires the prediction of mechanical loads, the estimation of their stress states, and comparison of that stress state against a failure criterion to meet a desired structural factor of safety.

The driving load for the cases of UAV propulsion rocket motors is the internal pressure load. This produces significant axial and circumferential (hoop) stresses.

In order to maximize motor length (and therefore endurance), rocket-propelled UAVs may be configured with the propulsion system occupying the bottom half of the vehicle and payload on top. In this case, the top of the motor case must have a flat "deck". The pressure applies a bending load to the deck, and the top-center of the deck is the location of maximum stress in such designs [Figure 75]. Rounding the corners where the deck meets the side walls is necessary to prevent a stress concentration there [Figure 74].

A finite element analysis was performed on the Firefly motor case. The model assumptions are listed in Table 12, and the results are shown in Figure 75.

With an internal pressure of 1.4 MPa, the predicted maximum von Mises stress in the Firefly case is 520 MPa. The yield tensile strength Ti-6Al-4V at the expected case temperature (450 K near location of max stress) is 800 MPa, giving a factor of safety of 1.5. From a thermal perspective, the case temperature could exceed the predicted value by up to 250 K before the case would yield. When the case is pressurized, the center of the deck is expected to bow out by 2 mm.

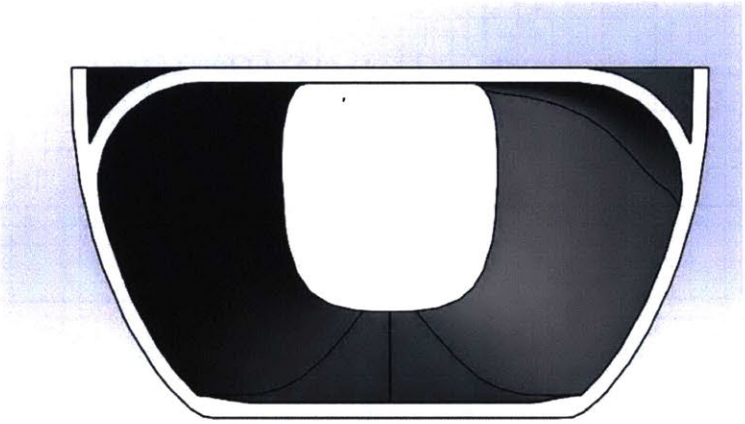

Figure 74: Rounding the corners of Firefly's deck reduces bowing and stress concentration.

Table 12: Assumptions of the motor case mechanical loads model.

Category	Property	Value
Loads	Internal pressure	1.4 MPa
Fixtures	Soft springs	
Material properties	Strength	Around nozzle: 620 MPa tensile yield Elsewhere: 800 MPa tensile yield
	Elastic modulus	110 GPa
	Poisson's ratio	0.31
	Yield criterion	von Mises

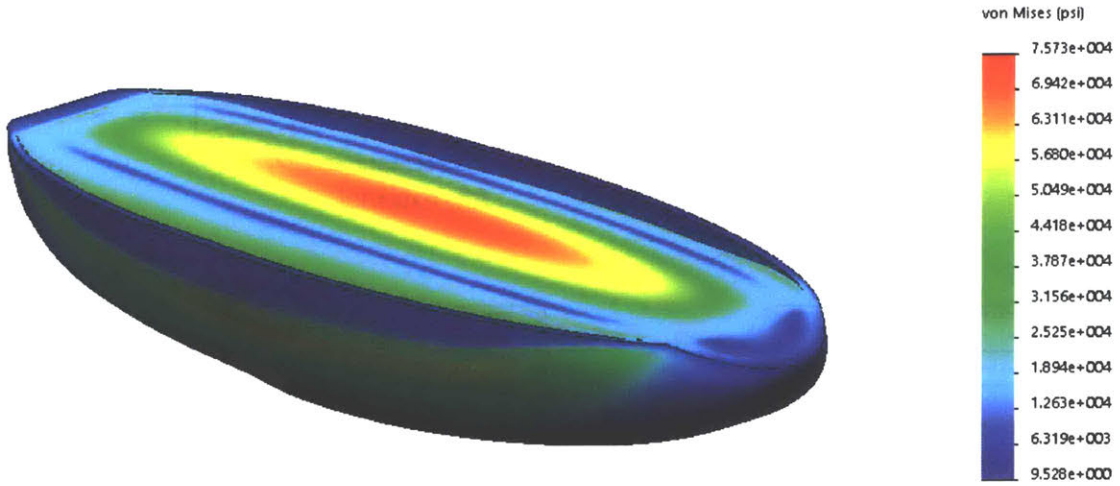

Figure 75: A mechanical finite element analysis of the Firefly motor case. The maximum predicted von Mises stress in the case is 520 MPa (75 ksi). The factor of safety is 1.5.

5.6 Ignition system

Solid rocket motors require safe, reliable and compact ignition systems. The development of laser-based ignition systems has been a recent advance in the field of pyrotechnics [38]; our research applied this to a novel laser-based ignition system for small, low-thrust rocket motors. This section explains that laser ignition is particularly well suited to the needs of small, low thrust rocket motors, and describes their use in the Firefly design.

5.6.1 Laser ignition

Laser ignition is favorable for small, low-thrust solid rocket motors. Compared to pyrotechnic ignition, the conventional solution, laser ignition is easier to package on small motors, and can be safer and more reliable.

Laser ignition systems are easier to package on small, low-thrust motors than pyrotechnic ignition systems. The common mounting locations for pyrotechnic igniters are shown in Figure 76. None of these are well-suited to small, low-thrust motors. The end-burning propellant grain configuration precludes the aft ignitor locations, and the nozzle's small throat diameter precludes the "forward, internal" option. The "forward, external" option is awkward to route past the nozzle and liner. By contrast, a laser system can be easily mounted outside of the motor, behind the nozzle. Although the nozzle throat is too narrow to accommodate pyrotechnics and wires, a laser beam can be easily shined through it onto the propellant. The laser system can be external to the motor and vehicle so as not to take up valuable space and mass.

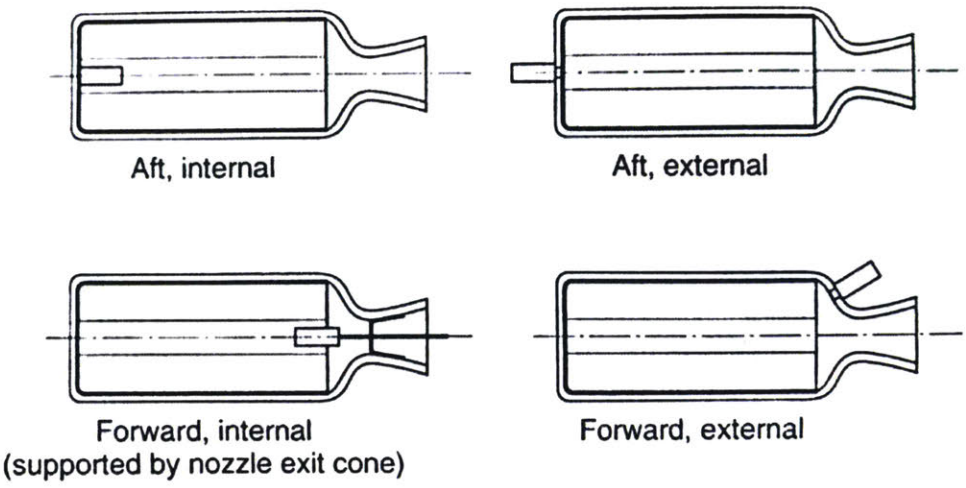

Figure 76: The common igniter mounting locations for solid rocket motors, none of which are well suited to small, low-thrust motors. Reprinted from Sutton [16].

Laser systems can also be made to be safer and more reliable than pyrotechnics. Laser systems are less prone to accidental ignition [16] [38], a valuable trait for deployable UAVs carried by risk-sensitive hosts. Small pyrotechnic igniters ("e-matches") are notoriously unreliable [20]. In contrast, modern solid-state laser diodes are very reliable [38].

5.6.2 Ignition system components

This section introduces the ignition system for Firefly as an example of the design of laser ignition systems for small, rocket-propelled UAVs. The ignitions system is composed of a laser, laser power supply, and a starter grain of fast-burning propellant. To save space and mass on the vehicle, the laser and power supply are carried in the shuttlecock, a device which is used to stabilize the vehicle during deployment and then discarded [Figure 77]. Ignition of the motor actuates the release of the shuttlecock.

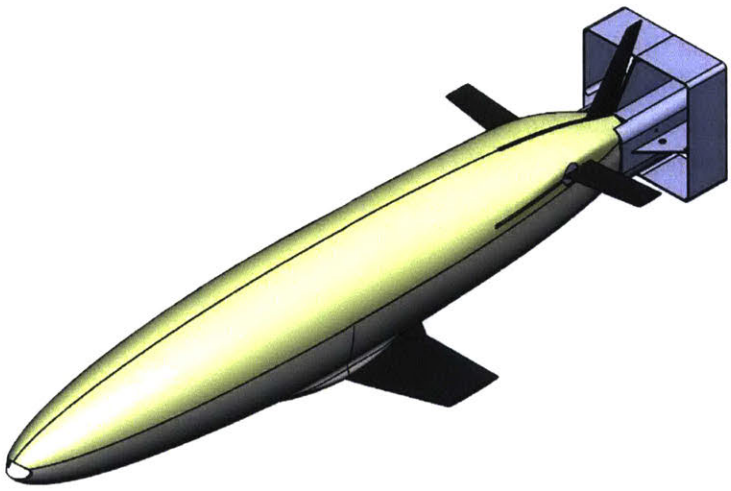

Figure 77: The ignition system's laser is carried outside the motor in the shuttlecock (grey).

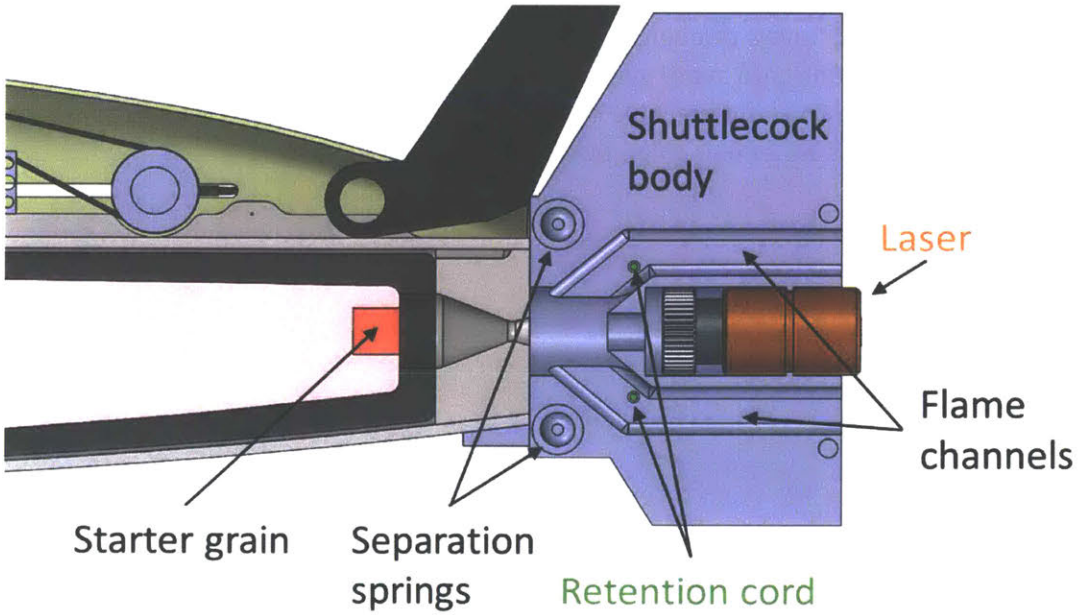

Figure 78: Ignition system components.

The major components of the ignition system are shown in Figure 78 and described below.

Starter grain – The starter grain is a piece of fast-burning ammonium perchlorate composite propellant. The fast-burning propellant is easier to ignite, and makes the motor's startup transient quicker.

Laser - The laser contains a gallium nitride (GaN) semiconductor laser diode[22], and emits a 6W beam at 450 nm. The laser is mounted to the shuttlecock body, which holds it in alignment with the nozzle throat and starter grain.

Laser power supply and ignition control – The laser is driven by a constant current power supply and a battery; these components are located on the shuttlecock but not shown in Figure 78. An ignition control circuit fires the laser once Firefly has stabilized and reached a safe distance from the host aircraft.

Shuttlecock body, retention cord and separation springs – The shuttlecock body is composed of two halves [see Figure 80] which clamp on to the aft of the motor case. It carries the laser and laser power supply. The halves are held together by a retention cord. When the cord is cut, separation springs drive the two shuttlecock body halves apart, releasing them from the motor. Flame channels in the shuttlecock direct exhaust gas from the motor onto the retention cord in order to break it after motor ignition.

5.6.3 Ignition sequence

The ignition sequence proceeds in three steps, as depicted in Figure 79. First, the laser fires through the nozzle onto the starter grain, causing it to ignite. As the starter grain burns, it brings up the chamber

[22] NUBM44 laser diodes from Nichia Corp. were used in this research.

pressure and temperature, and ignites the main grain. Hot gas begins to flow out of the nozzle into the shuttlecock body. There, it travels through two flame channels, which route the gas over the retention cord. This melts the retention cord and release the two halves of the shuttlecock, which spring apart and fall away from the vehicle. To endure reliable operation, the rendition cord is exposed to the flame at two redundant locations: if either one is cut, the shuttlecock will separate.

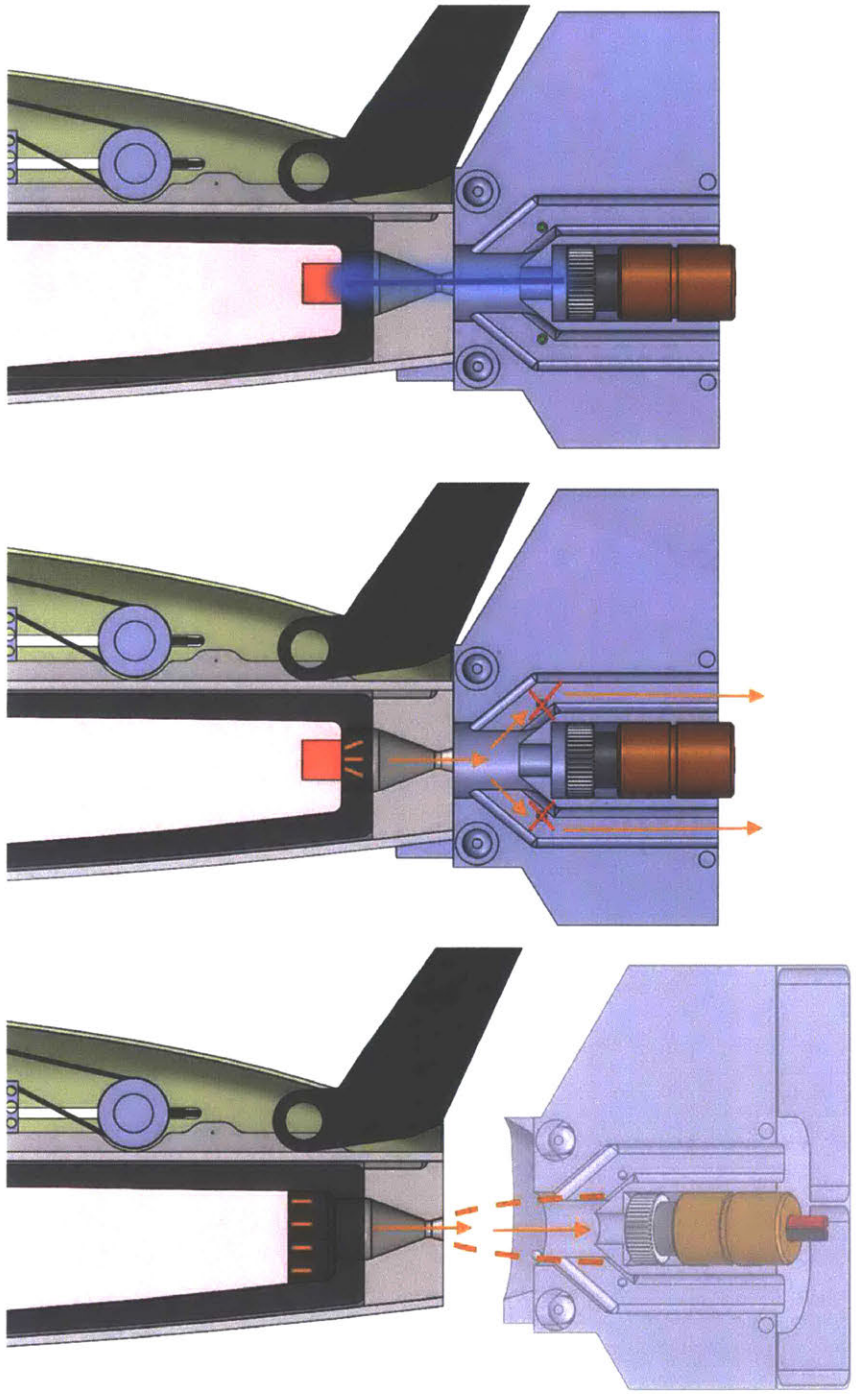

Figure 79: The ignition sequence. Top: the laser ignites the starter grain. Middle: the starter grain burns, igniting the main grain and cutting the retention cord. Bottom: The main grain burns and the shuttlecock falls away.

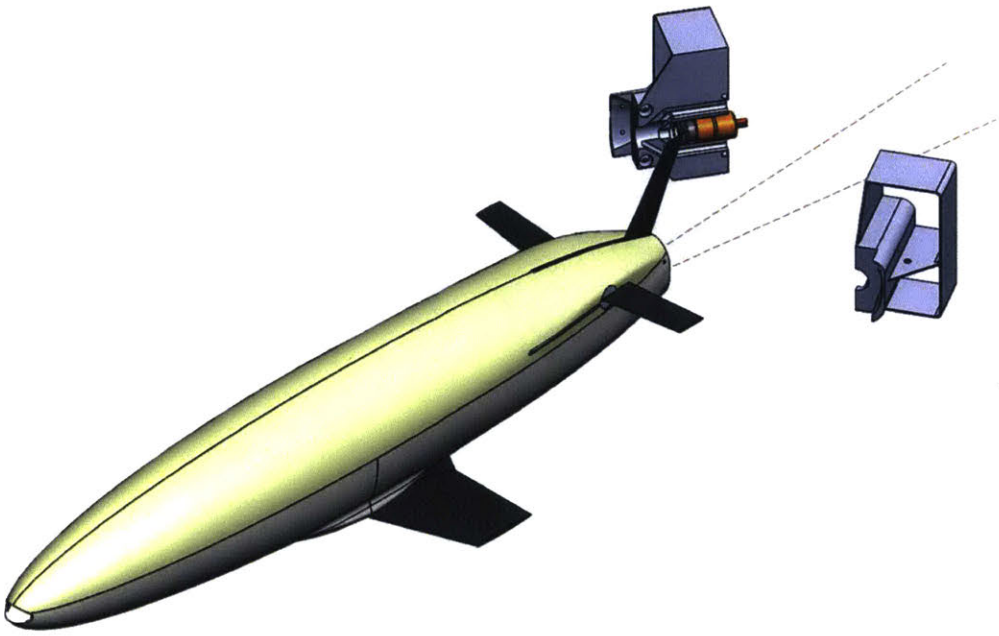

Figure 80: The shuttlecock and ignition system fall away from Firefly after the motor ignites.

6 Production

This chapter presents the production process used to make the Firefly rocket motor. The production process as described can produce the motor design described in the previous chapter. However, the process is in a pathfinding stage of development: it is currently labor intensive, and there is ample room for cost-reducing process improvements.

The first three sections detail the major steps of motor production: printing the motor case, casting the propellant grain and thermal liner, and casting the nozzle. Each section justifies a choice of manufacturing technique, lists the steps of the procedure, and describes the tools used. The fourth section describes assembling these components into a finished motor.

6.1 Motor case production

The motor case is made from Titanium alloy Ti-6Al-4V and is fabricated via additive manufacturing (printing). We need a manufacturing process which can produce the thin, complex geometry of the motor case from a difficult-to-work material. We must be able to do so at a reasonable price, with quick lead times and flexibility to design changes.

The shape and material of the motor case drives the choice to use additive manufacturing. Alternative manufacturing techniques (extrusion, milling, and casting) are less suited to this application. Manufacturing by extrusion is precluded by the complex, tapered geometry of the motor case. Milling from bar stock would be prohibitively expensive and time consuming, given the large material removal and difficulty of cutting titanium.

Casting is a viable alternative, but would be more difficult and expensive than printing. The motor case is a difficult shape to cast: it is thin (1.5 mm / 0.060 inch walls) and high aspect ratio (6:1). Similarly thin and high-aspect parts have been successfully investment cast from Ti-6Al-4V, but special techniques are required [67].

The strength of a typical casting is worse than that of a printed part. Flawless cast Ti-6Al-4V has comparable strength to forged product, but the presence of casting defects typically reduces the strength [67]. To account for these defects, the design's safety factor is multiplied by an additional casting factor, usually between 1.5 and 2.0. Only a few, premium-quality foundries can cast to a casting factor of 1.0 [67], and it is unclear whether this is possible for very thin parts. By contrast, Renishaw's Ti-6Al-4V prints come very close to forged strength [65]. To use casting instead of printing, we would need to either thicken the case walls (increasing vehicle mass) or pay extra for a premium casting.

Casting also is likely to have higher set-up costs and longer lead times than printing. The rapid flexibility of printing is appealing at the current early prototype stage. Additionally, it is likely that printing will also be the right choice for future volume productions runs: additive manufacturing technology is rapidly maturing, and costs should continue to fall in the coming years.

The following subsections describe the additive manufacturing system used, and explore details of how the design was adjusted and tested for compatibility with additive manufacturing.

Printing services and design-for-manufacturing consultation were provided by Renishaw plc. Motor case prototypes were produced on Renishaw's AM400 laser powder bed fusion printer.

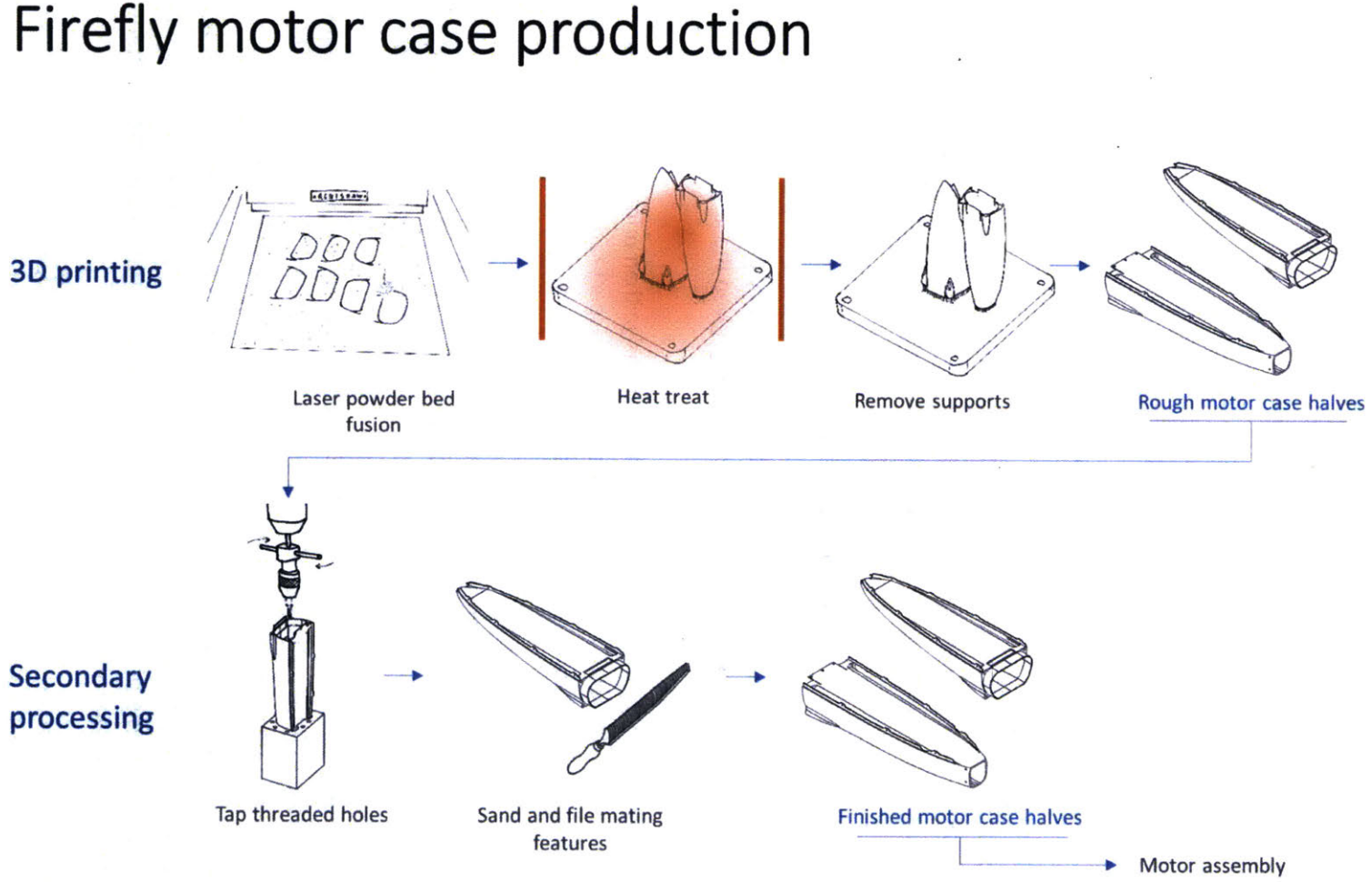

Image credit: File – Directorate of Employment and Training, Gujarat State.

Figure 81: The motor case halves are produced by 3D printing, followed by a few post-processing steps.

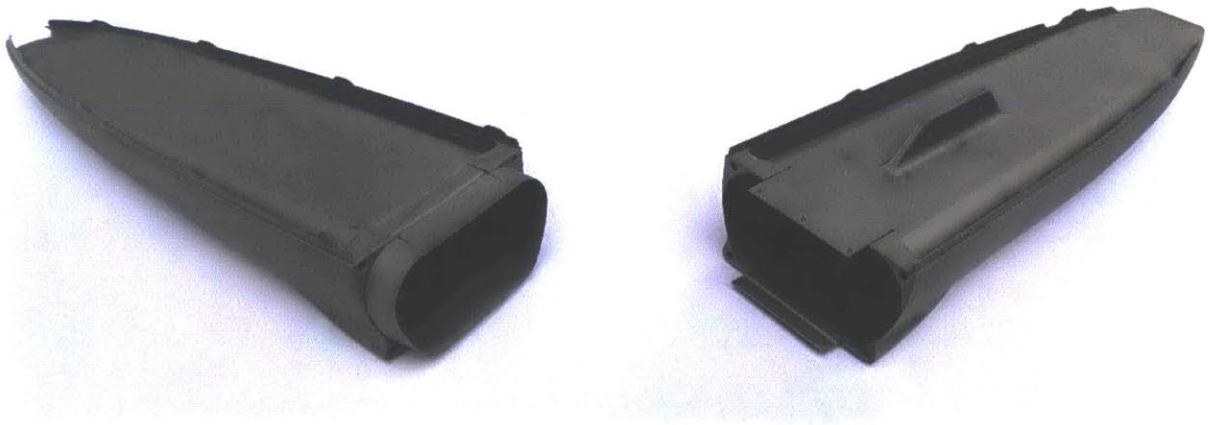

Figure 82: A printed motor case. This motor case has an additional bracket on the aft half, which mounts the motor to a load cell for static fire testing.

6.1.1 Case production procedure: Additive manufacturing and post-processing

Laser powder bed fusion – First, near net shape parts are printed from titanium powder via laser powder bed fusion. This process is carried out autonomously by the printer, although significant upfront human effort is required to calibrate and program the machine for a particular build.

The parts are printed onto a build platform in horizontal layers. The printer spreads a layer of powder across the platform, and a laser beam traces out a horizontal "slice" of the part onto the surface of the powder. The powder in the laser's path is heated, and fuses into a solid by melting or sintering. Then, the printer moves the build platform down by a small increment (tens of microns), spreads a new layer of powder, and fuses the powder onto the preceding layer. This process is repeated thousands of times until the part is built to its full height.

This process was performed on a Renishaw AM400 additive manufacturing system [68] [Figure 83]. Renishaw's precise laser, environmental control, advanced software and powder feedstock enable the high print quality demanded by the motor case.

This printer uses laser powder bed fusion to produce parts from a metal powder. The AM400 features a 400 W laser with a 70 µm spot size. The small spot size and high laser power enable fine features to be printed in high melting point alloys.

The AM400 prints in an inert atmosphere: before the print begins, the sealed build chamber is evacuated and then back-filled with 1 kPa (gauge) of high-purity argon [69]. The clean, inert atmosphere prevents oxide defects from forming in the part.

Figure 83: Left, the Renishaw AM400 printer. Right, the printer's laser fuses a Firefly motor case prototype. Photo credit Renishaw plc [69].

Renishaw's build preparation and control software enables faster and higher quality builds [69]. Three exposure parameters adjust the quality of the print: laser power, exposure time, and point distance (the spacing between points where the laser dwells). The build preparation software identifies three different types of region in each layer the part, and sets different exposure parameters for each region type:

1. *Volume hatch* regions are the interior of the part. Here, a high laser power and short exposure time is used to reduce build time.
2. *Contour* regions are the perimeter of each layer. Contours are traced with lower laser power and closer point distance to "give better detail and surface finish" [69].
3. *Downskin* regions have powder beneath them, not fused metal. Downskin regions heat up more quickly because the powder is less thermally conductive than fused metal.

Our parts were printed from a high-quality titanium powder feedstock. The powder metallurgy conforms to the standard for titanium alloy Ti-6Al-4V Extra Low Interstitial (ASTM B348, Grade 23) [69]. The nominal particle size range is 15 to 45 μm, and 95% of the powder (by mass) is within this range [69]. The powder's apparent density is 2.52 g cm^{-3} [69].

After the print is completed, the printed parts are extracted from the powder bed. At this point, the parts are still welded to the build platform by support material [Figure 84].

Figure 84: Near net shape parts emerge from the printer welded to a build platform by support material. Photo credit Renishaw plc [69].

Heat treating – The parts are then heat treated [Figure 85]. The heat treatment relaxes residual stresses from the fusion process and greatly improves the ductility of the material, at a very small strength penalty [69] [70]. To prevent oxidation and the formation of alpha case, the heat treatment is performed in an inert (argon) atmosphere. The heat treating schedule used on the Firefly case prototypes was:

1. Evacuate furnace chamber and backfill with Ar.
2. Heat to 620 K at a rate of 5 K min^{-1}.
3. Hold at 620 K for 60 min.
4. Heat to 1120 K at a rate of 8 K min^{-1}.
5. Hold at 1120 K for 60 min.
6. Allow furnace to cool naturally to 370 K or below.
7. Open the furnace chamber and remove parts.

Figure 85: Motor case parts are loaded into a gas-tight chamber and placed in a furnace for heat treatment. Photo credit Renishaw plc [69].

Support removal – After heat treatment, the parts are cut off of the build platform with a saw [Figure 86]. Then, the remaining support material is cut off using a belt sander and hand tools [Figure 87].

Figure 86: A saw cuts through support material to remove the parts from the build platform. Photo credit Renishaw plc [69].

Figure 87: A belt sander is used to remove support material from the part. Water cooling is required to prevent overheating because of titanium's poor thermal conductivity.

Secondary processing - The motor case requires secondary processing after printing to create fine mechanical features, as is typical of additively manufactured parts [70]. The following secondary operations are required:

- Tap 4x 2-56 threads for the mid-case joint axial screws.
- Tap 6x 000-102 threads for the mid-case snap tab screws.
- Tap 14x 0-80 threads for the top shell retaining screws.
- File the locking features of the mid-case snap tabs to a clean edge.
- Sand the mating faces of the mid-case joint to a smoother surface finish.

Tapping these holes requires care and craftsmanship. Titanium is hard to cut because of its high hardness and low modulus of elasticity. The hardness problem can be exacerbated by alpha case, a hard oxidized layer which forms if the part is heated in an atmosphere containing oxygen [70]. The mid-case joint axial screw holes are deeper and therefore more difficult to tap; for these we use a jig to hold the case upright in a tapping stand. The mid-case snap tab screws and top shell retaining screws are through thin walls (only 3 or 4 threads thick), and are therefore easier to tap. These are done with a handheld tap. In all cases, a steady hand and plenty of lubricant are required.

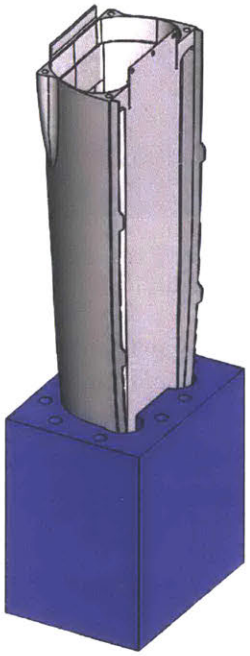

Figure 88: A jig hold the motor case aft half for tapping.

The mid-case joint axial screws carry a moderate tension load, so their holes are reinforced with helical inserts. There is a corrosion risk with the inserts: they are made from (non-passivated) 18-8 stainless steel, which has a significantly different electrochemical potential from titanium [71]. To mitigate this risk, we use fluoropolymer coated inserts.

6.1.2 Design for manufacturing

We designed the motor case to be compatible with the printing process. To be reliably manufactured via powder bed fusion, a part should:

- have no horizontal overhangs larger than 1 mm [69],
- have no large overhangs at a slope shallower than 30 degrees [69],
- have smooth variations in horizontal cross sectional area (this helps to reduce internal stresses) [69],
- and avoid large solid blocks (this also helps to reduce internal stresses) [70].

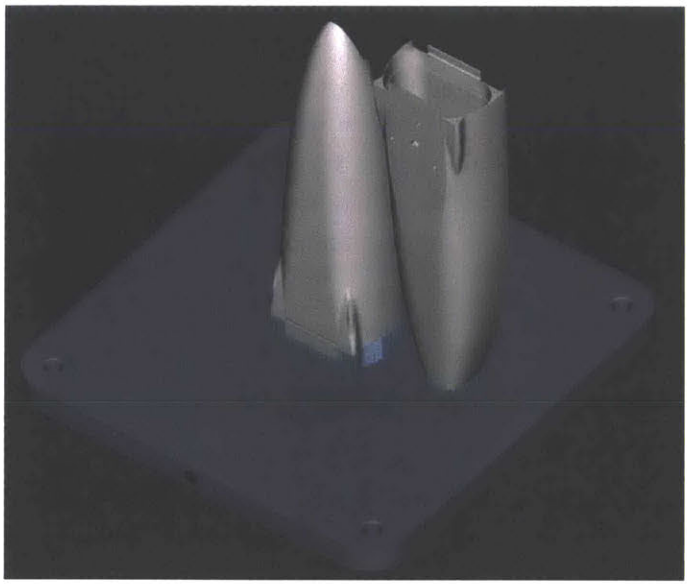

Figure 89: In a "vertical" orientation the motor case (light grey) has no extreme overhangs, and only requires a few supports (blue) around the base of the parts. Graphic credit Renishaw plc [69].

The build orientation of the motor case is chosen to avoid overhangs and minimize the use of supports. The strength of the material in different directions only varies by a few percent [65], so expected stress states are not an important consideration in the choice of build orientation. A "vertical" orientation (vehicle fore-aft axis parallel to printer z-axis) has no extreme overhangs, and minimizes the required supports. Unfortunately, this orientation increases the build height (and therefore the cost) compared to printing with the fore-aft axis horizontal.

Once the major build orientation was chosen, we designed the details of the case to be printable in that orientation. We filleted corners and added support fins to avoid overhangs and smooth the changes in cross-sectional area. Examples of these changes are shown in Figure 90 and Figure 91. The wing interface features, several pegs which stick out of the bottom of the case, have unacceptable overhang in the chosen build orientation [Figure 90]. As a remedy, support fins were added below the pegs. These are subsequently removed with a file. The original design of the fairing attachment tabs had corners which were unacceptably sharp for the printing process [Figure 91]. The design was modified for compatibility with printing by filleting these corners.

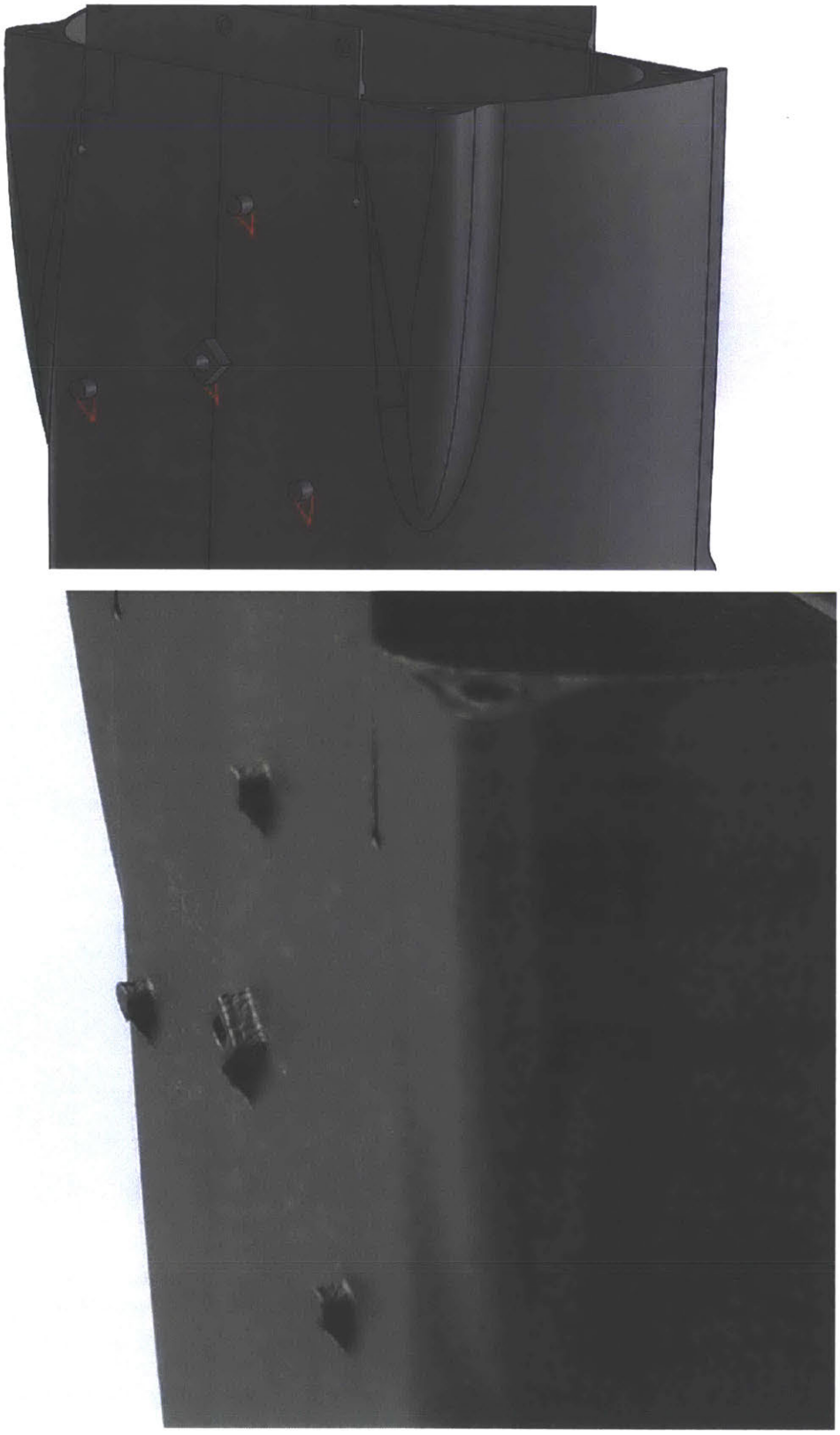

Figure 90: Support material was added to the wing interface features. Top: the wing interface features have unacceptable overhangs, marked in red. Bottom: The as-printed part has small support fin below each of these features.

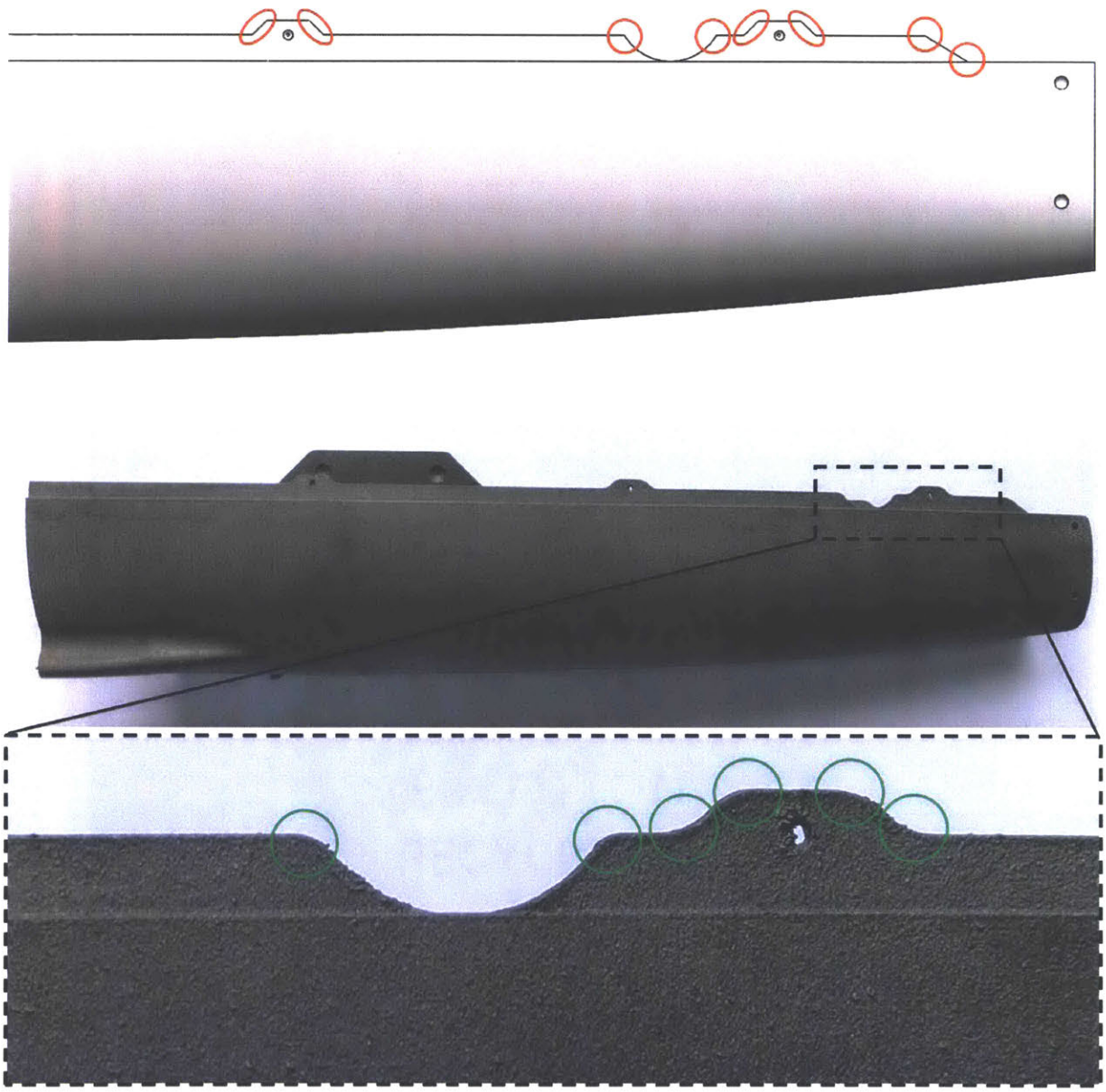

Figure 91: The fairing attachment tabs were filleted. Top: the original design had corners which were unacceptably sharp for printing, marked in red. Bottom: the printed part has filleted corners, marked in green.

6.1.3 Printing fine, highly-loaded features: the mid-case snap joint

The mid-case snap tab joint has very small features, and pushes the limits of precision for powder-bed fusion. Some of the snap tab features are as small as 250 µm (only 3.5 times the AM400's laser beam diameter), and there is only 100 µm nominal clearance between the mating faces.

These fine features required some experimentation to achieve a proper fit. We printed three test articles of the joint with different offsets on the mating geometry. We found that (with various amounts of sanding) all three articles would snap together [Figure 92].

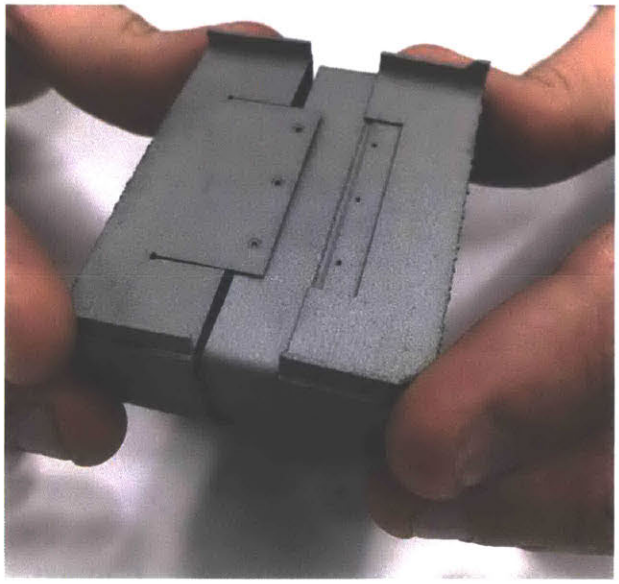

Figure 92: We printed several test articles of the mid-case snap-fit joint to determine the proper tolerances. Photo credit Renishaw plc [69].

Structural testing indicated that the joints were strong enough to carry the expected loads due to chamber pressure. The internal pressure load on the joint can be roughly approximated as an axial tension component, plus a radial component which causes the flat top and bottom of the joint to bow out. We expect an axial load of 2.2 kN (500 lbf) and a bowing deflection of 4 mm (0.15 inch)[23] at the nominal chamber pressure of 1.4 MPa (200 psi).

We simulated this load state using a universal testing machine and jack screws [Figure 93]. The sample was mounted on a pair of aluminum forks, which allowed it to be attached to the actuators of a universal testing machine. A pair of jack screws bowed the joint to the expected deflection [Figure 94]. In the bowed condition, the joint held an axial load of 3.3 kN (750 lbf, 1.5 times the expected load) without significant deformation.

[23] We used the Solidworks Simulation finite element analysis tool to predict the bowing deflection.

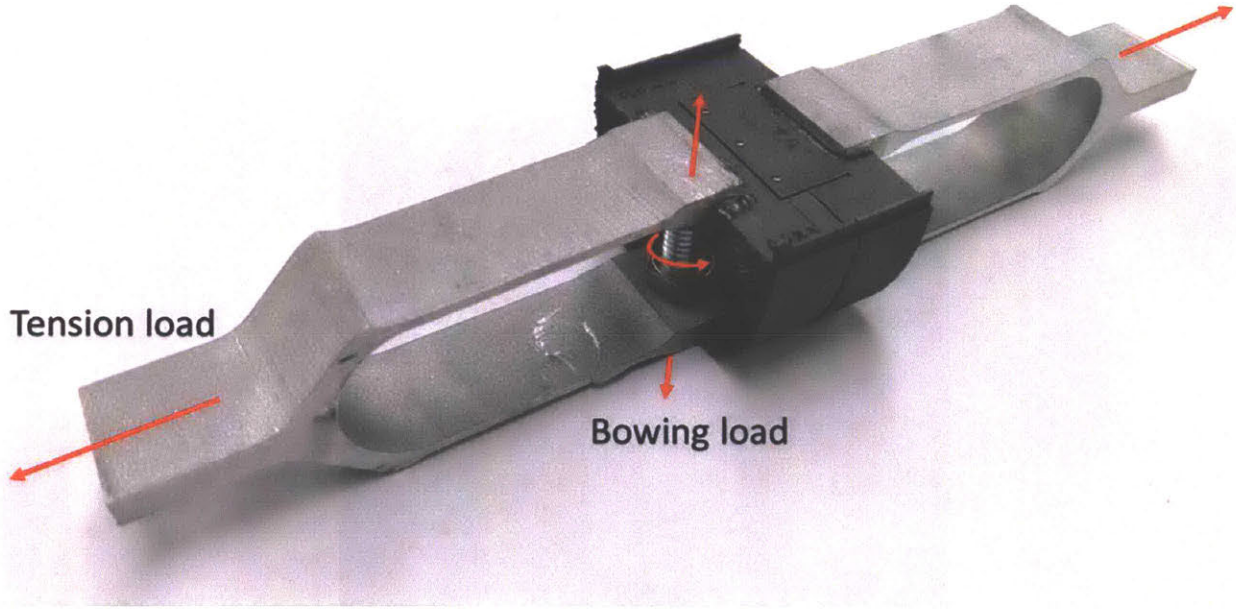

Figure 93: Tensile tests were performed on the mid-case snap-fit joint test articles. A tension load was applied to the articles with a universal testing machine, and a bowing load was applied with jack screws.

Figure 94: A joint test article, bowed to 4 mm deflection by jack screws.

6.2 Propellant and liner production

The internals of the rocket motor consist of a solid propellant grain wrapped in layers of inhibitors and thermal insulation, called the propellant package. Mechanically, the components of the propellant package are all composites bound by thermosetting polymers. We chose to produce the propellant package by a series of layups and castings; these are the preferred methods for making shells and solid parts from polymer composites.

This section describes the layup and casting procedure, which is illustrated by the flowchart in Figure 95. First, the inhibitor shells are produced by laying up fiberglass and epoxy in a mold. The inhibitor shells will surround the propellant grain and inhibit its outside edges from burning. Next, batches of propellant are mixed and cast into a mold, which is lined with the inhibitor shells. Because the inhibitor shells were made as four separate parts, the inhibitor layer on the propellant grain now has seams, which must be patched. Next, the inhibited propellant grain is loaded into a slightly larger mold, and the ablative liner is cast around it by injecting resin into the gap between the mold and the propellant grain. Then, a starter grain is installed in the aft end of the propellant grain. The propellant grain and liner are then radiographically inspected for voids. Finally, the propellant grain and liner are wrapped in fibrous insulation. This completes the propellant package, which is then sent to motor assembly.

The following subsections describe each step of this procedure in more detail.

Firefly propellant and liner production

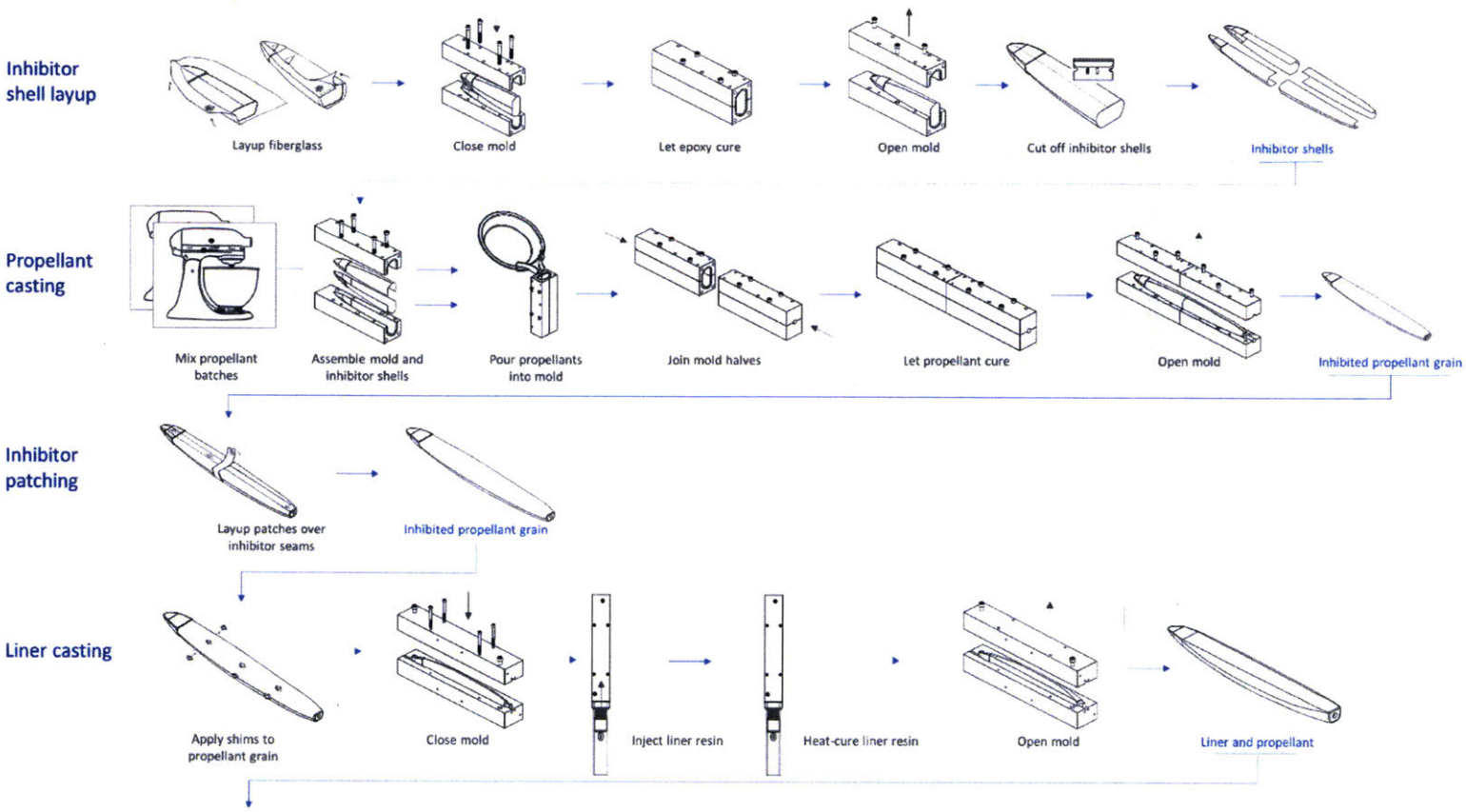

Continued on next page...

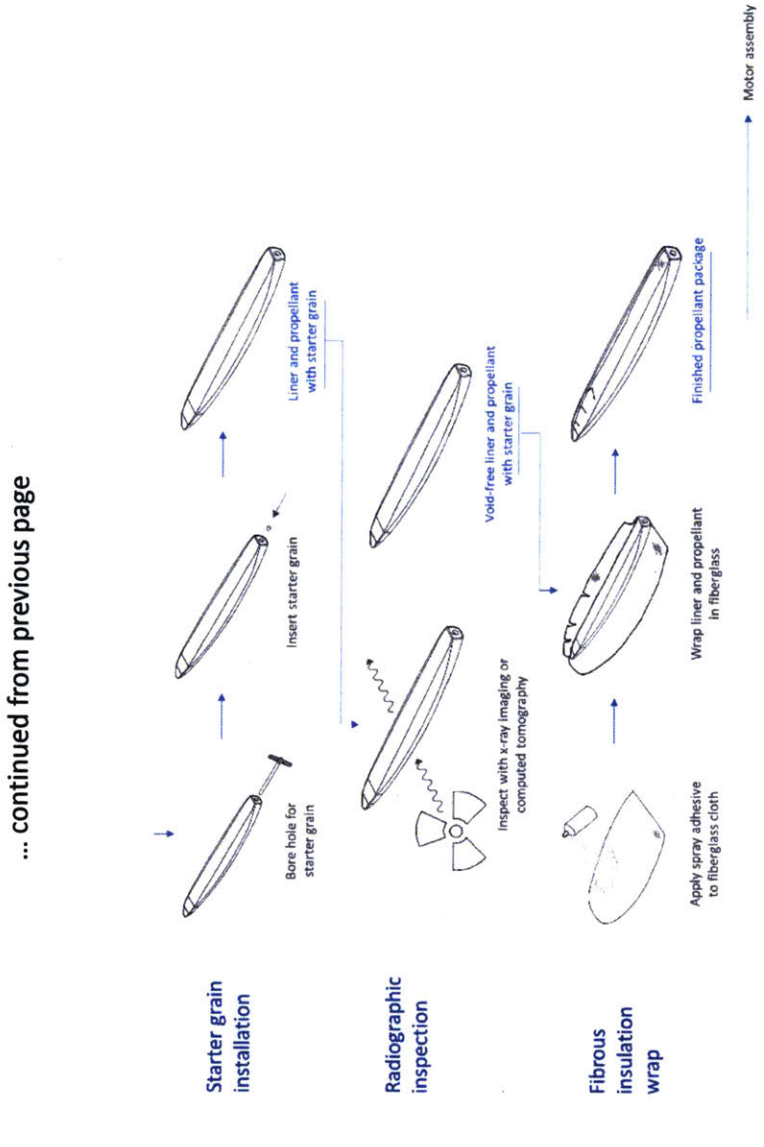

Figure 95: The propellant package consists of the propellant grain surrounded by layers of thermal insulation. It is produced by a complex series of layups and castings.

6.2.1 Inhibitor shell layup

The inhibitor is a thin shell of fiberglass which surrounds the propellant grain. It inhibits the sides of the propellant grain from burning and acts as a release layer to help demold the propellant grain from the propellant mold.

The inhibitor is made via a mold-and-plug layup. First, a patch of light fiberglass (1.4 ounce yard^{-2}) is wetted with epoxy (Hexion MGS 285 [72]). The fiberglass is folded around a silicone plug [Figure 96]. The plug has the geometry of the front half of the propellant grain. The plug is laid on the cloth with its fore-aft axis oriented 45 degrees to the fiber weave. A few slits need to be cut in the cloth so that it folds smoothly over the plug. Second, the forward half of the propellant mold is closed around the plug. The mold is coated with mold release before use. This process is then repeated for the aft half.

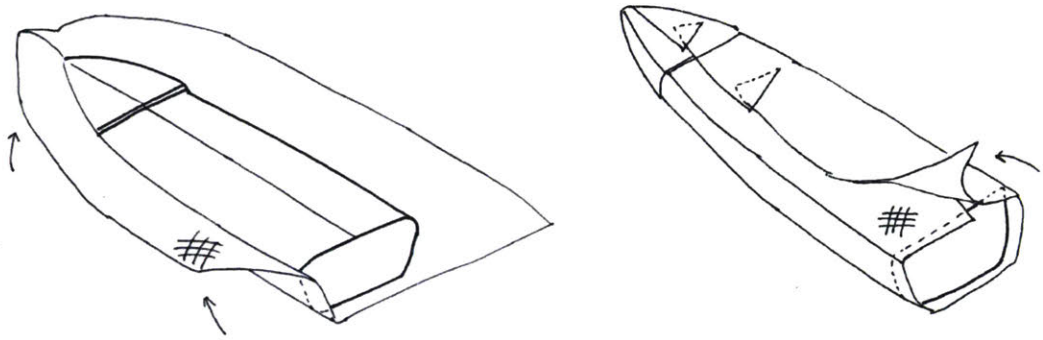

Figure 96: During the inhibitor shell layup, wet fiberglass is wrapped around a plug.

Once the epoxy has cured, the molds are opened [*Figure 97*]. The fiberglass shells are cut along the left-right symmetry plane, using a razor blade. This allows the inhibitor shells to be peeled off the plugs. The result of this process is four fiberglass inhibitor shells, matching the four quarters of the propellant mold.

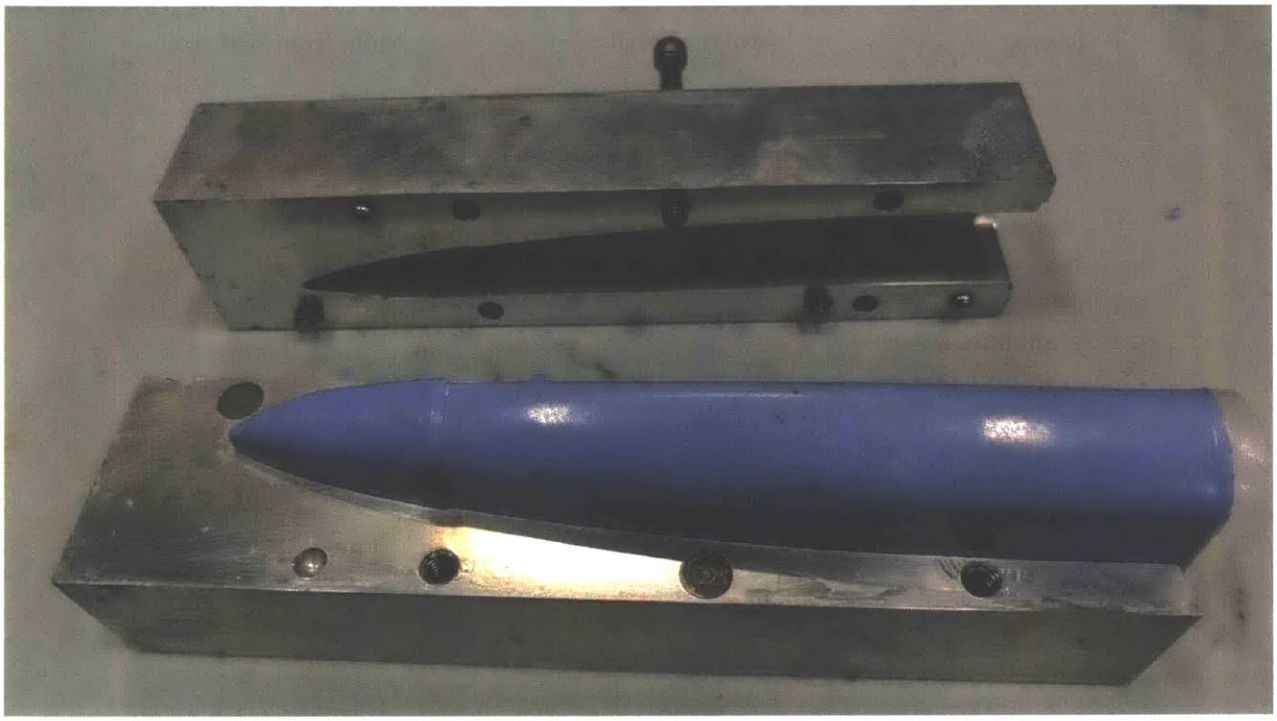

Figure 97: The propellant mold is opened to reveal a cured inhibitor shell on the silicone plug.

6.2.2 Propellant casting

The next step is the production of the propellant grain. This involves mixing several batches of ammonium perchlorate composite propellant, casting them into a mold, allowing the propellant to cure, and then de-molding the propellant grain. We use a special process in which different batches of propellant are cast on top of each other in the same mold [Figure 98]. This creates a segmented, variable burn rate grain with strong bonds between the segments.

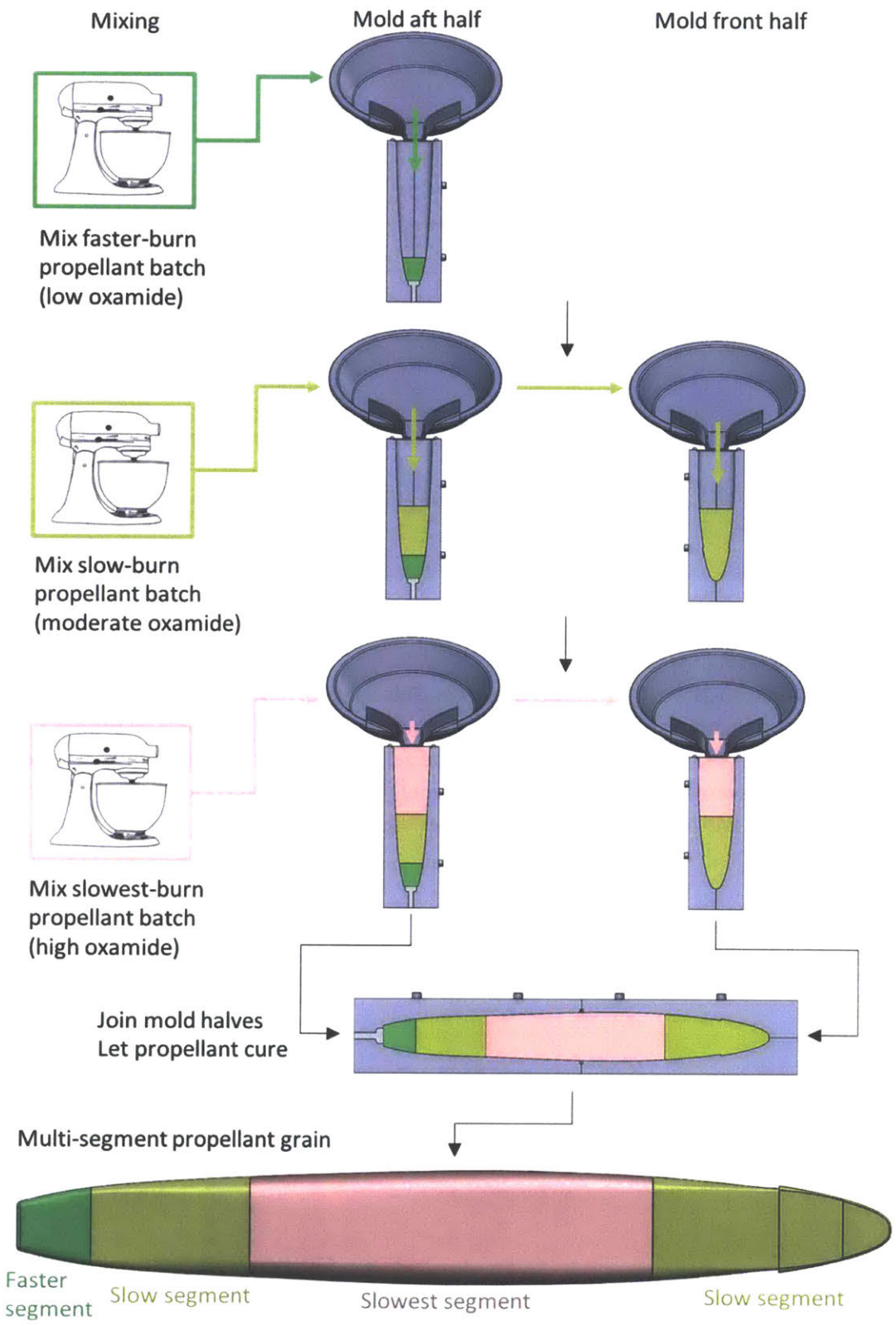

Figure 98: A multi-segment grain is produced by pouring different batches of propellant into a mold.

Mixing - First, the propellant is mixed. Mixing is done under vacuum to improve the relative density of the propellant. Rather than using a specialized vacuum mixer, we run an off-the-shelf kitchen mixer inside a vacuum chamber. This reduces equipment costs by an order of magnitude.

The propellant's binder, hydroxyl-terminated polybutadiene, is treated with an antioxidant (CAO-5, 1 phr) and a bonding agent (HX-752, 2.4 phr). The bonding agent creates bonds between the binder and AP particles, improving the strength and hardness of the propellant. The binder is cross-liked by a modified methylene diphenyl diisocyanate (MDI) curative.

The propellant formulation is designed to be castable. It has a moderate solids loading (80.% by mass). Also, it includes additives to aid mixing and pouring: a plasticizer (Isodecyl pelargonate, 41 phr), processing agent (castor oil, 2 phr), and surfactants (polydimethylsiloxane oil and Triton X-100, < 1 phr).

Ammonium perchlorate particles are screened for size with sieves, weighted out, and added to the propellant mixture.

The binder, MDI and AP are supplied by Rocket Motor Components, Inc. of Cedar City, Utah. Other propellant ingredients are supplied by Sigma-Aldrich of St. Louis, Missouri.

Casting – The propellant grain has several segments, with each segment having a different concentration of the burn rate suppressant oxamide. To produce a multi-segment grain, several batches of propellant are mixed, and then poured sequentially into the propellant mold. This process is illustrated in Figure 98. First a small batch of faster-burn propellant (e.g. 2% oxamide) is mixed, and the correct amount (by weight) is poured into the aft mold. Then, a batch of slow-burn propellant (e.g. 8% oxamide) is mixed, and the appropriate weight poured into both mold halves. Finally, a batch of slowest-burn propellant (e.g. 12% oxamide) is mixed and poured. The two mold halves are then joined together, and the propellant is allowed to cure. The resulting propellant grain has four segments of different burn rate: fast, slow, slowest, and slow. Good bonds are achieved between the segments because the propellant is still wet and sticky when the next batch is poured on top of it [Figure 102]. When this grain is burned, it will produce the desired thrust curve described in Section 5.1.

A four-part mold is used to cast the propellant into a grain of the proper shape [Figure 99]. The propellant is split into quarters; the front-aft split plane provides an opening to pour propellant into, while the port-starboard split plane is used to demold the propellant grain. The forward and aft halves of the mold each have 4 joining screws to hold the quarters together and 3 parting screws to jack them apart. A large clamp (not shown) is used to join the forward and aft halves, and alignment balls ensure that they are joined in the correct position.

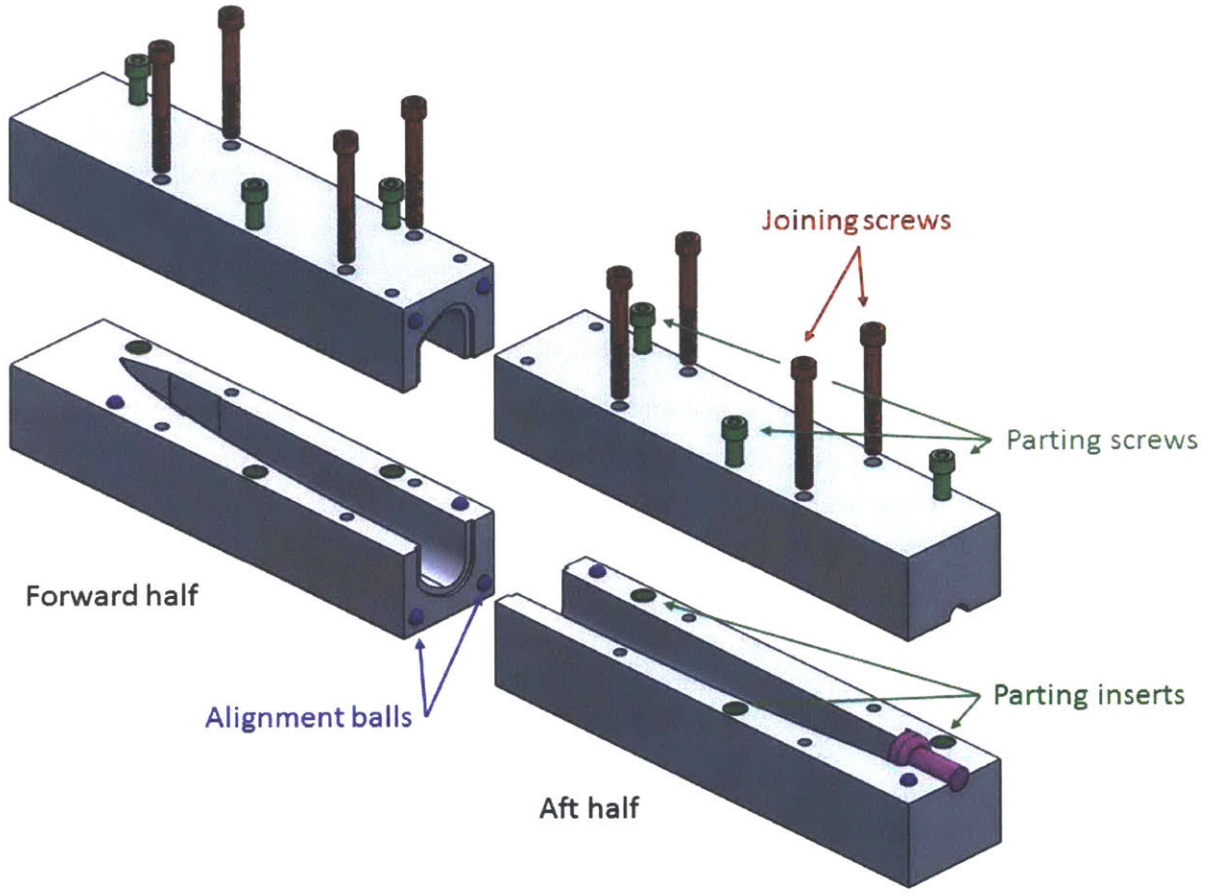

Figure 99: The propellant mold is used to cast the propellant grain and inhibitor shells.

To perform the casting, the molds are first coated with a solid-film release agent. Then, the inhibitor shells are inserted into the molds and lightly bonded to the release film [Figure 100]. The insides of the inhibitor shells are then coated with curative; this bonds the propellant to the inhibitor shells by cross-linking the HTPB to -OH groups in the epoxy. The two forward quarters are then mated together using their joining screws, as are the two aft quarters.

Figure 100: The front quarters of the propellant mold, coated with release agent (black) and containing the inhibitor shells (white).

Next, the propellant batches are poured into the mold halves, in the order described above. The propellant is very viscous (roughly 10^5 Pa s), so a vibrating platform is used to shake the mold and accelerate pouring [Figure 101].

Curing – After the propellant is cast, it is left to cure. The curing reaction occurs at room temperature and takes 24 to 48 hours.

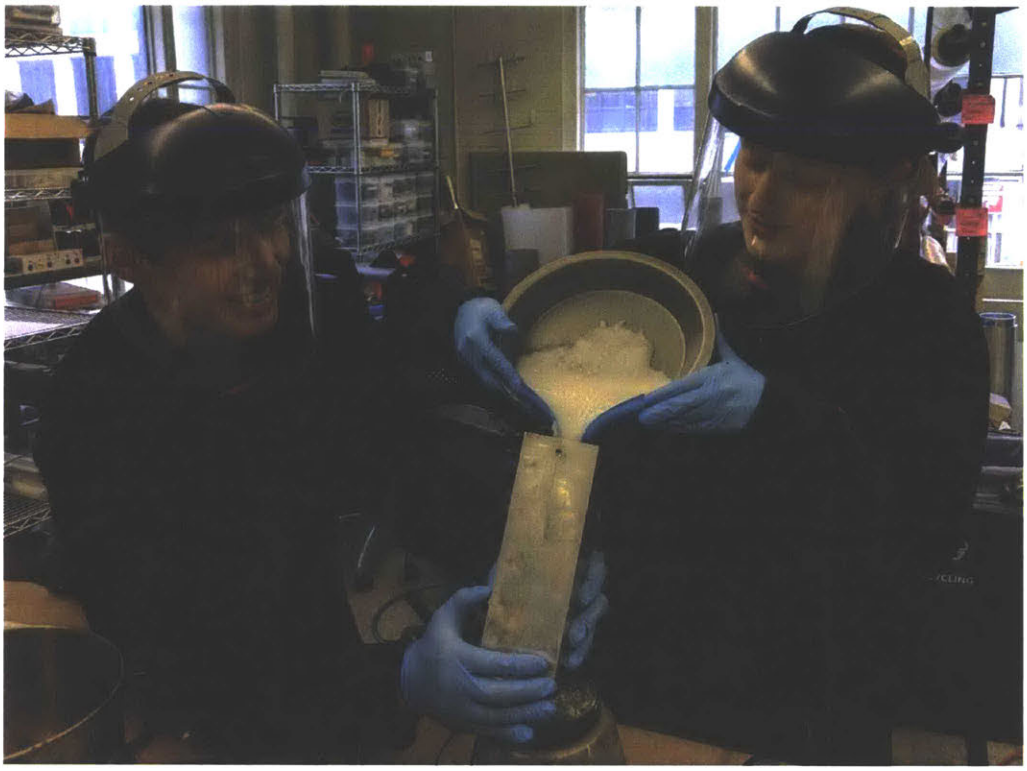

Figure 101: Researchers pour propellant into a mold. This photo was taken during a pathfinder casting with inert propellant; the propellant is white to signal that it is inert.

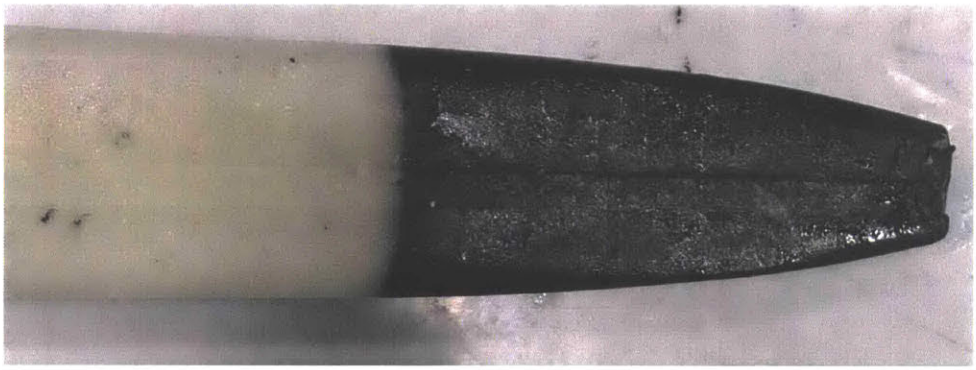

Figure 102: Example of a bond line between two propellant segments. To improve the visibility of the bond line, the left segment is made from a white (inert) propellant.

De-molding – Finally, the mold is opened and the propellant is removed. The propellant is tenaciously sticky (because of the HX-752 bonding agent), so proper precautions must be taken to enable easy de-molding. The inhibitor shells largely contain the propellant and prevent it from sticking to the mold. However, some binder does leak through the (semi-porous) inhibitor shell, so mold release is also used. The mold quarters are jacked open using parting screws [Figure 103].

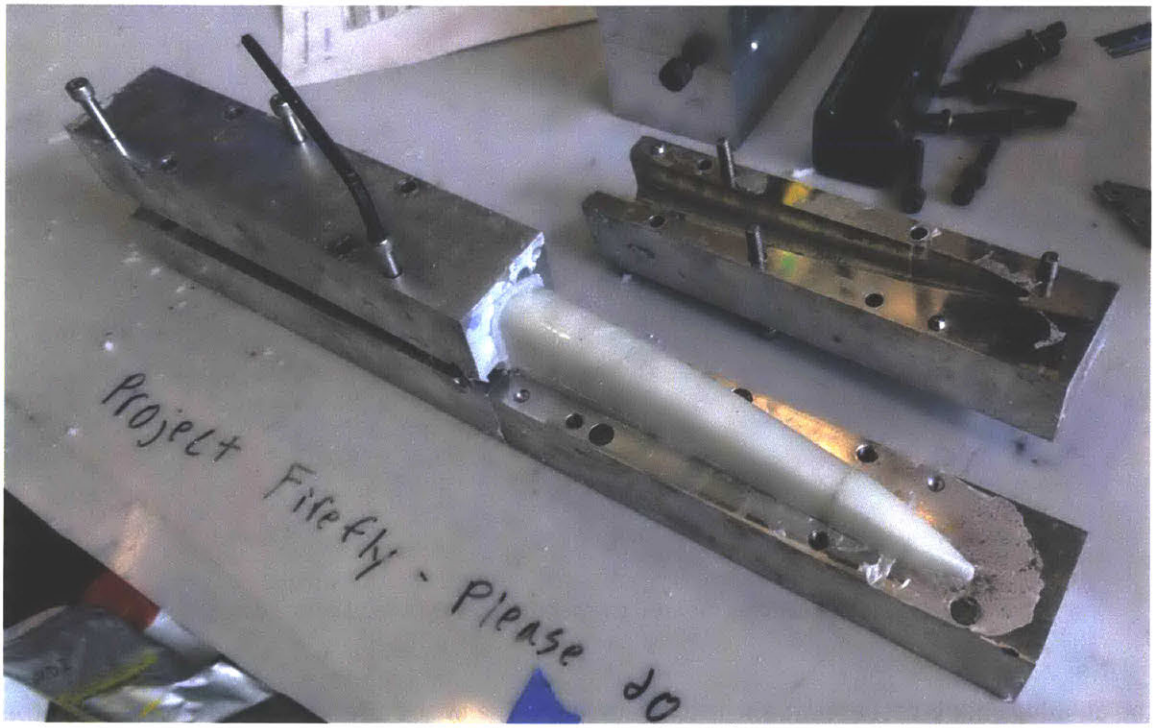

Figure 103: The propellant mold is opened using the parting screws. This photo was taken during a pathfinder casting with inert propellant; the propellant is white to signal that it is inert.

After the propellant is removed from the mold, the molds are cleaned. We peel off the remnants of the release film, and then clean the molds with mineral spirits in an ultrasonic cleaner.

6.2.3 Inhibitor patching

The previous steps left seams in the inhibitor, which must now be patched. Strips of fiberglass cloth are cut, wetted with epoxy, and laid over the seams.

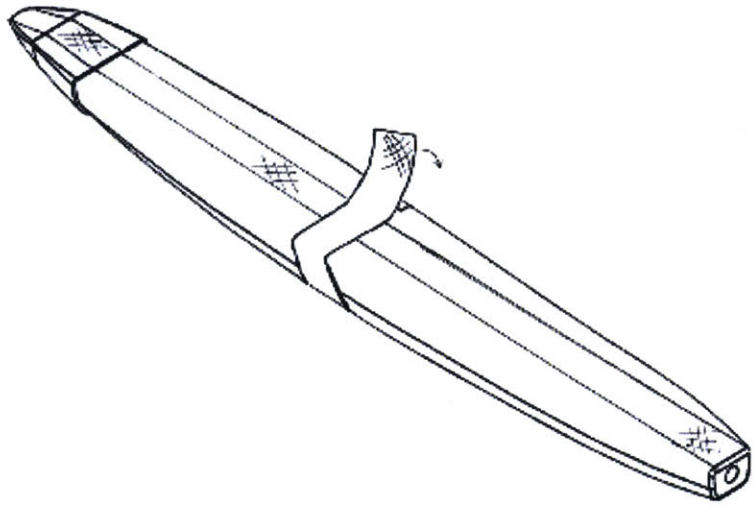

Figure 104: The seams between the inhibitor shells are patched with fiberglass and epoxy.

6.2.4 Liner casting

Next, the ablative liner is cast around the propellant grain. The liner protects the motor case and other vehicle systems from the heat of propellant combustion. It is made from a silicone-based ablative material, supplied by the Dow Corning Corp. of Midland, Michigan. The liner is produced by injecting the ablative material resin into a void between the propellant grain and the liner mold.

First, shims are applied to the outside of the propellant grain [Figure 105]. The shims control the thickness of the liner by ensuring that the propellant grain is properly positioned within the liner mold [Figure 106]. Because the liner thickness is tapered, thicker shims are used at the aft end of the propellant grain, and thinner whims at the front. The shims are cut from ablative material (previously cured), so their presence does not affect the thermal properties of the liner. They are bonded to the propellant grain with cyanoacrylate.

Figure 105: Applying shims to a propellant grain in preparation for liner casting. This photo was taken during a pathfinder casting with inert propellant; the propellant is white to signal that it is inert.

Figure 106: The shims control the gap between the propellant grain and the liner mold, thereby setting the thickness of the liner. This photo was taken during a pathfinder casting with inert propellant; the propellant is white to signal that it is inert.

Next, the propellant grain is placed in the liner mold, and the mold is closed. The mold is depicted in Figure 107. It parts along the vehicle's port-starboard symmetry plane. This parting orientation minimizes the depth of the mold and avoids negative draft (although some faces have zero draft). The liner mold has four sprues on its bottom face (right side of Figure 107) through which resin is injected. There is a single riser on the top face (left side of Figure 107).

The liner mold assembly includes several components for joining, aligning, and parting the mold halves. Four joining screws (shown in red) hold the two mold halves together, and an alignment pin and ball (blue) ensure that the halves mate together in the correct position. A support pin (pink) is included to help hold the propellant in place in the mold (along with a set of shims, which are not shown). During de-molding, the mold halves can be jacked apart by using two parting screws (light green) to push on inserts (dark green) in the opposite half.

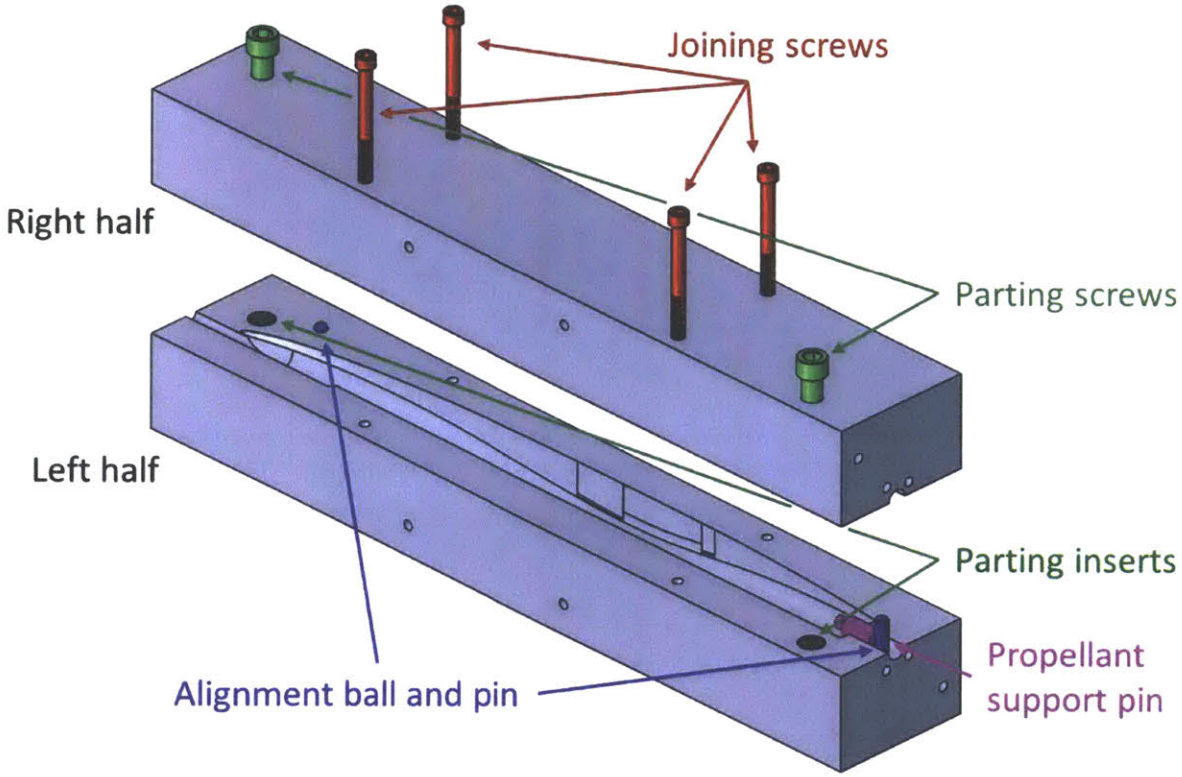

Figure 107: The liner mold is used to cast a thermal protection liner around the propellant grain.

After the mold is closed, the ablative material resin is injected into the mold. To perform the injection, the mold is placed on a vertical stand, and a cartridge filled with resin is attached to the bottom of the mold. The mechanical design of the mold and cartridge apparatus is presented in Figure 108 and Figure 109; Figure 110 shows the actual hardware.

The cartridge consists of a plate (shown in pink in Figure 108) and a tube (clear). A plunger (cyan) slides within the cartridge tube. To inject resin, resin is loaded into the cartridge above the plunger. The cartridge is mounted onto the mold, and the mold is evacuated by attaching a vacuum pump to the riser outlet. This creates a pressure imbalance across the plunger, pulling it up the tube. As the plunger rises, it pushes the resin through the sprues and into the mold. The injection takes about 10 minutes.

However, this process must be followed by a compression step to eliminate voids from the liner. If the resin were an inviscid fluid, the fluid's surface level would rise smoothly through the mold and no voids would be introduced. However, the resin is highly solids-loaded, and its consistency is akin to that of a

wet hairball. The resin appears to be shear-thinning; under a moderate pressure gradient it will flow well through an orifice (i.e. the sprues). However, in a lightly stressed state the resin is very viscous, and will support ridges in its surface against gravity. Scooping the resin into the cartridge leaves ridges in the surface; when the injection is performed these ridges fold over themselves, trapping voids in the resin. Because the injection is performed under vacuum, these voids contain very little gas, so applying moderate pressure (~0.4 MPa) to the resin crushes the voids to a negligible size. To apply this pressure, the riser is sealed off. Then, a plug (yellow in Figure 108) is inserted into the end of cartridge tube, and the space between the plunger and plug is pressurized with air.

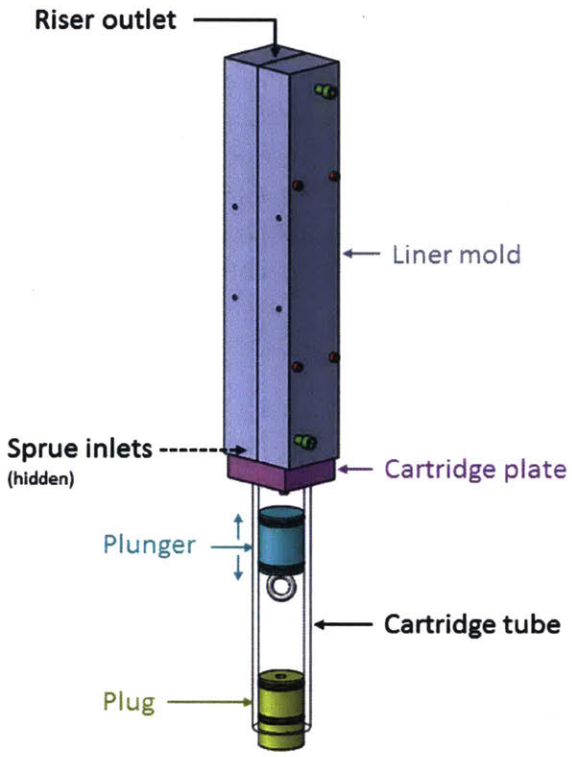

Figure 108: A cartridge and plunger system injects resin into the liner mold.

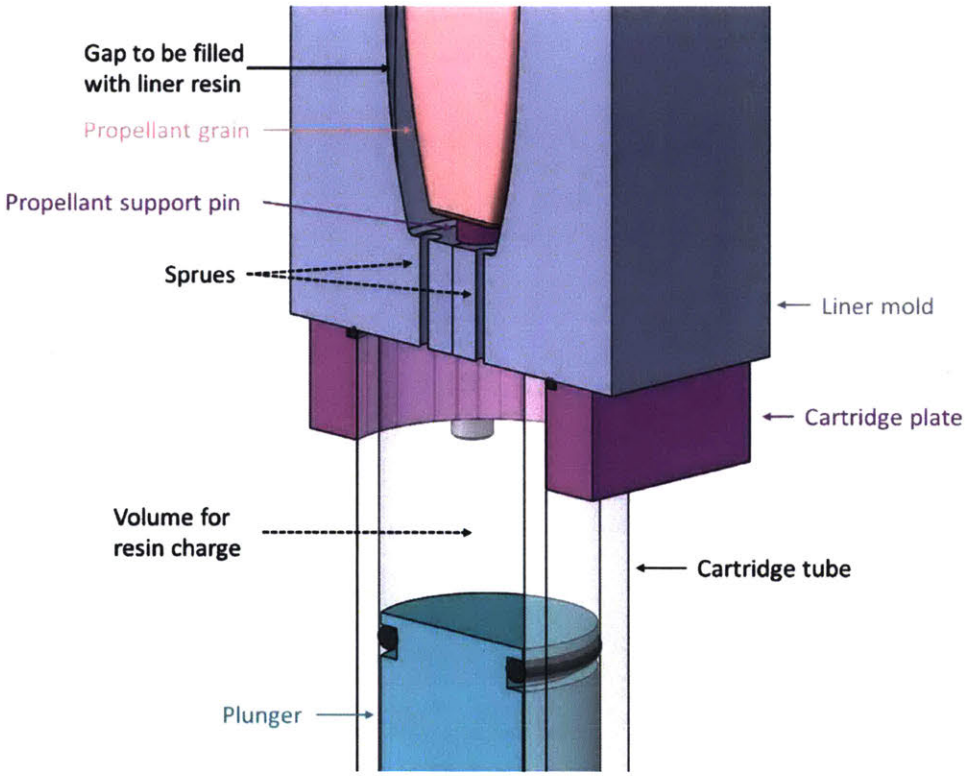

Figure 109: This cutaway view shows the volume of the cartridge which is filled with the resin charge, and the sprues through which the resin passes to enter the mold.

Figure 110: The assembled liner mold mounted on its stand.

Fourth, heat is applied to cure the ablative material resin. The mold is heated to 338 K (65 C) by an electric heating pad, and held at that temperature for 45 minutes. Because the propellant is in the mold at this point, excessive heating could degrade (or even ignite) the propellant. However, there is 60 K of margin between the curing temperature and the temperature at which the propellant would begin to degrade (398 K (125 C), at which point the oxamide would begin to decompose at a meaningful rate).

After heating, the ablative material is allowed to finish curing at room temperature for another 24 hours. Then, the mold is jacked open using its parting screws [Figure 111] The liner and propellant are removed [Figure 112]. The vestiges of the sprues and runners are then trimmed off with a razor blade. The resulting liner is shown in Figure 113.

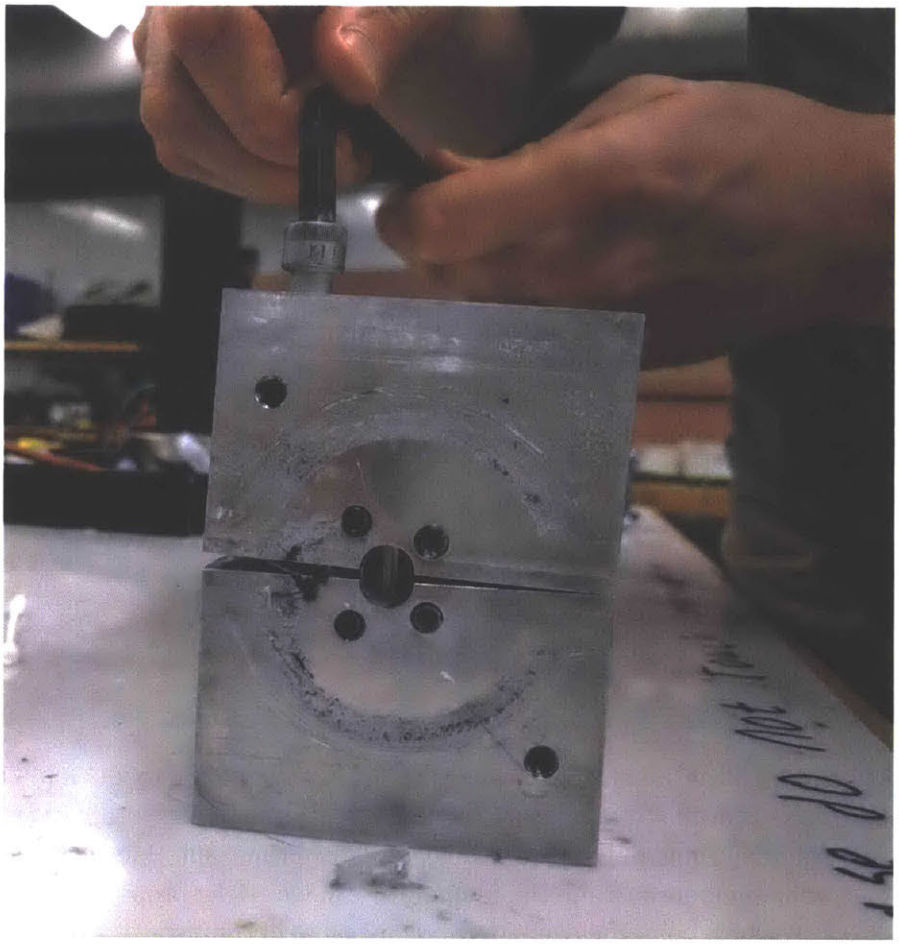

Figure 111: The liner mold is opened using the parting screws.

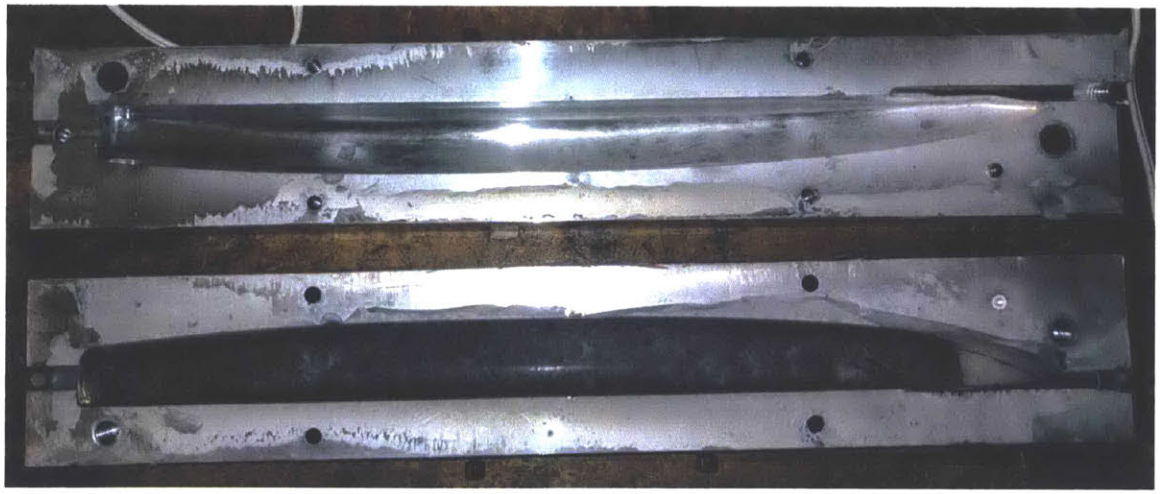

Figure 112: The open liner mold reveals the cured liner and propellant inside.

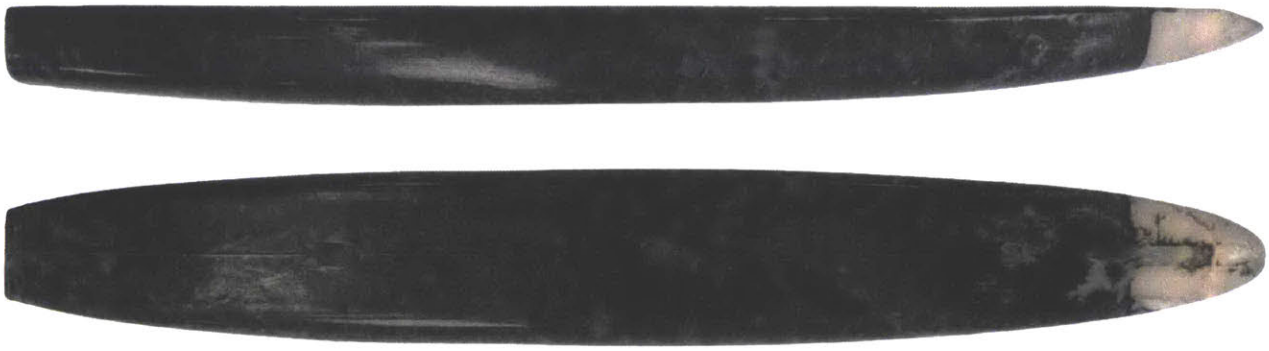

Figure 113: The propellant grain and liner, after removing from the liner mold and trimming the flashing and sprues. This photo was taken during a pathfinder casting with inert propellant; the propellant is white to signal that it is inert.

6.2.5 Starter grain installation

After the liner casting, the starter grain is installed into the aft face of the propellant. The starter grain is a small piece of faster-burning propellant which helps ignite our slower-burning propellant and kick up the chamber pressure. In the present prototype, the starter grain is made from "Vmax" ammonium perchlorate composite propellant, supplied by Cesaroni Technology Inc. of Gormley, Ontario.

First, a cork borer is used to cut a small cylinder (0.25 inch, 6.4 mm diameter) of starter propellant (the starter grain) from a larger grain supplied by Cesaroni. Then, the cork borer is used to cut a matching hole into the aft face of our propellant grain [Figure 114]. Finally, the starter grain is inserted into the hole [Figure 115].

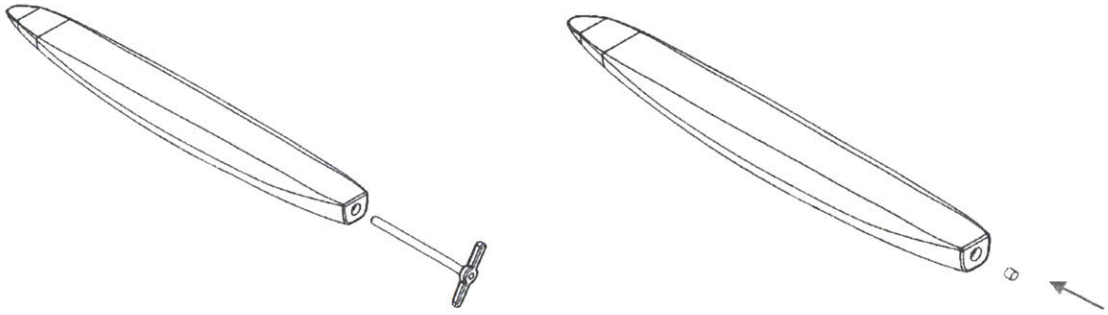

Figure 114: A cork borer is used to install the starter grain.

Figure 115: A starter grain (brown-red, center of image) after installation.

6.2.6 Radiographic inspection

The propellant and liner are then radiographically inspected for voids. In our early production runs we used 2D x-ray imaging, but a computed tomography scan would be preferred.

X-ray imaging was performed by the MIT Nuclear Science and Engineering Department. The imaging rig consisted of an x-ray tube placed 0.3 m in front of the sample, a gadolinium oxysulfide scintillator panel placed immediately behind the sample, and a DSLR camera placed 1 m behind the scintillator [Figure 116].

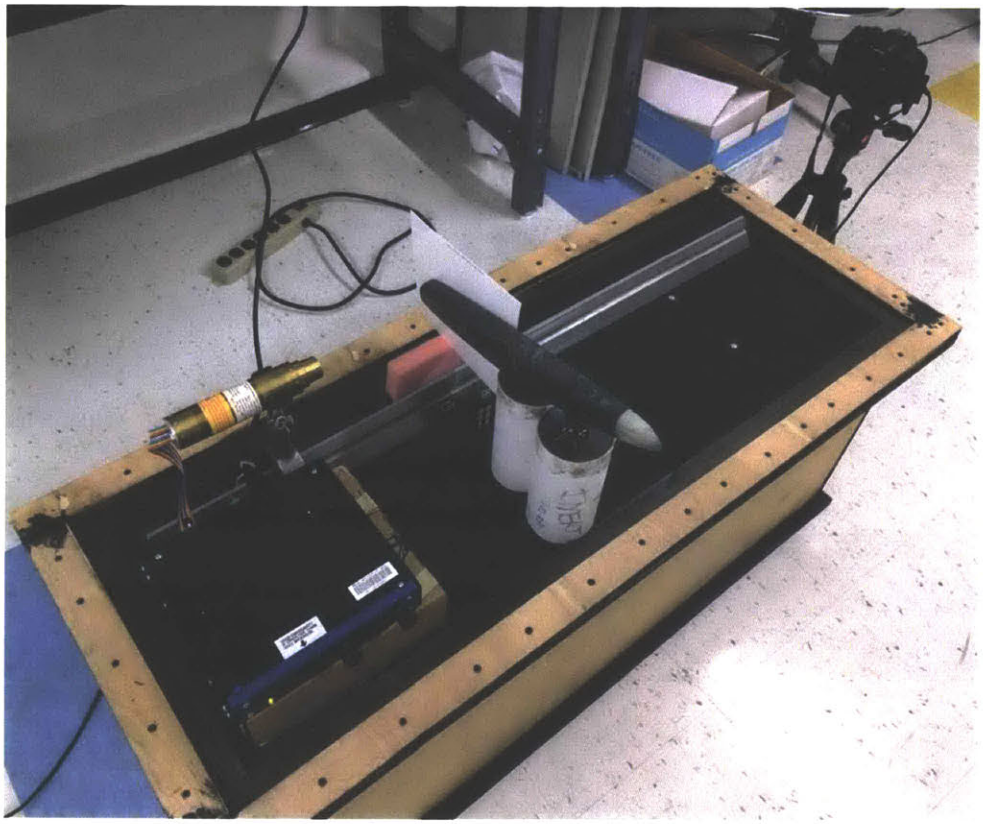

Figure 116: An improvised x-ray imaging rig was used to inspect our initial pathfinder product.

Example x-ray images are shown in Figure 117, with a model cross section and visible-light photographs for comparison. Two interesting measurements can be made from the image: the size and number of voids, and the thickness of the liner.

Figure 118 marks the location of visible voids in the x-ray image. Two large features are seen near the starter grain (right side of image), likely tears made in the propellant when the starter grain hole was cut out. The remainder of the image shows 16 voids with diameters between 2 and 4 mm, which together have a volume of 260 mm^3. Despite the large number of voids, the relative density of the propellant is still over 99%: 260 mm^3 of voids are spread through 90,000 mm^3 of propellant in the image.

I suspect that this void distribution and relative density are acceptable, and will not significantly impact the performance of the motor. However, this hypothesis must be tested against experimental data from

static firings of the motor. Using static firing data to develop void allowable for radiographic inspection will be an area of future research.

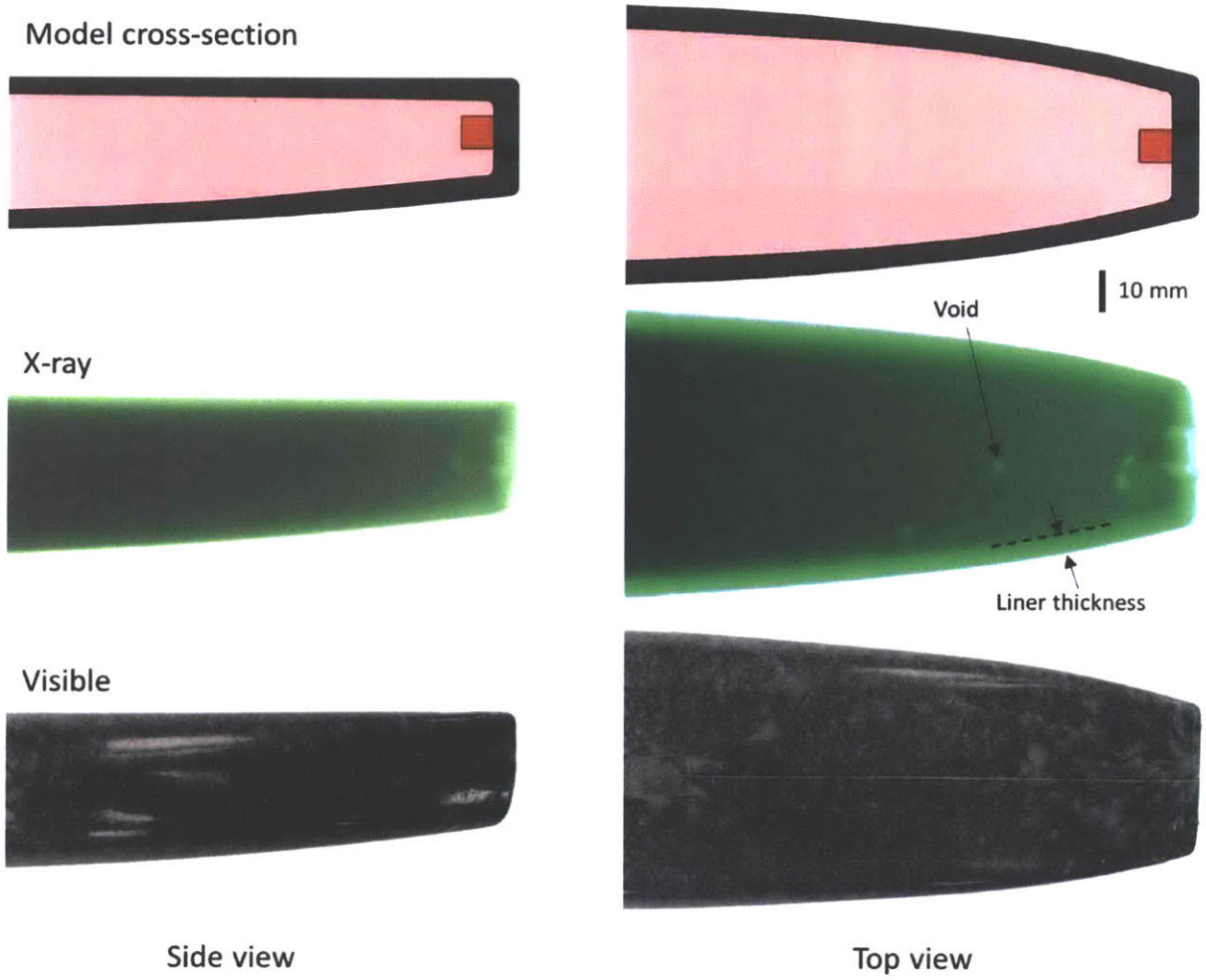

Figure 117: Radiographic inspection reveals small voids in the propellant grain, and shows the liner thickness to be proper and uniform. This figure compares CAD cross sections (top), x-ray images[24] (middle) and visual-light photographs (bottom) of the aft end of the propellant and liner.

[24] X-ray images were produced by a 42 kV, 45 μA x-ray source on a gadolinium oxysulfide scintillator, and captured with a DSLR camera (Canon EOS REBEL T2i) using a f/3.5 lens, 5 minute exposure, and 400 ISO sensitivity.

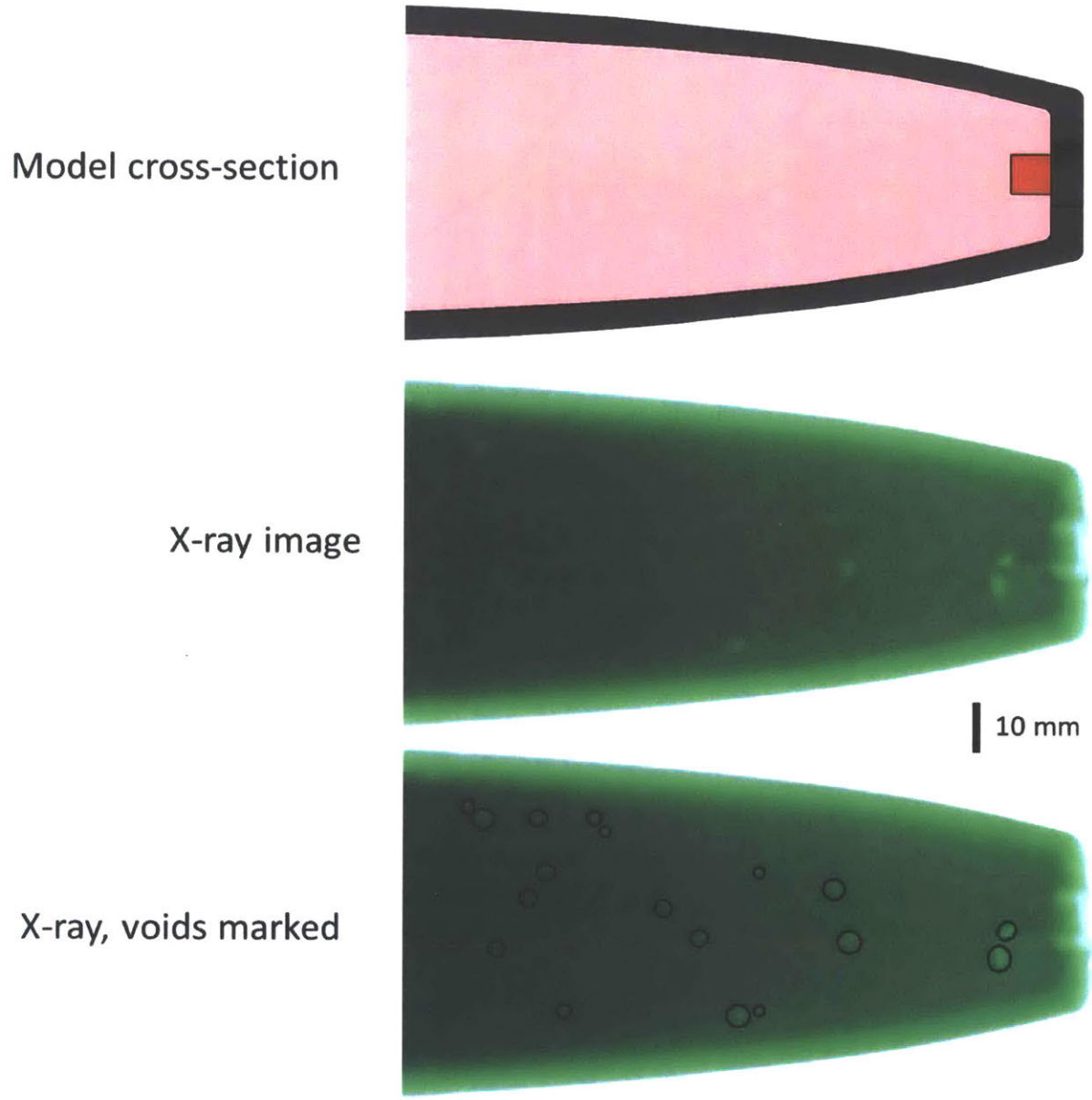

Figure 118: Analysis of the x-ray image reveals voids in the propellant, and can be used to estimate the relative density.

6.2.7 Fibrous insulation wrap

Finally, the fibrous insulation is wrapped around the propellant and liner. The wrap is an insulating layer of dry fiberglass cloth, which reduces thermal conduction from the liner to the motor case.

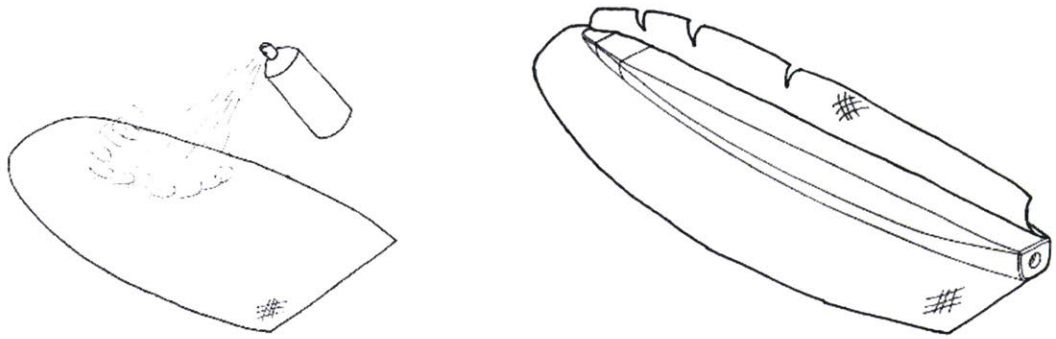

Figure 119: Fiberglass cloth is sprayed with a light amount of adhesive and then wrapped around the liner and propellant to form the fibrous insulation layer.

First, a sheet of fiberglass cloth (1.4 ounce/yard^2) is sprayed with a light coat of spray adhesive. Then, the cloth is then wrapped onto liner and propellant [Figure 119]. The fibrous insulation occupies a 0.6 mm (0.025 inch) gap between the liner and the motor case; 3 to 5 plies are required for a snug fit. The result is shown in Figure 120. This completes the propellant package.

Figure 120: The finished propellant package, with fibrous insulation wrapped around the propellant and liner.

6.3 Nozzle Production

The nozzle was cast in zirconia ceramic using a multi-piece mold. The following subsections justify the selection of casting as the nozzle manufacturing process, describe the casting procedure, and present the design of the molds used.

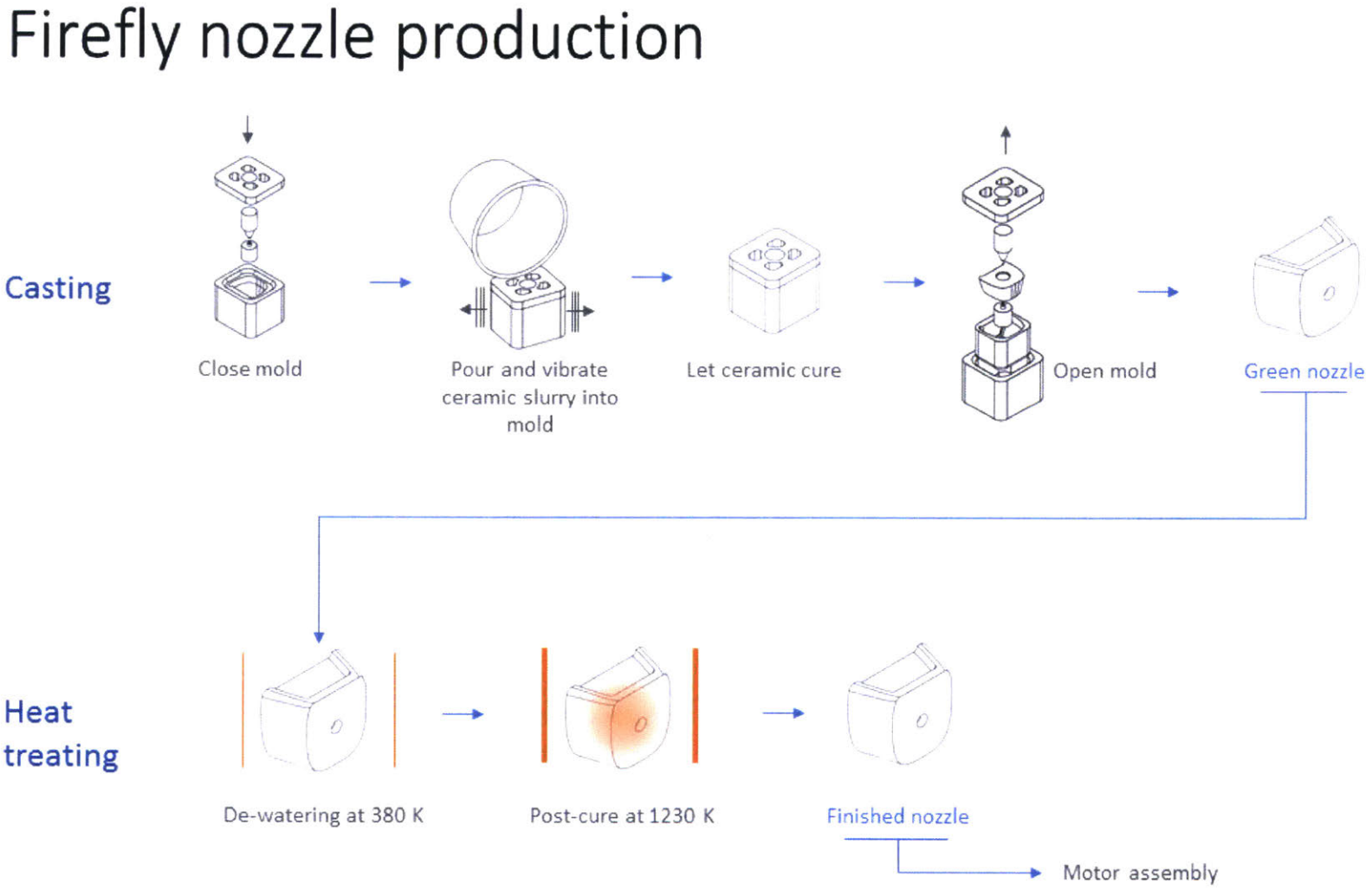

Figure 121: Nozzles are cast from a ceramic slurry and then heat treated.

6.3.1 Selection of manufacturing technique

Casting is the preferred method for manufacturing complex shapes from high-temperature ceramics. A wide variety of castable ceramics are available, and (once a mold is made) making parts is easy.

Machinable ceramics are available, but they are difficult to machine, and the selection of material properties is smaller than that of castable ceramics. Specifically, the thermal conductivity of high-performance machinable ceramics (e.g. [73]) is too high for the Firefly nozzle application. Machining the complex geometry of the nozzle would be difficult, and tooling cost would be high due to rapid wear.

Additively manufacturing for ceramics is possible, but still in its infancy [74]. The properties of these materials are not yet well known, particularly at high temperatures, and the dimensions of final parts are uncertain. At this stage, their use would present an inconveniently high developmental risk. However, printed ceramics may be of interest to later versions of Firefly, once the technology has matured.

6.3.2 Nozzle production procedure

To produce the nozzle, a ceramic slurry is cast in a mold. The green (i.e. not yet sintered) part is then removed from the mold and heat treated.

Mold - The mold has five components, as shown in Figure 122. A cup and lid (shown in grey) support and align the other mold components. Two cores (pink) form the inner, convergent-divergent surface of the nozzle. A flexible mold liner (cyan) forms the outer faces of the nozzle. A flexible liner is used because these features have overhangs [Figure 123], so the liner must be stretched off of the nozzle during demolding.

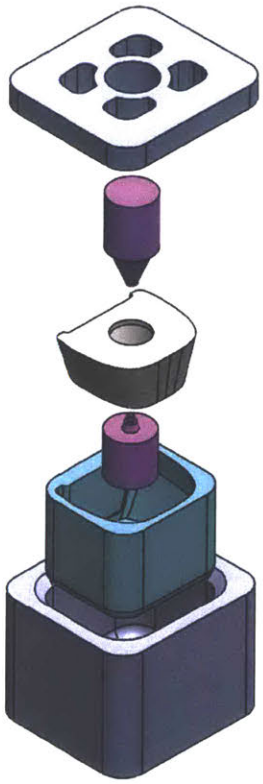

Figure 122: A five-part 3D printed mold is used to cast the nozzle.

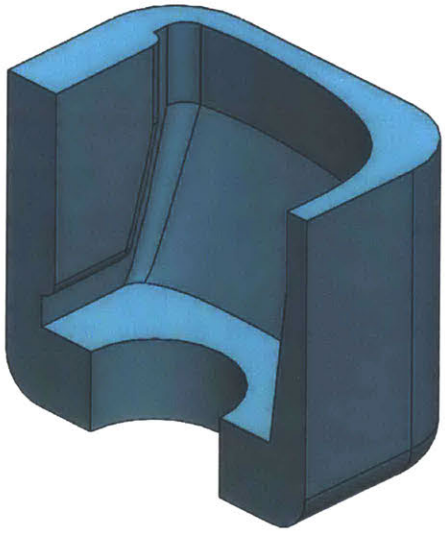

Figure 123: The mold has an overhang, so it is made from a flexible material which can be peeled off of the nozzle.

The rigid mold parts are printed on a Form 2 printer supplied by FormLabs of Somerville, Massachusetts. The print job used the Standard Resin and a 25 µm layer thickness. The flexible mold insert was cast from silicone rubber R2374, supplied by Silpak Inc. of Pomona, California.

Casting – First, the mold is assembled and mounted on a vibrating platform. Then, ceramic slurry is mixed. The ceramic is Rescor 760 zirconia, supplied by Cotronics Corp. of Brooklyn, NY. The slurry is supplied in two parts, a solid powder base and a liquid activator, which are weighed out and mixed. The slurry does not flow well under gravity alone, but with vibration it can be poured into the molds.

Figure 124: Two nozzle molds are mounted on a vibrating platform and filled with ceramic slurry.

The ceramic is left to cure for 24 hours, then the mold is opened and the green nozzle is removed.

Heat treating – Two heat treating steps are performed. First, the nozzle is heated to 380 K for 2 hours to remove water from the ceramic (the activator liquid contains water). The de-watering step is performed in a toaster oven. Second, the nozzle is post-cured at 1230 K. The high-temperature post-cure sinters together the particles of ceramic powder, increasing the strength of the part [75]. A programmable kiln is used for this step to achieve high temperatures and carefully control the heating rate.

6.4 Motor Assembly

After the propellant package, motor case halves, and nozzle are produced, they are assembled into a finished motor.

First, the nozzle is bonded to the aft motor case half. The bond is made with Resbond 904 zirconia adhesive supplied by Cotronics Corp.

Second, the motor halves are joined together around the propellant package. The mid-case joint is fastened together with 4 axial screws and 6 snap-tab screws. This completes the motor production process.

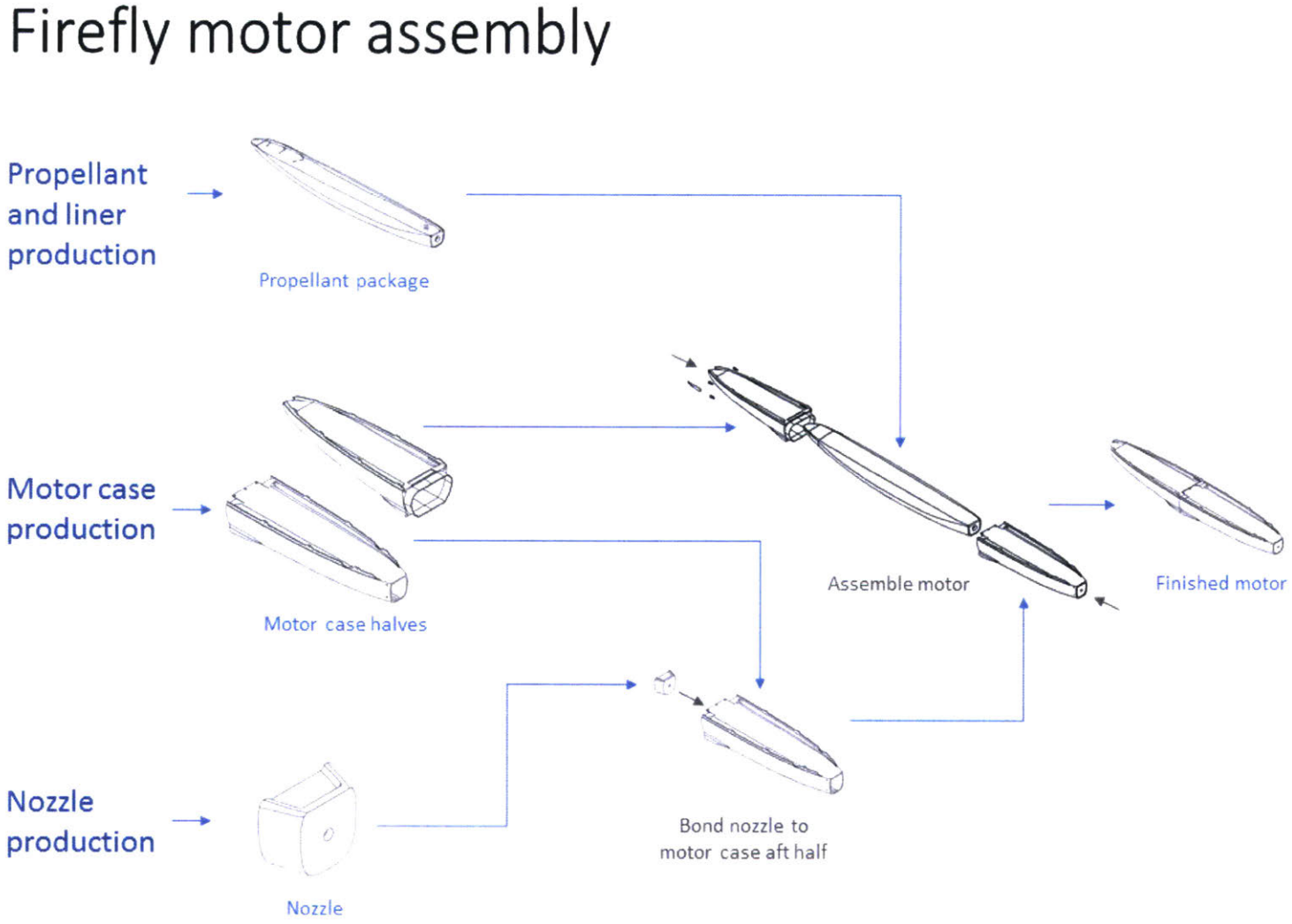

Figure 125: Flow-chart of the motor assembly process.

7 Conclusion

This thesis presented the development, modeling, and testing of a slow-burning solid rocket propulsion system. Interest in such system was motivated by an examination of the current capabilities of aircraft systems. Currently, no aircraft smaller than 10 kg are capable of flight faster than 100 m s^{-1}. It was found that filling this gap requires advances in propulsion technology. Slow-burning solid rocket motors were identified as an appealing solution to the propulsion needs of small, fast unmanned aerial vehicles (UAVs).

Slow-burning solid rocket motors require slow-burning propellant with a tailorable burn rate. A family of ammonium perchlorate composite propellants doped with the burn rate suppressant oxamide was developed to meet this need. To facilitate adjustment of the burn rate, a model of oxamide's effect on burn rate was derived from physical first principles and confirmed with strand burner and subscale motor experiments.

The key challenges to the development of small, slow-burning solid rocket motors were identified. Design principles for their solution were presented and applied to an example vehicle and motor. These principles include integrated motor-vehicle configurations, thrust profiles using segmented grains of variable burn rate, thin ablative thermal protection, and laser ignition.

Finally, production techniques for small, slow burning solid rocket motors were presented. These include additive manufacturing of thin-wall motor cases from titanium alloy. The example vehicle configuration required a complex case geometry; its production provided a case-study of additive manufacturing for propulsion components.

Continued development will yield new capabilities in compact, high-power propulsion. This propulsion technology will make feasible a new class of small, fast aircraft.

References

[1] E. Jones, E. Oliphant, P. Peterson and e. al., "SciPy: Open Source Scientific Tools for Python," 2001-. [Online]. Available: http://www.scipy.org/.

[2] B. N. Taylor and A. Thompson, "The International System of Units (SI)," National Institute of Standards and Technology , Gaithersburg, 2008.

[3] IHS Markit, Jane's All the World's Aircraft: In Service, London: IHS Markit, 2016.

[4] IHS Markit, Jane's All the World's Aircraft: Unmanned, London: IHS Markit, 2016.

[5] T. Tao, "Design and development of a high-altitude, in-flight-deployable micro-UAV," Massachusetts Institute of Technology, Cambridge, 2012.

[6] AeroVironment, "AeroVironment Inc. | Unmanned Aircraft Systems," 2016. [Online]. Available: https://www.avinc.com/.

[7] Raytheon, "Precision Weapons," 2016. [Online]. Available: http://www.raytheon.com/capabilities/precision/.

[8] Wikimedia Foundation, "Wikipedia, the Free Encyclopedia," 2016. [Online]. Available: en.wikipedia.org.

[9] B. Tipton, Interviewee, *Firefly UAV design review.* [Interview]. 2016.

[10] M. Lambert, "Lambert Microturbines," [Online]. Available: http://www.lambert-modellturbinen.de/html/english.html.

[11] HobbyKing Inc., "Dr. Mad Thrust Series Motor B3682 - 1700kv for 90mm EDF / 6S," 2017. [Online]. Available: https://hobbyking.com/en_us/dr-mad-thrust-series-motor-b3682-1700kv-for-90mm-edf-6s.html.

[12] HobbyKing Inc., "NGH GT9 9cc Gas Engine With Rcexl CDI Ignition," 2017, [Online]. Available: https://hobbyking.com/en_us/ngh-gt9-9cc-gas-engine-with-rcexl-cdi-ignition.html.

[13] C. Rossi, S. Orieux, B. Larangot, T. Do Conto and D. Esteve, "Design, fabrication and modeling of solid propellant microrocket-application to micropropulsion," *Sensors and Actuators A,* vol. 99, no. 1-2, p. 125–133, 2002.

[14] R. Valentine, " Ronald Valentine Engines," [Online]. Available: http://www.ronald-valentine-engines.com/Engine_Collection.html.

[15] Cesaroni Technology Inc., "Pro-X: a family of commercial-grade solid rocket motor systems," 2012. [Online]. Available: http://www.pro38.com/.

[16] G. P. Sutton and O. Biblarz, Rocket Propulsion Elements, Hoboken: John Wiley & Sons, 2010.

[17] N. Kubota, Propellants and Explosives: Thermochemical Aspects of Combustion, Hoboken: John Wiley & Sons, Inc., 2015.

[18] C. Guirao and F. A. Williams, "A Model for Ammonium Perchlorate Deflagration between 20 and 100 atm," *AIAA Journal,* 1971.

[19] J. K. Chen and T. Brill, "Chemistry and Kinetics of Hydroxyl-terminated Polybutadiene (HTPB) and Diisocyanate-HTPB Polymers during Slow Decomposition and Combustion-like Conditions," *Combustion and Flam,* 1991.

[20] T. McCreary, Experimental Composite Propellant, Murray, 2014.

[21] C. Huggett, C. E. Bartley and M. M. Mills, Solid Propellant Rockets, Princeton: Princeton University Pres, 1960.

[22] 3M, "Dynamar Curative/Bonding Agent HX-752," 2000. [Online]. Available: http://www.machichemicals.com/pdf/3M_HX-752.pdf.

[23] M. L. Gross and M. W. Beckstead, "Steady-State Combustion Mechanisms of Ammonium Perchlorate Composite Propellants," *Journal of Propulsion and Power,* vol. 27, no. 5, pp. 1064-1078., 2011.

[24] E. W. Price and R. K. Sigman, "Combustion of Aluminized Solid Propellants," in *Progress in Astronautics and Aeronautics: Solid Propellant Chemistry, Combustion, and Motor Interior Ballistics*, Reston, American Institute of Aeronautics and Astronautics, 2000, pp. 663-688.

[25] S.-T. Lee, E. W. Price and R. K. Sigman, "Effect of Multidimensional Flamelets in Composite Propellant Combustion," *Journal of Propulsion and Power,* vol. 10, no. 6, pp. 761-768, 1994.

[26] Orbital ATK, "Propulsion Products Catalog," October 2016. [Online]. Available: https://www.orbitalatk.com/flight-systems/propulsion-systems/docs/2016%20OA%20Motor%20Catalog.pdf.

[27] Z. Ma, F. Li and H. Bai, "Effect of Fe2O3 in Fe2O3/AP Composite Particles on Thermal Decomposition of AP and on Burning Rate of the Composite Propellant," *Propellants, Explosives, Pyrotechnics,* vol. 31, no. 6, pp. 447-451, 2006.

[28] D. Trache, F. Maggi, I. Palmucci, L. T. DeLuca, K. Khimeche, M. Fassina, S. Dossi and G. Colombo, "Effect of amide-based compounds on the combustion characteristics of composite solid rocket propellants," *Arabian Journal of Chemistry,* 2015.

[29] V. G. Ghorpade, A. Dey, L. S. Jawale, A. M. Kotbagi, A. Kumar and M. Gupta, "Study of burn rate suppressats in AP-based composite propellants," *Propellants, Explosives, Pyrotechnics,* vol. 35, pp. 52-56, 2010.

[30] L. H. Caveny, M. Summerfield, R. C. Strittmater and A. W. Barrows, "Solid Propellant Flammability Including Ignitability and Combustion Limits," Ballistics Research Laboratories, Aberdeen, 1974.

[31] D. Tingfa, "Thermal decomposition studies of solid propellant binder HTPB," *Thermochemical Acta,* vol. 138, pp. 189-197, 1989.

[32] F. M. Tayler and L. L. Bircumshaw, "The Thermal Decomposition of Oxamide," *J. Chem. Soc.,* pp. 3405-3410, 1956.

[33] National Institute of Standards and Technology, "NIST Chemistry WebBook," 2016. [Online]. Available: http://webbook.nist.gov/chemistry/.

[34] Y. Fabignon, O. Orlandi, J. F. Turbert, D. Lambert and J. Dupays, "Combustion of Aluminum Particles in Solid Rocket Motors," in *AIAA/ASME/SAE/ASEE Joint Propulsion Conference and Exhibit*, Hunstville, 2003.

[35] C. Price, T. Boggs and R. Derr, "Modeling of Solid Monopropellant Deflagration," *AIAA 16th Aerospace Sciences Meeting,* 1978.

[36] B. T. C. Zandbergen, "Physical properties solids," T.U. Delft, 2005. [Online]. Available: http://www.lr.tudelft.nl/en/organisation/departments/space-engineering/space-systems-engineering/expertise-areas/space-propulsion/design-of-elements/rocket-propellants/solids/physical-properties/.

[37] E. H. Buyco and F. E. Davis, "Specific Heat of Aluminum from Zero to Its Melting Temperature and Beyond," *Journal of Chemical and Engineering Data,* vol. 15, no. 4, pp. 518-523, 1970.

[38] S. R. Ahman and M. Cartwright, Laser Ignition of Energetic Materials, Hoboken: John Wiley & Sons, 2015.

[39] M. W. Beckstead, R. L. Derr and C. F. Price, "A model of composite solid-propellant combustion based on multiple flames," *AIAA Journal,* vol. 8, no. 12, pp. 2200-2207, 1970.

[40] V. P. Sinditskii, V. Y. Ergoshev, A. I. Levshenkov and V. V. Serushkin, "Ammonium Nitrate: Combustion Mechanism and the Role of Additives," *Propellants, Explosives, Pyrotechnics,* vol. 30, no. 4, pp. 269-280, 2005.

[41] H. O. Toft, "Voids in Solid Propellants," Dansk Amatør Raket Klub, Copenhagen, 2002.

[42] D. M. Bates and S. and DebRo, "R Documentation: Nonlinear Least Squares," Eidgenössische Technische Hochschule (ETH) Zürich, [Online]. Available: https://stat.ethz.ch/R-manual/R-devel/library/stats/html/nls.html.

[43] L. e. a. Gautier, "Documentation for rpy2," 2016. [Online]. Available: https://rpy2.readthedocs.io/en/version_2.8.x/.

[44] A. Parhi, V. Mahesh, A. Shaji, G. Levin, P. J. Abraham and V. Srinivasan, "Challenges in the Development of a Slow Burning Solid Rocket Booster," *Aerospace Science and Technology,* vol. 43, pp. 437-444, 2015.

[45] A. Ponomarenko, "Rocket Propulsion Analysis," 2017. [Online]. Available: http://www.propulsion-analysis.com.

[46] M. Natali, J. M. Kenny and L. Torre, "Science and Technology of Polymeric Ablative Materials for Thermal Protection Systems and Propulsion Devices: A Review," *Progress in Material Science,* no. 84, pp. 192-275, 2016.

[47] NASA Marshall Space Flight Center, "SRB Refurbishment Practices," [Online]. Available: https://oce.jpl.nasa.gov/practices/ops01.pdf.

[48] Y. V. Polezhaev, "Ablation," Thermopedia, 3 February 2011. [Online]. Available: http://www.thermopedia.com/content/285/.

[49] J. H. Koo, M. J. Miller, J. Weispfenning and C. Blackmon, "Silicone polymer composites for thermal protection system: fiber reinforcements and microstructures," *Journal of Composite Materials,* pp. 1-18, 2010.

[50] K. Gavitt, J. Hardgrove, T. Mueller, J. Weede, C. Johnson and M. Saville, "TRW's Ultra Low Cost LOX/LH2 Booster Liquid Rocket Engine," in *33rd Joint Propulsion Conference and Exhibit*, Seattle, 1997.

[51] Netzsch, "Polycrystalline Graphite — Thermal Conductivity," [Online]. Available: https://www.netzsch-thermal-analysis.com/us/materials-applications/polymers/polycrystalline-graphite-thermal-conductivity/.

[52] Cotronics, "960 Machinable alumina," [Online]. Available: http://www.cotronics.com/vo/cotr/pdf/55960.pdf.

[53] MatWeb, "Alumina, alpha Al2O3, 99.5%," [Online]. Available: http://www.matweb.com/search/datasheet.aspx?matguid=0654701067d147e88e8a38c646dda195&ckck=1.

[54] Cotronics, "902 Machinable Alumina Silicate," [Online]. Available: http://www.cotronics.com/vo/cotr/pdf/902.pdf.

[55] Zircar Ceramics, "Alumina-Silica Insulation Type ECO-27A & ECO-27B," [Online]. Available: http://www.zircarceramics.com/pages/rigidmaterials/specs/eco27.htm.

[56] Cotronics, "Rescor Castable Ceramics," [Online]. Available: http://www.cotronics.com/vo/cotr/pdf/onepg700.pdf.

[57] National Institute of Standards and Technology, "zirconium dioxide," 2016. [Online]. Available: http://webbook.nist.gov/cgi/cbook.cgi?ID=C1314234&Type=JANAFS&Plot=on.

[58] MatWeb, "Titanium Ti-6Al-4V (Grade 5), Annealed," [Online]. Available: http://asm.matweb.com/search/SpecificMaterial.asp?bassnum=MTP641.

[59] M. Vernacchia, "2016.07.18 case material trade study," Project Firefly internal document, Cambridge, 2016.

[60] United States Department Of Defense, "MIL-STD-1522A: Standard General Requirements for Safe Design and Operation of Pressurized Missile and Space Systems," Department Of Air Force, Washington, D.C., 1984.

[61] R. L. Norton, "Static Failure Theories," in *Machine Design: An Integrated Approach 2nd edition*, Worcester, Prentice Hall, 2000, pp. 253-316.

[62] J. R. Davis, "Corrosion of Aluminum and Aluminum Alloys," ASM International, 1999. [Online]. Available: http://www.asminternational.org/documents/10192/1849770/06787G_Sample.pdf.

[63] Federal Aviation Administration, "Metallic Materials Properties Development and Standardization MMPDS-08," 2013.

[64] EOS, "Materials for Metal Additive Manufacturing," [Online]. Available: http://www.eos.info/material-m.

[65] Renishaw plc, "Ti6Al4V ELI-0406 powder for additive manufacturing," Staffordshire, UK, 2016.

[66] "SAE 4340M Material Properties," MakeItFrom, [Online]. Available: http://www.makeitfrom.com/material-properties/SAE-AISI-4340M-300M-K44220-Silicon-Vanadium-Steel#Properties.

[67] L. Nastac, M. N. Gungor, I. Ucok, K. L. Klug and W. T. Tack, "Advances in investment casting of Ti–6Al–4V alloy: a review," *International Journal of Cast Metals Research,* vol. 19, no. 2, pp. 73-97, 2006.

[68] Renishaw plc, "AM 400 additive manufacturing system," Staffordshire, UK, 2015.

[69] M. Kirby, Interviewee, *Second round of Firefly printing.* [Interview]. 7 May 2017.

[70] S. Wright, "3D printing titanium: Learning to learn from success," 11 Aug 2015. [Online]. Available: http://pencerw.com/feed/2015/8/6/3d-printing-titanium-learning-to-learn-from-success. [Accessed 2017].

[71] Stanley Engineeered Fasteing, "HELI-COIL: Corrosion Screw Threads and Methods," 2014.

[72] Hexion Specialty Chemicals, "Laminating resin MGS L 285," January 2006. [Online]. Available: http://www.cozybuilders.org/ref_info/MGS_L285_properties.pdf.

[73] Cotronics, "960 Machinable Alumina," [Online]. Available: http://www.cotronics.com/vo/cotr/pdf/55960.pdf.

[74] FormLabs, "Usage and Design Guide: Ceramic Resin," January 2017. [Online]. Available: https://formlabs.com/media/upload/formlabs_ceramic-usage-design-guide.pdf.

[75] Y.-M. Chiang, D. P. Birnie and W. D. Kingery, Physical Ceramics: principles for ceramic science and engineering, New York: John Wiley & Sons, 1997.

[76] National Oceanic and Atmospheric Administration, "Aircraft Operations," [Online]. Available: https://www.omao.noaa.gov/learn/aircraft-operations/about/hurricane-hunters.

[77] United States Air Force Reserve, "53rd Weather Reconnaissance Squadron "Hurricane Hunters"," 2011. [Online]. Available: http://www.403wg.afrc.af.mil/About/Fact-Sheets/Display/Article/192529/53rd-weather-reconnaissance-squadron-hurricane-hunters/.

[78] Office of the Secretary of Defense: Strategic Capabilities Office, "Perdix fact sheet," 2017. [Online]. Available: https://www.defense.gov/Portals/1/Documents/pubs/Perdix%20Fact%20Sheet.pdf.

[79] AeroVironment, "Switchblade," 2017. [Online]. Available: https://www.avinc.com/images/uploads/product_docs/SB_Datasheet_2017_Web_rv1.1.pdf.

[80] University of Pennsylvania, "Nusselt Correlations," [Online]. Available: http://www.seas.upenn.edu/~meam333/correlation/CorrelationsList.pdf.

[81] F. A. Guevara, B. B. McInteer and W. E. Wageman, "High-Temperature Viscosity Ratios for Hydrogen, Helium, Argon and Nitrogen.," *Phys. Fluids,* vol. 12, no. 12, 1969.

[82] LMNO Engineering, Research, and Software, Ltd., "Gas Viscosity Calculator," 2013. [Online]. Available: http://www.lmnoeng.com/Flow/GasViscosity.php.

[83] J. Etele, J. P. Sislian and B. Parent, "Effect of Rocket Exhaust Configurations on Ejector Performance in RBCC Engines," *AIAA Journal of Propulsion and Power,* vol. 21, no. 4, 2005.

[84] C. E. Peters, W. J. Phares and T. H. M. Cunningham, "Theoretical Studies of Ducted Mixing and Burning of Coaxial Streams," *AIAA Journal of Spacecraft,* vol. 6, no. 12, 1969.

[85] S. Ueda, T. Hiraiwa, M. Takegoshi, K. Tani, T. Kanda and H. Nagata, "Subsonic Flight Experiments of Ejector-Rocket using Hybrid-Rocket CAMUI," in *AIAA/DLR/DGLR International Space Planes and Hypersonic Systems and Technologies Conference*, Bremen, Germany, 2009.

[86] B. Rasof and V. P. Roberts, "Theoretical Subsonic Performance of a Ducted Rocket," California Institute of Technology, Pasadena, 1945.

[87] J. Etele, B. Parent and J. P. Sislian, "Analysis of Increased Compression Through Area Constriction on Ejector-Rocket Performance," *AIAA Journal of Spacecraft and Rockets,* vol. 44, no. 2, 2007.

[88] SRM University, "The Turbofan Engine," [Online]. Available: http://www.srmuniv.ac.in/downloads/turbofan-2012.pdf.

[89] M. Lambert, "Lambert Microturbines T32 Kolibri: Important User Information and Check List," [Online]. Available: http://www.lambert-modellturbinen.de/Kolibri-Checklist.pdf.

[90] H. Singh and H. Shekhar, Solid Rocket Propellants: Science and Technology Challenges, Royal Society of Chemistry, 2016.

[91] R. Nakka, "Richard Nakka's Experimental Rocketry," [Online]. Available: https://www.nakka-rocketry.net/.

[92] S. B. Judd and M. T. Vernacchia, "Solid Rocket Propellant Combustion, 2.28 Final Report," Unpublished, Cambridge, 2015.

1 Appendix: Potential missions for small, fast UAVs

This appendix presents a few hypothetical missions for small, fast, deployable UAVs. This class of aircraft can be usefully applied for storm monitoring, as a decoy, as a rapid reconnaissance platform, or as an ultra-low collateral damage weapon. While these potential missions provide important motivation, this work is devoted to the development of a flexible propulsion technology, not optimization for a particular mission.

Storm monitoring – Weather reconnaissance missions are flown into extreme storm systems to collect meteorological data for scientific and forecasting purposed. Small UAVs are currently unable to fly in extreme wind shear, so this data is collected by crewed aircraft [76] [77] or unguided dropsondes. However, a transonic UAV could have a sufficiently high ballistic coefficient to penetrate storm winds. This could enable precise measurements from a guided platform, while keeping people safely outside the storm.

Decoy – A small, fast UAV could be deployed from a host aircraft to serve as a decoy. The decoy could be used to distract hostile weapons from the more valuable host aircraft. Alternatively, many decoys could be launched to confuse measurements of the size or flight path of an air squadron.

Rapidly-deployed, over-the-horizon reconnaissance – There is interest in the aerospace and defense community to use rapidly-deployed UAV swarms as *intelligence, surveillance and reconnaissance* (ISR) tools. Current deployable UAVs (e.g. MIT Lincoln Lab's Perdix [78] [5]) offer excellent surveillance capabilities. However, their limited speed and range requires the host aircraft to fly close to the surveillance target, which may be tactically infeasible in certain scenarios. A faster, longer range deployable UAV could allow the host aircraft to remain at a greater standoff distance (i.e. over the horizon) from the target. It is also conceivable that, with a proper booster, small, fast UAVs could be deployed from ships, land vehicles, or man-portable platforms.

Ultra low collateral damage weapon – Small UAVs have been successfully deployed as high-precision, low collateral damage weapons systems (e.g. Aerovironment's Switchblade [79]). Deployment from a host aircraft can allow such systems to be fielded against more remote targets. Further, a transonic UAV could be used as a kinetic weapon, eliminating the need for a warhead and reducing collateral damage.

2 Appendix: Convection coefficient estimation

Thermal analysis of the motor requires estimates of the convection heat transfer to the motor from combustion gases, and from the motor to the surrounding air. This appendix presents the estimation of the convection coefficients of the internal and external flows on a typical small, slow-burning solid rocket motor for UAV propulsion.

To obtain a quick, rough estimate of the convection coefficients, I use Nusselt number correlations. These calculations are only approximations; their results should be viewed with skepticism and tested against experiments before being applied to critical designs.

The convection coefficient h is related to the Nusselt number Nu by the Stanton number formula:

$$S_t = \frac{h}{\rho\, v\, c_p} = \frac{Nu}{Re\ Pr}$$

Where:

- ρ is the density of the fluid.
- v is the fluid velocity over the surface.
- c_p is the fluid heat capacity.
- Nu is the Nusselt number.
- Re is the Reynolds number.
- Pr is the Prandtl number.

Solve for h:

$$h = \rho\, v\, c_p \frac{Nu}{Re\ Pr}$$

$$h = \rho\, v\, c_p \frac{Nu}{\left(\frac{\rho\, u\, L}{\mu}\right) Pr}$$

$$h = \frac{c_p\, \mu}{L} \frac{Nu}{Pr} = Nu \frac{k}{L}$$

where μ is the fluid viscosity and L is the length scale, and k is the fluid thermal conductivity.

Estimation of Nu and the other parameters required to calculate h is presented for the inner (combustion gas) flow in section A 2.1, and for the outer freestream) flow in section A 2.2.

2.1 Inner boundary: Combustion to liner

Calculation the Nusselt number is more complicated. For the inner boundary with the combustion gas, the correlation [80]

$$Nu = 0.023\, Re_D^{4/5} P_r^{0.3}$$

is used.

The length scale L is the diameter of the combustion chamber, approximately 40 mm.

The fluid velocity v is given by

$$v = \frac{\dot{m}}{\rho A} = 4.0 \text{ m s}^{-1}$$

Where $A = \pi \left(\frac{L}{2}\right)^2$ is the cross-sectional area of the combustion chamber.

I estimate the dynamic viscosity μ by averaging the viscosity of the majority gases in the exhaust, hydrogen (34% mole fraction) and carbon monoxide (31%) mole fraction. The viscosity of hydrogen at 1890 K is 3.26×10^{-5} Pa s (3.71 times its room temperature value) [81]. Sutherland's formula predicts the viscosity of carbon monoxide to be 5.84×10^{-5} Pa s at 1890 K, although I am not sure over what temperature range the coefficients of the formula are valid [82]. I assume the average viscosity of the exhaust to then be 4.6×10^{-5} Pa s.

These values give a Reynolds number of 4690, Nusselt number of 16.4, and a convection coefficient of $h = 81.5 \text{ W m}^{-2} \text{ K}^{-1}$.

Parameter	**Value for internal exhaust gas**
Prandtl number	0.52
length scale [m]	0.038
viscosity [Pa s]	4.60E-05
heat capacity [J / kg K]	2140
velocity [m/s]	4
density [kg/m^3]	1.42
Reynolds number	4.69E+03
Nusselt number	16.4
convection [W/ m^2 K]	81.5

The ablation gases from the liner will reduce the convection coefficient; this is not accounted for in the above analysis.

2.2 Outer boundary: Case to freestream

I could not find any Nusselt number correlations for flow over bodies which approximate the shape of a transonic UAV, so I use the flat plate correlations. The correlations for laminar and turbulent flow are different; I assume the flow is laminar until the local Reynolds number Re_x reaches 10^6, and then is turbulent.

Laminar:

$$Nu = 0.664 \, Re_L^{\frac{1}{2}} P_r^{\frac{1}{3}}$$

Turbulent:

$$Nu = \left(0.037 \, Re_L^{\frac{4}{5}} - 0.037 \, Re_x^{\frac{4}{5}} + 0.664 \, Re_x^{\frac{1}{2}} \right) P_r^{\frac{1}{3}}$$

These correlations are valid for $Re_L < 10^8$, our Re_L is $\approx 6 \times 10^6$.

Because the Nusselt number depends on the distance from the nose of the vehicle, x, the convection coefficient will also vary along the length of the vehicle. The convection coefficients are then calculated for each position on the vehicle using

$$h(x) = Nu(x)\frac{k}{L}$$

and assuming standard properties for dry air at 30,000 ft altitude.

Obviously, this model is limited. The heat transferred from the motor to the air will warm the outer boundary layer, changing its flow in ways which the model does not fully capture. Further, the airflow along a patch of the vehicle does not only depend on x, it also depends on the vehicle's shape and flight conditions. However, the above model is a decent first approximation.

3 Appendix: Effect of voids on propellant burn rate

This appendix presents a model for the effect of voids on propellant burn rate. This model is based on similar work by Toft [41]. In the main work, a linear model was proposed for the effect of relative density on the propellant burn rate:

$$\phi_v(D_r) = \frac{r(D_r)}{r^*} = b_v\,(D_r - 1) + 1$$

Where ϕ_v is the burn rate multiplier due to voids, D_r is the relative density, and b_v is a model parameter called the *void parameter*. b_v should be negative, i.e. relative densities less than one should increase the burn rate.

This model is derived from regression on a Monte-Carlo numerical simulation. A model was developed for the burning of propellant strand with voids. The Monte-Carlo simulation ran this model with a range of void counts and void sizes. A correlation between burn rate and relative density was extracted from the results.

3.1 Numerical model of propellant burn rate with voids

A numerical model was developed for the progress of a flame front through a 3-dimensional rod of propellant with spherical voids. It was assumed that the flame front advances at a constant rate r, and always advances normal to the burning surface. Therefore, a spherical void burning from the inside will remain spherical. The burnt volume is modeled as the union of a set of burnt spheres. These spheres expand in radius as the flame front progresses.

The model algorithm is illustrated by Figure 126. The algorithm progresses in discrete time-steps. It tracks 3 sets of spheres: active A, waiting W and burnt-out B.

Initially, A contains a single large sphere representing the nearly flat initial burning surface, and the voids in the propellant are represented by spheres in W (see top subfigure of Figure 126) . At each time step, the radius of each sphere in A is incremented by Δr. If a sphere $s \in W$ intersects a sphere in A, s is removed from W and added to A ("activated", second subfigure). If a sphere $t \in A$ is completely eclipsed by the other spheres in A, t is removed from A and added to B ("burnt-out", third subfigure).

At each time-step, the shape of the burning surface is computed. A grid is projected from the back side of the propellant rod onto the foremost surface of the union of spheres in A (bottom subfigure). Note that this technique does not permit overhangs of the propellant surface.

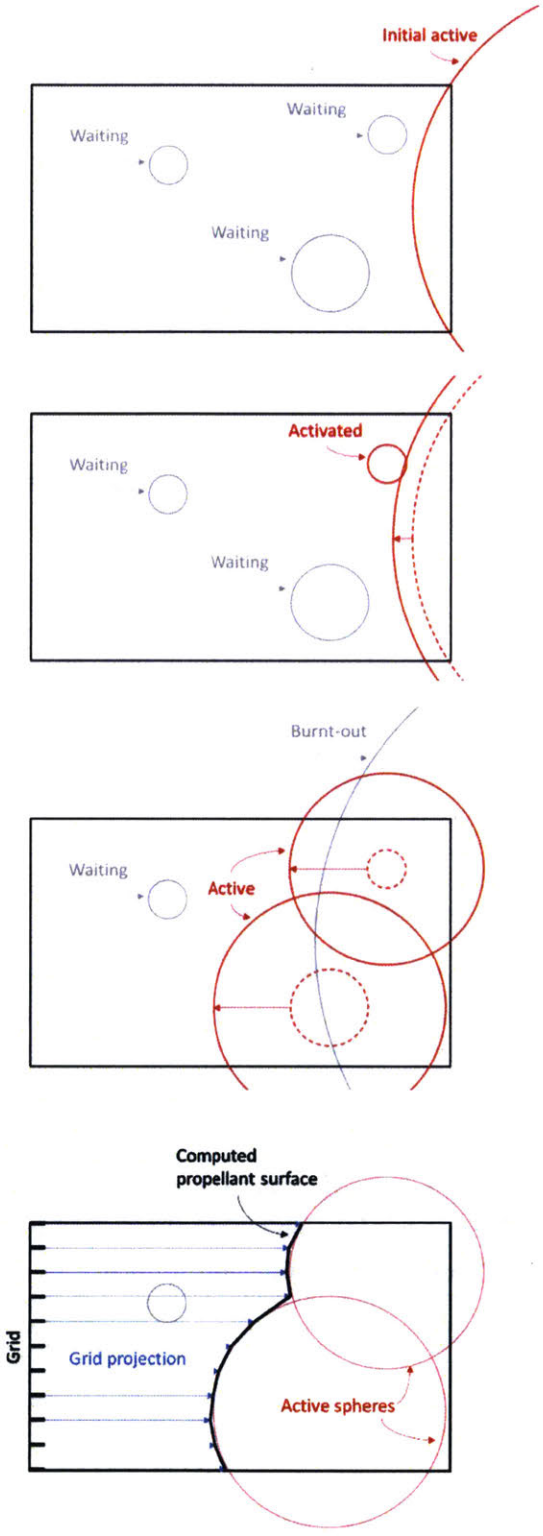

Figure 126: Void-burning model.

The progress of the flame front through a propellant rod is shown in Figure 127. The full model is 3-dimensional, but was run in two dimensions to produce this figure. The 2-D propellant rod contains 9 circular voids, of random location and radius, marked by black circles. Starting at the right, the flame front begins as a nearly flat (large-radius circle) surface. Its location at each time step is shown by a colored curve. As the flame front progresses through voids, it is accelerated and distorted.

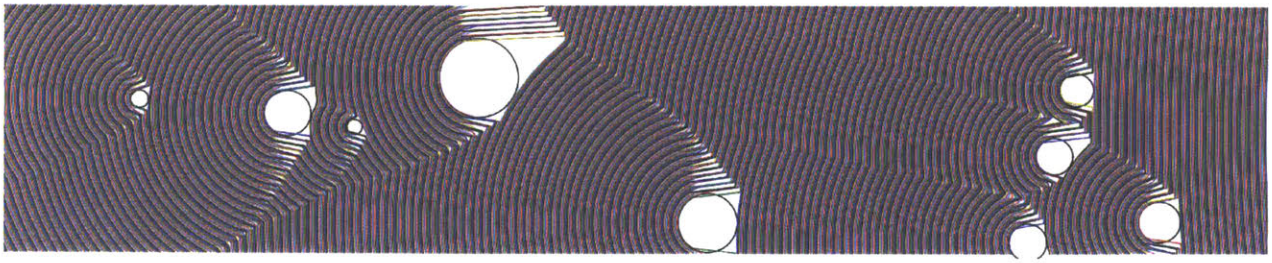

Figure 127: The progress of a flame front (right to left) through a 2D propellant rod with circular voids.

3.2 Monte-Carlo simulation of relative density's effect on burn rate

This model was run 400 times in a Monte-Carlo simulation. Propellant rods were modeled with $N = 10, 50, 100$ or 200 voids of random location and radius. The simulated propellant rods were 50 mm long, and the void radii were drawn from a normal distribution[25] of mean 0.5 mm and standard deviation 0.5 mm.

The results of this simulation are plotted in Figure 128. The results support the use of a linear model, and predict $b_v = -9.9$; i.e. relative densities less than one should strongly increase the burn rate. However, this prediction was not confirmed by a statistical analysis of experimental data collected in the strand burner. The experimental evidence showed a weak correlation between relative density and burn rate, with $b_v = -0.55 \pm 0.53$.

[25] Negative or zero radii were rejected and resampled.

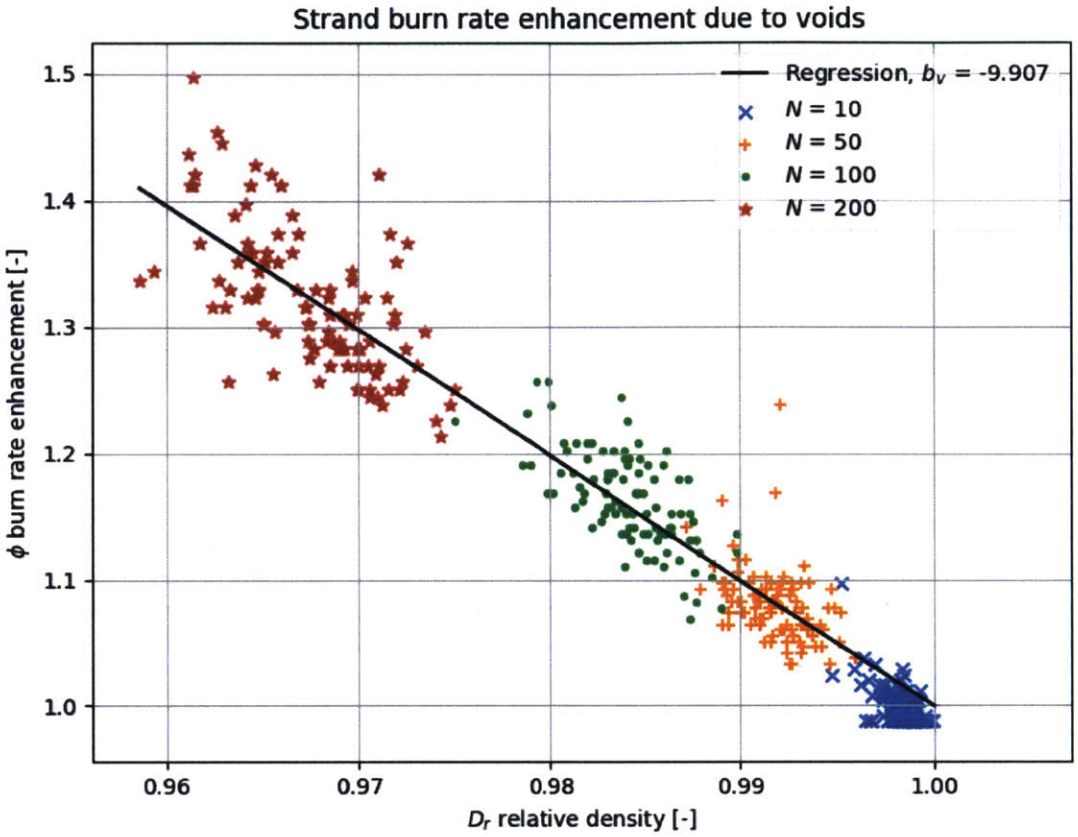

Figure 128: Effect of relative density on the propellant burn rate, as predicted by Monte Carlo simulation of a numerical void burning model.

----- END DOCUMENT -----

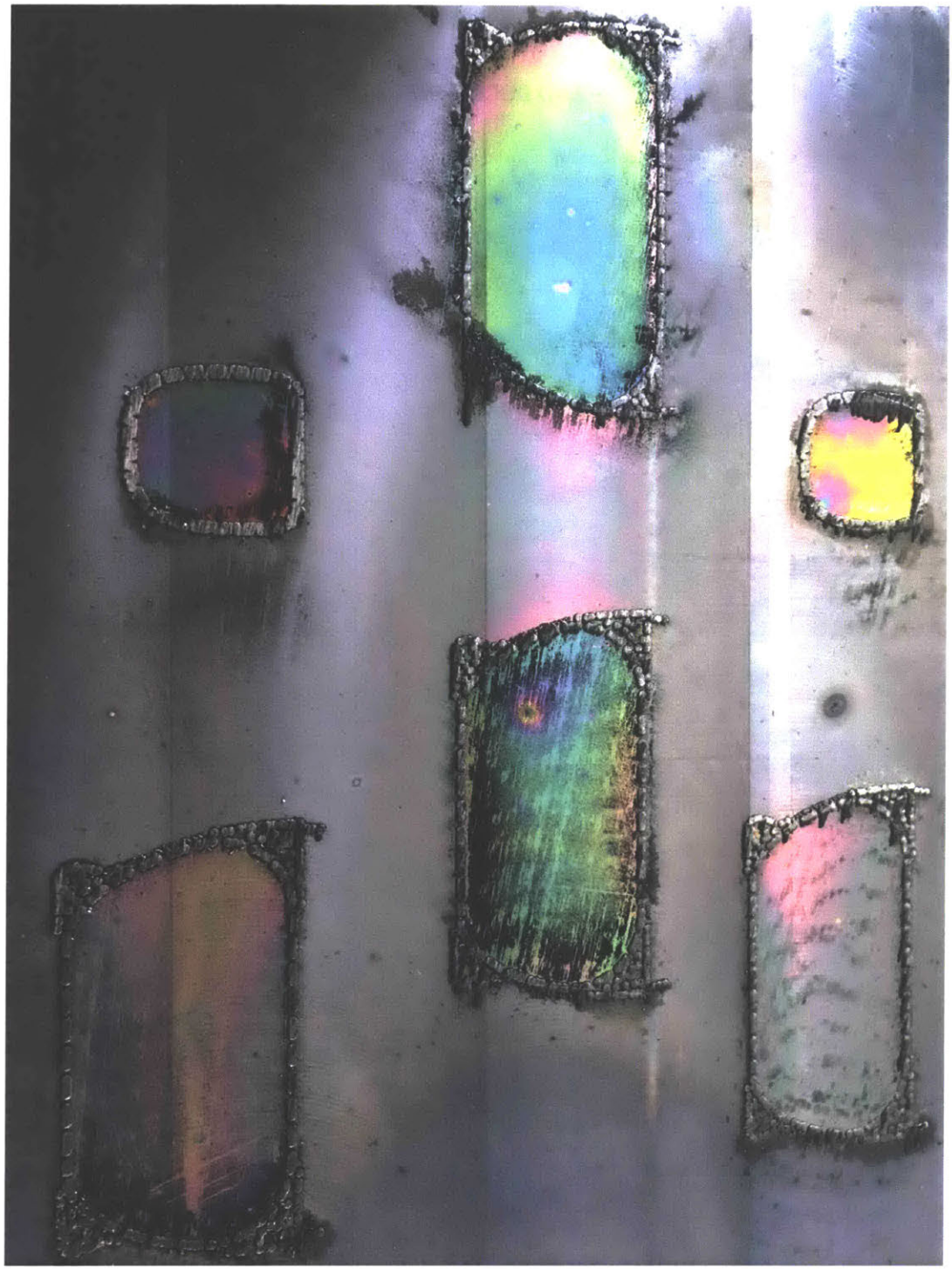

Back cover art: A used build plate from a metal additive manufacturing system, Renishaw plc.